Sedimentology and Sedimentary Geochemistry of the Eagle Ford Group, Texas

James D. Scaife

Thesis submitted to The University of Oxford for the degree of Doctor of Philosophy in Earth Sciences



Department of Earth Sciences and Linacre College, University of Oxford, Trinity Term 2017

Supervised by Prof. Joe Cartwright, Prof. Stephen Hesselbo and Dr. Micha Ruhl

”In the beginning the Universe was created. This has made
a lot of people very angry and been widely regarded
as a bad move” — Douglas Adams

Abstract

Sedimentology and Sedimentary Geochemistry of the Eagle Ford Group, Texas

James D. Scaife, Linacre College
Thesis submitted to The University of Oxford for the degree of Doctor of Philosophy in Earth Sciences
Trinity Term 2016

THE Eagle Ford Group is an organic-rich succession of rhythmically interbedded packstones and wackestones, deposited in the southern Western Interior Seaway during the Cenomanian-Turonian of the Upper Cretaceous. Recent investigations have suggested that either eustatic sea level change, astronomical forcings, change in primary productivity and dilution, or changes in local and global benthic oxygenation may be responsible for the Eagle Ford Groups lithological and geochemical variations. However, no consensus has yet been reached. Chapter 3 examines cm-scale geochemical, mineralogical and sedimentological changes to investigate the temporal and spatial variabilities of the Eagle Ford Group. This study suggests the stratigraphical cyclicity of the Eagle Ford Group is a function of alternating periods of high and low primary productivity and accumulation rates possibly modulated by the fertilizing effect of ash falls. Lateral variabilities are determined by the reworking of pelagic sediment by bottom currents, below storm wave base. Chapter 5 investigates changes in water-mass exchange, climate, water-column anoxia and hydrodynamics during the deposition of the Eagle Ford Group. The results of this study show four distinct stages in the deposition. The lowermost stratigraphic third of the Lower Eagle Ford was deposited under a humid climate with high continental runoff, anoxic/euxinic benthic conditions and exchange with a nutrient-rich water mass. The upper stratigraphic two thirds of the Lower Eagle Ford was deposited during a more arid climate, with lower continental runoff, a highly restricted anoxic benthic zone with some periods of euxinia, and little siliciclastic input. The lowermost stratigraphic half of the Upper Eagle Ford was deposited during a mostly humid climate with high continental runoff and the presence of a suboxic benthic zone that experienced multiple periods of oxygenation related to a more open water mass exchange. The upper stratigraphic half of the Upper Eagle Ford exhibits deposition under a more arid climate with lower continental runoff and reduced benthic oxygen content. Global controls, such as perturbations of the global carbon cycle, exert a fundamental role in the large-scale deposition of organic carbon. As such it is important to understand the effect and causes of global events when studying sedimentary systems. The Eagle Ford Group contains one such event Oceanic Anoxic Event 2 (OAE 2). However, the fundamental cause of OAE 2 is still poorly constrained. As such in Chapter 4 mercury concentrations are examined in sedimentary successions spanning the Mid-Cenomanian to Early Turonian interval. The data presented here are consistent with an initial magmatic pulse at the time of the MCE, with a second and greater, pulse at the onset of OAE 2, possibly related to the emplacement of LIPs in the Pacific Ocean and/or the High Arctic.

Extended Abstract

Sedimentology and Sedimentary Geochemistry of the Eagle Ford Group, Texas

James D. Scaife, Linacre College
Thesis submitted to The University of Oxford for the degree of Doctor of Philosophy in Earth Sciences
Trinity Term 2016

CURRENTLY there is a lack of understanding in the systems that form mudrocks. Furthermore, although mudrocks appear deceptively homogeneous at core-scale, they are often both temporally and spatially heterogeneous and complex. Furthermore, as a result of the recent revolution in unconventionals, comprehension of the depositional and sedimentological variabilities of mudrocks has become increasingly important. The Eagle Ford Group is an organic-rich mudrock, comprised of a succession of rhythmically inter-bedded packstones and wackestones, deposited in the southern Western Interior Seaway during the Cenomanian-Turonian with stratigraphic intervals encompassing both Oceanic Anoxic Event 2 (OAE 2) and the Mid-Cenomanian Event (MCE). This study uses an integrated multidisciplinary approach of sedimentology, mineralogy, geochemistry and stratigraphy to examine the local, regional and global processes that have led to its formation.

Recent investigations have suggested that either eustatic sea level change, astronomical forcings, change in primary productivity and dilution, or changes in benthic oxygenation may be responsible for the Eagle Ford Groups lithological alternations. However, no consensus has yet been reached which satisfactorily explains the vertical cyclicity and lateral variabilities that are visible in this formation. Chapter 3 examines the cm-scale sedimentological, geochemical and mineralogical changes of the packstone-wackestone couplets as well as whole core-scale stratigraphy, sedimentology and mineralogy. This chapter demonstrates that the depositional dynamics of the Eagle Ford Group are a function of primary productivity and reworking by bottom currents rather than eustatic sea level change. The vertical cyclicity occurs as a result of periods of low primary productivity and low accumulation rates forming foraminiferal wackestones, and periods of high productivity and high accumulation rates which lead to the formation of foraminiferal packstones. Chapter 3 suggests that these changes occur due to periodic fertilization of the nutrient limited southern Western Interior Seaway by iron, nitrates and other nutrients from ash falls derived from volcanic eruptions of the Cordilleran Orogenic Belt. Lateral variations are controlled by the deposition and reworking of pelagic sediment under the influence of oceanic currents, below storm wave base, resulting in the formation of carbonate sand ridges, sheets and isolated dunes. The isolation of these carbonate sand bodies is modulated by the cohesive effect of clay and the relative concentrations of clay in each carbonate sand body.

Oceanic anoxic events were major climatic perturbations during which widespread marine anoxia and euxinia developed, and large amounts of organic carbon were buried on the ocean floor and in large lakes. Oceanic Anoxic Event 2 (OAE 2),

at the Cenomanian-Turonian boundary (∼94 Ma), is the largest perturbation of the global carbon cycle in the mid-Cretaceous and can be recognized by a characteristic positive carbon-isotope excursion in sedimentary strata. Although OAE 2 has been linked to large-scale volcanism, several large igneous provinces (LIPs) were active at this time (e.g. Caribbean, High Arctic, Madagascan and Ontong-Java) and little clear evidence has emerged linking OAE 2 to a specific LIP. Chapter 4 investigates the timing and influence of global volcanism on the Eagle Ford Group. It reports sedimentary mercury enrichments coinciding with OAE 2 and the MCE in both the Western Interior Seaway and the proto-North Atlantic Ocean. The enrichment-sizes are muted compared to other Mesozoic OAEs possibly suggesting a marine rather than atmospheric dispersal of mercury for both events. The data is consistent with LIP emplacement in the ancestral Pacific Ocean and/or the High Arctic.

Besides the large positive carbon-isotope excursion Oceanic Anoxic Event 2 is discernible in many areas of the world by the development of a 'black-shale' record, and evidence of anoxic-euxinic conditions in the water-column. However, in the southern Western Interior Seaway, the onset of OAE 2 is marked by significant reductions in concentrations of redox sensitive trace metals, and organic-lean sediments. Chapter 5 integrates high-resolution geochemical, sedimentological and mineralogical data in order to understand the hydrodynamic, climatic and depositional environment of the southern Western Interior Seaway. It finds four distinct periods of deposition termed geochemical units and defined herein. The first (A), composing the basal third of the Lower Eagle Ford and containing the Mid-Cenomanian Event, suggest a humid climate with high continental runoff prevailed during the deposition of this stratigraphic interval as well as anoxic/euxinic benthic conditions and exchange with a nutrient-rich water mass leading to resupply of the trace metal inventory. The geochemistry and mineralogy of geochemical unit B, which encompasses the upper two-thirds of the Lower Eagle Ford, suggest an arid climate with low continental runoff existed during the deposition of this stratigraphic interval, as well as a highly restricted anoxic benthic zone in the study area with some periods of euxinia and little siliciclastic input. The third geochemical unit (C), comprised of the lower half of the Upper Eagle Ford containing OAE 2, was deposited under a mostly humid climate with high continental runoff and a more dynamic ocean system, due to the presence of a suboxic benthic zone that experienced multiple periods of oxygenation possibly related to multiple periods of open water mass exchange. This section also contains the Plenus Cold Event (PCE) interval which exhibits a switch to a more arid climate during this interval and the possible influx of a volcanically derived nutrient-rich subaqueous plume. The final stage of deposition, geochemical unit (D), occurred during a more arid climate with lower continental runoff, lower benthic oxygen contents and enhanced concentration of organic matter due to a reduction in detrital and siliciclastic input.

Acknowledgements

I would like to thank my supervisors Joe Cartwright, Micha Ruhl and Steve Hesselbo for giving me the opportunity to take my project in the direction that it has ended up going as well as the continued advice, assistance and resources throughout the last 4 years. For various levels of academic and technical support I'd like to express thanks to Alex Dickson, John Hooker, Lawrence Percival, Claudia Bertoni, Mel Murphy, Sietske Batenburg, Tamsin Mather and Hugh Jenkyns. Thanks also to Steve Wyatt, Jenny Hugget, Elaine Sherrott, Maria Petrunova, Jane Barling, Jon Wells and Owen Green from Oxford Earth Sciences department for their help running samples, learning new methods, or sorting out admin for me.

For funding this project and access to the cores and samples of Innes-1 and Iona-1 I'd like to acknowledge and thank Shell Global Solutions International. I'd also like to acknowledge Daniel Minisini, James Eldrett and Steve Bergman from Shell for their extensive help in getting access to cores and samples, technical support and hospitality in Houston. I'd also like to show appreciation to Blackbrush Oil and Gas L.P. for providing access to the Chittim-2H core and samples, and Sanchez Oil and Gas Corporation for access to C4H. Furthermore, I thank the International Ocean Discovery Program (IODP) for providing access to core-samples from Site 1258 at Demerara Rise.

For all the good times at Oxford I'd like to thank Ben, Jonathan, Tim, Morgan, Adam, both Davids, Harry, Olu, Arran, and all my friends from Linacre, the boys at OURFC, and everyone else who made my time here worth it!

Finally, a huge thanks to the love and support of my parents and sisters who undoubtedly made this all possible and to whom I dedicate this thesis.

Contents

Abstract i

Extended Abstract ii

Acknowledgements iv

1 Background 1

2 Introduction 2

2.1 Global Geological Setting 6

2.1.1 Greenhouse Climates 7

2.1.2 Cenomanian-Turonian 9

2.2 Oceanic Anoxic Events 10

2.2.1 Large Igneous Provinces 13

2.3 Tectonic and Stratigraphic Setting 16

2.3.1 Cretaceous Western Interior Seaway 16

2.4 Local Geological Setting 20

2.4.1 South Texas Tectonic Framework 20

2.4.2 South Texas Stratigraphic Framework 23

2.4.3 Sedimentology 26

2.5 Thesis Objectives 30

CONTENTS

3 Depositional Controls on Vertical Cyclicity and Lateral Variability within the Eagle Ford Group, South Texas, USA 33

3.1 Introduction 35

3.2 Geological and Stratigraphical Setting 38

3.3 Analytical methods 39

3.3.1 X-Ray Diffraction Mineralogy (XRD) 39

3.3.2 Rock-Eval and Coulomat TOC analyses 40

3.3.3 X-Ray Fluorescence (XRF) 41

3.3.4 Thin Section and SEM Analysis 41

3.4 Results 46

3.4.1 Sedimentology 46

3.4.2 High Resolution Chemostratigraphic Analysis 60

3.4.3 High Resolution Total Organic Carbon and Rock Eval Analysis 62

3.5 Discussion 64

3.5.1 Interpretation 66

3.5.2 Stratigraphical Lithological Cyclicity 71

3.5.3 Potential Causes for and Consequences of Bentonite Cyclicity 82

3.5.4 Lateral Variations 86

3.5.5 Implications 90

3.6 Conclusions 92

4 Sedimentary mercury enrichments as a marker for submarine Large Ig-

CONTENTS

neous Province volcanism: evidence from the Mid-Cenomanian Event and Oceanic Anoxic Event 2 (Late Cretaceous) 94

4.1 Introduction 95

4.2 Geological Setting 103

4.3 Analytical Methods 106

4.3.1 Mercury Analyses 106

4.3.2 Organic-Carbon Isotope Analysis ($\delta^{13}C_{org}$) 106

4.3.3 Rock-Eval and Coulomat TOC analyses 107

4.3.4 ICP-MS 107

4.4 Results 108

4.4.1 New Carbon-Isotope Stratigraphy of the MCE 108

4.4.2 Hg/TOC: Eagle Ford 109

4.4.3 Hg/TOC: Demerara Rise (ODP Site 1258) 112

4.5 Discussion 115

4.5.1 Hg vs Major and Redox-sensitive Trace-Metal Concentrations . 115

4.5.2 MCE and OAE 2 Hg/TOC Excursions 116

4.5.3 Submarine LIPs and Hg Dispersal Mechanism 120

4.5.4 Comparisons to OAE 1a 124

4.5.5 Minor Cenomanian carbon-cycle perturbations: *Jukes-Browne Event* 126

4.6 Conclusions 127

CONTENTS

5 Environmental and Climatic Evolution of the Cenomanian-Turonian Southern Western Interior Seaway 129

5.1 Introduction 131

5.2 Geological Setting 134

5.3 Analytical methods 136

5.3.1 Sampling 136

5.3.2 X-Ray Diffraction 137

5.3.3 X-Ray Fluorescence (XRF) 137

5.3.4 Organic-Carbon Isotope Analyses (δ^{13}_{org}) 138

5.3.5 Coulomat TOC analyses 138

5.4 Results 139

5.4.1 Carbon Isotopes 139

5.4.2 Total Organic Carbon 139

5.4.3 Geochemistry 141

5.4.4 Depositional units 143

5.4.5 Mineralogy 147

5.5 Discussion 150

5.5.1 Principal Component Analysis (PCA) 150

5.5.2 Geochemical proxies as an environmental index 155

5.5.3 Depositional and environmental control on deposition of the Eagle Ford Group 169

5.6 Conclusions 171

CONTENTS

6 Overall Conclusions and Future Directions **173**

6.1 Overall Conclusions 174

6.2 Implications 177

6.3 Future Work and Directions 180

7 References **187**

8 Appendix **229**

List of Figures

2.1 Paleogeographic map of Texas at the Cenomanian-Turonian time boundary 4

2.2 Global map showing the distribution of Phanerozoic LIPs and hot spot tracks (plume trails) 7

2.3 Stratigraphic chart displaying the temporal correlation of Large Igneous Provinces (LIPs), Ocean Anoxic Events (OAEs), extinction events and organic-rich formations 10

2.4 An illustration displaying the Cretaceous stratigraphy of south Texas, including lithostratigraphic units as well as their lateral and temporal associations 14

2.5 Diagram comparing the south Texas stratigraphy to various other Cretaceous carbonate reference sections, including generalized depositional profiles, formations, lithological distributions and temporal durations 16

2.6 Model illustrating the variety of geochemical processes characteristic of OAEs modified from Jenkyns (2010) and Weissert (2000) 17

2.7 Annotated regional map with geological features that impacted the Eagle Ford 19

2.8 Local map with geological features that impact the Maverick Basin and the Eagle Ford Group 21

2.9 Palaeogeographic reconstruction of the Mowry Seaway and Western Interior Seaway from the Lower Cenomanian (∼98.5 Ma) to the Middle Turonian (∼93 Ma) 24

LIST OF FIGURES

2.10 Facies distribution in the Mowry and Western Interior Seaways from the Lower Cenomanian (∼98.5 Ma) to the Middle Turonian (∼93 Ma) . 27

2.11 Seismic profile trends across the Maverick Basin 28

2.12 Composite stratigraphic chart reviewing nomenclature used in the Central Texas Eagle Ford intervals, compared with those used in West Texas and near Waco, Texas 29

3.1 Diagrams displaying the position of the study area and Maverick Basin cores in the Cretaceous Western Interior Seaway in both map form and 3D 36

3.2 Generalized cross section through the Cretaceous Gulf of Mexico Basin 38

3.3 Stratigraphic columns and suggested correlation of the Innes-1, Iona-1 and Chittim-2H cores showing the internal architecture of the Eagle Ford formation as well as part of the Austin Chalk and Buda Limestone 44

3.4 Photomicrographs of argillaceous wackestones from the Lower Eagle Ford 45

3.5 Core photographs of the characteristic features of argillaceous wackestones 48

3.6 Photomicrographs of the argillaceous wackestone from the Upper Eagle Ford 50

3.7 Photomicrographs of laminated argillaceous foraminiferal wackestones 52

3.8 Core photographs of the characteristic features of laminated argillaceous foraminiferal wackestones 53

3.9 Photomicrographs of laminated foraminiferal packstones 55

3.10 Core photographs of the characteristic features of laminated foraminiferal packstones 56

LIST OF FIGURES

3.11 Photomicrographs of massive foraminiferal packstones 58

3.12 Core photographs of the characteristic features of massive foraminiferal packstones 59

3.13 Core photographs of the characteristic features of bentonitic claystones 61

3.14 Photomicrographs of a calcispheral wackestone from the Buda Formation 63

3.15 Photomicrographs of a skeletal packstone of the Buda Formation . . . 63

3.16 High resolution chemostratigraphic data from foraminiferal packstone-wackestone couplets in the Chittim-2H core 65

3.17 Idealised depositional model of the couplet cycle 70

3.18 Integrated model for sedimentary transport and deposition for the Lower Eagle Ford 73

3.19 Integrated model for sedimentary transport and deposition for the Upper Eagle Ford 77

3.20 Graphs showing the occurrence of bentonitic claystones in the lower 30 m of the Iona-1 core in relation to depth and time 83

4.1 Map showing the positions of the Caribbean, High Arctic and Madagascar LIPs during the Cenomanian-Turonian time interval, as well as the Central American Seaway, Maverick Basin, Demerara Rise and the Vocontian Basin 97

4.2 Calcium Carbonate ($CaCO_3$), $\delta^{13}C_{org}$ Total Organic Carbon (TOC), Mercury (Hg) and Hg/TOC data from the Western Interior Seaway and Demerara Rise 101

4.3 Data from the Western Interior Seaway and Demerara Rise plotting Hg against TOC 105

LIST OF FIGURES

4.4 Data from Innes-1 showing cross-plots between Hg and Al, TiO_2, Ca, V and Mo 108

4.5 Histograms of the number of samples, from the Innes-1 and Iona-1 cores, occurring per succeeding bin of 5 ppbHg/wt%TOC class widths 113

4.6 Comparison of biostratigraphy, $\delta^{13}C_{org}$, $^{187}Os/^{188}Os$, εNd and Hg/TOC data from the Western Interior Seaway, Demerara Rise and the Vocontian Basin 117

4.7 Palaeoceanographic model of the Cenomanian-Turonian Pacific and Atlantic Oceans and Western Interior Seaway 122

5.1 Map and 3D diagram displaying the positions of the Innes-1, Iona-1, Chittim-2H and C4H core at the Cenomanian-Turonian boundary . . . 133

5.2 δ^{13}_{org}, TOC, Mo_{EF}, U_{EF} and V_{EF} data from the Western Interior Seaway 140

5.3 δ^{13}_{org}, TOC, Cu_{EF} and Ni_{EF} data from the Western Interior Seaway . . 142

5.4 δ^{13}_{org}, TOC, Al, Ti and Zr data from the Western Interior Seaway . . . 144

5.5 δ^{13}_{org}, TOC, Fe_{EF} and Mn_{EF} data from the Western Interior Seaway . . 146

5.6 Bulk rock analysis of the mineralogy of the Iona-1 core 148

5.7 Bulk rock analysis of the mineralogy of the Chittim-2H core 149

5.8 Clay mineralogical analysis of the Iona-1 core 150

5.9 Clay mineralogical analysis of the Chittim-2H core 151

5.10 Correlatable transect of gamma ray, δ^{13}_{org}, and overlain redox sensitive trace metal enrichment factor data (Mo_{EF}, U_{EF} and V_{EF}) from the Western Interior Seaway 152

5.11 PCA results showing principle axis/eigen scores 153

LIST OF FIGURES

5.12 Logarithmic plots of Mo_{EF}:U_{EF} covariance for Innes-1, Iona-1, Chittim-2H and C4H 154

5.13 Comparison of Hg/TOC, δ^{13}_{org}, TOC, Mo_{EF}, V_{EF}, Ni_{EF} and Fe_{EF} from Chittim-2H 158

5.14 Comparison of Hg/TOC, δ^{13}_{org}, TOC, Mo_{EF}, Cu_{EF}, Ni_{EF}, Mn_{EF} and Fe_{EF} from Innes-1 160

5.15 Comparison of Hg/TOC, δ^{13}_{org}, TOC, Mo_{EF}, V_{EF}, Cu_{EF}, Ni_{EF}, Mn_{EF}, Fe_{EF}, Ti and Al from Iona-1 163

5.16 TOC versus Mo concentrations from the Innes-1, Iona-1, Chittim-2H and C4H cores 167

5.17 The depositional and environmental evolution of the study area 170

6.1 Palaeogeographic map showing organic-rich formations deposited between 100 and 90 Ma 182

List of Tables

3.1 Petrographic summary of the 5 dominant facies in Upper and Lower Eagle Ford of the Innes-1, Iona-1 and Chittim-2H core as described from 48 photomicrographs 42

3.2 Summary of foraminiferal and bioclast counts from 1 cm^2 polished blocks of the Chittim-2H core. 54

1 Background

For the last decade academic and industrial interest in unconventional petroleum plays has increased dramatically. Understanding depositional and sedimentological variabilities of these plays is essential to enable success throughout the production lifecycle of the unconventional hydrocarbon reservoir rocks. Most unconventional plays are hosted in organic-rich mudstones or organic-rich mixed-carbonate-clastic ”mudrocks.

The same strata that act as reservoirs in unconventional plays act as source rocks in conventional plays. As a result they have primarily been studied as source rocks, trap seals and permeability baffles, and therefore the understanding of these systems is limited. Furthermore, until the recent revolution in unconventionals, few organic-rich mudrock cores were available to study detailed sedimentology and stratigraphy. As such there is a lack of understanding of the processes that form mudrocks. Understanding the geological processes that control the deposition of mudrocks is fundamental to understanding mudrock variability, both temporally and spatially, and to facilitate the development of process-based predictive models for organic rich source rocks and unconventional reservoirs.

This study involved integrated research into the sedimentology, geochemistry and stratigraphy of an intrashelf carbonate mudrock deposited in an epicontinental seaway, the Eagle Ford Group. It focuses on the depositional environment and stratigraphic architecture as well the relative effects of global and regional forcings.

This chapter introduces the Eagle Ford Group and its regional geology, the Cretaceous Western Interior Seaway, the Late Cretaceous climate and a basic introduction to Oceanic Anoxic Events and Large Igneous Provinces. Full details are not given where they are either unnecessary for, or are sufficiently introduced in, subsequent chapters. The chapter concludes with a brief statement of research objectives outlining research presented in Chapters 3-5.

2 Introduction

The Upper Cretaceous Eagle Ford is an organic-rich, calcareous sequence present in the Maverick Basin and surrounding areas of Texas (Figure 2.1). The Eagle Ford Group represents one of the largest active unconventional reservoirs in the United States and serves as a source rock for conventional hydrocarbon reservoirs in the adjacent Woodbine, Austin Chalk and Buda Formations (Frébourg et al., 2016). In East Texas, South Texas and the Gulf of Mexico it also serves as a seal for underlying formations. The Eagle Ford was named in 1887 after the town of Eagle Ford, where it crops out in stream cuts on the surface as swelling clay soil (Sellards, 1932). The town of Eagle Ford is approximately 6 miles west of Dallas, Texas.

The Eagle Ford is not a homogenous unit, but a complex, vertically heterogeneous organic-rich carbonate succession. It has formed as the result of a mixed-carbonate-clastic mudrock system and has multiple sections which show distinctive characteristics and properties that have been imparted by sediment production and distribution processes, diagenesis and depositional water column chemistry. Though commonly referred to as a shale because of its fine grain-size, the Eagle Ford units consist of inter-bedded limestones and marlstones. In the Eagle Ford Groups northern equivalent, the Bridge Creek Member of the Greenhorn Formation in Central Colorado, similar inter-beds were initially hypothesised to be the expression of climate cycles (Gilbert, 1895). Subsequently, the nature and origin of these sediments have been extensively studied (e.g., Hattin, 1971, 1975, 1986; Fischer, 1980, 1985; Kauffman, 1977, 1988, 1995; Scholle and Arthur, 1980; Pratt, 1981, 1984, 1985; R.O.C.C. Group, 1986; Arthur et al., 1984, 1985, 1987; Barron et al., 1985; Eicher and Diner, 1985, 1989, 1991; Ricken, 1986; Arthur and Dean, 1991; Pratt et al., 1993; Ricken, 1993, 1994; Elder et al., 1994; Savrda and Bottjer, 1994). However, fundamental questions still remain and further study is required to understand the controls, types and scales of lateral and vertical heterogeneities within the Eagle Ford Group. As such the learnings of this study will lead to enhanced comprehension of other mixed-carbonate-clastic mudrock depositional systems worldwide.

The Eagle Ford Group contains an interval coincident with Oceanic Anoxic Event 2 (OAE 2) and the Cenomanian-Turonian boundary (C-T; Phelps, 2011; Fairbanks,

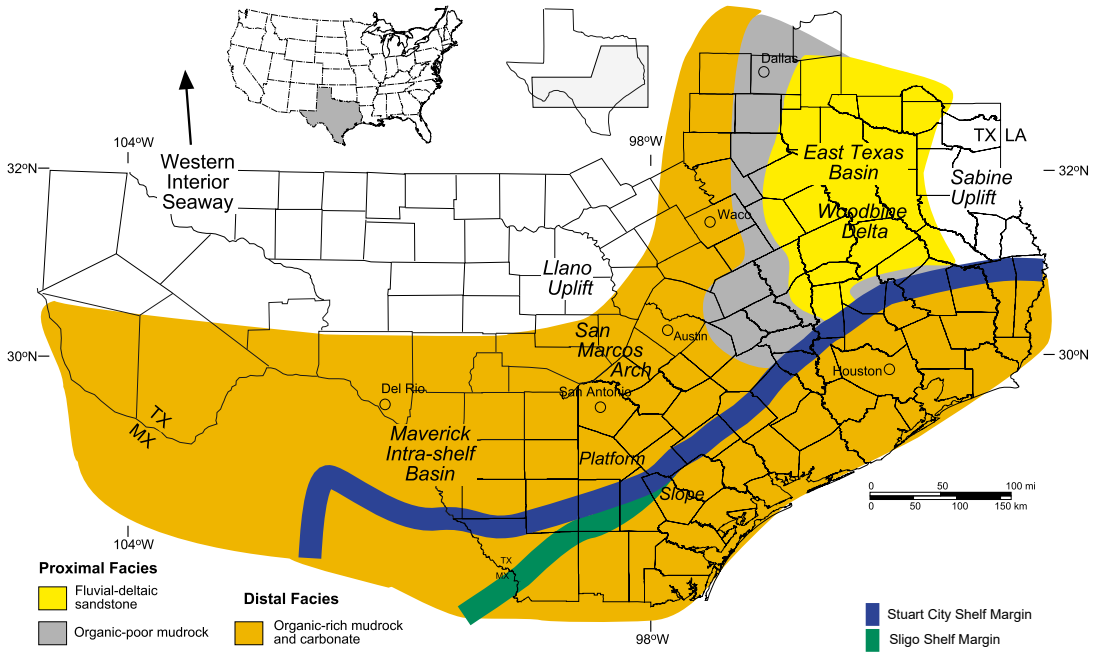

Figure 2.1: Paleogeographic map of Texas at the Cenomanian-Turonian time boundary. The Sligo and Stuart City shelf margins form a physiographic break toward the downdip extent of the Eagle Ford. Modified from Ruppel et al. (2012) and Fairbanks et al. (2016).

2012). This event is globally recognized by a positive carbon isotope excursion (CIE) reflecting the widespread sequestration of ^{12}C-enriched organic matter in marine sediments under global anoxic conditions (see Jenkyns, 2010 and references therein). Proposed hypotheses for initiation of global anoxia and enhanced carbon sequestration include long term triggers such as changes in ocean circulation and eustatic sea level rise, flooding large areas of continental shelves promoting global stratification and stagnation in greenhouse climates (Erbacher et al. 2001), abrupt episodes of volcanogenic activity and emplacement of large igneous provinces (LIPs; Orth et al. 1993; Snow et al. 2005; Turgeon and Creaser, 2008; Kuroda et al. 2007; Du Vivier et al. 2014) releasing large quantities of CO_2 in the atmosphere and increasing delivery of hydrothermally-derived and weathered nutrients into the photic zone enhancing primary production (e.g., Adams et al., 2010); or a combination of both (e.g., Kidder and Worsley, 2010).

A number of epicontinental seaways and gateways formed during the Cenomanian-Turonian such as the Equatorial Atlantic Seaway, Central American Seaway and the Trans Saharan Seaway (Schlanger and Jenkyns, 1976; Jenkyns, 1980; Arthur et al., 1987; Schlanger et al., 1987; Jenkyns, 2010). Throughout OAE 2 these

basins are generally characterized by abundant marine organic matter preservation (e.g. Schlanger and Jenkyns, 1976; Orth et al., 1993; Kuhnt and Wiedmann, 1995) and a number of geochemical anomalies displaying relatively high concentrations of redox related trace metals indicating oxygen deficient conditions (e.g. Schlanger and Jenkyns, 1976; Brumsack, 1980; Orth et al., 1993).

Much of the OAE 2 and C-T research undertaken to date in North America has focused on strata deposited to the north of the Eagle Ford in the central Western Interior Seaway (e.g. Elder, 1987, 1991; Kirkland, 1991; Obradovich, 1993; Kennedy et al., 2005; Meyers et al., 2012). Recent work has looked to fill this gap (e.g. Eldrett et al., 2014; Fairbanks et al., 2016; Scaife et al., 2017; Chapters 3, 4 and 5) and has found that the southern Western Interior Seaway experienced anoxia and the deposition of organic-rich black shales prior to the OAE 2 interval. However, in comparison to other Cenomanian-Turonian epicontintental seaways and studied sections such as the Bonarelli interval in Europe (e.g. Meyers et al, 2007), the southern Cretaceous Western Interior Seaway during the OAE 2 interval displays relatively low concentrations of redox related trace metals and comparatively little organic matter is preserved (e.g. Orth et al., 1993; Kuhnt and Wiedmann, 1995; Eldrett et al., 2014).

Investigation of the changing redox state and organic matter deposition of oceans and seas during OAEs suggests that the paleogeography of narrow oceans and epicontinental seas, in so far as it controlled water column stratification, was a significant factor in promoting photic zone euxinic conditions, as well as intensified carbon flux from zones of upwelling and high productivity (Sinninghe Damsté and Köster, 1998; Schouten et al., 2000; Kuypers et al., 2002a; Pancost et al., 2004; Schwark and Frimmel, 2004; Bushnev, 2005: Kolonic et al., 2005; van Breugel et al., 2006; Meyer and Kump, 2008; van Bentum et al., 2009). For example, sediments from the palaeostraits of Gibraltar display sedimentary intervals which suggest several longer anoxic intervals were interrupted by shorter dysaerobic and oxic periods (Rodriguz-Tovar et al., 2009). Similarly, sediments from the Norwegian Seaway display relatively low abundances of organic matter deposition during the Valangian

and OAE 2 intervals which has been suggested to indicate greater ventilation and more active flow through the seaway as the sea level rose (Mutterlose et al., 2003; Gebhardt et al., 2010).

As such the Eagle Ford Group provides an excellent opportunity to investigate the modulation of organic-rich sediments by local and regional processes (basin restriction, water stratification, bottom currents, sediment input) and global phenomena (e.g. eustatic sea level change, orbital forcing) during OAE 2.

2.1 Global Geological Setting

The Early Mesozoic breakup of the Pangean Supercontinent resulted in the North American Continent drifting away from Eurasia and Africa as the Atlantic Ocean widened, with the Gulf of Mexico basin opening during the Late Jurassic as the Yukatan drifted away from Texas, and the eastern and southern North American margins developing subsiding passive margins and continental shelves (Muehlberger, 1966; Stewart, 1976; Ewing, 1985; Ewing and Caren, 1985; Keppie et al., 2003). On the western margin of North America, the Farallon and Kula plates were subducting to the east, producing an active margin, the Western Cordilleran Mountain belt, with associated magmatic belts, and retro-arc fold and thrust belts (Muehlberger, 1966; Stewart, 1976; Ewing, 1985; Ewing and Caren, 1985).

The Cretaceous was an exceptional time in that: (a) global plate motions were among the highest recorded in the Phanerozoic due to exceptionally rapid seafloor spreading (e.g. Larson and Pitman, 1972; Seton et al., 2009); (b) five major large igneous province emplacement events (LIPs) occurred: Parana-Etendeka, Ontong Java-Manihiki Plateau, Kerguelan-Rajmahal Traps, Caribbean-Columbia Province and the Deccan Traps (Figure 2.2 and 2.3; Courtillot and Renne, 2003; Bryan et al., 2010); (c) the global climate was relatively warm (Frakes, Francis and Syktus, 1992; Cronin, 2009); (d) global sea levels were high, resulting in epicontinental seas flooding many continents (Ogg and Hinnov, 2012; Haq, 2014); and (e) marine and terrestrial flora and fauna responded to the exceptional climate in both diversity

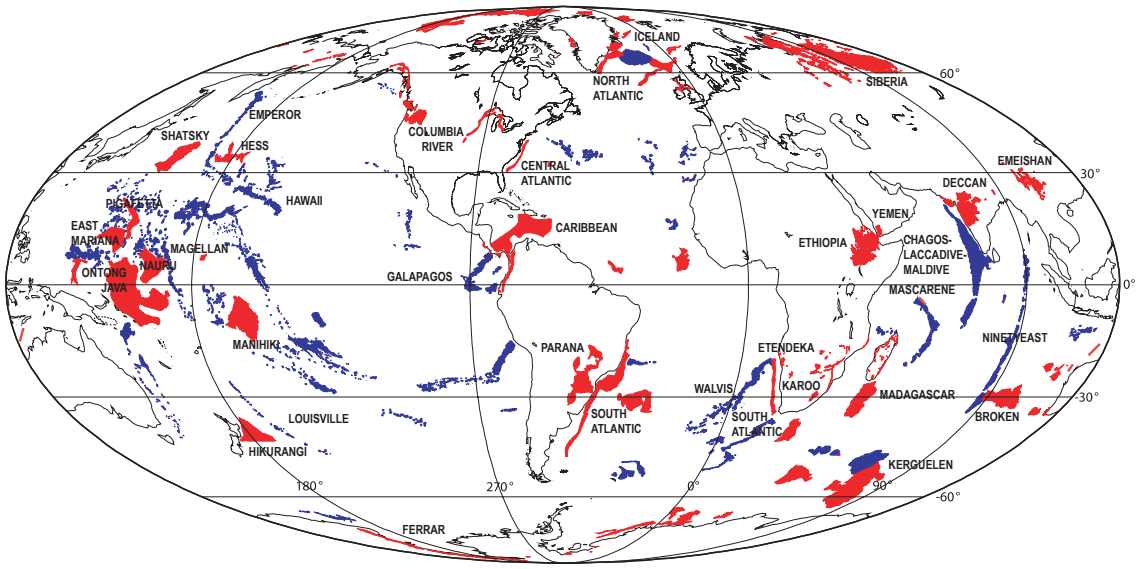

Figure 2.2: Global map showing the distribution of Phanerozoic LIPs in red and hot spot tracks (plume trails) in blue. Modified from Coffin and Eldholm (1991, 1994).

and abundance, yielding globally extensive marine chalk deposits from calcareous nanoplankton as well as angiosperms, gymnosperms, dinosaurs, and other groups populating landmasses from the tropics to the polar regions (Frakes, Francis and Syktus, 1992; Cronin, 2009; Ogg and Hinnov, 2012; Haq, 2014).

2.1.1 Greenhouse Climates

The Earth alternated between greenhouse and icehouse climate states several times during the Phanerozoic era (e.g. Frakes, Francis and Syktus, 1992; Cronin, 2010). The 80 Myr long Cretaceous Epoch ($\sim$146-65.5 Ma) was unique in that it was characterised by an exceptionally long greenhouse climate with a single long transgressive-regressive cycle beginning in the Late Berriasian, peaking in the early Turonian and ending in the Paleogene (Ogg and Hinnov, 2012). The warm Cretaceous climate has generally been attributed to the greenhouse effect of CO_2 related to enhanced volcanic activity due to rapid seafloor spreading and the emplacement of five major LIPs (Orth et al. 1993). One of the long-standing controversies is how short term, global variations in sea level could have occurred during a greenhouse climate that is assumed to have been free of continental ice sheets such as those that have dominated much of the last 5 Myr of Earth's history (icehouse; Frakes, Francis and Syktus, 1992; Cronin, 2009). The assumption of a warm, ice sheet free

Earth during the Cretaceous has been based on a variety of geochemical data, including TEX_{86}, Mg:Ca ratios and stable isotopes, and palaeontological evidence that the oceanic and continental temperatures were between 10°C and 20°C warmer in the north and south polar regions (e.g. Huber et al., 1995, 2002; Huber, 1998; Clarke and Jenkyns, 1999; Jenkyns et al, 2004; Steuber and Rauch, 2005; Forster et al., 2007; Sinninghe Damsté et al., 2010; Littler et al., 2011; Owens et al., 2017).

Though direct evidence of high frequency Cretaceous sea level changes of greater than 30 m, based on foreset heights, is lacking in the literature, correlations among oxygen isotopic data, strontium concentrations and sedimentological observations have been proposed as evidence for the existence of polar ice sheets at various times during the Cretaceous (Sageman, 1996; Gale et al., 2000; Tibert et al., 2003). Moreover, the rhythmic limestone-shale deposits of the Cenomanian-Turonian Bridge Creek Limestone in the Western Interior basin have been suggested to reflect a high frequency eustasy signal (Elder et al., 1994; Sageman et al., 1998; Laruin and Sageman, 2001) and sea level changes of tens of meters within 20 to 400 Kyr cycles are suggestive of glacio-eustatic control (Sageman et al., 1998). Therefore, in the absence of direct geological evidence such as ice raft debris the case for Cretaceous polar ice sheets requires demonstration that proxy signals of sea level and climate change are globally synchronous and consistent in their magnitude and direction of change.

A number of studies that postulate ice sheet growth and decay as the cause for Cretaceous sea level change and geochemical shifts (e.g. Stoll and Schrag, 1996; Miller et al., 1999; Gale et al., 2000; Stoll and Schrag, 2000) demonstrate a need to delineate which sea level changes were truly eustatic. Various controls on eustasy other than glaciation have been proposed and include tectonic or basin subsidence (e.g. Kauffman and Caldwell 1993; Pang and Nummedal, 1995) and the role of lakes (e.g. Sames et al., 2016; Wendler et al., 2016), which are regional by nature, as well as the thermal expansion of sea water (e.g. Wigley and Raper, 1987; Church et al., 2001), and charge of groundwater reservoirs (e.g. Hay and Leslie, 1990; Church et al., 2001).

2.1.2 Cenomanian-Turonian

The Cenomanian-Turonian is believed to have been a globally warm period with equitable climate states lacking polar continental ice sheets (Wilson et al., 2002; Moriya et al., 2007; Ando et al., 2009; Sinninghe Damsté et al., 2010). The Eagle Ford Group is interpreted to have been deposited as a result of the second order transgression-regression cycle (Figure 2.4; Dawson, 1997; Donovan and Staerker, 2010; Hentz and Ruppel, 2010) with much of the Eagle Ford representing deposition during a global transgression and highstand of the eustatic sea level (Figure 2.4; Haq et al., 1987). This was interpreted to be within transgressive and early highstand system tracts deposited during Cycle 2.5 of the UZA-2 supercycle, the Cenomanian-Turonian tectnoeustatic transgressive systems tract (Haq et al., 1988) due to the Eagle Ford Formation overlying the Buda Limestone, which forms a carbonate ramp-like succession (Figure 2.4 and 2.5; Lehman et al., 2000; Goldhammer and Johnson, 2001; Phelps et al., 2013). The occurrence of a number of condensed intervals occurring around the Cenomanian boundary in other parts of the world has been suggested to be further evidence for this (Figure 2.4 and 2.5; Sass and Bein,1982; Flexer et al., 1986; Bertani and Carozzi, 1985; Alsharhan and Nairn, 1993; Ebert et al., 1993; Ross and Skelton, 1993; Vahrenkamp et al., 2003).

The formation of neritic conditions (100s meters) to facilitate the deposition of the Eagle Ford Group on top of platform interior carbonates of the Buda Formation would have needed sea level rise to drastically outpace carbonate production rates, a fact which is largely out of step with the Cretaceous rock record (Figure 2.4 and 2.5; Bertani and Carozzi, 1985; Alsharhan and Nalm, 1993; Eberli et al., 1993; Ross and Skelton, 1993; Vahrenkamp et al., 1993). Furthermore, other Cenomanian-Turonian sections, such as the Majella massif, Italy; Judea group, Israel, do not record facies offsets commensurate with a high-frequency, high-amplitude sea level sea level rise (Sass and Bein, 1982; Flexer et al., 1986; Eberli et al., 1993). However, several species of platform biota are known to have gone extinct at the Cenomanian-Turonian boundary, including many rudists (e.g. caprinids and ichthyosarcolitids), the loss of which may have dramatically reduced on-platform car-

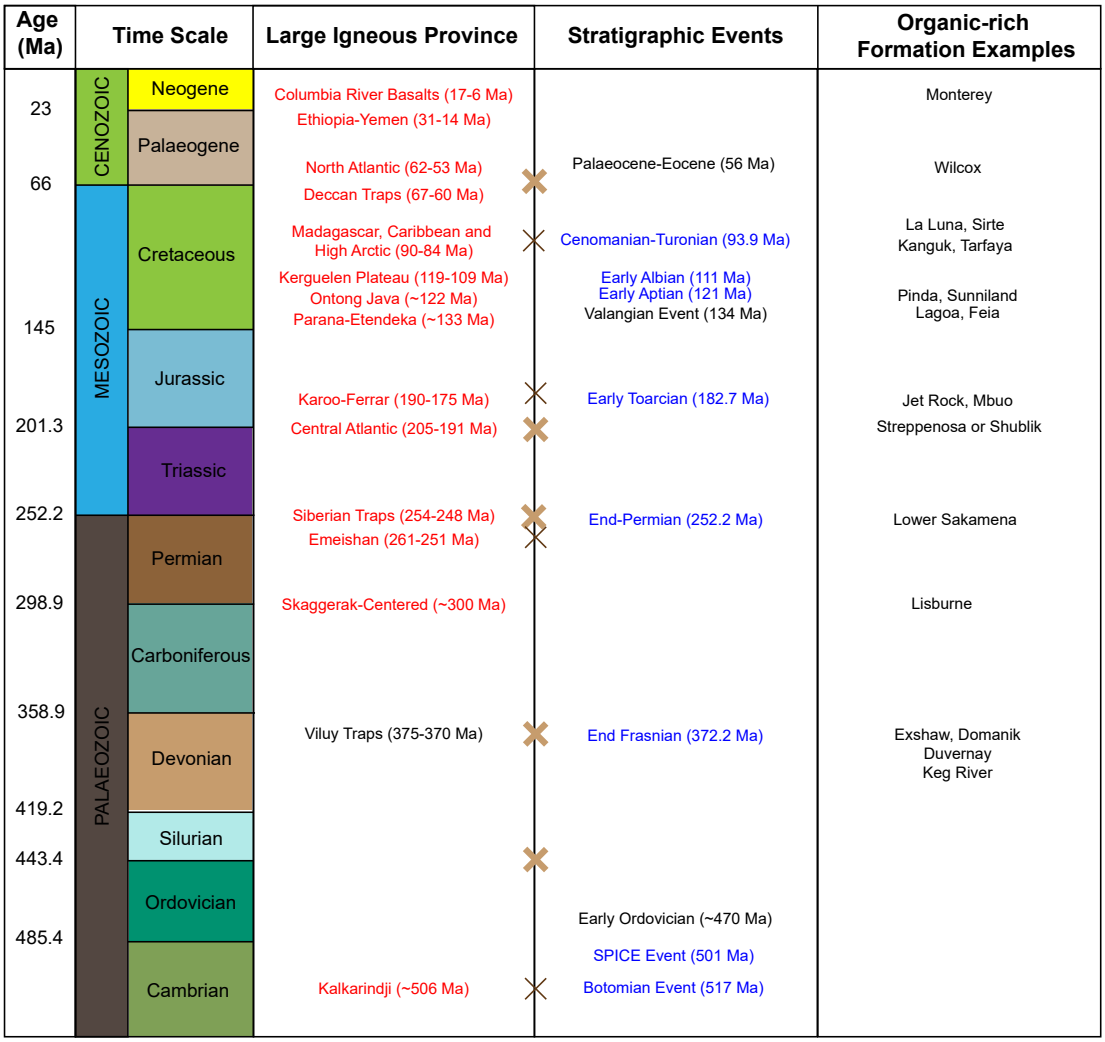

Figure 2.3: Stratigraphic chart displaying the temporal correlation of Large Igneous Provinces (LIPs), Ocean Anoxic Events (OAEs), extinction events and organic-rich formations. LIP ages are taken from Courtillot and Renne (2003) and Bryan et al. (2010). Ages refer to the onset of emplacement. Organic-rich formations and their ages are taken from Katz (1995) and references there in. This diagram is based on the reviews of Courtillot and Renne (2003) as well as Wignall (2005) and is inspired by Percival et al. (2015). The correlations are best in the Mesozoic. This is because Palaeozoic provinces are less likely to be preserved and Cenozoic provinces were emplaced in an "icehouse climate. As a result they were less likely to facilitate regional anoxia. Gaps in the correlation include the two most recent provinces as no major environmental impact has yet been found in the rock record. However, the timing of the Columbia River Basalts does coincide with the deposition of the Monterey Formation.

bonate production rates (Ross and Skelton, 1993).

2.2 Oceanic Anoxic Events

Oceanic Anoxic Events (OAEs) are short duration (<1-2 Myr) intervals of geological time characterized by extremely high burial rates of organic carbon that led to the deposition and preservation of organic-rich black shales in many areas of

the global ocean (Figure 2.6; Schlanger and Jenkyns, 1976; Arthur and Schlanger, 1979; Jenkyns, 1980; Scholle and Arthur, 1980; Herbin et al., 1986; Arthur et al., 1987, 1988; Weissert and Lini, 1991; Jenkyns et al., 1994; Sinninghe Damste and Koster, 1998). These perturbations in the global carbon cycle are normally reflected by positive carbon isotope excursions (e.g. Kuypers et al., 2002; Tsikos et al., 2004).

Initial studies recognized OAE 1 (Aptian-Albian) and OAE 2 (Cenomanian-Turonian) (Schlanger and Jenkyns, 1976). With the advancement of stratigraphic techniques, characterization and improved resolution, OAE 1 was subsequently split into four sub events (1a-1d) and a Jurassic event was recognized in the Toarcian (T-OAE) (Jenkyns, 1980, 1988; Arthur et al., 1990; Jenkyns, 2010). At present the T-OAE ($\sim$183 Ma), Early Aptian OAE 1a ($\sim$120 Ma) and OAE 2 ($\sim$94 Ma) are believed to have been the largest and most extensive during the Mesozoic (Figure 2.4).

Oceanic Anoxic Event 2 spans the Cenomanian-Turonian boundary (94 Ma) and represents one of the largest perturbations in the Mesozoic global carbon cycle. The duration of OAE 2, as based on biostratigraphic evidence and carbon isotope excursions, was originally believed to have lasted between 0.4 to 0.8 Myr (Arthur et al., 1988; Caron et al., 1999). More recently, orbital cyclicity has been used to approximate the duration of the event, with estimates of 0.72 Myr in Colorado (Meyers et al., 2001), 0.4 Myr in Tarfaya basin (Kuhnt et al., 1997), 0.32 Myr in Western Canada (Prokoph et al., 2001) and 0.6 Myr (Meyers et al., 2012).

OAE 2 is characterized by a large, positive global CIE in both carbonate and organic matter that was caused by a major perturbation of the global carbon budget, most likely due to the extensive burial of organic matter in black shales (Figure 2.6; Schlanger and Jenkyns, 1976; Arthur and Schlanger, 1979; Jenkyns, 1980; Scholle and Arthur, 1980; Herbin et al., 1986; Arthur et al., 1987; Arthur et al., 1988; Weissert and Lini, 1991; Jenkyns et al., 1994). The CIE accompanying OAE 2 can be separated into three divisions: Phase A the initial build-up stage of the European reference section at Eastbourne, England (Paul et al., 1999); Phase B, a second build up stage which leads to high values corresponding to a plateau, commonly containing a trough (Paul et al., 1994, 1999); Phase C, a recovery period which

marks the gradual return to nearly pre-excursion values (Paul et al., 1994, 1999). Phase A and B are referred to as OAE 2 whereas C represents the recovery phase where values decrease after the OAE 2 interval (Kuypers et al., 2004; Tsikos et al., 2004; Kolonic et al., 2005).

OAE 2 also featured changes in assemblages of planktonic and benthonic calcareous microbiota such as foraminifera and ostracods, as well as dinoflagellates, nannofossils and, locally, radiolarians (Jarvis et al., 1988; Erba, 2004; Musavu-Moussavou et al., 2007; Coccioni et al., 2016; Falzoni et al., 2016, Eldrett et al., 2017). In northern Europe, invasion of boreal 'pulse faunas', including a belemnite (*Praeactinocamax plenus*), was a feature of the early to mid-phase of OAE 2, equally reflected in increases in bulk oxygen-isotope values of enclosing chalks and signifying a fall in surface-water temperatures (Lamolda et al., 1994; Gale and Christensen, 1996; Jenkyns et al., 2017). This so-called Plenus Cold Event was also registered in the western Atlantic and at the southern end of the Western Interior Seaway by invasion of boreal dinoflagellates (Eldrett et al., 2014; van Helmond et al., 2014), as well as by falls in temperature in the proto-Atlantic determined by the organic geochemical TEX_{86} proxy (Forster et al., 2007; Sinninghe Damsté et al., 2010). The global nature of the Plenus Cold Event is signified by a drop in pCO_2 reconstructed from organic geochemical proxies, stomatal indices of fossil leaves, and carbonate and organic-carbon isotopes (Kuypers et al., 1999; Barclay et al., 2010; Jarvis et al., 2011). Overall, the pattern of extinctions and originations, also involving macrobiota such as ammonites and bivalves, is significant enough to have originally defined the Cenomanian-Turonian stage boundary (Jarvis et al., 1988).

It has been proposed that the major forcing behind OAEs was an abrupt rise in temperature induced by the rapid influx of CO_2 into the atmosphere from volcanogenic or methanogenic sources associated with the formation of LIPs (Figure 2.6; e.g. Coffin and Eldholm, 1994; Ernst et al., 2005). Global warming, and release of toxic compounds, was accompanied by catastrophic oceanographic and climatic changes (Figure 2.6; Kidder and Worseley, 2010), which impacted on and initiated a number of interconnected processes such as (i) water-column stratification and stagnation

(Erbacher et al., 2001), (ii) elevated productivity resulting from enhanced silicate weathering (Blättler et al., 2011; Pogge von Strandmann et al., 2013; van Helmond et al., 2014), and (iii) an accelerated hydrological cycle (van Helmond et al., 2014). However, the exact relationship between the isotope curve and the TOC stratigraphy of OAE 2 is complex. Many sections show that the initial CIE does not coincide with the deposition of organic rich black shale such as the USGS Portland 1 core, Colorado where organic carbon accumulation rates seem to have increased after the OAE (as defined by the CIE; Du Vivier et al., 2015).

2.2.1 Large Igneous Provinces

Large Igneous Provinces (LIPs) represent extremely large volcanic events where tens to hundreds of millions of cubic kilometres of mainly mafic silicate magma is erupted in intraplate settings as flood basalt provinces and intruded in the crust as sill complexes and dike swarms (Figure 2.2; e.g. Coffin and Eldholm, 1994; Ernst and Buchan, 2001; Bryan and Ernst, 2008; Neal et al., 2008). They are emplaced in a short duration pulse or multiple pulses (1-5 Myr) with a maximum duration of $<$ c. 50 Myr (e.g. Ernst, 2005). Silicic magmatism, carbonatites and kimberlites, may also be associated with LIP volcanism (Ernst, 2005).

A number of models have been proposed to explain the origin of LIPs. Currently, the most widely accepted mechanism suggests that LIPs are the result of small amounts of partial melting of the upper mantle (15-25%) caused by the upwelling of anomalously hot and buoyant asthenosphere that has been suggested to be associated with mantle plume heads derived from the core mantle boundary or influenced by shallower mantle processes near the edges of subducted lithospheric slabs (e.g. Sleep, 1990, 2006; Campbell, 2005, 2007; Beier et al., 2008; Burke, 2011). However, other proposed models include impact-induced decompression melting (e.g. Jones et al., 2002; Ingle and Coffin, 2004); lithospheric delamination (Elkins-Tanton and Hager, 2000; Elkins-Tanton, 2005, 2007; Hales et al., 2005); decompression melting during rifting (White and McKenzie, 1989) or following mantle heating beneath supercontinents (Coltice et al., 2007); edge-driven convection (King and An-

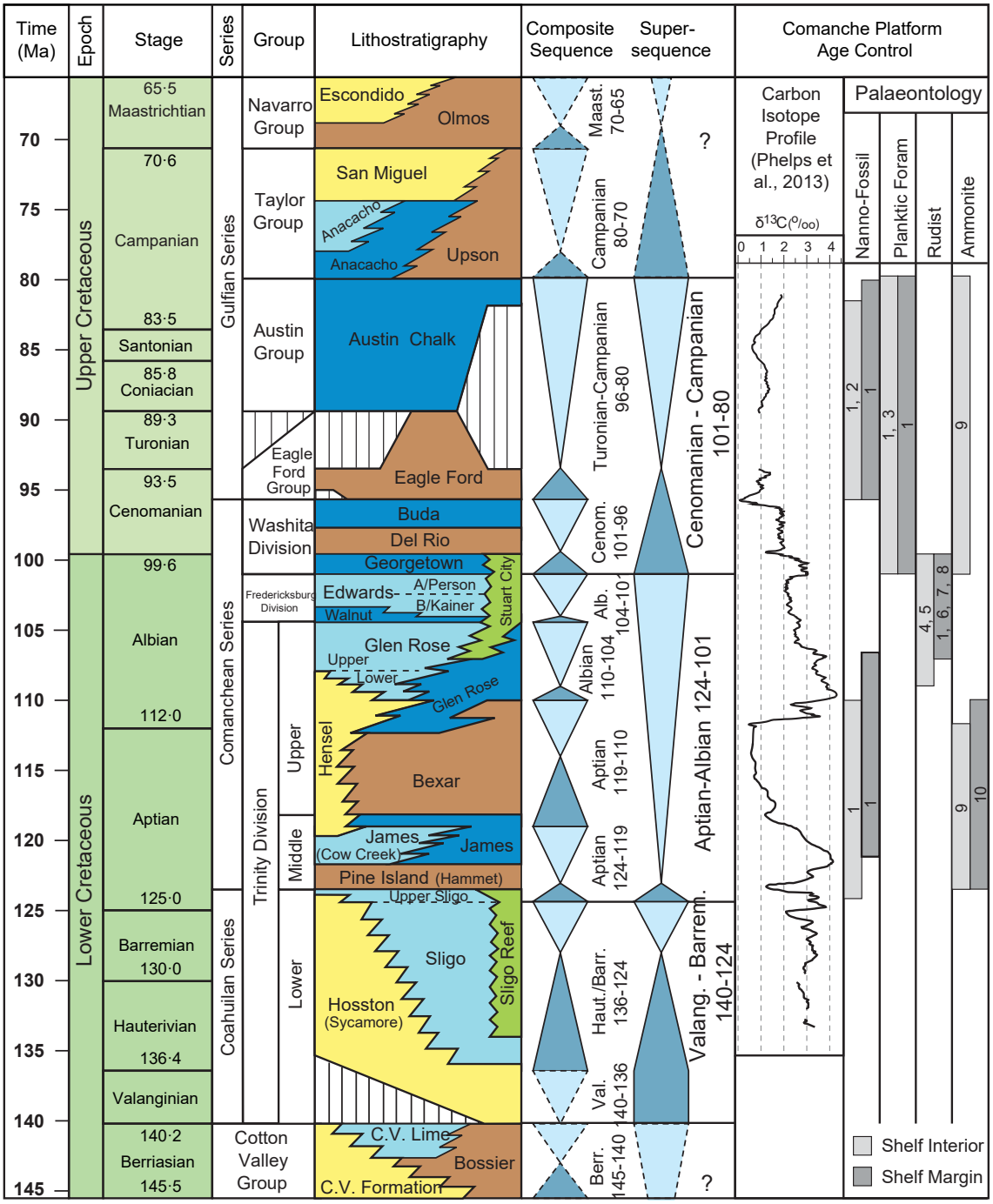

Figure 2.4: An illustration displaying the Cretaceous stratigraphy of south Texas, including lithostratigraphic units as well as their lateral and temporal associations. Ages of stratigraphic units are determined based on correlations of stable isotope data to other global sections (Phelps, 2011; Phelps et al., 2013) and palaeontological data. Numbered references for palaeontological age control are as follows: 1 - This study; 2 - Jiang, 1989; 3 - Scott et al., 2002; 4 - Scott, 2002; 5 - Scott et al., 2007; 6 - Scott et al., 1994; 7 - Coogan, 1977; 8 - Waite et al., 2007; 9 - Young, 1986; 10 - Hull, 2011. Modified from Phelps et al. (2013).

derson, 1998); melting of fertile mantle without excess heat (Anderson, 2005); or shallow melting anomalies generated by plate-tectonic-related processes (Foulger, 2007).

LIPs are believed to have had significant effects on many parts of the Earths system including continental break-ups, plate re-organisation, plate boundary evolution, lithosphere evolution, extinction events, and ocean and atmosphere chemistry (Rampino and Stothers, 1988; Larson, 1991; Courtillot, 1994, 1999; Deckart et al., 1998; Milner et al., 1995; Courtillot and Rene, 2003). The temporal link between LIPs and extinction events appears robust (Figure 2.3). Many major and some minor LIP events occur within several million years or less of global extinctions (e.g. Wignall, 2001; Courtillot and Renne, 2003). For example, the Deccan ($\sim$65 Ma), Central Atlantic Magmatic Province (201 Ma) and Siberian Traps ($\sim$252 Ma) LIPs match in age to the Cretaceous–Tertiary, Triassic–Jurassic and Permian–Triassic Boundary Extinctions respectively (Courtillot and Rene, 2003; Isozoki, 2009; Saunders and Reichow, 2009; Melott et al., 2010). Only the major Ordovician-Silurian boundary extinction has not been correlated with a LIP event (Khudoley et al., 2013). Furthermore, Phanerozoic marine fossil data records and ocean $^{87}Sr/^{86}Sr$ and $\delta^{34}S$ records have been recognized to exhibit 62 Myr and 140 Myr cyclicities (Rohde and Muller, 2005; Prokoph et al., 2008).

LIP events are associated with a wide array of environmental impacts with causal links established between the mass release of SO_4 and CO_2, resulting in rapid changes in global temperatures, perturbations of the global climate, widespread oceanic anoxia and changes in ocean chemistry and marine biodiversity (Figure 2.3; Courtillot and Rene, 2003; Isozoki, 2009; Saunders and Reichow, 2009; Melott et al., 2010; Prokoph et al., 2013). Current estimates suggest that decreases of roughly 120 genera/Myr correspond to roughly 600,000km^3 of erupted magma (Prokoph et al., 2013).

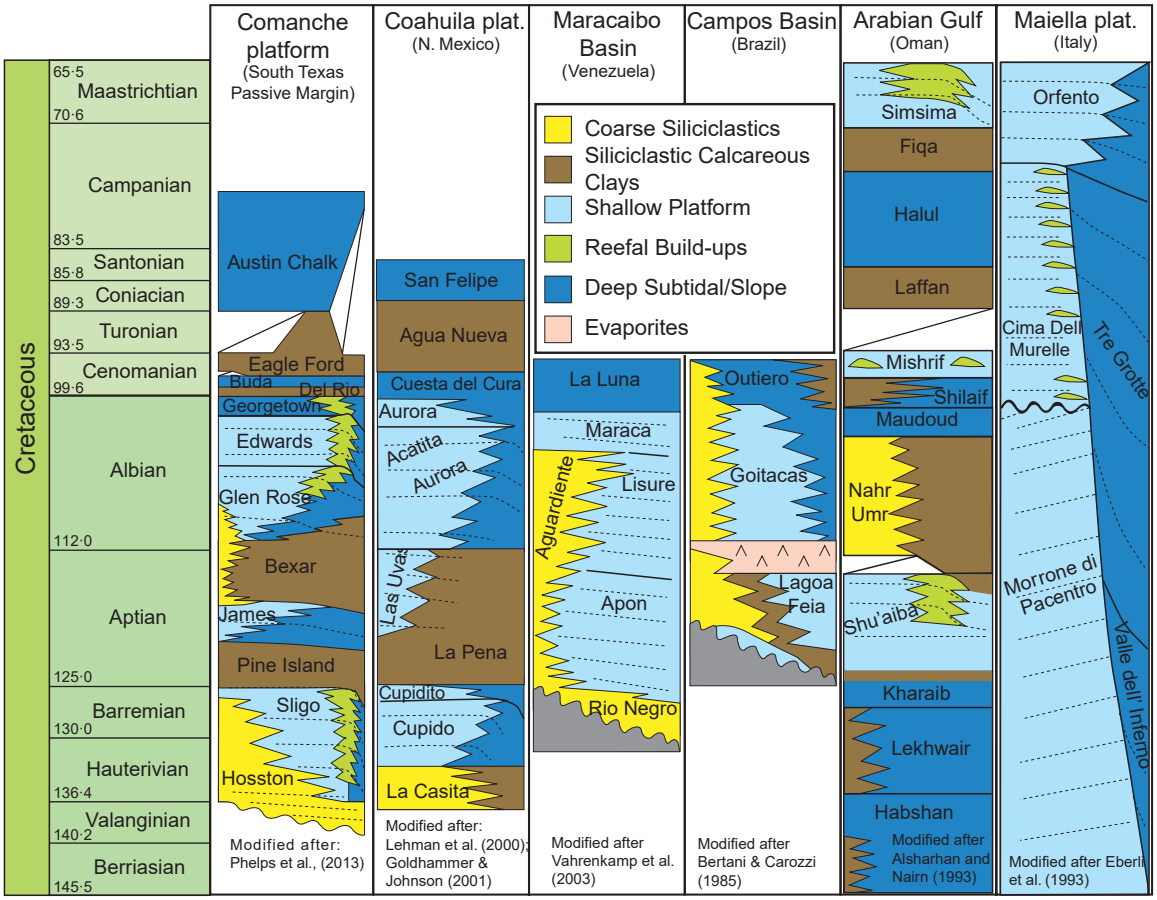

Figure 2.5: Diagram comparing the south Texas stratigraphy to various other Cretaceous carbonate reference sections, including generalized depositional profiles, formations, lithological distributions and temporal durations. Modified after Phelps et al. (2013).

2.3 Tectonic and Stratigraphic Setting

2.3.1 Cretaceous Western Interior Seaway

The Cretaceous Western Interior Basin and Epicontinental Seaway (KWIS) forms part of the 3,000 km long foreland basin that formed behind the greater Cordilleran retro-arc fold and thrust belt during the Late Mesozoic through to the Eocene along the continentally inward side of the Cordilleran magmatic arc and accreted allochtonous terranes of North America (Figure 2.9 and 2.10; Burchfiel et al., 1992; Allmendinger, 1992; Miller et al., 1992; Bird, 1998; Dickinson and Lawton, 2001; Dickinson, 2004). The Cordilleran orogenic belt and related basins were products of the convergence between the North American and Farallon plates, and they were strongly influenced by the dynamic topography associated with the negative mantle buoyancy due to slab effects (Burchfiel et al., 1992; Allmendinger, 1992).

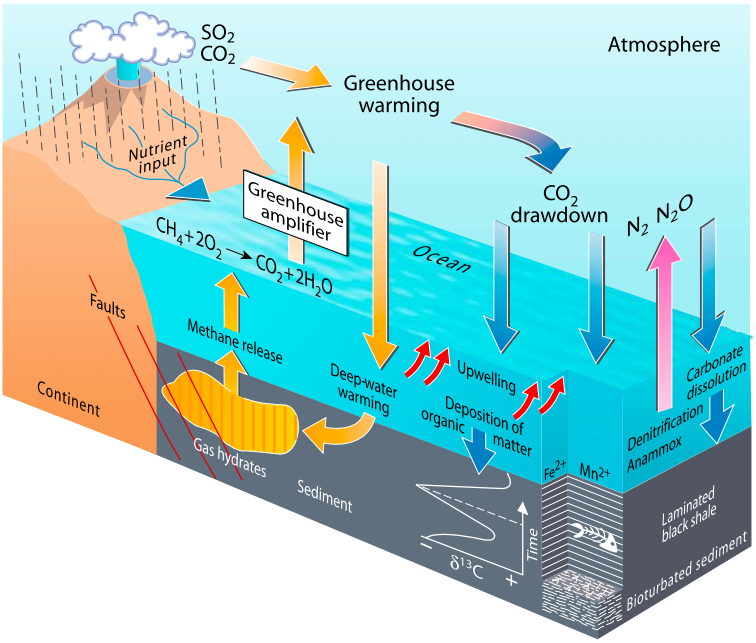

Figure 2.6: Model illustrating the variety of geochemical processes characteristic of OAEs modified from Jenkyns (2010) and Weissert (2000). The possible cause of volcanism, which through the venting of greenhouse gases, initiates global warming resulting in increased acidification of the oceans from dissolution of CO_2 and SO_2. This in turns results in increased carbonate dissolution and methane release from gas hydrates, as a result of either the warming of bottom waters and the subjacent sedimentary pile and/or synsedimentary faulting, produces further increase in temperature in seawater and atmosphere. The hydrological cycle accelerates with increased nutrient flux to the oceans; upwelling intensifies, as does organic productivity. As depicted in this early phase of the OAE, oxygen depletion has advanced to a state where denitrification and the anammox process have reduced nitrate and nitrite, such that nitrous oxide (a potent greenhouse gas that would promote further global warming) and elemental dinitrogen are being lost from the ocean. Organic-rich sediments change from bioturbated to laminated (rich in fish remains) as the benthos is excluded from the sea bottom by the spread of anoxic conditions. Manganese is fixed as early diagenetic carbonate phases at or just below the seafloor; iron is fixed as pyrite below the seafloor. The carbon isotope profile illustrated shows the effect of a global increase in carbon burial, causing a positive $\delta^{13}C$ excursion interrupted by a negative excursion produced by the input of isotopically negative methane and its oxidation product carbon dioxide

Mid-Cretaceous thrust loading of the Sevier-Hidalgo orogens flexed the lithosphere, creating a north-south trending subsiding foredeep to the east and a broad ramp-shelf, with reactivated basement arches defining localized sub-basin domains such as the Maverick Basin (Dickinson and Lawton, 2001; Dickinson, 2004). Early to Mid-Cretaceous times were tectonically quiet in the Trans-Pecos region, resulting in the stable platform conditions with gradual subsidence and relatively few tectonic inversion events (Ewing and Lopez, 1991; Burchfiel et al., 1992; Allmendinger, 1992; Miller et al., 1992). These intrashelf basins provided the ideal settings in which to develop restricted marine conditions following marine transgressive events (Ewing and Lopez, 1991; Dickinson and Lawton, 2001; Dickinson, 2004; Phelps, 2011,

2013). The architecture of these sub-basin domains was influenced by basement geology and the pre-Cretaceous basin evolution with possible salt withdrawal and extensional deformation (Ewing and Lopez, 1991; Scott, 2004; Alexander, 2014). Following relatively stable deepwater (hundreds of meters water depth) carbonate platform conditions, parts of the Balcones fault zone experienced emplacement of hundreds of mantle derived, alkaline volcanic complexes including lava lakes, tuff cones, maars and plugs between 75 Ma and 80 Ma (Griffin et al., 2010). This is most likely associated with the asthenospheric upwelling at the southern North American lithospheric margin. These volcanic rocks may also be present in the Chittim anticline, where Laramide compression has inverted the Jurassic graben (Figure 2.8 and 2.11; Scott, 2004; Alexander, 2015).

In the Mid-Cretaceous (120-80 Ma), deposition in the Maverick Basin occurred during the Sevier-Hidalgo orogeny, which is likely to have caused loading induced subsidence along the Cordillera as well as a subsequent marine transgression (Figure 2.9 and 2.10; Ewing and Lopez, 1991). This, along with thermal subsidence in the Gulf of Mexico basin, formed the Western Interior Seaway as we know it during the Cenomanian (Figure 2.9 and 2.10; Ewing and Lopez, 1991).

The regional tectonic evolution in this area was extremely complex. Though an overall compressive stress field during a protracted plate convergence existed throughout the Cretaceous, there were definite periods of local extension related to mantle delamination (Wells and Hoisch, 2008).The Maverick basin initially formed as one of a number of fault-bounded Jurassic rift basins in the southern KWIS, these basins subsided during the Early and Middle Cretaceous due to both post-rift thermal relaxation and foreland loading of the Cordilleran fold and thrust belt (Figure 2.8; Wells and Hoisch, 2008; Ewing, 2009). They were then inverted in the Late Cretaceous during the Laramide Orogeny forming NW-SE trending upright open folds (Figure 2.8; Saleeby, 2003; Scott, 2004) which include both the Chittim anticline and the Rio Grande syncline (Scott, 2004; Ewing, 2009). The NW-SE trending folds are likely to have been compressed and shortened in a NE-SW trending direction just as other Laramide structures in the KWIS such as those found in the Sierra Navada

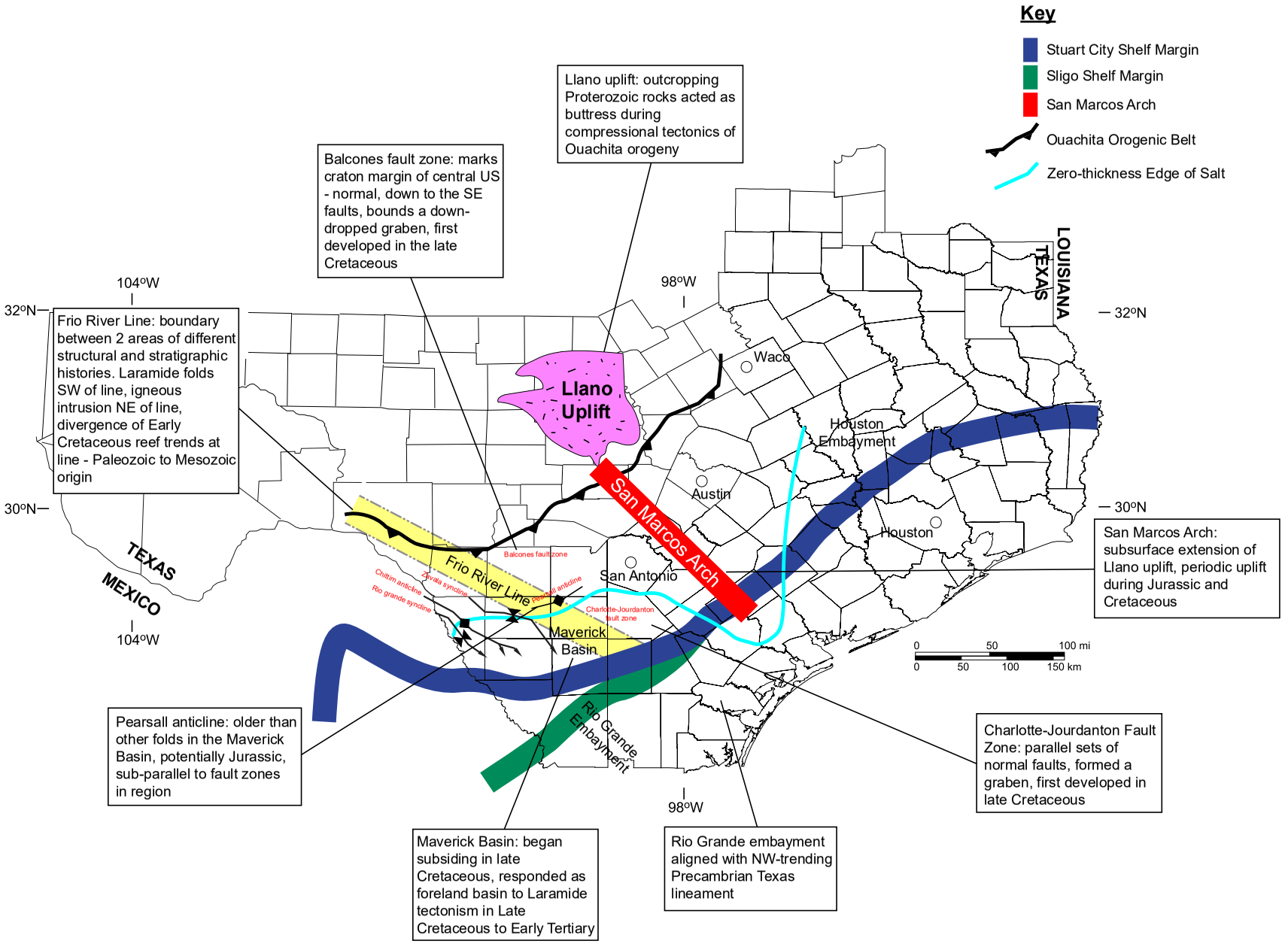

Figure 2.7: Annotated regional map with geological features that impacted the Eagle Ford. The Maverick Basin is located southwest of the Frio River Line (light yellow NW-SE trending zone) and northwest of the Early Cretaceous shelf edge (blue line). Terminal shelf-margin locations are controlled by the tectonic hinge between more rapidly subsiding thin transitional continental crust and more slowly subsiding thick transitional continental crust. Map modified after Winker and Buffler (1988), Ewing (1991), McFarlan and Menes (1991), Goldhammer and Johnson (2001) and Phelps et al. (2013).

region (Saleeby, 2003).

The Laramide orogeny (80 to 40 Ma) is characterized by thick-skinned, basement-involved structures east of the Sevier orogenic thrust belt (Figure 2.8; Coffin and Eldholm, 1994; Miller et al., 1999; Saleeby, 2003). It is thought that the Laramide deformation was the result of increased traction and tectonic erosion of the mantle lithosphere due to flat slab subduction along the western margin of the North American Plate (Burchfiel et al., 1992; Allmendinger, 1992; Saleeby, 2003) and subsequently slab segmentation during the partial subduction of the Hess-Shatsky Rise (Saleeby, 2003). It has been suggested that part of the southern Western Interior Seaway including the Maverick Basin and surrounding area became inverted during a period of flat slab subduction between 80 Ma and 60 Ma (Saleeby, 2003; Scott, 2004).

Following the Laramide orogeny, a widespread phase of magmatism due to asthenosphere induced crustal melting characterized the Big Bend region during the Eocene to Oligocene peaking during the late Eocene and early Oligocene (McDowell and Clabaugh, 1979; Henry and Price, 1984). During this period, tectonic reorganization along the North American plate and the development of the San Andreas fault, resulted in the Tran-Pecos region undergoing E-W trending extension, crustal thinning and high flow particularly over the last 25 Myr (Price and Henry, 1985; Dickinson, 2004). Furthermore the region was subjected to epeirogenic uplift, tilting and erosion resulting in the formation of the High Plains and Llano Estacado erosional surfaces (Horak, 1985).

2.4 Local Geological Setting

2.4.1 South Texas Tectonic Framework

The Eagle Ford Group was deposited in the Late Cretaceous on the southern edge of the Western Interior Seaway and the northwest margin of the Gulf of Mexico carbonate shelf (Figure 2.4 and 2.10; Goldhammer and Johnson, 1999, 2001). The

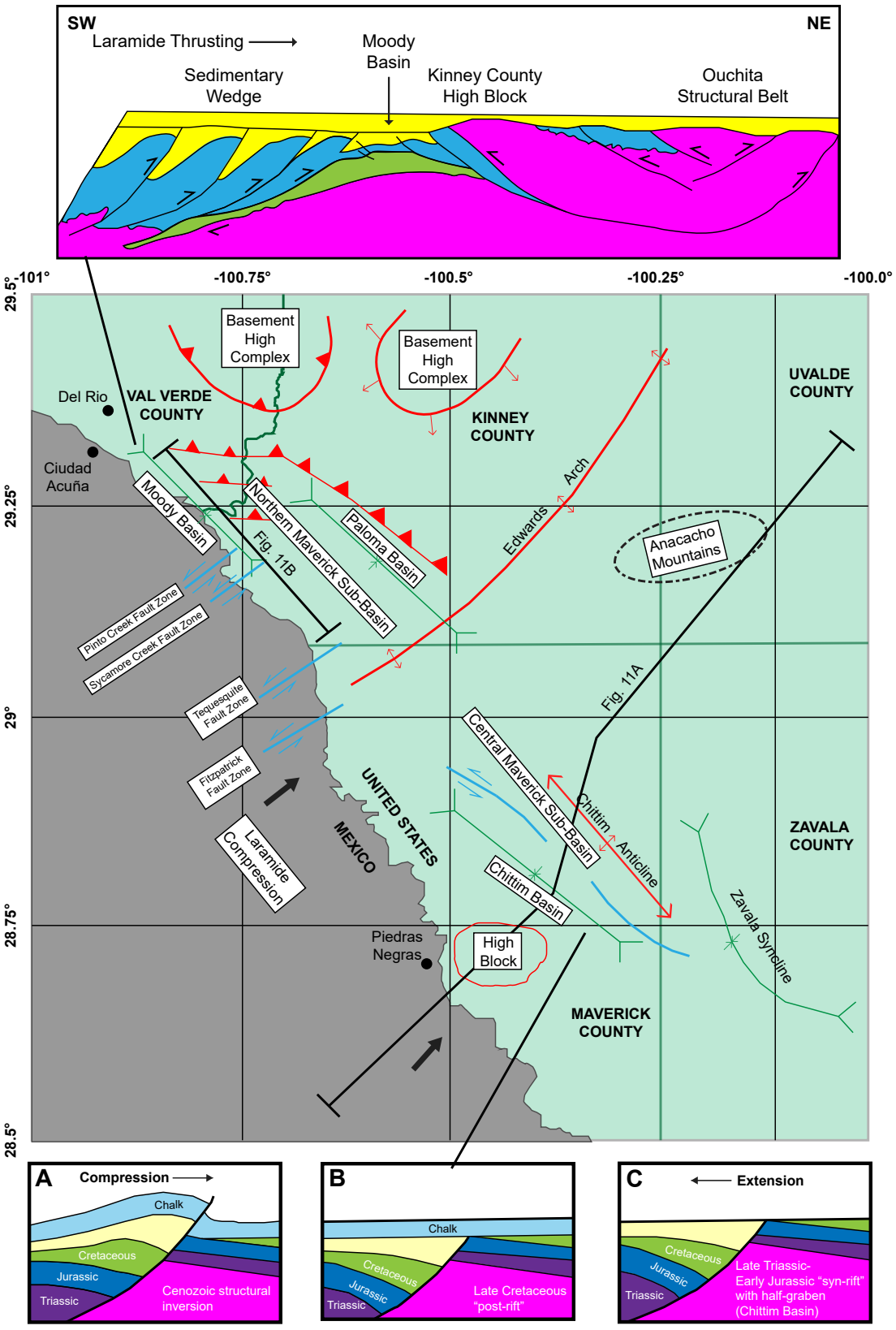

Figure 2.8: Local map with geological features that impact the Maverick Basin and the Eagle Ford Group. Modified after Lowell et al. (1985), Underhill and Paterson (1998), Alexander, (2015). The northern part of the Maverick Basin is centered in northwestern Kinney County-southeastern Val Verde County. Northeast-trending basement high blocks of the Edwards Arch separate it at depth from the broader and deeper sub-basins to the southeast in Maverick and Dimmit counties. The Devils River Uplift in Val Verde County, immediately to the northwest, is recognized as a basement-thrust uplift of Late Paleozoic age (Nicholas and Rozendal, 1975; Webster, 1980; Nicholas, 1983). Laramide compression from Mexico produced folded or thrusted anticlines along the southwest flank of the basin. Basement high blocks in Kinney County acted as a buttress impeding northeast-directed thrusting and possibly inducing back-thrusting. The central part of the Maverick basin lies south of the northeast-trending Tequesquite and Fitzpatrick shear faults and a series of basement high blocks trending southwest from the Edwards Arch. Its southwest flank is formed by an alignment of magnetic basement high blocks in Mexico, paralleling the Rio Grande. Major structural features include the Cretaceous Chittim Anticline, an elongate Jurassic rift basin sometimes referred to as the Chittim Basin, and the Zavala Syncline. The development of the Chittim Basin and Chittim Anticline appears similar to that of the Lulworth area in the U.K. (Underhill and Paterson, 1998).

carbonate shelf formed a gently dipping homocline that extended for ∼1500 km from the Ouchita Mountains in the north to the Sigsbee Escarpment, formed by thermal subsidence related to Jurassic seafloor spreading, at the base of the continental slope in the south (Miller et al., 1992; Goldhammer and Johnson, 1999, 2001). The Cretaceous Western Interior Seaway was a foreland basin epicontinental seaway related to the greater Cordilleran fold and thrust belt that extended from Alaska to Mexico (Burchfiel et al., 1992; Miller et al., 1992) which itself developed on the intra-continental side of the Cordilleran magmatic arc and allochthonous terranes in the Late Mesozoic (Allmendinger, 1992; Burchfiel et al., 1992; Miller et al., 1992; Dickinson, 2004).

The study area is approximately a 300 km long transect in south-west Texas including two cores (Innes-1 and Iona-1) in the Trans-Pecos outcrop belt, located near the towns of Del Rio and Langtry. These are situated north of the Early Cretaceous carbonate shelf edge and southwest of the Frio River Line, encompassing the northern end of the intrashelf platform (Scott, 2004). During the Jurassic and Early Cretaceous, the clastic and carbonate sediments in the Maverick basin were deposited in a series of half-grabens trending NW-SE (Scott, 2004). This extensional basin is thought to represent a failed rift arm that formed during the Late Jurassic opening of the Gulf Coast basin (Scott, 2004). During the Mid to Late Cretaceous, deposition in the Maverick Basin was coincident with the widespread marine incursion and transgression that formed the Cretaceous Western Interior Seaway (Phelps, 2011, 2013). An important basement feature in the Del Rio area is the Frio River line, a northwest-southeast trending boundary zone that separates disparate structural and depositional styles (Ewing, 1987). Northeast of the line, structures are primarily pre-Triassic in age, including the Llano uplift and Pearsall Arch (Ewing, 1987) whereas southwest structures are dominated by NW-SE trending, low amplitude folds similar in structural style and age to Laramide structures in northeastern Mexico (Ewing, 1987; Scott, 2004).

Innes-1 and Iona-1 sit west of the Late Cretaceous (75-80 Ma) Balcones Igneous Province (Figure 2.7 and 2.8), which comprises several hundred mafic alkaline vol-

canic complexes in Uvalde County (Griffin et al., 2010) including a volcanic complex composed of an olivine nephelenite lava lake and hyaloclastite with mantle xenoliths (Young and Lee, 2009; Raye et al., 2011). Such features were emplaced along the Llano thrust front through crustal-scale fractures due to reactivation during the Late Cenozoic to form the Balcones fault zone (Griffin et al., 2010).

To the east of the Innes-1 and Iona-1 cores is the San Marcos Arch area. At present day this encompasses the cities of Austin and San Antonio. The San Marcos Arch originated as a toe of the Ordivician southward prograding Texas peninsula of the Simpson group shelf and is characterised by a Cretaceous palaeohigh (Goldhammer and Johnson, 2001). It was uplifted along with part of a Grenville-age granitic intrusion complex as part of the regional affects during the Llano uplift (Young, 1986). Consequently sections of the Northwestern San Marcos Arch were exposed above sea level during the deposition of the Eagle Ford (Goldhammer and Johnson, 2001).

2.4.2 South Texas Stratigraphic Framework

During the Early Cretaceous two major carbonate platforms developed: the Neocomian to Early Aptian Cupido-Sligo platform and the Early Albian Stuart City Platform (Figure 2.4; Miller, 1990; Goldhammer and Johnson, 1999). In the Late Aptian, northern upwarping and southern downwarping of the craton created a rapid transgression resulting in the influx of the Pearsall fine-grained clastics and the subsequent cessation of platform carbonate deposition (Smith, 1981). Carbonate deposition did not return until the Glen Rose Formation, which is only seen in the Del Rio and Big Bend areas (Figure 2.4; Smith, 1981).

During the early and middle Albian the Stuart City carbonate ramp formed, prograding southwards in an arc, extending 150 km north of Laredo to the Big Bend area, reaching its greatest extent towards to the end of the middle Albian (Figure 2.4; Smith, 1970; Smith and Bloxom, 1974; Smith, 1981). To the north of the Stuart City ramp, in the area that will become the Maverick Basin, deposition of the Lower Knights Formations evaporites and limestones indicate the development of

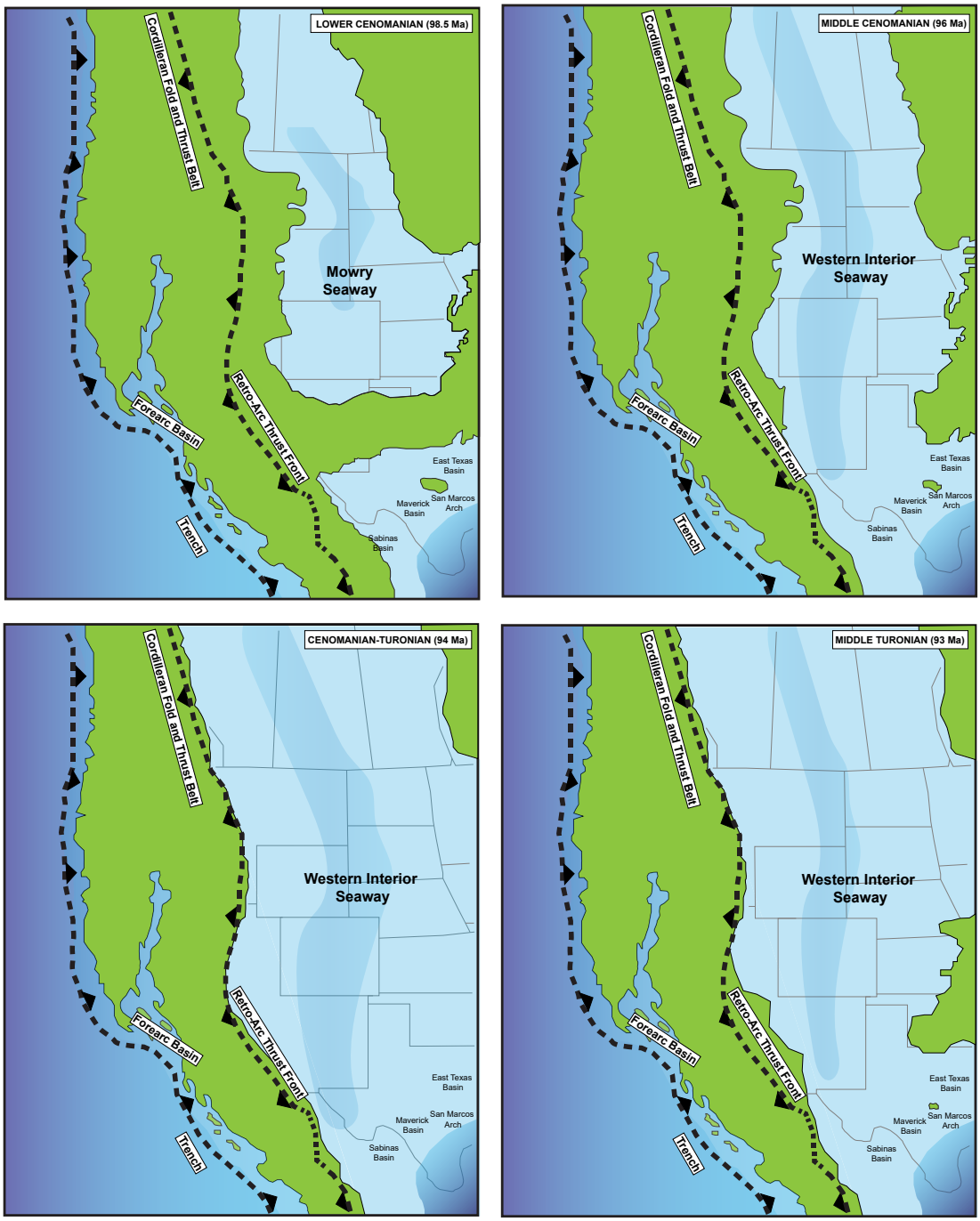

Figure 2.9: Palaeogeographic reconstruction of the Mowry Seaway and Western Interior Seaway from the Lower Cenomanian (∼98.5 Ma) to the Middle Turonian (∼93 Ma). Based on the work of Winker and Buffler (1988), Ewing (1991), McFarlan and Menes (1991), Dean and Arthur (1998), Goldhammer and Johnson (2001), Phelps et al (2013). Inspired by the diagram of Eldrett et al. (2014).

restricted marine conditions (Figure 2.4; Winter, 1961). Development of the Stuart City ramp and the Devils River platform as well as subsidence of the structural embayment of the region in between resulted in the formation of the Maverick Basin (Smith, 1970a, 1970b).

At this time in the Big Bend area, the Del Carmen Limestone and its equivalents were covering the platform interior (Winter, 1961; Miller, 1990), however, during the Late Albian, dramatic changes in depositional patterns occurred resulting in these being overlain by the marls of the Sue Peaks formation (Winter, 1961; Smith, 1970a; Smith, 1981). To the east, in the Maverick Basin, these changes resulted in the deposition of pelagic lime mudstones of the Salmon Peak formation (Smith, 1981), however, towards the end of the Late Albian carbonate deposition resumed in the NW of the Maverick Basin forming the upper Devils River limestone (Winter, 1961; Smith, 1970a; Smith, 1981; Miller, 1990).

Cessation of limestone deposition relating to the Stuart City platforms started towards the end of the Early Cenomanian with the influx of the Del Rio clay (Smith, 1981). The Del Rio clay, dominated by reworked volcanogenic detritus, filled the irregular topography of the Stuart City platform resulting in a highly variable thickness and a disconformable contact (Smith, 1981; Miller 1990). Overlaying the Del Rio clay, the Buda limestone signals reignition in carbonate production and may have formed a new prograding ramp if not for the influx of the fine grained sediments which form the Eagle Ford Group, sometimes known as the Boquillas Formation (Figure 2.4 and 2.10; Smith, 1981; Miller, 1990). The resultant Cenomanian-Turonian argillaceous carbonates of the Eagle Ford Group bracket the OAE 2 and in turn are overlain by the coccolith limestones and marls of the Austin Chalk (Figure 2.4 and 2.11; Winter, 1961; Smith, 1970; Smith, 1981; Eldrett et al., 2014).

In the Iona-1 and Innes-1 cores, the Eagle Ford Group is typically divided into two informal units, the Upper and Lower Eagle Ford (Figure 2.11; Eldrett et al., 2014) and this study will follow this method. However, previous studies have divided the Eagle Ford in West Texas into Lower, Middle, Upper and Acto Member (Lock and Peschier, 2006), but also in the A, B, C, D and E units (Figure 2.12; Donovan et al.,

2012).

2.4.3 Sedimentology

2.4.3.1 Georgetown Formation

The Georgetown formation, composed of interbedded fossiliferous micrite and marl beds, unconformably overlies formations of the Fredericksburg Group and is conformably overlain by the Del Rio formation (Figure 2.4 and 2.10; Atchison, 1954). The presence of shallow marine fossils such as oysters and various sub-species of ammonite suggest deposition in a sub-tidal, open shelf environment (Wilbert, 1966; Young, 1977).

2.4.3.2 Del Rio Clay

The Del Rio Clay is a $\sim$25 m thick dark olive-blue clay containing illite, montmorillonite and kaolinite (Figure 2.4 and 2.10; Young, 1977). A high pyrite content, the presence of the mollusc *Ilymatoqyra arientina* as well as a number of smaller species and lack of a normal bottom assemblages indicate that the Del Rio Clay has been deposited in a lagoon with abnormal benthic conditions (Young, 1977). The upper contact with the Buda Limestone is scoured and so disconformable (Young, 1977).

2.4.3.3 Buda Limestone

The Buda Limestone, a well-known petroleum reservoir formation, is a $\sim$30 m thick carbonate unit characterized by benthic fauna representing a quiet, semi-restricted depositional environment (Figure 2.4 and 2.10; Miller, 1990). This depositional environment is believed to have been the result of the southern platform rim of the Maverick Basin as Buda Limestone equivalents south of this are composed of pelagic foraminiferal wackestones (Trevino, 1988; Miller, 1990). Meter scale variations in the

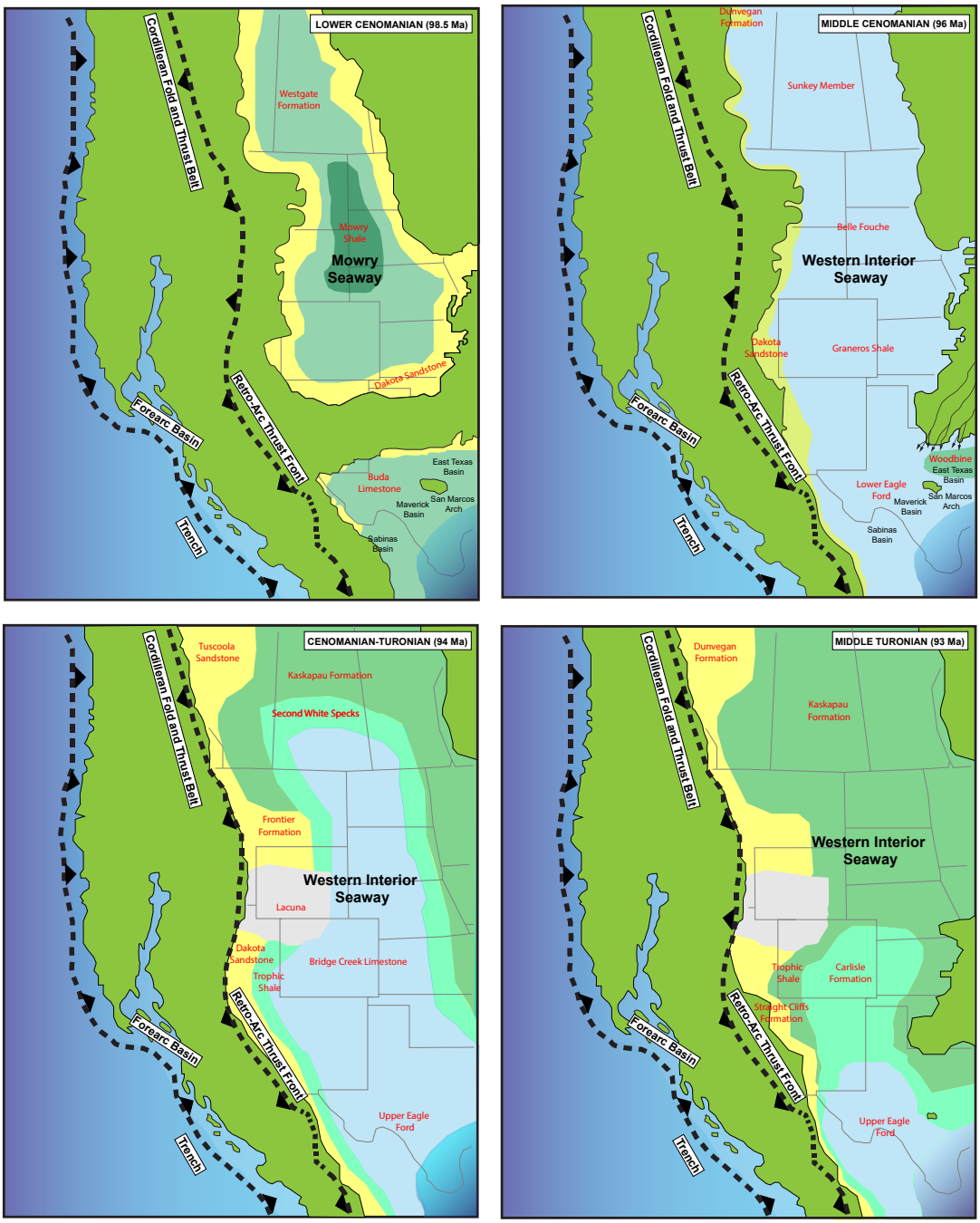

Figure 2.10: Facies distribution in the Mowry and Western Interior Seaways from the Lower Cenomanian (∼98.5 Ma) to the Middle Turonian (∼93 Ma). Based on the work of Winker and Buffler (1988), Ewing (1991), McFarlan and Menes (1991), Dean and Arthur (1988, 1998), Goldhammer and Johnson (2001), Phelps et al (2013). Inspired by the diagram of Eldrett et al. (2014).

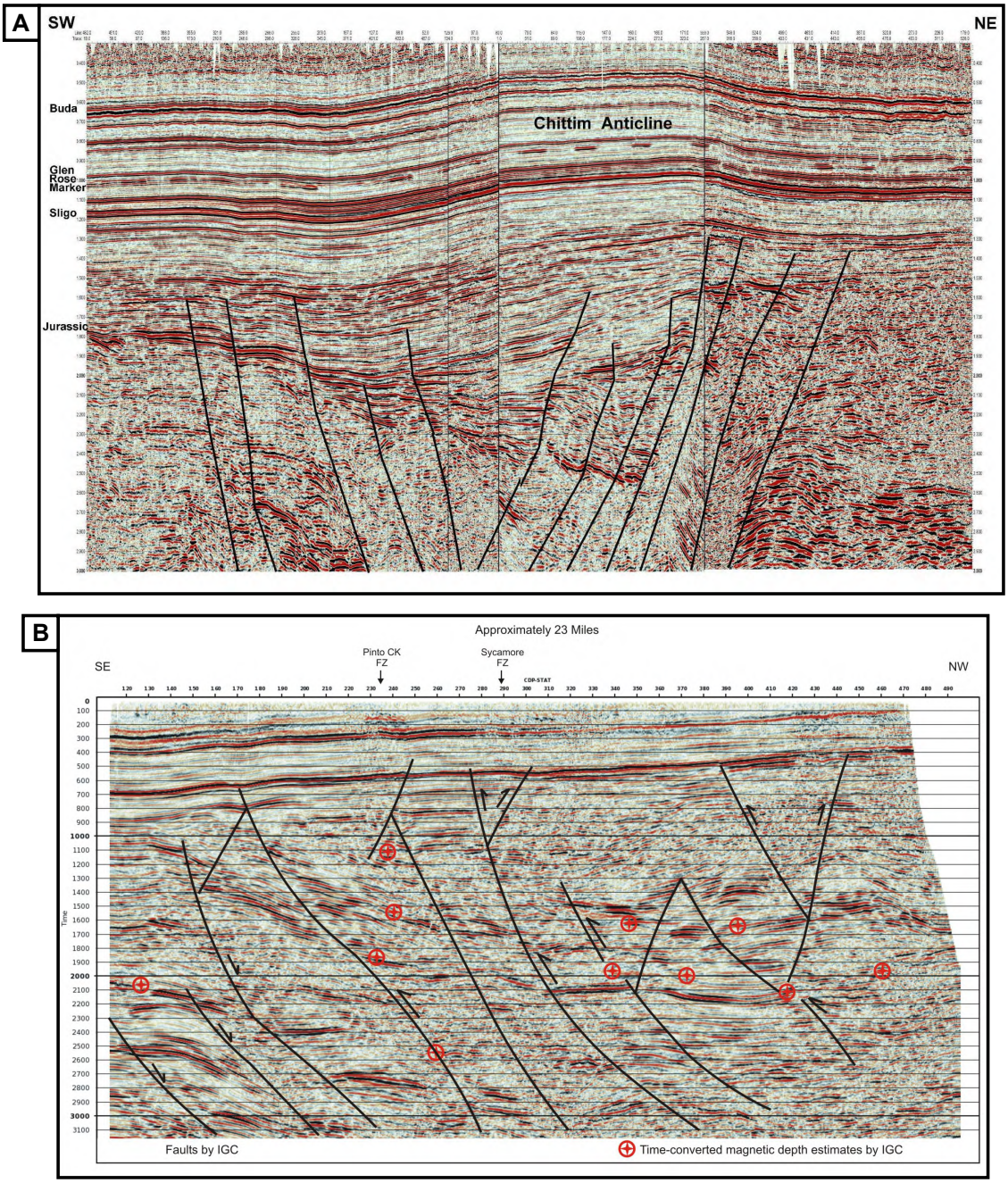

Figure 2.11: (A) Three dimensional seismic profile trending approximately SW-NE across the Maverick Basin (Scott, 2004). Note the steeply dipping normal faults and half-grabens that define the Jurassic extensional basin. This extensional basin is thought to represent a failed rift and is of similar structural style to the Eat African Rift basin (Scott, 2004). This profile also images the Chittim anticline: an SE plunging, upright open fold. The Chittim anticline is consistent with Laramide deformation in northeast Mexico and this has been suggested to have inverted the graben during the Laramide Orogeny (Alexander, 2015). (B) Three dimensional seismic profile trending approximately NW-SE across a northern part of the Maverick Basin (Scott, 2004). The northern section of the Maverick Basin can be separated into two Jurassic rift basins, the Moody and the Paloma (Alexander, 2015). The Moody Basin trends northwesterly along the Rio Grande and is interpreted to be the narrower and more structured of the two (Alexander, 2015). The Paloma Basin lies south and east of the Moody Basin; the two are offset by the Pinto Creek and Sycamore Creek left-lateral shears formed due to Laramide compression (Alexander, 2015).

Buda Limestones thickness have been suggested to be related to the formation of the pre-Gulfian erosion zone and the formation of small karst like depressions due to subaerial exposure prior to the deposition of the Eagle Ford formation (Dawson, 1986; Trevino, 1988; Miller, 1990).

2.4.3.4 Eagle Ford Group

Named for the town of Eagle Ford, the Eagle Ford Group is a mixed siliciclastic-carbonate mudstone succession with rhythmic bedding of varying thickness (Figure 2.4 and 2.10; Sellards, 1932). It has traditionally been divided into five facies: black shale, flag, clay, chalky limestone and marginal igneous (Hill, 1887; Sellards, 1932; Pessagno, 1969) and ranges from 120 m in the centre of the Maverick Basin to 5 m on the margin of the Stuart City carbonate platform (Desmares et al., 2007). It is time equivalent to the San Felipe, Agua Nueva, Cuesta del Cura, Tamaulipas, Boquillas and Chispa Summit formations in the west, the Benton Shale, Indianola Group, Mancos and Colorado shales to the northwest and the Tokio and Tuskaloosa

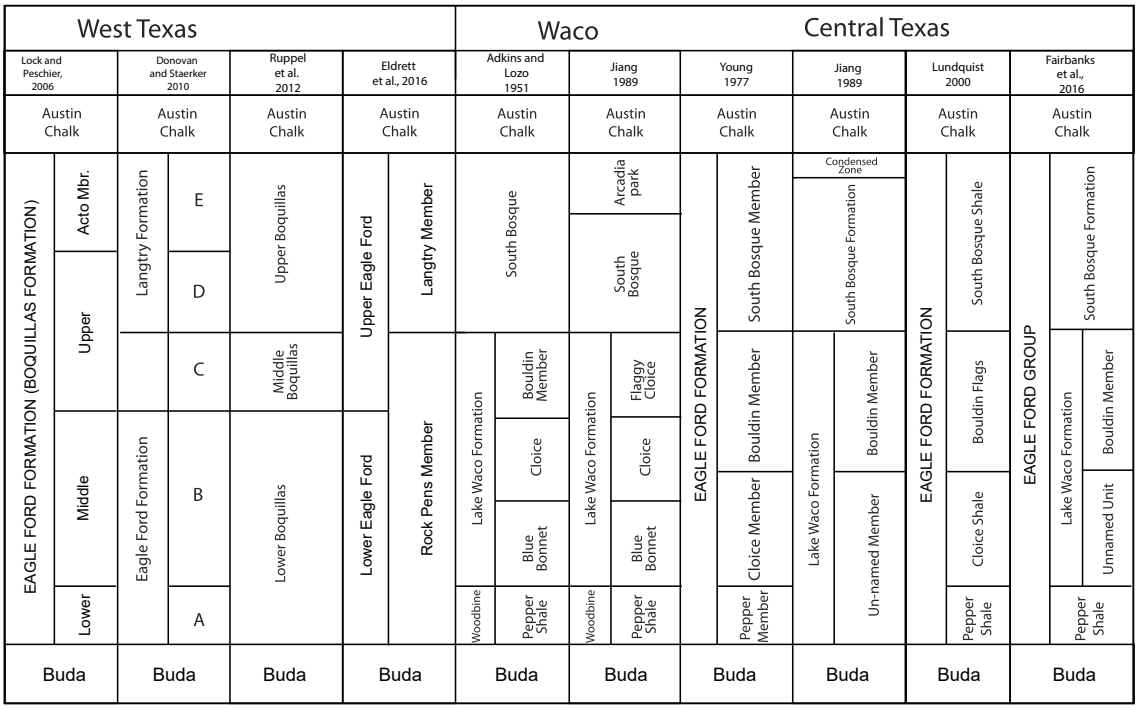

Figure 2.12: Composite stratigraphic chart reviewing nomenclature used in the Central Texas Eagle Ford intervals, compared with those used in West Texas and near Waco, Texas. This study adopts the names of Upper Eagle Ford and Lower Eagle Ford. Modified after Fairbanks et al., (2016).

formations to the east (Pessagno, 1969).

The Eagle Ford is separated into upper and lower members in the Maverick Basin. However, the positioning is highly variable as the exact subdivision is largely dependent on the location of the study and proxy used (Arthur et al., 1987; Trevino, 1988; Dawson, 2000). Irrespective of the division, many of the facies of the Eagle Ford in the Maverick Basin often have carbonate contents above 50% with the exception of the bentonites, which are altered volcanic facies (Desmares et al., 2007). In this study we use an abrupt fall in gamma ray log values associated with thick limestones of 2-5 m in total thickness is used as the base of the upper Eagle Ford formation.

2.4.3.5 Austin Chalk

The Austin Chalk is composed of massive, chalky and argillaceous blocky limestones interbedded with thin, grey, platy marls (Figure 2.4 and 2.10; Maxwell et al., 1967). The Austin Chalk is believed to have been deposited on an open, shallow marine shelf (Maxwell, 1967). The exact boundary between the Austin Chalk and the Eagle Ford is difficult to distinguish due to the similar compositions of their limestone units. As a result gamma ray logs are most often used to determine the boundary due to the Austin Chalk displaying lower values than the Eagle Ford Group (Trevino, 1988).

2.5 Thesis Objectives

As mentioned previously this project focuses on understanding the depositional environment and stratigraphic architecture of the Eagle Ford Group as well the relative effects of global and regional forcings on its sedimentary composition and organic matter enrichment. Firstly, this thesis investigates controls on stratigraphical and lateral changes in lithology in the study area. Vertical lithological variations are dependent on changes of sediment type and fluxes through time whereas lateral variations depend on the sedimentary processes involved with the deposition of the sediment,

as well as its type and supply. Chapter 3 presents a high resolution sedimentological study of the Eagle Ford Group in the southern Western Interior Seaway. This chapter presents an investigation of the controls on temporal and spatial variations in lithology within the study area and creates a detailed understanding of both sedimentological and geochemical changes in the marlstone-limestone couplets.

Given the fundamental role of global controls, such as perturbations of the global carbon cycle and sea level change, in the large-scale deposition of organic carbon it is important to understand the effect and causes of global events when studying sedimentary systems. The Eagle Ford Group contains one such global event OAE 2, which is known to have resulted in the sequestration of organic carbon in many areas of the world's oceans. However, the fundamental cause of OAE 2 is still poorly constrained. As such, in Chapter 4 Hg concentrations are examined in sedimentary successions spanning the Mid-Cenomanian to Early Turonian interval. This is in effort to further understand the role of LIP volcanism in initiating climatic and oceanographic change during the Mid-Cenomanian Event and the Cenomanian-Turonian OAE 2. This study compares Hg/TOC data with published neodymium-isotope data (εNd(t)) from Demerara Rise and osmium isotope data ($^{187}Os/^{187}Os$) from the Vocontian Basin, NW Tethys Ocean, as well as with palaeoceanographic models reconstructing dominant palaeo-current directions. This study uses these various lines of evidence to assess the most likely volcanic source of the Hg, its timing and its mode of transport.

Finally, recent studies from the central and southern Western Interior Seaway possibly indicate a complex oceanographic system with strong cyclonic gyres developing and drawing in both Tethyan and Boreal water-masses during the Cenomanian and Turonian (Slingerland et al., 1996; Kump and Slingerland, 1999; Elderbak and Leckie, 2016) including a southward migration of Boreal dinoflagellates during the Plenus Cold Event (Eldrett et al., 2014; van Helmond et al., 2014). As such to investigate the study areas oceanographic system and regional controls on the formation of the Eagle Ford Group Chapter 5 produces high resolution palaeoenvironment and palaeoclimatic constructions as well as investigates potential periods of water mass

exchange including the evolution of the basins dynamic hydrography.

3 Depositional Controls on Vertical Cyclicity and Lateral Variability within the Eagle Ford Group, South Texas, USA

This chapter is modified from **J. D. Scaife** et al., Depositional Controls on Vertical Cyclicity and Lateral Variability within the Eagle Ford Group, South Texas, USA. *Sedimentology*, in prep.

Abstract

The Eagle Ford Group of Texas is a succession of rhythmically inter-bedded packstones and wackestones deposited in the southern Western Interior Seaway during the Cenomanian-Turonian of the Upper Cretaceous. Recent investigations have suggested that either eustatic sea level change, astronomical forcings, changes in primary productivity and dilution, or changes in benthic oxygenation may be responsible for its lithological alternations. However, no consensus has yet been reached which satisfactorily explains the vertical cyclicity and lateral variabilities that are visible in this formation. In order to better understand the controls on the temporal and spatial changes in the Eagle Ford Group this study examines cm-scale geochemical, mineralogical and sedimentological changes in the metre-scale packstone-wackestone couplets as well as whole core-scale stratigraphy, sedimentology and mineralogy.

This chapter presents x-ray diffraction, x-ray fluorescence, total organic carbon (TOC) and log data collected from a northwest-southeast transect of 3 cores covering the Comanche Shelf to the Maverick intra-shelf basin. The results demonstrate that the depositional dynamics of the Eagle Ford Group are a function of interacting primary productivity and reworking by bottom currents, below storm wave base, rather than eustatic sea level change. Vertical lithological alternations result from alternating periods of low primary productivity and low accumulation rates (wackestone facies), and periods of higher primary productivity and accumulation rates (packstone facies).

Periods of high primary productivity are a function of ash falls (bentonitic claystones) that periodically fertilized the nutrient limited system of the southern Western Interior Seaway. Reworking of pelagic sediment by bottom currents resulted in high degrees of lateral variability (and low degrees of lateral continuity) in both the packstones and the wackestones. In the case of the laminated and massive foraminiferal packstones reworking resulted in the accumulation of carbonate sand ridges, sheets and isolated hydraulic dunes. The degree of reworking and dune separation within

this facies is likely a function of clay contents, with higher abundances resulting in a cohesive effect and acting against hydrodynamic critical shear stress, thereby preventing dune isolation.

3.1 Introduction

Mudrocks can appear deceptively homogenous due to their fine grain size and dark colour but are in-fact extremely vertically and laterally heterogeneous. These lateral and vertical variations can be used to interpret changes in their depositional environment and sediment delivery processes. One such heterogeneous system is the Eagle Ford Group, long exploited in south Texas as an unconventional oil and gas reservoir. Though commonly referred to as a shale due to its fine grain size the Eagle Ford is largely composed of alternating organic matter-rich argillaceous foraminiferal wackestones and foraminiferal packstones, giving the Eagle Ford an apparent cyclicity (e.g. Gilbert, 1895; Sellards, 1932; Fairbanks et al., 2016).

Rhythmically inter-bedded limestones and marlstones or shales, or 'rhythmites', occur commonly within Phanerozoic hemi-pelagic and pelagic successions of intrashelf basins from epicontinental seas (Einsele et al., 1991 and references therein). The origin of the lithologic rhythmicity has been strongly debated over the last century, as to reflect primary depositional conditions, i.e. climate and/or eustasy (e.g. Research On Cretaceous Cycles Group, 1986; Elder et al., 1994) or modified by secondary diagenetic processes (Ricken, 1986; Westphal et al., 2010 and references therein). Thus, chronologic and paleoclimate interpretations of the rhythmic intercalation of the two lithologies requires that unequivocal proof of a primary sedimentary origin of the rhythmicity is determined (Westphal et al., 2010). Rhythmically deposited inter-bedded limestones and marls or shales are particularly well expressed in the Cretaceous Western Interior Seaway (KWIS) of North America i.e. Bridge Creek Member, Greenhorn Formation of Central Colorado (e.g. Hattin, 1971, 1975; Elder, 1994; Meyers et al., 2001). As a result, the nature and origin of these rhythmic sediments have been extensively studied (e.g., Hattin, 1971, 1986; Fischer, 1980; Kauffman, 1995; Scholle and Arthur, 1980; Pratt, 1984, Arthur

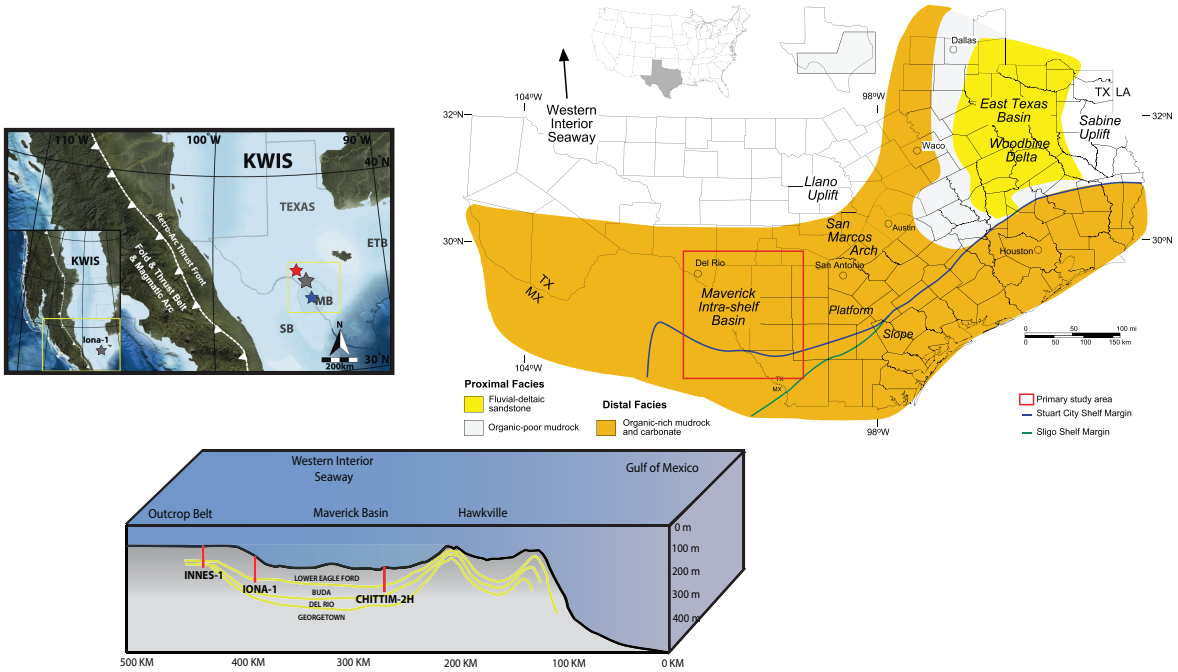

Figure 3.1: Cretaceous Western Interior Seaway (top left) displaying the position of the Maverick Basin cores as stars (red-Innes-1; green-Iona-1; blue-Chittim-2H; SB-Sabinas Basin; ETB-East Texas Basin; Figure modified after Eldrett et al., 2014). The 3D diagram (bottom figure) displays the position of these cores within and around the Maverick Basin at the southern edge of the Western Interior Seaway (left to right–north to west). The paleogeographic map of Texas (top right) at the Cenomanian-Turonian boundary shows the study area lies in and around the Maverick Intra-shelf Basin (modified after Ruppel et al., (2012) and Fairbanks et al., (2016)). The Sligo and Stuart City shelf margins form a physiographic break toward the downdip extent of the Eagle Ford.

et al., 1985, 1987; Eicher and Diner, 1985, 1991; Ricken, 1986; Arthur and Dean, 1991; Elder et al., 1994; and Savrda and Bottjer, 1994).

Most of the KWIS studies hypothesized that the driving mechanisms for deposition of rhythmically bedded strata were climate-controlled variations in: i) primary productivity (productivity model); ii) input of terrigeneous sediments (dilution model); iii) the intensity of bottom currents (scour model); iv) benthic oxygenation and hence, the extent and preservation of organic matter (redox model); and v) climatic response to changes in solar insolation driven by Milankovitch cycles, with the latter potentially forming the base of all of the previous models.

Recent studies have suggested that the lithological alternations and control of organic matter enrichment in the Eagle Ford are dependent on global astronomical forcing of the Cenomanian-Turonian climate (Sageman et al., 1997, 1998; Meyers et al., 2001; Eldrett et al., 2015a, 2015b). In this model the organic matter-poor limestones derive from a solar insolation maxima leading to more energetic environ-

ments, de-stratification of the water column and a nutrient-rich, unstable water column conditions (Eldrett et al., 2015b). Whereas the marlstones are due to periods of insolation minima which create periods of reduced energy gradients and stably stratified waters, resulting in water column stagnation and restriction, expansion of the oxygen minimum zone and importantly reduced biogenic carbonate-silicate production leading to the deposition of organic-rich marl beds as evidenced by redox-sensitive trace metals (TM) leading to preservation of amorphous organic matter (AOM) (Eldrett et al., 2015b).

However, no consensus on the controlling forces mean the following fundamental questions driving the research presented in this chapter remain:

1. What controls vertical variations in lithology and geochemistry in the Eagle Ford;

2. What controls lateral variations throughout the Eagle Ford sedimentary record and laterally across the Maverick Basin and surrounding Commanche shelf;

3. What controls the rhythmicity of the Eagle Ford's lithological couplets.

This study uses a unique data set along a $\sim$300 km transect of cores deposited with increasing palaeobathymetry to prove a primary sedimentary origin of the rhythmicity and constrain the controls on the facies lateral and vertical heterogeneities and variabilities within the southernmost Western Interior Seaway (Figure 3.1).

The analytical approach of this study consists of using a combination of sedimentological analysis (rock eval, coulomat, core-scale and thin sections), mineralogical analysis (XRD) and geochemical analysis (XRF). All of which are proven tools for reconstructing high-resolution depositional and environmental conditions under which a sedimentary interval has been deposited (e.g., Kuhnt et al., 1997, 2004; Caron et al., 1999; Meyers et al., 2001, 2012a,b; Prokoph et al., 2001; Kuypers et al., 2004; Sageman et al., 2006; Mitchell et al., 2008; Voigt et al., 2008; Lanci et al., 2010; Ma et al., 2014) and as such primary objectives of this study are to understand:

1. What are the lithofacies present in the Eagle Ford of west Texas;

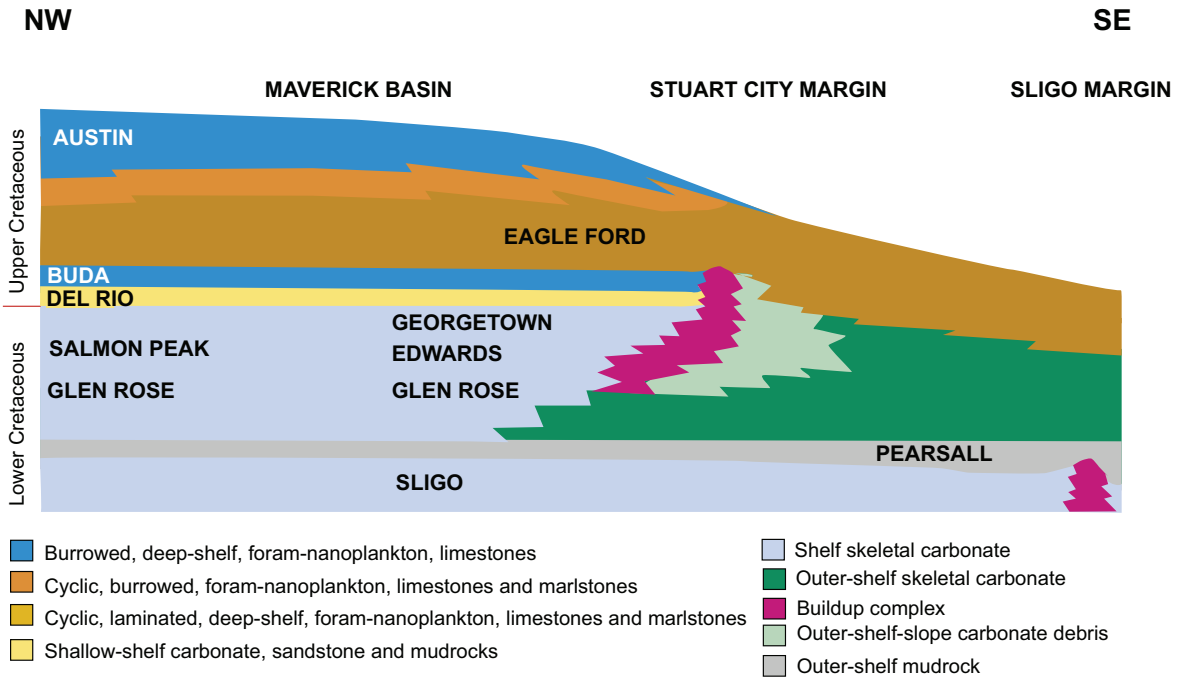

Figure 3.2: Generalized cross section through the Cretaceous Gulf of Mexico Basin. The Eagle Ford overlies thick progradational packages of the Lower Cretaceous Comanche Shelf. Modified after Ruppel et al., (2012) and Fairbanks et al., (2016).

2. What is the depositional enviroment and dynamics of the Eagle;

3. What are the sedimentary processes that control lateral changes and differences in sediment type and supply through time;

4. How continuous are the packstone and wackestone facies and what are the processes that control this;

5. Can high-resolution geochemical data be used to constrain the fine-scale evolution of the lithological facies within the metre-scale lithological couplets in the Eagle Ford.

3.2 Geological and Stratigraphical Setting

For the purpose of this chapter three marine mudrock successions were studied spanning the Mid-Cenomanian to Early Turonian interval in the Maverick Basin and surrounding Commanche shelf. All three sequences are from drilled research cores (Innes-1, Iona-1 and Chittim-2H), which sample the Eagle Ford Group, Buda For-

mation and Austin Chalk in the Southern Western Interior Seaway (Maverick Basin, Texas, USA, Figure 3.1). In the Iona-1 and Innes-1 cores, the Eagle Ford Group is typically divided into two informal units, the Upper and Lower Eagle Ford (Figure 3.2; Eldrett et al., 2014).

The sequences is typically defined as a 60-130 m thick sequence of metre-scale organic-rich marl-limestone couplets underlain by the Early to Mid-Cenomanian Buda Formation (homogenous bioclastic limestone; Pessagno, 1969; Eldrett et al. 2014; Denne et al., 2014; Lowery et al., 2014; Eldrett et al., 2015b; Miller, 1990) and unconformably overlies the Coniacian-Santonian Austin Chalk (Maxwell, 1967; Trevino, 1988).

The Eagle Ford was deposited in a distal, clastic-sediment starved, intra-shelf basin along the retro-arc foreland basin of western North America, with a suggested palaeowater depth of $\sim$50-100 m (Pessagno, 1969; Eldrett et al. 2014; Denne et al., 2014; Lowery et al., 2014; Eldrett et al., 2015b).

The total duration of the preserved Eagle Ford sedimentary record is close to 8 Myr $\pm$ 0.3 Myr (Eldrett et al., 2015a) and comprises a number of sedimentary cycles, including a major transgression of the Upper Comanche Shelf of the Gulf Coast Margin within the southern portion of the Epicontinental Seaway of western North America (Dawson and Almon, 2010).

3.3 Analytical methods

3.3.1 X-Ray Diffraction Mineralogy (XRD)

Four-hundred samples were measured by XRD from the Innes-1, Iona-1 and Chittim-2H taken at an average of $\sim$30-40 cm intervals. In Iona-1 these were measured between the depths of $\sim$80-150 m, Innes-1 $\sim$42-80 m and Chittim-2H $\sim$1490-1520 m. Forty-eight samples were also measured by XRD to correspond to the samples used for thin sections and the scanning electron microscope (see section 3.4.4). Powdered 50 mg samples were analyzed by powder XRD using a

Siemens D500 X-ray diffractometer with a Co Ka source, operated at 40 kV and 25 mA, and scanned between 5 and 80 degrees 2Q, at the Department of Earth Sciences at Oxford University. Powders were back loaded into sample holders in the anaerobic chamber, although most specimens were not sufficiently abundant to completely fill the sample cavities. To prevent any oxidation during preparation and analysis, powders were coated with a thin layer of glycerol in the anaerobic chamber, which maintained stability well beyond the data collection period. Final X-ray diffractograms are shown with ”background” patterns of analyses performed on sample holders with identical amounts of glycerol removed.

3.3.2 Rock-Eval and Coulomat TOC analyses

TOC samples were measured at a regular average spacing of $\sim$10-15 cm for the Innes-1, Iona-1 and Chittim-2H cores irrespective of lithology, however, avoiding bentonitic claystones (see Results section). Six high resolution sections across the metre-scale couplets were also chosen from the Chittim-2H core with an average sample spacing of 1.5 cm. Total carbon (TC) and total inorganic carbon (TIC) were determined for around 130 samples from Chittim-2H with a Strohlein Coulomat 702 Analyzer (see details in Jenkyns, 1988). For TC and TIC analyses, sample aliquots were measured, with one aliquot having been heated overnight at 450℃ to remove organic matter. Total organic carbon (TOC) was calculated as the difference between TC and TIC. The long-term average value and reproducibility of TOC measurements on the in-house SAB134 standard is 2.95 $\pm$0.14 wt% (2 S.D., n = 27).

For all remaining Eagle Ford samples (cores Innes-1, Iona-1 and Chittim-2H), TOC was measured by Rock-Eval pyrolysis on a Rock-Eval VI standard instrument with pyrolysis and oxidation ovens, at the Department of Earth Sciences, Oxford University. Laboratory procedures as described in Behar et al. (2001) were used. Quality control was provided by the in-house SAB134 standard and the certified IFP160000 standard, which were regularly run between samples. The reproducibility of TOC analyses of the in-house SAB134 and the reference IFP160000 standards were, respectively, $\pm$ 0.22% and $\pm$ 0.08% (2 S.D.). The long-term average TOC values of

SAB134 standard and IFP160000 were 2.98 % and 3.27 %, respectively.

3.3.3 X-Ray Fluorescence (XRF)

High-resolution (1-4 cm) elemental concentrations (e.g. Ca, Ti, Fe, Rb, Zr) were obtained by hand-held X-ray fluorescence (XRF) analysis on eight metre-scale lithological couplets from the slabbed archive halves of the Chittim-2H core. XRF analyses were conducted with a Thermo Scientific Niton XL3 instrument, with a 120-sec measurement window. Long-term drift in measurement values was counteracted by regular internal calibration. Internal measurement uncertainty, partly due to internal calibration and Compton normalization, differs between elements. Long-term drift in analyses was further checked by repeated analysis of the NIST2780 and NIST2709 international reference standards. Repeated analysis of the NIST2780 standard showed for calcium (Ca) an average of 1426 ppm, with a standard deviation (S.D.) of 205 ppm and an average internal error of 112 ppm, and for iron (Fe) an average of 28395 ppm, with a standard deviation of 240 ppm and an average internal error of 216 ppm. Repeated analysis of the NIST2709 standard showed for calcium an average of 21130 ppm, with a standard deviation of 362 ppm and an average internal error of 476 ppm, and for Fe an average of 34678 ppm, with a standard deviation of 382 ppm and an average internal error of 454 ppm. Reproducibility of XRF-based calcium concentration data was further confirmed by comparison to Rock-Eval derived calcium carbonate content ($CaCO_3$; calculated from the mineral carbon content).

3.3.4 Thin Section and SEM Analysis

Seventy-five thin sections from the Innes-1 and Chittim-2H cores were petrologically interpreted at the Shell and Weatherford facilities in Houston, Texas. Using these samples an initial assessment of the microfacies found in these thin sections was compiled and applied to the Innes-1 and Chittim-2H cores. Subsequently, forty-eight further thin sections were produced from conventional core samples and petrolog-

Table 3.1: Petrographic summary of the 5 dominant facies in Upper and Lower Eagle Ford of the Innes-1, Iona-1 and Chittim-2H core as described from 48 photomicrographs. This includes: 1. Micro-textures and fabrics; 2. Allochems; 3. Cements; 4. Matrix; 5. XRD Mineralogy.

Facies	Micro-Texture/Fabrics	Allochem	Cements	Matrix	Mineralogy
Argillaceous Wackestone Lower Eagle Ford	elongate allochem alignment and zones of concentrated allochems indicate faint parallel lamination; compacted; parallel-aligned, compacted, micritic peloids dispersed throughout matrix	5-10% planktonic foraminifers; 1-5% mollusk fragments, unidentified skeletal grains, peloids	5-10% calcite cement (grain-replacing and filling some foraminifers); 1-5% framboidal pyrite; <1% authigenic kaolinite, dolomite, chert, iron oxides, hydrocarbons (dead oil)	mixtures of >20% micrite, 5-10% detrital clay, and 5-10% organic matter	65% calcite, 18% quartz, 11% clays, 3% pyrite, 2% plagioclase, marcasite 1%
Argillaceous Wackestone Upper Eagle Ford	parallel laminae defined by compacted, lenticular micritic peloids and continuous zones of concentrated allochems	5-10% unidentified skeletal fragments; 1-5% planktonic foraminifers, mollusks fragments, peloids	5-10% calcite cement; 1-5% chert, pyrite, authigenic kaolinite, dolomite; <1% iron oxides, hydrocarbon (dead oil)	mixtures of >20% micrite, detrital clay, and <1% organic matter	45% calcite, 15% quartz, 25% clays, 6% plagioclase, 6% pyrite, 2% marcasite
Foraminiferal argillaceous wackestone	Even, parallel laminae defined by alternating matrix-rich and fossil-rich beds; compacted; parallel-aligned, compacted, micritic peloids dispersed throughout matrix	10-20% planktonic foraminifers; 5-10% unidentified skeletal grains; 1-5% mollusk fragments, peloids, Inoceramus debris	10-20% calcite cement (mostly grain-replacing and filling foraminifer chambers); 1-5% framboidal pyrite, authigenic kaolinite; <1% dolomite, chert, iron oxides, hydrocarbon (dead oil)	mixtures of >20% micrite, 10-20% detrital clay, and 5-10% organic matter	61% calcite, 16% quartz, 15% clays, 2% plagioclase, 4% pyrite, 2% plagioclase, 1% marcasite
Massive foram packstone	neomorphosed, spar and microspar calcite fabric; mostly massive with a few noticeable, parallel, discontinuous matrix layers	>20% calcite-replaced fossil fragments; 5-10% planktonic foraminifers; <1% mollusks, echinoderms, calcispheres, Inoceramus, peloids	>20% calcite cement; 1-5% pyrite, dolomite; <1% kaolinite, iron oxides, hydrocarbon (dead oil)	mixtures of 5-10% detrital clay and 1-5% organic matter	86% calcite, 5% quartz, 5% clays, 1% pyrite, 0.5% plagioclase
Laminated foram packstone LEF	neomorphosed, spar and microspar calcite fabric; mostly laminated with some massive sections, due to parallel alignment of fossil-rich laminae	>20% calcite-replaced fossil fragments; 5-10% planktonic foraminifers; <1% mollusks, echinoderms, calcispheres, peloids	>20% calcite cement; 1-5% pyrite, dolomite; <1% kaolinite, iron oxides, hydrocarbon (dead oil)	mixtures of 1-5% detrital clay and organic matter	76% calcite, quartz 7%, 12% clays, 2% pyrite, 0.5% plagioclase
Laminated foram packstone UEF	neomorphosed, spar and microspar calcite fabric, indication of parallel alignment from elongate allochem alignment and zones of concentrated allochems	10-20% planktonic foraminiferal debris (lesser amounts of agglutinated foraminifers, higher numbers of benthonic foraminfer); 5-10% unidentified skeletal fragments; 5-10% mollusk fragments (including a few large Inoceramus)	10-20% calcite cement; 1-5% pyrite, kaolinite; <1% dolomite, chert, chalcedony, iron oxides,	mixtures of >20% micrite matrix; 10-20% detrital clay matrix; moderate organic matter	18% quartz, 69% calcite, 2% plagioclase, 2% pyrite, 1% marcasite, 14% clays
Bentonitic Claystone					75% clays, 10% quartz, 10% calcite, 5% plagioclase

ically intepreted under a standard election microscope at the University of Oxford, Department of Earth Sciences from the Chittim-2H, Innes-1 and Iona-1 cores.

Sampling at the University of Oxford was dependent on their stratigraphic position within the core and lithology using the first pass approach from the Innes-1 and Chittim-2H cores. Twenty-four were analysed from the packstone facies, twelve of which were from the Upper Eagle Ford and twelve from the Lower Eagle Ford. Twenty-four were also analysed from the wackestone facies, twelve of which were taken from the Upper Eagle Ford and twelve from the Lower Eagle Ford. The final assignment of microfacies to the cores was achieved by then applying the interpretation of these thin sections to the rhythmites in the cores.

For the thin-sections a 4-by-2 cm portion of each of the forty-eight core samples

was used for thin section analysis. Any mud cake or obvious contamination of the sample was removed from samples prior to thin section preparation. Samples were dried in a conventional oven at 60℃ overnight. After drying the samples were vacuum/pressure impregnated with blue epoxy resin. After the epoxy cures, thin section were cut and polished to approximately 30 microns thickness. All of the thin sections were stained with Alizarin Red S and potassium ferricyanide stains. This combination stain caused calcite to stain red, ferroan calcite to stain mauve to purple, ferroan dolomite to stain light blue, and ankerite to stain dark blue. Dolomite is typically unstained during this process although it can sometimes stain pink (see Appendix A). The thin sections were photographed at low magnification (50X) in order to document the texture and fabric of the sample. Higher magnification photomicrographs (200X) were taken to document the details of the pore system and other features of interest.

A freshly broken surface of each sample was mounted on an aluminium stub with carbon paint, and given a thin coating of gold (or gold/palladium alloy). The sample was subsequently examined under a FEI Quanta 650 scanning electron microscope at the University of Oxford Earth Sciences Department to document the nature of any pore systems and to provide high magnification images showing the distribution of clay minerals and other cements associated with the samples. Minerals were analyzed using the EDS system in order to determine the elemental and mineral composition of the samples. The EDS system uses x-rays generated by the electron beam in the SEM to identify the characteristic radiation of each element present in the target (sample). The SEM/EDX system operates a light element detector, which allows for the detection of most elements heavier than sodium. Under favourable conditions, elements between carbon and sodium may also be detected. At least two SEM images of each sample were obtained. Lower magnification views (50X-150X) provided a general overview of the texture of the sample and nature of the macroporosity of the sample. Higher magnification views (typically $>$1000X) were obtained to illustrate specific features of the sample (usually morphology of the clay minerals or details of authigenic minerals associated with the pore system).

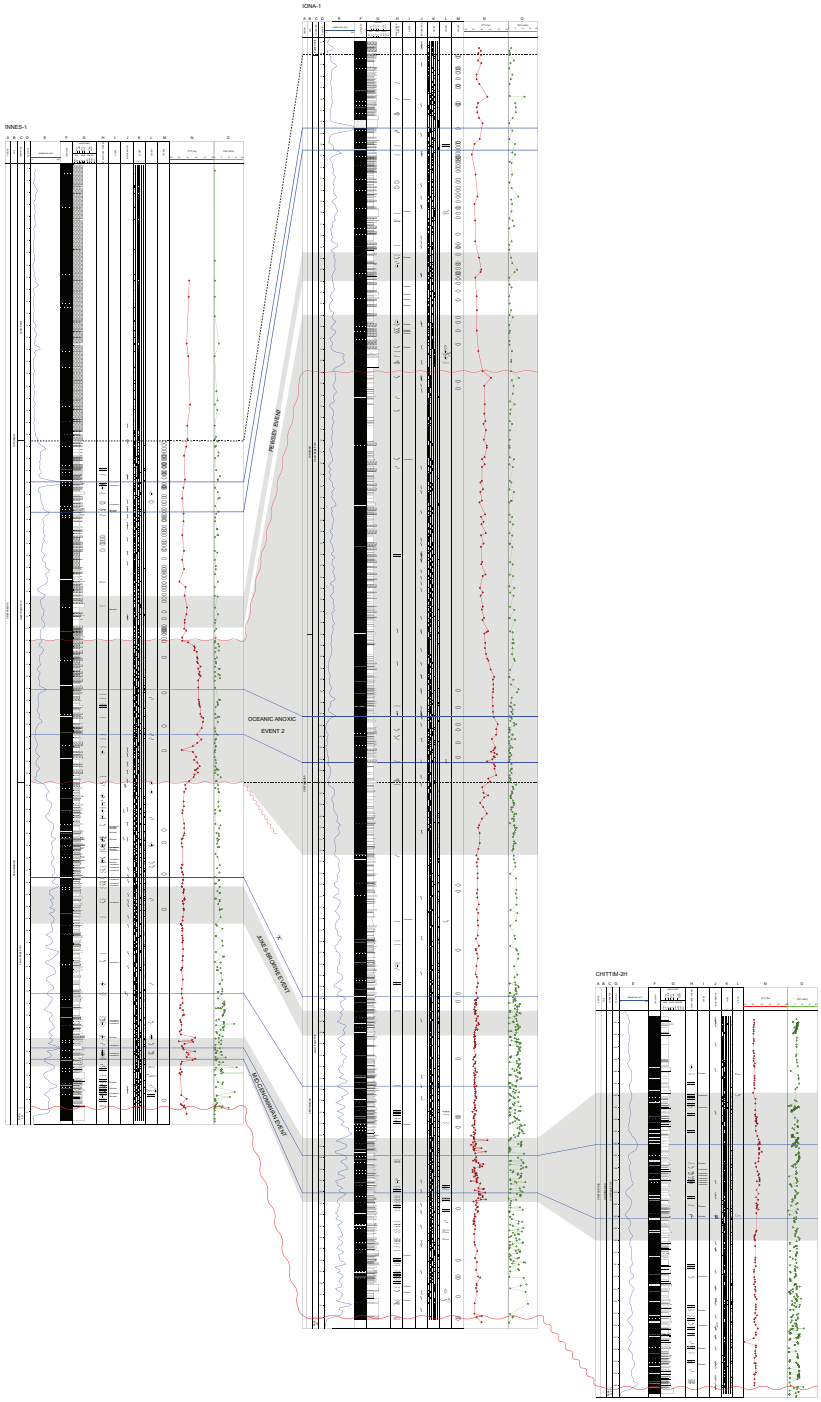

Figure 3.3: Stratigraphic columns and suggested correlation of the Innes-1, Iona-1 and Chittim-2H cores showing the internal architecture of the Eagle Ford formation as well as part of the Austin Chalk and Buda Limestone. A. Period; B. Age; C. Formation; D. Depth (m); E. Gamma Ray (API; this study); F. Lithology (this study); G. Grain Size/ Dunham Classification (this study); H. Sedimentary Structures/ Fossils 1 (this study); I. Notes (this study); J. Bioturbation (this study); K. Facies (this study); L. Other Sedimentary Structures/ Fossils 1 (this study); M. Other Sedimentary Structures/ Fossils 2 (this study); N. $\delta^{13}C$ (; Eldrett et al., 2014, 2017; Scaife et al., 2017); O. TOC (wt%; this study; Eldrett et al., 2014, 2017; Scaife et al., 2017). Facies codes are as follows: 1. Argillaceous Wackestone; 2. Laminated Argillaceous Foraminiferal Wackestone; 3. Laminated Foraminiferal Packstone; 4. Massive Foraminiferal Packstone; 5. Bentonitic Claystone. Correlation (this study) is based on sedimentological changes, gamma ray, occurrence and architecture of bentonitic claystones, carbon isotope excursions and sedimentary structures. 'X is marked as it refers to a previously discussed correlative 'bentonite (described as a bentonitic claystone in this study) in Eldrett et al., 2017.

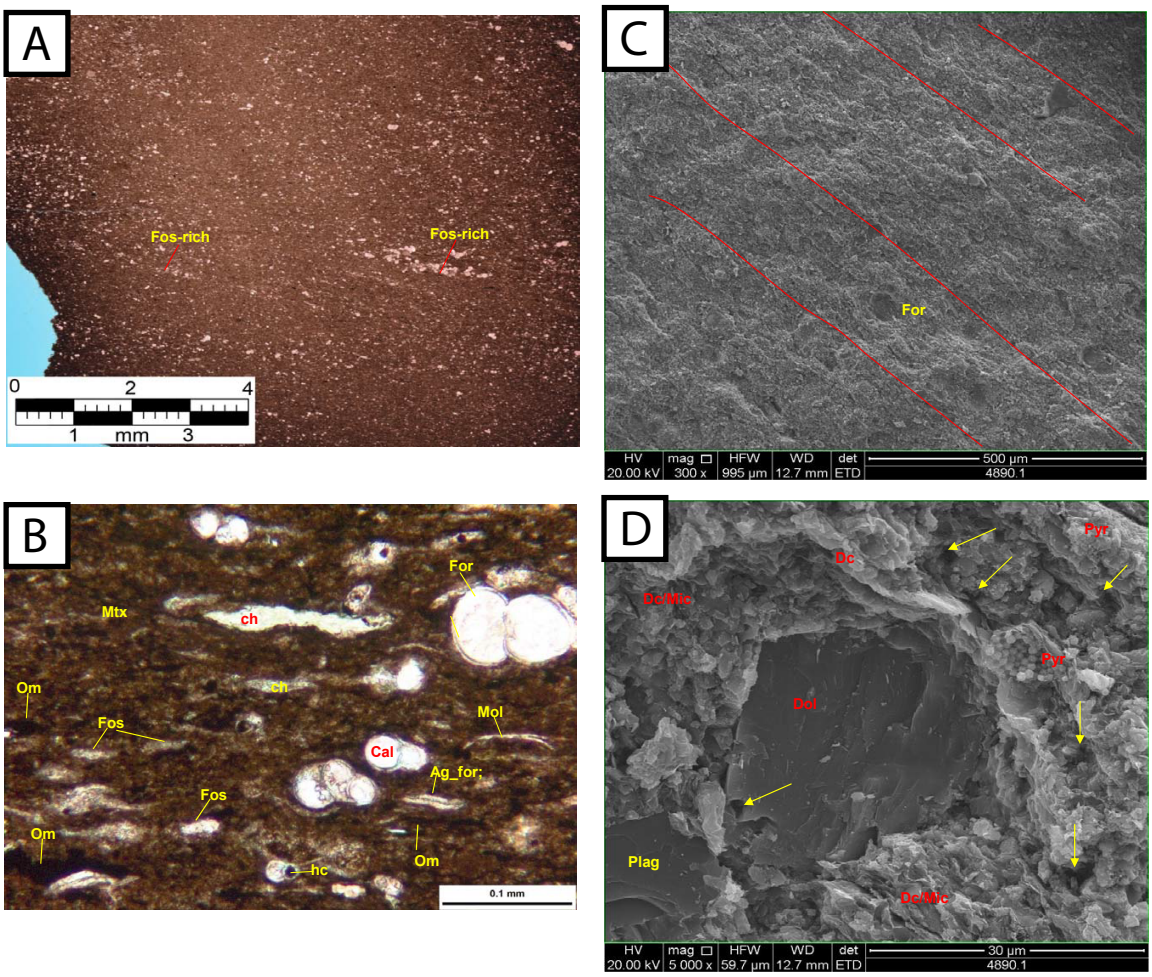

Figure 3.4: Photomicrographs of argillaceous wackestones from the Lower Eagle Ford, 1490.5 m in Chittim-2H. Recognizable planktonic foraminifers (For) and unidentifiable fossil fragments (Fos) characterize this argillaceous limestone; note less abundant agglutinated foraminifers (Agfor) and mollusk fragments (Mol). The abundant matrix consists mainly of micrite and detrital clay (Mtx). This section analysis indicates wispy seams of opaque, organic-rich stringers (Om) dispersed sub-parallel to faint, discontinuous, fossil-rich laminae (Fos-rich). Authigenic calcite (Cal), pyrite, chert (ch), and hydrocarbons (dead oil; hc) fill foraminferal chambers and replace fossil grains. Authigenic pyrite framboids and dolomite rhombs are scattered throughout the matrix. faintly laminated texture (Photo C; red lines) comprised of an abundant amount of matrix material. Higher magnification imagery in Photo D reveals a micritic matrix intermixed with a moderate amount of detrital clay (Dc/Mic) surrounding silt-size, detrital plagioclase grains (Plag), spherical, calcite-filled foraminifers (Photo C; For), and authigenic, dolomite crystals (Dol). Authigenic clusters of pyrite framboids (Pyr) replace and dolomite crystals displace the matrix.

3.4 Results

3.4.1 Sedimentology

Based on the Dunham Classification scheme (Dunham, 1962) using thin-section analysis as well as XRD and mineralogical analysis the following five distinctive facies are identified within the Eagle Ford Group of south Texas: (1) argillaceous wackestone facies, (2) laminated argillaceous foraminiferal wackestone facies, (3) laminated foraminiferal packstone, (4) massive foraminiferal packstone facies, (5) massive bentonitic claystone. A synopsis of the Eagle Ford facies and their associated attributes are found in Table 3.1 and summarised in the sections below.

3.4.1.1 Core Sedimentology

The Buda Limestone underlies the Eagle Ford Group in the Southern Western Interior Seaway. It is dominated by two dominant lithologies: (1) calcispheral wackestones, and; (2) skeletal packstones (section 3.5.1.7). Within this dataset a gamma ray increase of $\sim$100 API at $\sim$82 m in Innes-1, $\sim$153 m in Iona-1 and $\sim$1521 m in Chittim-2H divides the Eagle Ford from the Buda Limestone (Figure 3.3). Visually in the Innes-1, Iona-1 and Chittim-2H cores the contact between the Lower Eagle Ford Formation and the Buda Formation is sharp with an irregular base and occurs at 80.65 m, 152.97 m and 1521.21 m in Innes-1, Iona-1 and Chittim-2H. The bed stratigraphically above this contact is a packstone/breccia containing sub-angular fragments of both the skeletal packstones and calcispheral wackestones of the Buda Limestone in Innes-1 to rounded/sub-rounded fragments in Chittim-2H.

The Lower Eagle Ford is dominated by alternating laminated foraminiferal packstones and laminated argillaceous foraminiferal wackestones (Figure 3.3). Within the Lower Eagle Ford the laminated argillaceous foraminiferal wackestones are often grade into argillaceous wackestones (Figure 3.3). Argillaceous wackestones are also found around the base and top of the Lower Eagle Ford as well as the

Mid-Cenomanian Event. Some massive foraminiferal packstones are also found in the Lower Eagle Ford (Figure 3.3). The Lower Eagle Ford interval is ∼48 m in Iona-1, ∼29 m in Innes-1 and composes the whole core available for the Chittim-2H core (∼32 m), though Chittim-2H only contains the lowest most part of the Lower Eagle Ford. Within the Lower Eagle Ford of Innes-1, Iona-1 and Chittim-2H the Mid-Cenomanian Event shows significant influxes of benthic organisms such as inoceramus and other unidentifiable shell fragments as well as intense bioturbation in Chittim-2H.

Overlying the Lower Eagle Ford is the Upper Eagle Ford, which is dominated by lightly bioturbated argillaceous wackestones and heavily bioturbated laminated foraminiferal packstones (Figure 3.3). These bioturbated beds commonly have higher clay contents by 3-10% in the laminated foraminiferal packstones and 10-20% in the argillaceous wackestones, most often dominated by mixed smectite and illite. The division between the Upper and Lower Eagle Ford is based on a drop in gamma ray of 50-100 API, in Innes-1 this occurs around 54 m and in Iona-1 this occurs around 106 m (Figure 3.3). Visually, the contact between the Upper and Lower Eagle Ford is more subtle with the core sedimentology transitioning to bioturbated Upper Eagle Ford facies between 54.2-53.1 m in Innes-1 and 106.3-104 m Iona-1. The stratigraphic section corresponding with the positive CIE of OAE 2 in the Upper Eagle Ford shows significant influxes of mollusc, inoceramid and unidentifiable shell fragments compared to other sections of this interval.

Overlying the Upper Eagle Ford is the Austin chalk, which in both Innes-1 and Iona-1 is dominated by heavily bioturbated, skeletal packstones interbedded with light grey, weakly laminated wackestones. The contact between the Upper Eagle Ford and Austin Chalk is gradational and occurs around ∼25.5 m in Innes-1 and ∼42.1 m in Iona-1 (Figure 3.3). The contact is not cored in the Chittim-2H section.

3.4.1.2 Argillaceous Wackestone Facies

Petrography

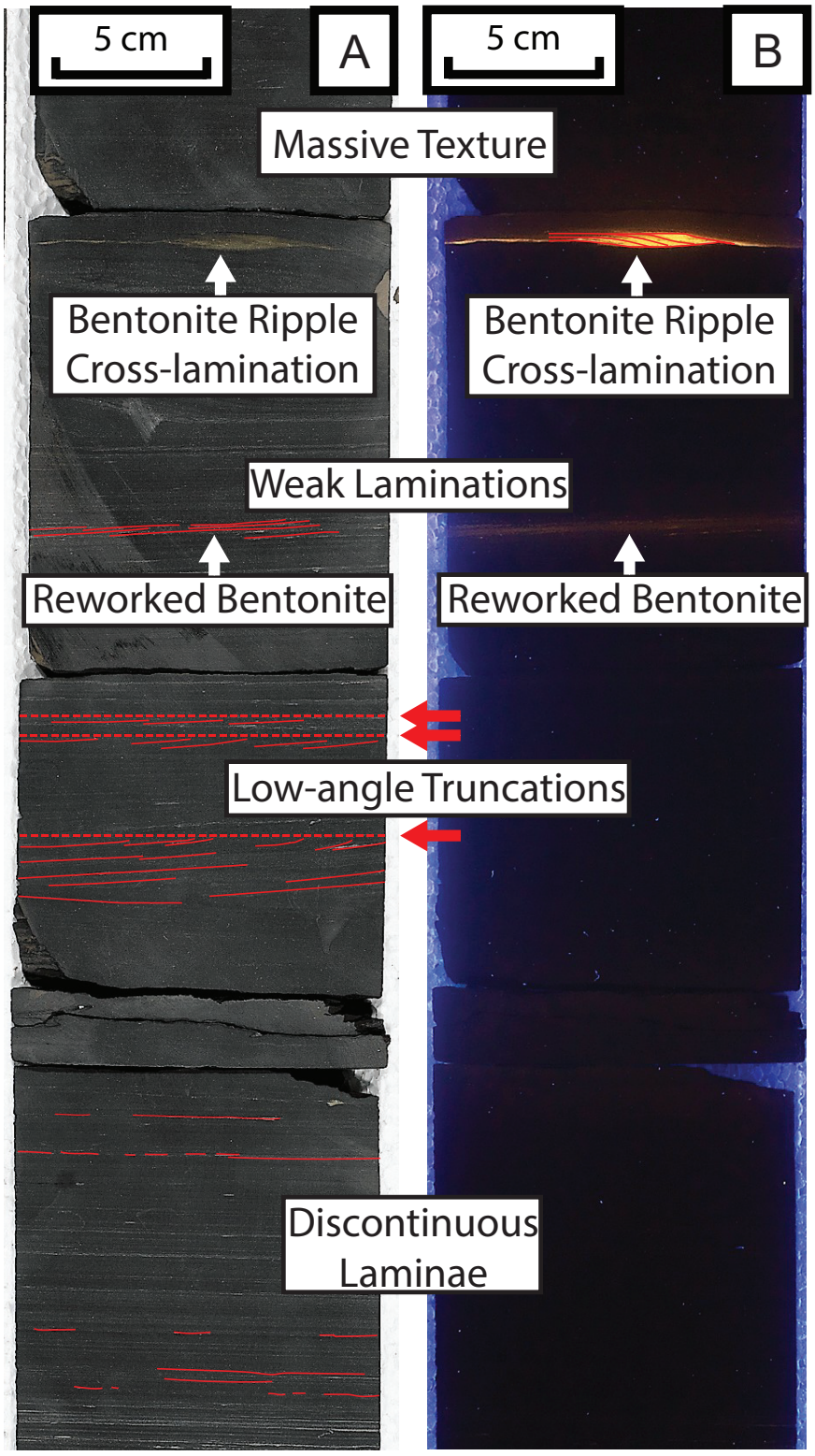

Figure 3.5: Core photographs of the characteristic features of argillaceous wackestones in: (A) normal light; (B) ultraviolet (UV) light. Structures commonly found in this facies include generally weak laminations to massive texture, low angle truncations, discontinuous laminae, scours and erosional boundaries (red arrows).

As per the thin section analysis the argillaceous wackestone facies is composed of 5-10% of foraminiferas by area, with minor mollusc fragments, skeletal grains and peloids (Figure 3.4). This facies type tends to have a micritic matrix, with 5-10% amounts of detrital clay and organic matter, and a calcite cement normally with minor framboidal pyrite, $<$1% authigenic kaolinite and rhomboidal dolomite scattered throughout the abundant ($>$20%) matrix. These mineralshave a vague elongate allochem alignment creating zones of very faint parallel lamination. Thin section analysis indicates thin,wispy seams of opaque, organic-rich stringers dispersed subparallel to faint, discontinuous, fossil-rich laminae (Figure 3.4). Authigenic calcite, pyrite, chert, and hydrocarbons fill foraminferal chambers and replace fossil grains. Within the Lower Eagle Ford this facies is dark-to-medium-dark gray in core (Figure 3.5).

In the Upper Eagle Ford this facies is medium grey at core scale with alternating parallel laminae defined by increasing amounts of fossil concretions and concentrated amounts of matrix material (Figure 3.6). Larger, planktonic foraminifers show replacement in the form of calcite cement and lesser amounts of kaolinite and pyrite within their spherical, intraskeletal chambers (Figure 3.7). Mollusc fragments, muscovite grains, and compacted, micritic peloids are parallel aligned to laminae. Framboidal pyrite, rhombic dolomite, and nodular chert visibly replaces matrix and organic material (Figure 3.6).

XRD reveals that within the Lower Eagle Ford this facies is largely composed of calcite ($\sim$65%), quartz ($\sim$18%) and clays ($\sim$10%), with smaller amounts of pyrite ($\sim$3%), plagioclase ($\sim$2%), marcasite ($\sim$1%) and dolomite ($\sim$1%; Table 3.1). The clays are composed mostly of illite ($\sim$3.5%), mica ($\sim$3%), smectite (1.5%) and kaolinite ($\sim$1%). Within the Upper Eagle Ford this facies type has significantly lower concentrations of calcite ($\sim$41%) and slightly lower concentrations of quartz ($\sim$15%). Clay concentrations are significantly higher (average $\sim$25%) and plagioclase ($\sim$6%), pyrite ($\sim$6%) and marcasite ($\sim$2%) are also higher (Table 3.1). The majority of the clays are mixed illite and smectite ($\sim$16%), illite and mica ($\sim$8%), and kaolinite ($\sim$3%).

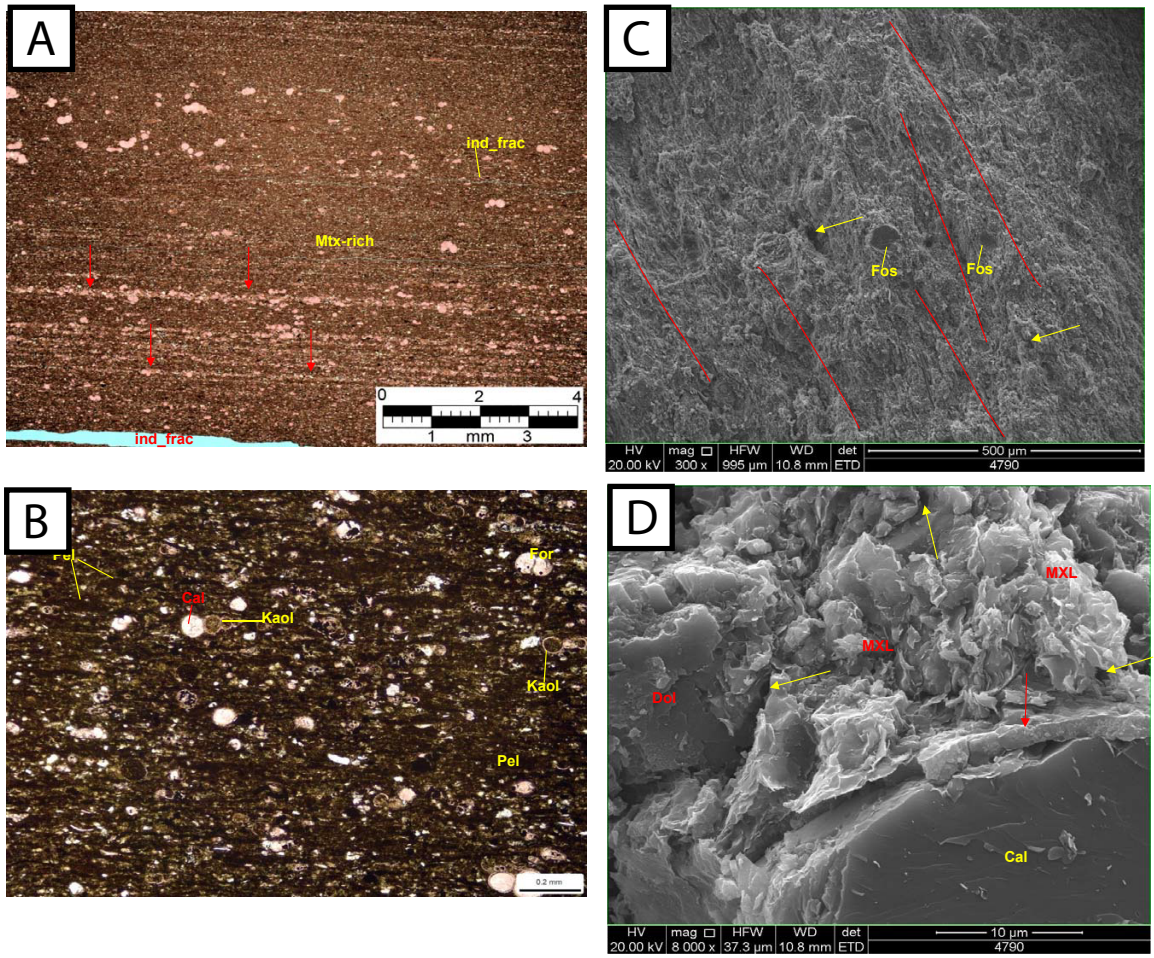

Figure 3.6: Photomicrographs of the argillaceous wackestone from the Upper Eagle Ford, 51.95 m in Innes-1. This sample an abundant amount of matrix consisting of micrite and detrital clay. XRD analysis indicates that detrital clays are mixed-layer illite/smectite and illite. Weak parallel laminae are defined by alternating zones of denser fossil accumulations (red arrows) and matrix concentrations (Mtx-rich). Larger, planktonic foraminifers (For) show replacement in the form of calcite cement (Cal) and lesser amounts of kaolinite (Kaol) and pyrite within their spherical, intraskeletal chambers. Mollusk fragments, muscovite grains, and compacted, micritic peloids (Pel) are parallel aligned to laminae. Framboidal pyrite, rhombic dolomite, and nodular chert replace mostly matrix and organic material. SEM photomicrographs reveal an abundance of matrix surrounding sparse fossil fragments (Fos). Photo C is a relatively low magnification overview showing the typical fabric of the sample. Note the abundance of matrix material exhibiting subparallel laminae (red lines). Higher magnification reveals a matrix mostly comprised of detrital clays (XRD of less than four-micron clay size fraction indicates illite/smectite as the predominant clay present; MXL). Dolomite crystals less than .02 millimeters sporadically replace the matrix. Authigenic calcite fills foraminifer chambers; note the thin wall structure (red arrow) that surrounds a large calcite-replaced skeletal grain (Cal) possibly indicating the presence of planktonic foraminifers.

Sedimentary Structures

The argillaceous wackestone facies are poorly laminated to massive. The laminations where they exist are discontinuous, sometimes displaying low-angle truncation by reactivation and/or erosional surfaces (Figure 3.5).

3.4.1.3 Laminated Argillaceous Foraminiferal Wackestone Facies

Petrography

Found primarily in the Lower Eagle Ford, this facies is dark-to-medium grey. It is an organic-rich, argillaceous wackestone, with a laminated fabric resulting from alternating foraminifera-rich laminae and foraminifera-poor beds (Figure 3.7). The most abundant ($>$20%) allochems are foraminiferas characterized by thin, calcitic tests with chambers cemented by calcite, kaolinite and pyrite (Figure 3.7). This facies also contains 5-10% amounts of skeletal grains, peloids and minor mollusc fragments (Figure 3.7). It has calcite cement, which mostly replaces grains and fills foraminifera chambers (Figure 3.7). Pyrite framboids and dolomite rhombs are dispersed throughout the matrix which also contains $<$1% authigenic kaolinite, dolomite, chert and iron oxides. Organic material is dispersed throughout the matrix as wispy, discontinuous, organic-rich stringers. Mollusc fragments and skeletal grains are similarly aligned and micritic peloids, which are randomly dispersed throughout, are lenticular (Figure 3.7). Both of these are possibly due to compaction.

This facies is primarily composed of calcite ($\sim$63%), quartz ($\sim$17%) and clays ($\sim$15%) with small amounts of plagioclase ($\sim$2%), pyrite ($\sim$5%) and marcasite ($\sim$1%) (Table 3.1). The clays are dominated by illite ($\sim$5%), illite and mica ($\sim$4%), and kaolinite ($\sim$2%).

Sedimentary Structures

At core scale this facies is composed of very thinly planar-to subplanar laminations (Figure 3.8). Laminations are primarily composed of foraminifera, with lesser amounts of inoceramid and other bivalve fragments. At microphotograph and thin

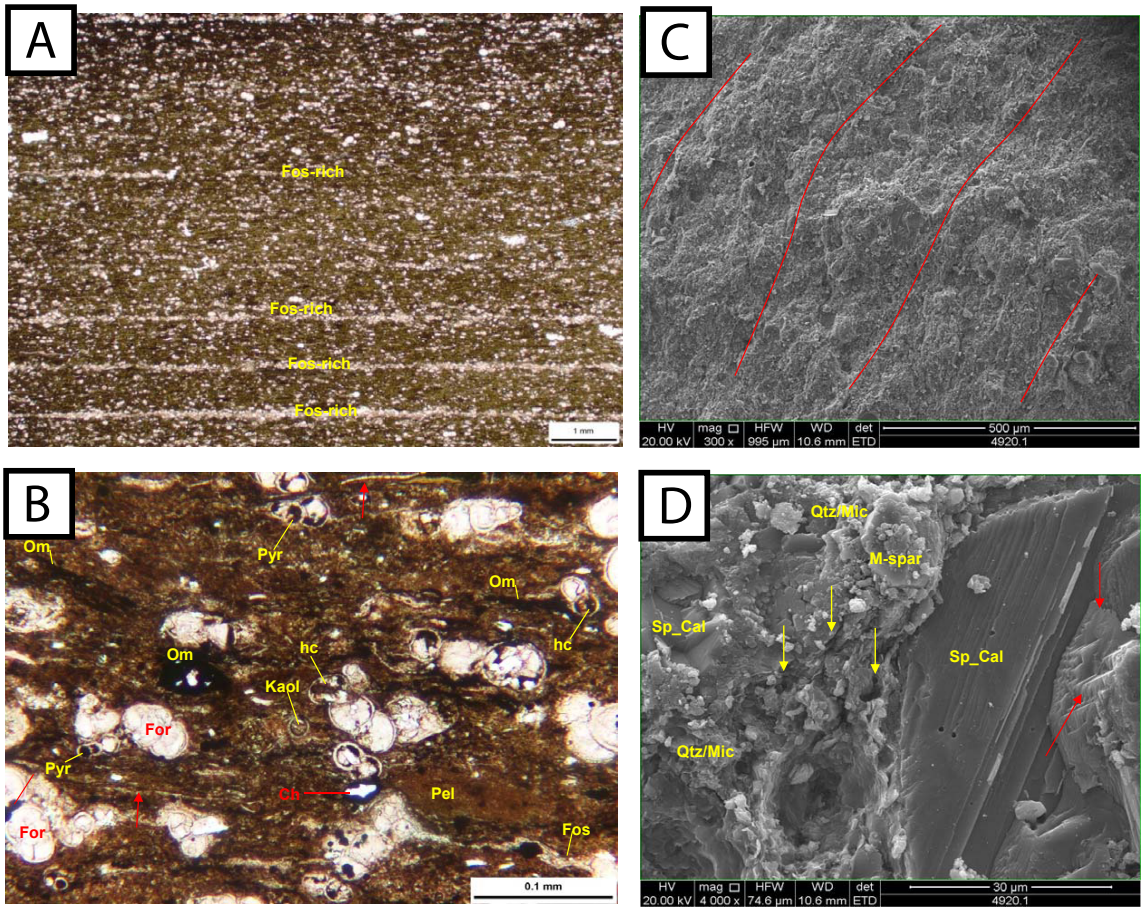

Figure 3.7: Photomicrographs of laminated argillaceous foraminiferal wackestones, 1499.64 m in Chittim-2H. An organic-rich, argillaceous wackestone with a laminated fabric that resulted from alternating foram-rich laminae (Fos-rich) and foram-poor beds (Photo A). Organic material is dispersed throughout the matrix as wispy, discontinuous, organic-rich stringers (Om) that appear to thicken near allochem, outer skeletal borders. The most abundant allochems are planktonic foraminifers (For), characterized by thin, calcitic, tests with chambers cemented by calcite (Cal), kaolinite (Kaol), and pyrite (Pyr); note that chambers are stained dark brown due to hydrocarbons (hc). Mollusk fragments and unidentified skeletal grains are similarly aligned probably due to compaction (red arrows). Micritic peloids (Pel) are randomly dispersed and are lenticular due to compaction. Pyrite framboids and dolomite rhombs are dispersed throughout the matrix. laminated texture (Photo C; red lines) comprised of an abundant amount of matrix material. Higher magnification imagery in Photo D reveals a micritic matrix intermixed with a common amount of silt and clay-sized quartz (Qtz/Mic). Microspar (M-spar) and sparry calcite (Sp_Cal) are likely grain-replacing and are not part of the matrix. Thinly foliated, calcareous sheets (red arrows) surrounding sparry calcite-filled, spherical grains indicate the presence of planktonic foraminifers.

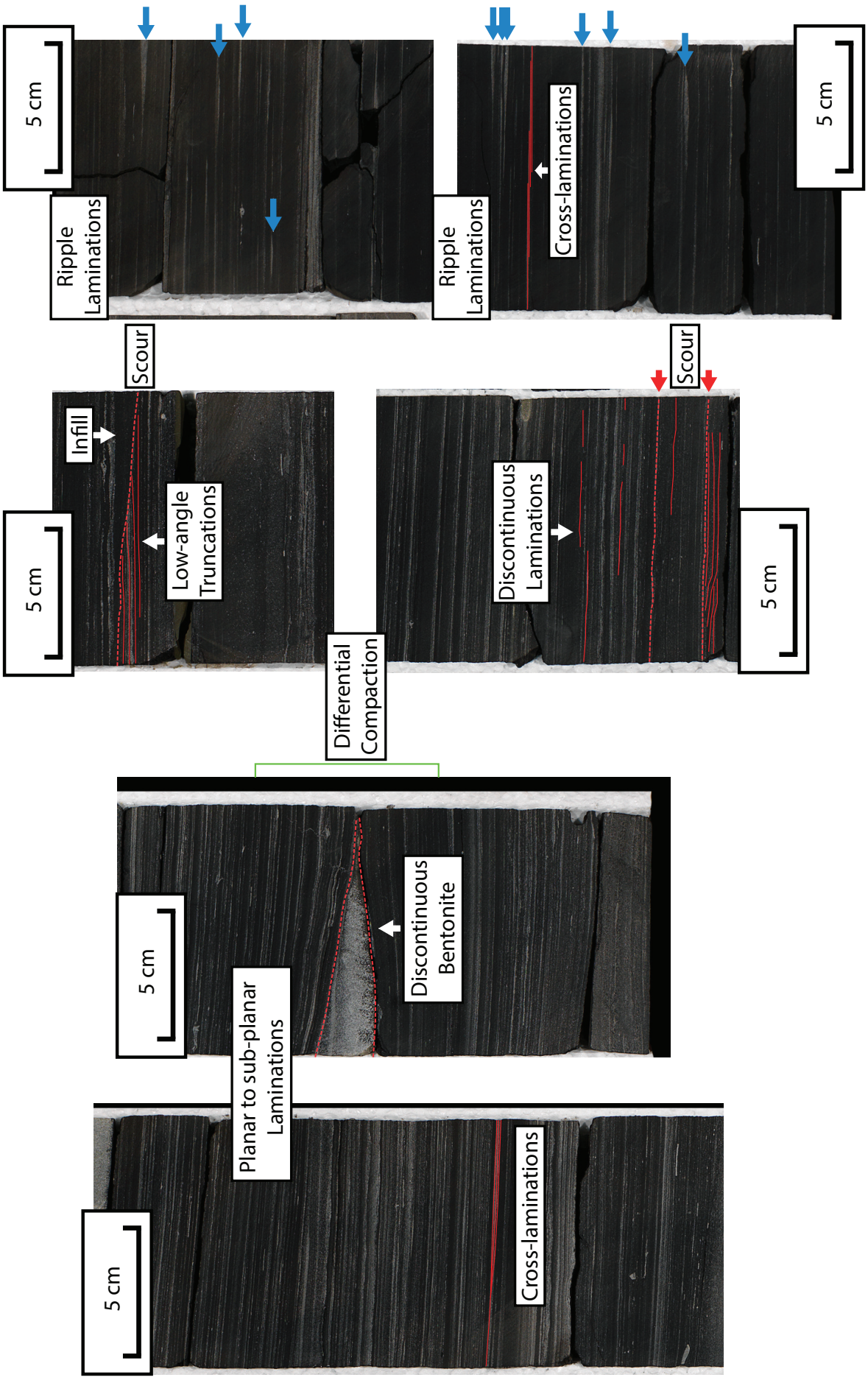

Figure 3.8: Core photographs of the characteristic features of laminated argillaceous foraminiferal wackestones. Structures commonly found in this facies include cross lamination, planar to sub-planar laminations, low angle truncations, scours with infill, discontinuous laminations. Unidirectional flow ripples are a common feature in this facies (blue arrows). This figure also displays a discontinuous bentonite, with no sign of reworking, which has caused differential compaction around it.

section scale the laminated argillaceous foraminiferal wackestone facies display low-angle laminations which in a number of sections are discontinuous and in some cases end in truncations and/or erosional surfaces (Figure 3.7). Scouring, filing and contorted strata are also observed (Figure 3.7 and 3.8). Bioturbation is uncommon, large bioclasts are common with highest concentrations at the base of the wackestone facies and decreasing upwards to the top of this facies (e.g. 1491.8 m–1491.01 m; Table 3.2). At core scale scoured surfaces and small-scale low-angle cross stratification, ripple lamination and current ripples are observed (Figure 3.8).

3.4.1.4 Laminated Foraminiferal Packstone Facies

Petrography

Light-to-medium grey in colour the laminated foraminiferal packstone facies is a partly recrystallized, laminated, foraminiferal rich packstone (Figure 3.9). The remnant, original laminations are slightly obscured in some places as many of the fossils

Table 3.2: Summary of foraminiferal and bioclast counts from 1 cm^2 polished blocks of the Chittim-2H core.

Chittim-2H		Foram Counts	Bioclast Counts
Base (m)	Top (m)		
1490.7	1490.71	32.5	33.2
1490.8	1490.81	15.3	36.3
1490.9	1490.91	23.4	45.7
1491	1491.01	4.6	4.5
1491.1	1491.11	3.7	3.3
1491.2	1491.21	5.2	2.8
1491.3	1491.31	8.5	6.6
1491.4	1491.41	11.5	6.1
1491.5	1491.51	6.1	4.7
1491.6	1491.61	14.1	9.6
1491.7	1491.71	18.4	12.2
1491.8	1491.81	25.3	46.2
1491.9	1491.91	8.2	26.8

have been recrystallized and so fewer foraminiferas still preserve the original internal structure (Figure 3.9). A number of recrystallized fossils are characterized by spherical shapes aligned with thin, calcitic, external wall structures, which suggests that planktonic forams were probably an important fossil component (Figure 3.9). Calcite crystals (mostly sparry calcite) are present intermixed with a matrix of detrital clay suggesting recrystallization of the calcareous matrix (Figure 3.9). Organic material is minor. Pyrite is present as nodules (often associated with organic matter) and is displacing the matrix and replacing skeletal fragments (Figure 3.9). In the Upper Eagle Ford this facies displays higher concentrations of benthonic foraminifers and mollusc fragments, in particular large inoceramid fragments.

XRD analyses indicates that this facies is characterized by high calcite (Lower Eagle Ford average 76%, Upper Eagle Ford average 69%), quartz (Lower Eagle Ford average 8%, Upper Eagle Ford average 18%) and clays (Lower Eagle Ford average 12%, Upper Eagle Ford average 14%) with small amounts of plagioclase (Lower Eagle Ford average 0.5%, Upper Eagle Ford average) and pyrite (Lower Eagle Ford average 2%, Upper Eagle Ford average 2%; Table 3.1). Though generally

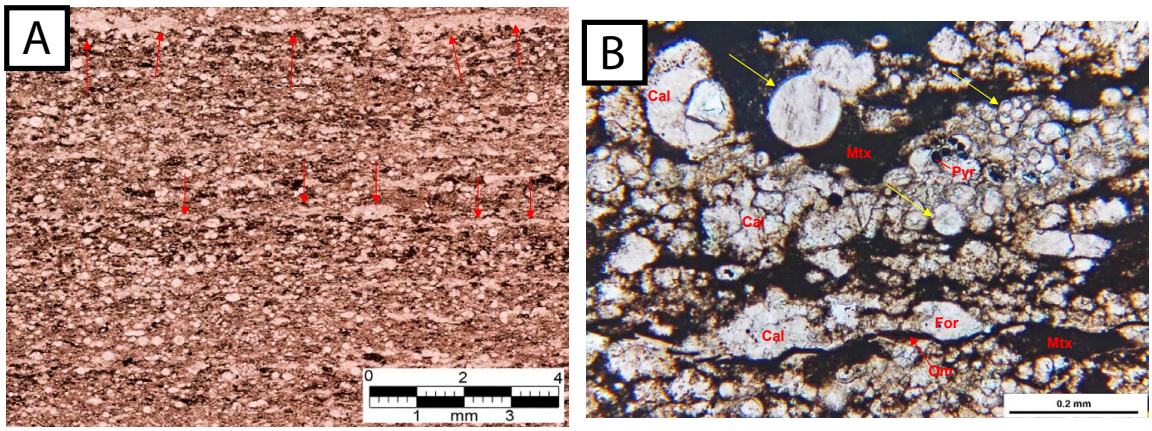

Figure 3.9: Photomicrographs of laminated foraminiferal packstones, 99.75 m from Iona-1. This sample is a limestone that resulted from the recrystallization of a laminated, mostly foraminiferal-rich limestone; note remnants of the original lamination illustrated in Photo A (red arrows). Most of the fossils are recrystallized, and only a few foraminifers (For) still preserve the original internal structure. A number of recrystallized fossils are characterized by spherical shapes aligned with thin, calcitic, external wall structures which suggests that planktonic forams were probably an important fossil component (yellow arrows). Calcite crystals (mostly sparry calcite; Cal) are present intermixed with a matrix of detrital clay (Mtx) suggesting recrystallization of the calcareous matrix. Organic material (Om) is minor. Pyrite is present as nodules (often associated with organic matter) and is displacing the matrix and replacing skeletal fragments (Pyr).

a foraminiferal packstones in places these rocks grade into wackestones, this is particularly prevalent in the Upper Eagle Ford such as at 32.6 m in Innes-1 and 95.55 m in Iona-1.

Sedimentary Structures

At core scale the laminated foraminiferal packstone facies contains planar-to subplanar laminations composed of abundant foraminifera and fossil fragments (Figure 3.10). It contains a high number of current-induced structures (very thin planar and subplanar laminations, fine ripple laminations, scours) and slump folds. Instances of this facies with cross-laminated structures tend to have marginally higher calcite percentages averaging 86% and tend to contain high numbers of foraminifera tests,

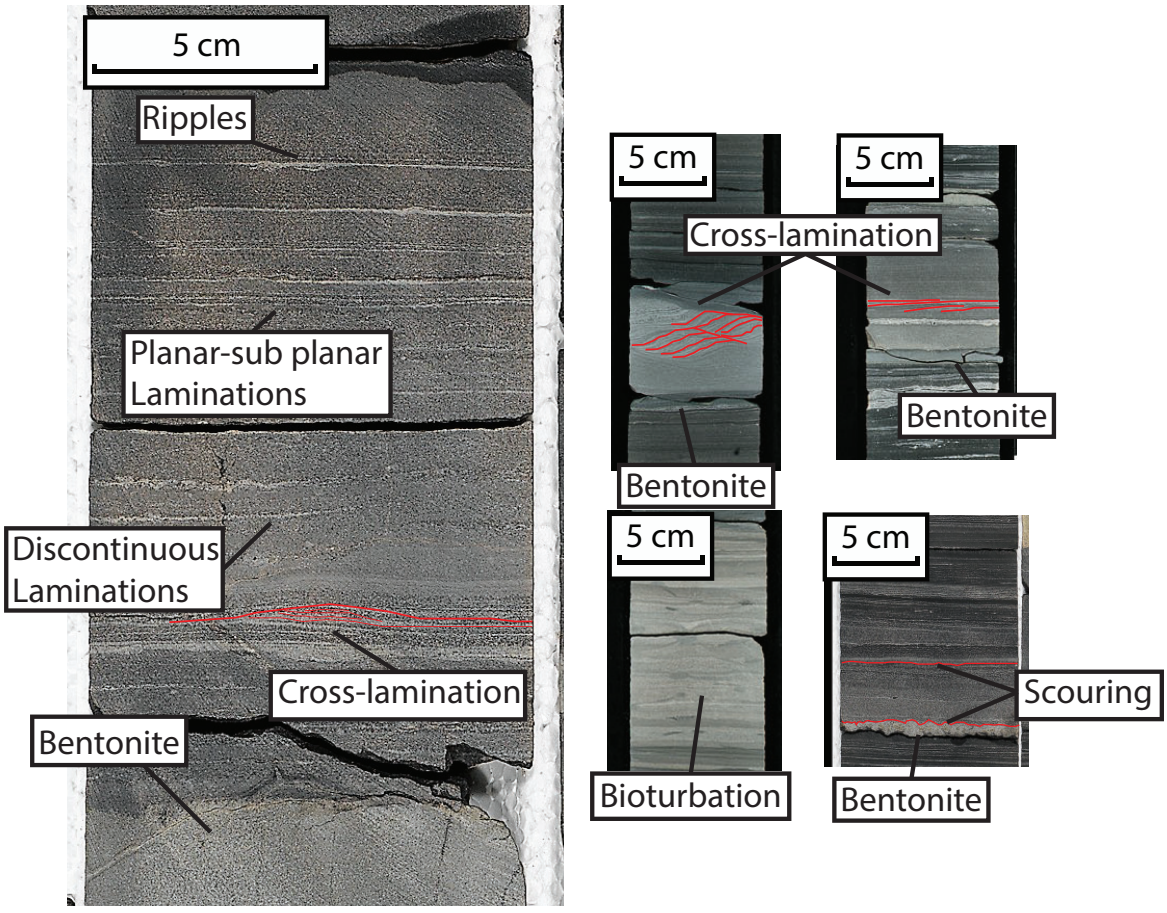

Figure 3.10: Core photographs of the characteristic features of laminated foraminiferal packstones. Structures commonly found in this facies include ripples, cross-laminations, planar to sub-planar laminations, discontinuous laminations and scours. Bioturbation, as shown, is common in the Upper Eagle Ford. The majority of laminated foraminiferal packstones have a bentonitic claystone at their base.

as well as highly abraded bivalve fragments and other unidentifiable skeletal fragments. Highly abraded inoceramid fragments occur, but are rare, in the Lower Eagle Ford; they are more common in the Upper Eagle Ford. This facies contains copious amounts of bioturbation in the Upper Eagle Ford, which distorts, destroys and obscures the remnant laminations (Figure 3.10).

3.4.1.5 Massive Foraminiferal Packstone Facies

Petrography

Light-to-medium grey in core, thin section analyses of this facies indicate it is a packstone that has been intensely recrystallized. The fabric of the facies is predominantly massive with dark, lenticular, discontinuous matrix-rich layers that may possibly indicate an extremely weak laminated texture (Figure 3.11). Thin sections often show a mosaic of anhedral, sparry calcite crystals surrounded by thin veins of organic-stained, detrital clay matrix (Figure 3.11). Relic calcispheres or foraminifera, thin-shelled mollusk fragments, and Inoceramus shells are preserved throughout the samples (Figure 3.11). Preserved foraminifers are characterized by thin, calcitic walls filled with calcite cement (Figure 3.11). Patches and veins of dark matrix are composed of detrital clays with lesser amounts of organic matter. Pyrite and marcasite are mostly grain replacing in origin (Figure 3.11).

This facies is composed primarily of calcite ($\sim$86%), quartz ($\sim$5%) and clays ($\sim$5%), with minor amounts of pyrite ($\sim$1%) and plagioclase ($\sim$0.5%) (Table 1). The clays are composed of mixed layer illite and smectite ($\sim$3%), kaolinite ($\sim$2.5%), and illite and mica ($\sim$1%).

Sedimentary Structures

In core it appears that a number of instances of this facies comprises horizontal lenses that exhibit oblate ellipsoidal cross sections and may have caused differential compaction in adjacent mudstones (Figure 3.12). This facies differs from the laminated foraminiferal facies largely in that it is laterally discontinuous at core scale

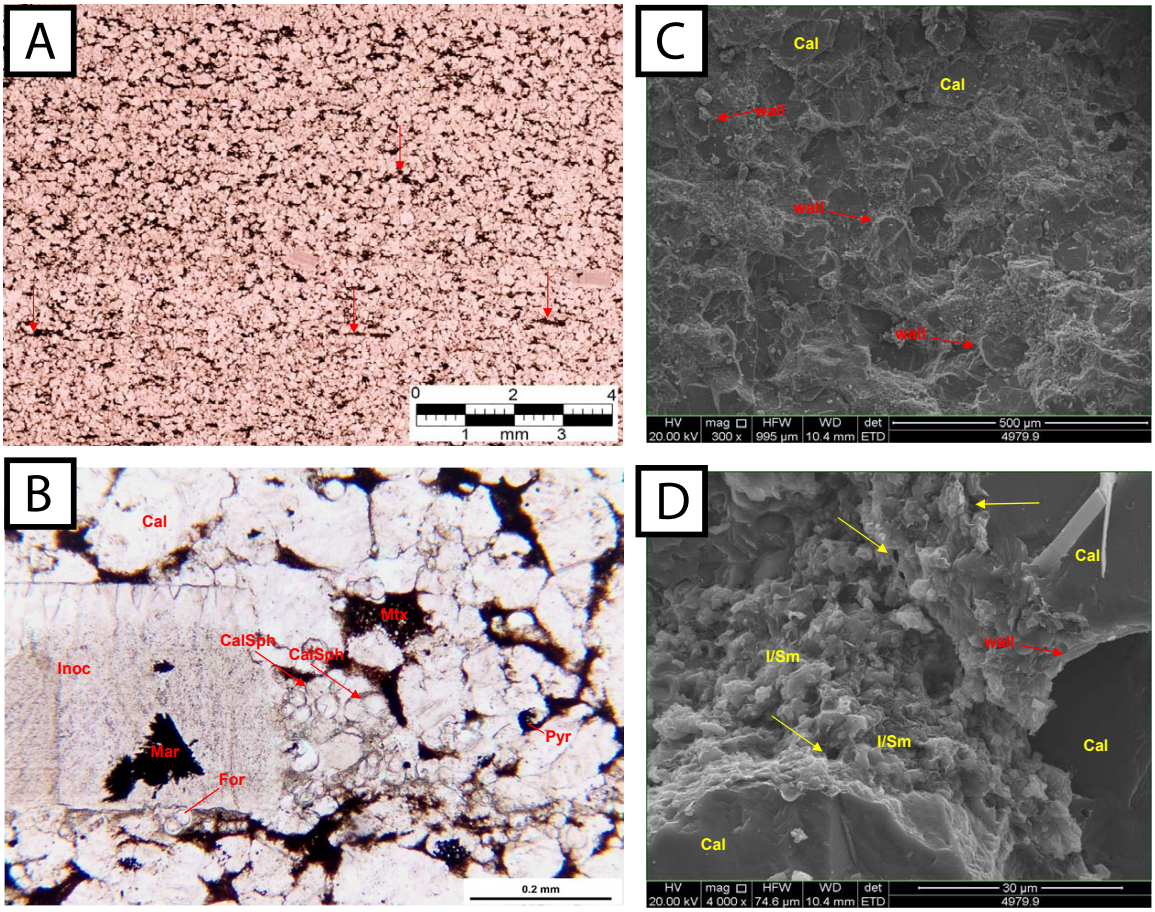

Figure 3.11: Photomicrographs of massive foraminiferal packstones. This sample is a limestone that has been intensely recrystallized (packstone). Although the fabric of the rock is predominantly massive, dark, lenticular, discontinuous matrixrich layers may indicate a very weakly laminated texture (Photo A). This sample consists of a mosaic of anhedral, sparry calcite (Cal) crystals surrounded by thin veins of organic-stained, detrital clay matrix. According to the XRD data, the calcite content of this limestone is 86.9% by weight. Relic calcispheres (yellow arrows) or foraminifer tests (For), thin-shelled mollusk fragments, and Inoceramus shells (Inoc) are preserved throughout the sample. Preserved foraminifers are characterized by thin, calcitic walls filled with calcite cement. Patches and veins of dark matrix (Mtx) are composed of detrital clays with lesser amounts of organic matter. Pyrite (Pyr) and marcasite (Mar) are mostly grain replacing in origin. Calcite-replaced bioclastic material and calcite-filled foraminifers (Cal) are the most abundant constituent in this sample. Thinly layered, calcitic wall structures surrounding spherical chambers are characteristic of planktonic foraminifers which is evident in Photo C (yellow arrows). SEM imagery shows mixed layer illite/smectite occluding the interparticle pore space (I/Sm) between spherical, sparry calcite-replaced grains (Cal).

(Figure 3.12). In core, it is difficult to differentiate between this facies and laminated foraminiferal packstone facies. It was previously proposed that similar nodular foraminiferal Cretaceous packstones in West Texas were deposited by bottom currents, as sediment waves and dunes, and that they represent reworked accumulations of planktonic debris (Frébourg et al., 2016).

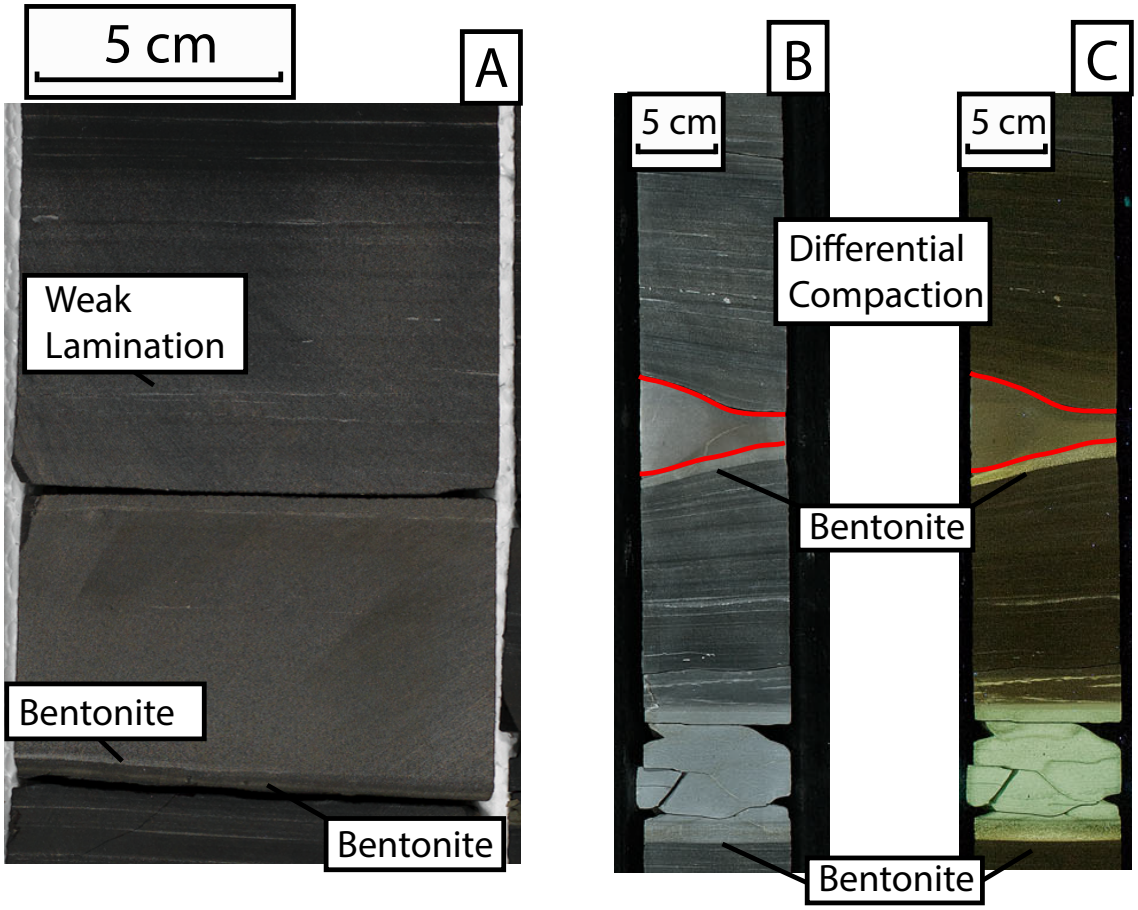

Figure 3.12: Core photographs of the characteristic features of massive foraminiferal packstones. Structures commonly found in this facies include weak laminations to a massive texture. Discontinuity of the facies and differential compaction in the sediment above and below are common. A and B are core photographs that have been taken under normal light and C has been taken under UV light.

3.4.1.6 Bentonitic Claystone Facies

Petrography

The XRD analysis reveals that clay minerals, dominated by illite/smectite (∼52%), illite and mica (∼36%), and kaolinite (12%) are their dominant constituents, averaging 75% of the total weight. The remainder of this facies is composed of quartz

(∼10%), plagioclase (∼5%) and calcite (∼10%) (Table 3.1).

Sedimentary Structures

In cores, thin (1-25 cm) bentonitic claystone beds display a range of different attributes (Figure 3.13). They are coarse to fine, poor to well lithified, can be structureless or partly laminated, and often show scouring and flow structures including ripples and cross-laminations (Figure 3.13).

3.4.1.7 Buda Limestone Facies

The Buda Limestone is dominated by two lithologies: (1) calcispheral wackestones (Figure 3.14); and, (2) skeletal packstones (Figure 3.15). The skeletal packstones have an abundant calcite cement and contain neomorphosed, spar and microspar calcite fabrics, they're mostly massive with a few parallel, fossil-rich laminae (Figure 3.14). They have abundant calcite-replaced fossil fragments and less than 10% calcispheres, foraminiferas, mollusks and peloids (Figure 3.14). The calcispheral wackestones contain many organic-rich microstylolites as well as burrows and zoned laminae due to the apparent parallel alignment of elongated skeletal grains (Figure 3.15). They contain abundant calcispheres and mollusc fragments as well as minor foraminifera and skeletal debris (Figure 3.15).

3.4.2 High Resolution Chemostratigraphic Analysis

Energy-dispersive XRF analysis provided elemental composition data that were used to evaluate the inorganic geochemistry of the Eagle Ford. Molybdenum (Mo) and uranium (U) have both been widely used to infer paleo-redox conditions in modern and ancient sediments and depositional environments, as they are redox sensitive and relatively immobile in the sediment, thus preserving primary signals (e.g. Brumsack, 2006; Tribovillard et al. 2006; Algeo et al. 2012; Figure 3.16).

Molybdenum-concentration measurements have widely been used as a proxy for benthonic redox potential because of its generally strong enrichment in organic-

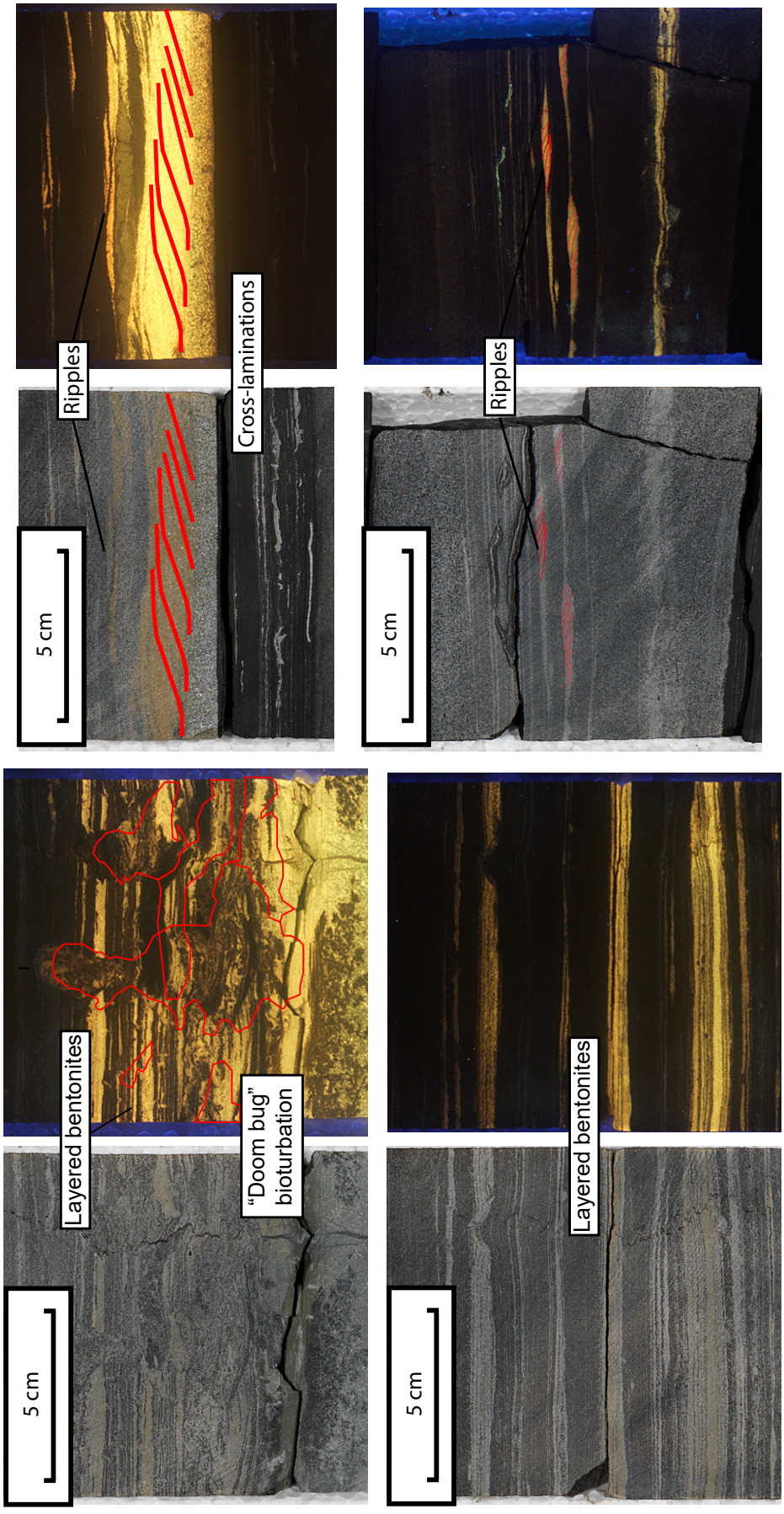

Figure 3.13: Core photographs of the characteristic features of bentonitic claystones. Structures commonly found in this facies include cross-laminations and ripples. In some instances this facies is layered. In one section during the carbon isotope excursion of the Mid-Cenomanian Event this facies is heavily bioturbated.

rich facies deposited under oxygen-depleted, sulphide-rich conditions (e.g. Algeo and Lyons, 2006; Tribovillard et al., 2006). Comparatively, U is used as a proxy for benthonic redox potential because of its enrichment in organic-rich facies under oxygen depleted, but sulphide-poor conditions (e.g. Algeo and Lyons, 2006; Tribovillard et al., 2006). Mo and U concentrations are often converted to enrichment factors, a technique commonly used to account for those trace metals added to a system by terrigenous input (e.g Tribovillard et al., 2006: (EF): $EF_{element}$ $X=X/Al_{sample}/X/Al_{average\ shale}$.). Similarly, aluminium (Al) and titanium (TiO_2) are commonly utilised as a proxy for terrigenous detrital material due to their relative chemical inertness and detrital origin (e.g. Brumsack, 2006; Tribovillard et al. 2006; Algeo et al. 2012).

Molybdenum enrichment factors (Mo_{EF}) within the argillaceous wackestones and laminated argillaceous formaniferal wackestones range from around 150 to 1200 and tend to be significantly higher than those in the laminated foraminiferal packstone facies, which range from around 25 to 350, and the massive foraminiferal packstone, which range from 25 to 150 (Figure 3.16). In high-resolution sections within the Chittim-2H core, Mo_{EF} increases from the stratigraphic base to the top of the wackestone (Figure 3.16). Going in to a packstone Mo_{EF} drops significantly (Figure 3.16). U enrichment factors (U_{EF}) show little difference between facies in the high-resolution sections. In comparison to Mo_{EF} profiles, in most high-resolution profiles U_{EF} decrease from the stratigraphic base to the top of the wackestones (Figure 3.16. Mo_{EF} and U_{EF} whole core chemostratigraphy are discussed in Chapter 5.

3.4.3 High Resolution Total Organic Carbon and Rock Eval Analysis

The Eagle Ford is an organic-rich succession and has long been considered a proven source rock in Texas (Robison, 1997). High-resolution TOC measurements (1-3 cm) from the metre-scale couplets of Chittim-2H show that the packstone facies typically have low TOC concentrations of between 1-3%, whereas the wackestone facies have a wide range of TOC concentrations of between 2.5-13% (Figure 3.3 and 3.16). The results from the couplet analysis (Figure 3.16) show that TOC

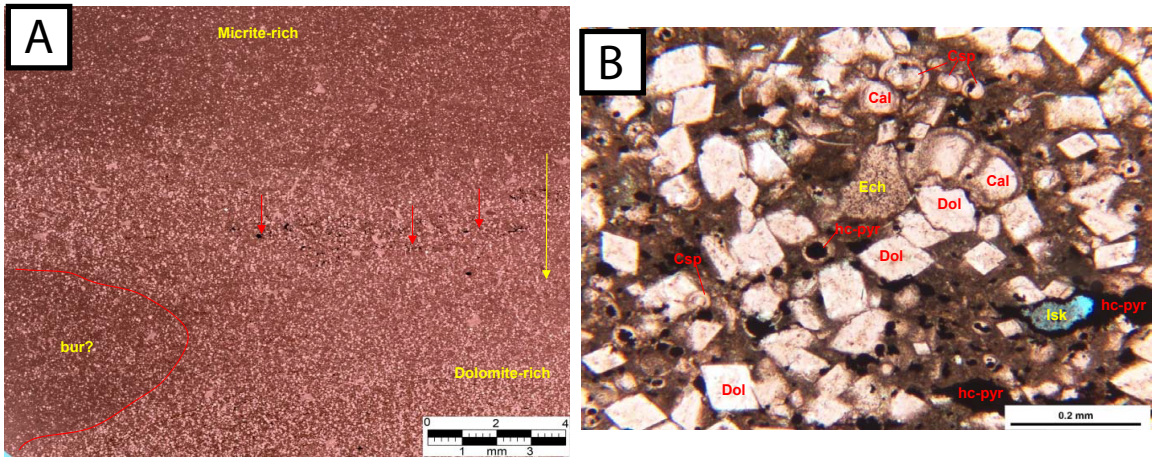

Figure 3.14: Photomicrographs of a calcispheral wackestone from the Buda Formation. This limestone exhibits a gradational increase of matrix replacing dolomitic rhombs (yellow arrow in Photo A). Possible burrows occur within the dolomite-rich portion of the sample. Calcispheres (Csp) and unidentified skeletal grains show calcite cementation especially within their internal chambers (Cal). A few echinoderms (Ech) and foraminifers are also noted. Micrite matrix is abundant in over half of the sample in areas where dolomite replacement is less common. A later stage of diagenesis produced abundant amounts of medium crystalline, euhedral dolomite rhombs (Dol). Pyritized organic matter appears enclosed within several skeletal grains and is also present throughout the matrix (hcpyr). Heavier accumulations of these concretions occur in dolomite-rich sections of the sample.

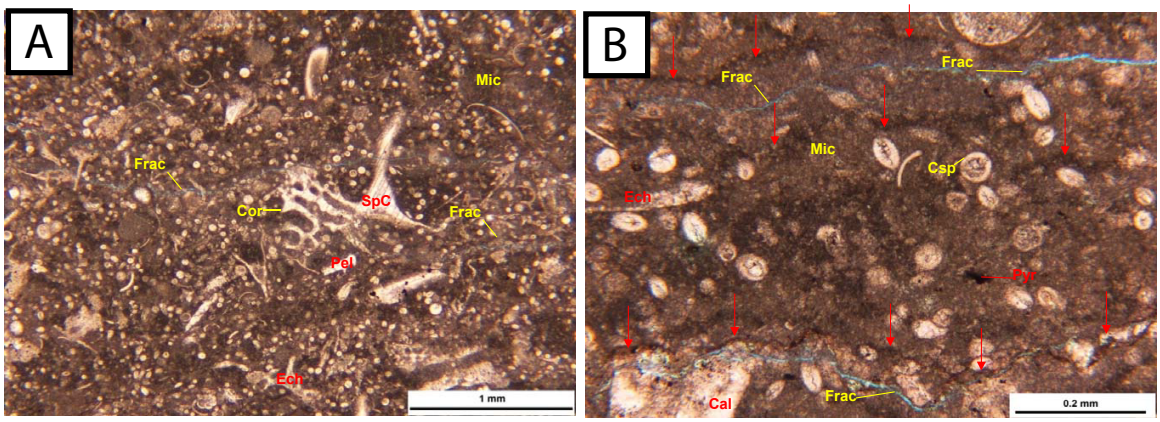

Figure 3.15: Photomicrographs of a skeletal packstone of the Buda Formation. Two continuous sets of organic-rich microstylolitic seams (red arrows) radiate subparallel to opened, hairline fractures (Frac). Allochems include calcispheres (Csp), echinoderms (Ech), pelecypods (Pel), planktonic foraminifers, gastropods, and corals (Cor). Some of these skeletal grains appear to have been recrystallized and some have been filled with sparry calcite (SpC). Micrite (Mic) matrix is abundant. Dolomite replacement of matrix is evident, although the replacement patterns appear random. Framboidal pyrite is sporadic and typically occurs within skeletal chambers, although some appear within the matrix (Pyr).

concentrations increase systematically by up to 6.5% from ∼2-3% at the packstone-wackestone boundary at the base of couplet to ∼8-9% at the wackestone-packstone boundary at the top of the couplet.

High-resolution hydrogen index (HI) measurements (1-5 cm) in Chittim-2H show HI values increasing upwards, from 240 to 360 mg of HC/g of TOC, from the stratigraphic base to the top of each wackestone prior to the Mid-Cenomanian Event (MCE) and after. However, this trend becomes reversed during the MCE and values decrease from the stratigraphic base of the wackestone, in the range of 320 to 220 mg of HC/g of TOC.

3.5 Discussion

Lithological variations in the Eagle Ford are controlled by interacting sedimentary and depositional mechanisms and processes. These changes are linked to environmental changes affecting both the sediment type and volume supplied to the system as well as processes controlling the formation of sediment bodies of varying geometries i.e. reworking of pelagic carbonate sands by bottom currents into distinct sand bodies.

The scope of this discussion looks at understanding both the sedimentology of the Eagle Ford and the controls on the temporal and spatial sedimentological changes using cm-scale geochemical, mineralogical and sedimentological changes in the metre-scale packstone-wackestone couplets as well as whole core-scale stratigraphy, sedimentology and mineralogy.

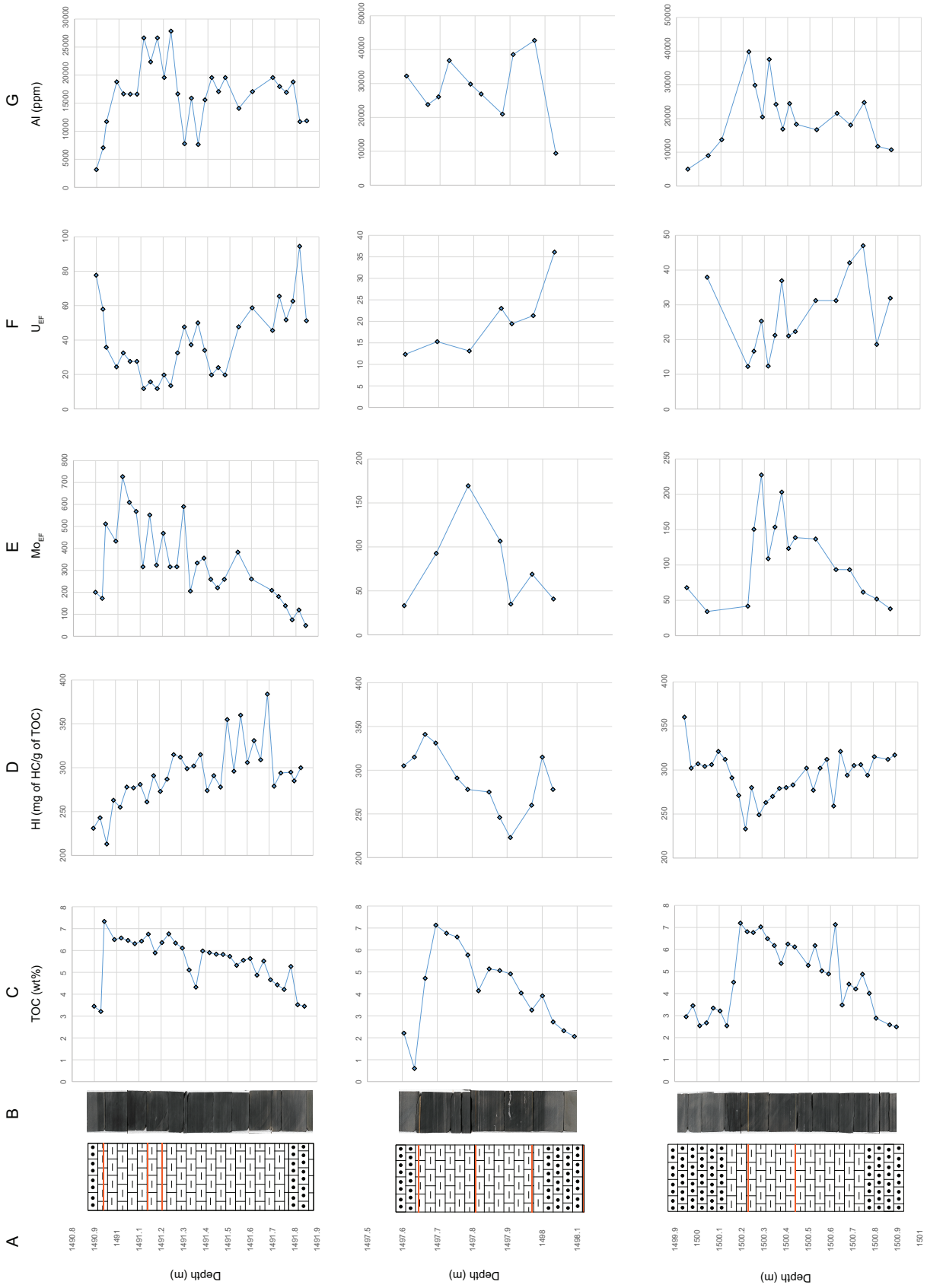

Figure 3.16: High resolution chemostratigraphic data from foraminiferal packstone-wackestone couplets in the Chittim-2H core. For the top 3 rows: A. Depth (m) with lithological column displaying wackestone (boxes with dashes), packstone (boxes with black circles) and bentonitic claystones (orange boxes); B. Core Images; C. TOC (wt%; this study); D. HI (mg of HC/g of TOC; this study); E. Mo_{EF} (this study); F. U_{EF} (this study); G. Al (ppm; this study).

3.5.1 Interpretation

3.5.1.1 Laminated Argillaceous Foraminiferal Wackestone and Argillaceous Wackestone Facies

Both argillaceous wackestone facies and laminated argillaceous foraminiferal wackestone facies are fine-grained rocks with >20% mud-sized particles. These mud sized particles likely formed carbonate mud floccules with settling speeds of several centimetres per second (up to 50 cm/sec; Schieber et al., 2007). This is indicated by sedimentary features of the Upper and Lower Eagle Ford such as low-angle lamination, low-angle foresets, discontinuous laminae, ripples, cross stratification, scouring and erosional surfaces because these features are created by the formation, accretion, and/or migration of floccule ripples by currents (Schieber et al., 2007, 2013). Furthermore, Schieber et al. (2013) defined low-angle, discontinuous downlapping laminae, such as those observed in the laminated argillaceous foraminiferal wackestones, as a key criterion for discriminating carbonate mud deposited by current action from simple sediment settling and as such preclude the settling of this facies in quiescent waters.

The foraminifer rich beds which form laminations in the laminated argillaceous foraminiferal wackestone facies in the Lower Eagle Ford of Innes-1, Iona-1 and Chittim-2H may have formed due to high levels of primary productivity in surface waters, as increased numbers of primary producers can lead to blooms in higher trophic levels due increase food availability, or due to periods of particularly high-energy conditions which prevent the deposition of floccules. However, the alternation of silt- and sand-sized laminae in laminated sediment has been suggested to be indicative of continuous deposition under constant current regimes instead of fluctuation of flow conditions and/or sediment supply (Schieber et al., 2013).

Planar bedding and subhorizontal lamination form in sand-sized and finer sediment under upper flow regime when currents are too fast to form current ripples (Allen, 1984). This indicates that the key differences between the argillaceous wackestone

and the laminated argillaceous foraminiferal wackestone are: firstly, a difference in current regime; and secondly, a lower level of primary productivity in the argillaceous wackestone facies. In the Lower Eagle Ford laminated argillaceous foraminiferal wackestones often grade into or are preceded by argillaceous wackestones (Figure 3.3). This indicates a gradual decrease in energy regime or highly variable sediment supply as a result of decreasing planktonic foraminifer (Schieber et al., 2007, 2013).

Studies have shown that photosynthetic production of organic matter is critically dependent on supply of nutrients from the subsurface ocean to the euphotic zone (Falkowski et al., 1988; Gruber et al., 2002). High levels of primary productivity create high oxygen demands, which can lead to anoxic benthic zones and the preservation of organic matter (e.g. Schlanger and Jenkyns, 1976; Christensen, 2000). The occurrence of intense bioturbation in the Upper Eagle Ford and a reduction in total organic carbon suggests an oxygenated benthic zone around this time, or at least intermittently.

The dominant occurrence of argillaceous wackestones in the Upper Eagle Ford signifies lower levels of euphotic zone primary productivity due to the lower numbers of foraminifers in this facies (Table 3.1). As such it is likely that the prevalence of the argillaceous wackestone in the Upper Eagle Ford indicates both a reduction in primary productivity and energy of flow regime throughout this section of core.

3.5.1.2 Laminated Foraminiferal Packstone Facies and Massive Foraminiferal Packstone Facies

The laminated foraminiferal packstone bodies in the Upper and Lower Eagle Ford show abundant sedimentary features associated with subaqueous transport and formation in coarser-grained, sand-sized sediment. The massive foraminiferal packstone facies have undergone intense recrystallization resulting in a near massive fabric. However, a weakly laminated texture can still be discerned. This suggests that features, which once existed in these bodies may have been obscured. The higher concentrations of calcite and lower clay contents may indicate that when ini-

tially deposited the massive foraminiferal packstone facies had a greater porosity and permeability compared to the laminated facies. As a result diagenesis may have preferentially affected the clay-depleted facies culminating in them becoming significantly more recrystallized and cemented.

The sedimentary features found in the laminated foraminiferal packstone bodies at core scale in the Lower and Upper Eagle Ford of all three cores include low-angle cross stratification (Figure 3.10), sigmoidal foresets (Figure 3.10), low-angle tangential bottom foresets (Figure 3.10), and current ripples up to several cm long (Figure 3.10). The sedimentary structures found in the packstone bodies indicate they were all deposited by unidirectional currents rather than oscillatory current features. Outcrop studies of the Ernst Member of the Eagle Ford in Brewster County, time equivalent to the Eagle Ford Groups section B in Val Verde County (Donovan and Staerker, 2010), encountered similar bodies, there described as pelagic grainstones (Frébourg et al., 2016). In this location the foresets of these packages all dip in the same direction also indicating deposition under unidirectional currents. In outcrop these bodies formed barchanoid morphologies, hydraulic dunes that only form in unidirectional currents (Endo et al., 2005), reinforcing the evidence of deposition under unidirectional currents.

Depending on the volume, unidirectional bottom currents can rework pelagic sand-sized sediments into deposits that vary in morphology (Flemming, 1980). Close to the source, where the coarse-grained pelagic sediment input is maximal, the bottom currents rework the sediment into a sand sheet (Rodriguez and Anderson, 2004). Further away, the sediment accumulates in the form of ridges (Flemming, 1980) and finally separates into isolated hydraulic dunes (Flemming, 1980; Shanmugam et al., 1993; Endo et al., 2005).

The relative abundance of the planktonic foraminifera is dependent on nutrient availability and the availability of primary producers. As areas of high primary productivity are spatially variable so are the areas of maximum foraminifer production. Previously such mechanisms have been suggested for the Carnegie Ridge, in the eastern equatorial Pacific, where planktonic foraminiferal sands form belts of isolated

barchan and transverse dunes due to unidirectional, >30 cm/sec currents which allow for bed-load transport away from regions of high-productivity (Lonsdale and Malfait, 1974).

The significantly higher concentrations of clays in the laminated foraminiferal packstone facies compared to the massive foraminiferal packstones was likely to have had an effect on the cohesion of the resultant packstone beds. Experiments have shown that the addition of silts and clays in beds composed predominantly of sand-sized particles have a cohesive effect against hydrodynamic forces associated with critical shear stress (Mitchener and Torfs, 1996; Van Ledden et al., 2004).

The most significant effects on erosion resistance occurs with the addition of small amounts of muds, between 3 % and 15 % by weight (Mitchener and Torfs, 1996). This addition causes the dominant mode of erosion to change from cohesion-less to cohesive behaviour (Van Ledden et al., 2004). The higher concentrations of clays in the laminated foraminiferal packstone facies may have prevented them from separating and forming barchan dunes due to the higher critical stress required.

Episodic sediment transport and deposition by mass-wasting processes cannot be ruled out for some of the beds. It is possible that mass-wasting processes supplied coarser sediment to the study area but that evidence of these deposits was later partially or totally lost because of reworking by bottom currents. However, the plane-bedded packstone beds have sedimentary features that are more consistent with bottom current deposition, rather than mass wasting.

Previous studies of the Eagle Ford have suggested its deposition was under the influence of bottom currents (Lock and Peschier, 2006; Frébourg et al., 2016), and others have interpreted it as being shallow-water, above-storm wave base, under periodic agitation by storms (Donovan et al., 2012). Storms would be expected to have oxygenated the bottom waters periodically, allowing the settlement of benthic communities (Luther et al., 2004). However, the packstones are strongly dominated by planktonic foraminifera and with the exception of some inoceramid prisms the packstones consist almost exclusively of material derived from planktonic organ-

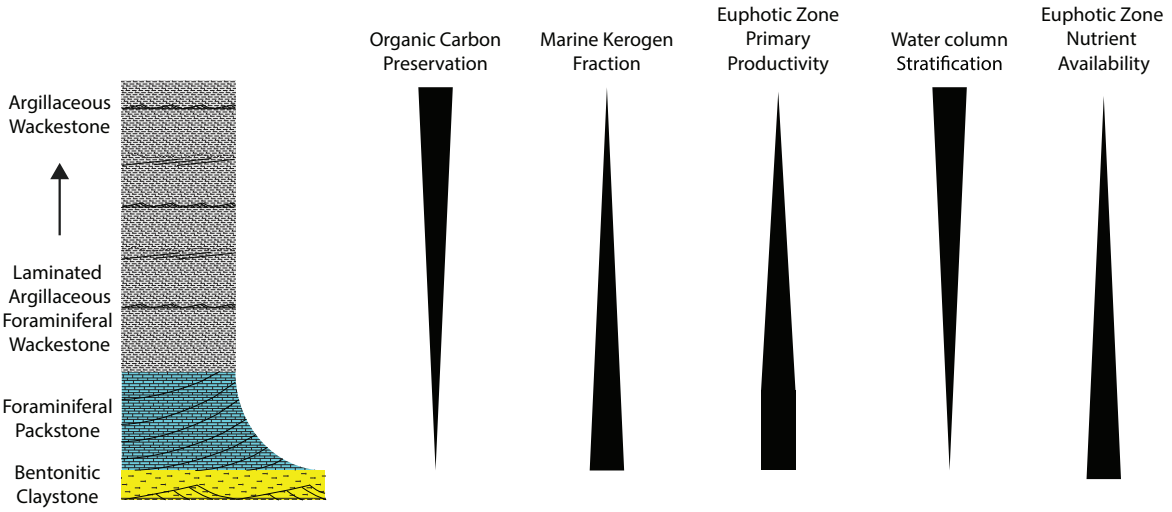

Figure 3.17: Idealised depositional model of the couplet cycle. The left hand side of the figure shows the idealised sedimentological column, a bentonitic claystone is followed by a foraminiferal packstone. This in turn is followed by a laminated argillaceous foraminiferal wackestone which grades into an argillaceous wackestone. Increases in atmosphericocean thermal gradients as a result of periods of solar insolation maxima lead to greater, more frequent storms and stronger bottom currents resulting in de-stratification of the water column. The deposition of the bentonitic claystone dramatically increases the euphotic zone nutrient availability stimulating increased primary productivity. With time euphotic zone primary productivity decreases in line with increasing water column stratification which occurs as a result of reduced latitudinal energy gradients and increasing solar insolation minima. This leads to a decrease in the marine kerogen fraction but an increase in organic carbon preservation. In the Upper Eagle Ford higher levels of water column mixing and benthic oxygenation likely leads to less water column stratification, slower decrease in nutrient availability and lower preservation of organic matter.

isms. This suggests that the depositional environment of the packstones is in the pelagic, open-marine realm. Hence, the packstone beds in the Lower Eagle Ford are interpreted to be pelagic carbonate sediment deposited and reworked by bottom currents below storm wave base in a dysaerobic-to-anoxic environment. With the low TOC values likely a result of dilution due increased carbonate sedimentation.

3.5.1.3 Bentonitic Claystones

The bentonitic claystone bodies display abundant sedimentary features associated with subaqueous transport and deposition. The sedimentary features observed in the bentonitic claystones such as low-angle lamination, low-angle foresets, discontinuous laminae, current ripples, cross stratification, scouring and erosional surfaces (Figure 3.13), similarly to the wackestone facies, preclude the settling of many of these facies in quiescent waters. The low-angle cross stratification (Figure 3.13),

sigmoidal foresets (Figure 3.13), low-angle tangential bottom foresets and current ripples (Figure 3.13) indicate a unidirectional current. No oscillatory features are found.

As with the foraminiferal packstones differential compaction is sometimes seen in the bentonitic claystones. This is possibly linked to an early compaction phenomena whereby, as the lateral translation of the bentonitic claystone body ceases, the coarser sediment accumulation of the bentonitic claystone body overlying the soft mud settles into the mud and deforms the bottom of the sand wave (Frébourg et al., 2016).

A number of bentonitic claystone beds show minor bioturbations in both the Lower and Upper Eagle Ford (Figure 3.3 and 3.13) possibly relating to an increased supply of nutrients to the benthic zone and brief increase in productivity (Boyd et al., 2007). Comparatively, an intensely bioturbated bentonitic claystone around the Mid-Cenomanian Event of Chittim-2H may be a result of a number of interconnected oceanographic and climatic processes related to the MCE and its LIP-associated large-scale, release of greenhouse gases and other compounds during the MCE (Erbacher et al., 2001; Blättler et al., 2011; Pogge von Strandmann et al., 2013; van Helmond et al., 2013; Scaife et al., 2017). In some such scenarios it's possible for water column instability, higher energy more frequent oceanic bottom currents and storms to form (Erbacher et al., 2001; Blättler et al., 2011; Pogge von Strandmann et al., 2013; van Helmond et al., 2013). The transmission of energy from the storms and bottom currents in turn may have led to increases in turbidity and density flows to deeper waters, transporting larger organisms from shallower areas.

3.5.2 Stratigraphical Lithological Cyclicity

The vertical variations in facies type (i.e.laminated foraminiferal packstones and laminated foraminiferal argillaceous wackestones), sediment type (i.e. sediment input to the basin) and grain size are interpreted to be a function of changing rates of productivity (Figure 3.17, 3.18 and 3.19). The mud fraction of the laminated argillaceous

foraminiferal wackestone facies is composed of clays and coccolith debris (Figure 3.4) and the coarser fraction consists mainly of planktonic, globigerinid foraminifera, with some mollusc, echinoderm and inoceramid fragments. The massive and laminated foraminiferal packstone facies are dominated by planktonic foraminifera with some peloids and calcispheres as well as some rare mollusc and echinoderm fragments.

There are a number of significant differences in both palynological and nannofossil assemblages to the limestones (Eldrett et al., 2015b). The amount of amorphous organic matter (AOM), relative and absolute abundances of Prasinophyte algae, relative abundance of P- and G-cysts and coccolithophores and the Nannofossil nutrient index vary significantly between limestone (laminated and massive foraminiferal packstones) and marlstone (laminated foraminiferal argillaceous wackestone and argillaceous wackestone) facies within the Eagle Ford (Eldrett et al., 2015b). The increased abundance in packstone facies, of calcisphere, primary producer algal cysts and globigerinids, which are first trophic level predators, suggests a sustained increase in trophic demand. This suggests increased primary productivity, which likely depended largely on nutrient availability (Figure 3.17).

Within the Eagle Ford formation many limestones (67% in Chittim-2H, 56% in Innes-1 and 65% in Iona-1) are directly preceded by bentonites (Figure 3.3). This may suggest a genetic relationship in which the deposition of ash could have provided essential nutrients to the ecosystem, which were otherwise depleted (Figure 3.18 and 3.19). When entering seawater such ashes may have released macronutrients and bioactive trace metals, especially phosphates and iron (2.5%-12% Fe in volcanic rocks; Le Maitre, 1976); such macronutrients and metals were subsequently available for primary producers (Frogner et al., 2001) and may have promoted primary productivity (Jones and Gislason, 2008).

Present day phytoplankton growth in nutrient-rich, high-nitrate low-chlorophyll (HNLC), regions of the world's oceans is limited by the availability of iron (Fe) and possibly other nutrients such as manganese (Mn; Boyd et al., 2007). Studies that have articially delivered HNLC areas with these nutrients typically generated strong

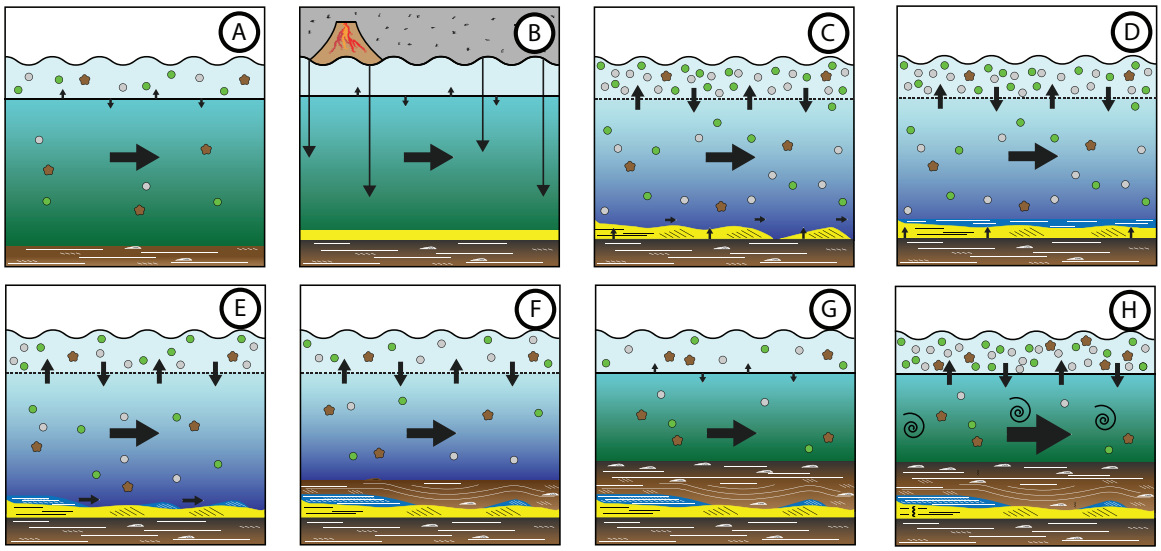

Figure 3.18: Integrated model for sedimentary transport and deposition for the Lower Eagle Ford. (A) Nutrient depleted oceanic system resulting in low primary productivity leading to little deposition of planktonic foraminifera. (B) Volcanic eruption and ash deposition adding previously depleted nutrients to the system. Increases in atmospheric–ocean thermal gradients as a result of periods of solar insolation maxima lead to greater, more frequent storms and stronger bottom currents resulting in a short term periodic de-stratification of the water column. (C) Increased numbers of primary producers lead to blooms in higher trophic levels. The ash fall deposit is reworked by the deep oceanic currents leading to the formation of the Bentonitic Claystone and the unidirectional flow structures seen within this facies. (D) This bloom eventually leads to the deposition of high numbers of planktonic foraminifera and other upper trophic level organisms, these are (E) reworked into laminated and massive foraminiferal packstones, which display a range of unidirectional currents structures. (F) In time a decrease in nutrient availability leads to lower concentrations of planktonic debris being deposited resulting in the formation of the laminated argillaceous foraminiferal wackestones and higher preservation of organic carbon. (G) Over time increasing stratification results in lower euphotic zone nutrient availability and productivity, greater preservation of organic carbon and the deposition of the argillaceous wackestone facies. (H) During the MCE an unstable water column or periodic influx of oxygenated waters may have led to periods of higher euphotic nutrient availability and benthic oxygenation resulting in the preservation of higher numbers of inoceramus.

responses in the phytoplankton communities (Boyd et al., 2007). In most cases these responses included a greater efficency of photochemical energy conversion, an increase in total biomass, and a shift in the species composition of phytoplankton to a diatom-dominated community (Boyd et al., 2007).

Increased marine primary productivity and other associated biogeochemical responses to Fe fertilization have the potential to sequester CO_2 from the atmosphere and enable an increased flux of carbon from surface waters into the deeper ocean environment (Blain et al., 2007; Smetacek et al., 2012). The rapid fertilizing potential of volcanic ash particles arises from a coating containing nutrient-bearing soluble salts formed from the gas phase during the eruption (e.g. condensed vol-

canic gases and adsorbed aerosols; Frogner et al., 2001). It has been proposed that the atmospheric CO_2 drawdown that occurred after the Pinatubo 1991 eruption was the result of increased marine primary productivity following Fe-related fertilization (Watson, 1997). Additionally, ash fertilization mechanisms has been suggested to have resulted in significant, long term perturbations in sedimentary and biogeochemical cycles (Bay et al., 2004; Cather et al., 2009).

Traditionally, the volcanic ash fertilization hypothesis has relied on analysing the response of phytoplankton cultured in the laboratory to ash addition (e.g. Duggen et al., 2007; Hoffmann et al., 2012), measuring trace metals released from ash (e.g., Olgun et al., 2011, 2013; Duggen et al., 2007; Achterberg et al., 2013), and using remote sensing to analyse post-eruptive phytoplankton blooms (Hamme et al., 2010; Langmann et al., 2010; Achterberg et al., 2013). More recently results from a suite of Fe and volcanic ash addition experiments conducted across a range of oceanic regimes (subtropical gyre, productive shelf, and HNLC waters) provided evidence for the potential for volcanic ash deposition to stimulate phytoplankton growth in the Southern Ocean (Browning et al., 2014).

Results from experiments in the North Atlantic and North Pacific have demonstrated the fertilization potential of volcanic ash in regions not normally considered to be classic HNLC system (Achterberg et al., 2013; Mlanon et al., 2014). Studies of ash fertilization and its role in the availability of nutrients in the Cretaceous surface ocean strongly suggests it affected marine primary productivity and therefore may have had a substantial influence on both regional and global oceanic conditions throughout this period (Olgun et al., 2011; Frébourg et al., 2016; Tessin et al., 2016).

Similar concepts have previously been suggested in the Eagle Ford equivalent Lake Waco Formation and the middle Boquillas of Val Verde and Brewster County where the strong association between abundant planktonic foraminifera and bentonite claystones suggests that these deposits are genetically related (Fairbanks et al., 2016; Frébourg et al., 2016). Planktonic globigerinid foraminifera are the dominant grain type within the Bouldin Member of the Lake Waco Formation and the pelagic grainstone facies of the middle Boquillas in Val Verde County (Fairbanks et al., 2016;

Frébourg et al., 2016).

In both areas it was suggested that the sediment type is likely to have been sourced from the photic zone and should reflect surface water, and not bottom water environmental conditions. The high concentration of planktonic debris in the pelagic grainstones of the middle Boquillas of Val Verde County and Ernst Member of the Lake Waco Formation suggests accentuated productivity during their deposition (Fairbanks et al., 2016; Frébourg et al., 2016), providing high rates of carbonate sediment supply.

A strong association exists between the massive bentonitic claystone layers and calcareous foraminiferal units, and the massive bentonitic claystones are largely restricted to the Bouldin Member, Lake Waco Formation (Fairbanks et al., 2016). This close relationship suggests that heightened productivity in the oxic zone of the water column was stimulated by nutrient enrichment from volcanic input, and it drove sediment supply independent of eustatic forcing (Figure 3.17, 3.18 and 3.19). In turn this implies that nutrients introduced into the ocean water system by volcanic eruptions led to higher productivity within the oxic zone and stimulated planktonic blooms that led to higher rates of carbonate sedimentation, resulting in the formation of packstone facies in both the Upper and Lower Eagle Ford such as at 1500.1-1499.9 m in Chittim-2H. Similarly, the strong association between bentonites and limestones in the Eagle Ford may be related to changes in carbonate sedimentation rates that were driven by surface water nutrient enrichment, stimulated in part by volcanic activity (Figure 3.18 and 3.19).

Decreases in marine productivity can be seen to occur gradually at couplet scale through the packstone and wackestones in sections such as 1500.9-1500.1 m, 1502.5-1501.65 m and 1491.7-1490.95 m of Chittim-2H. In these couplets HI values tend to trend from high in the base packstone facies gradually decreasing to lower values at the stratigraphic top of the wackestone. This suggests a reduction in the marine kerogen fraction and a slow shift towards a more mixed marine-terrestrial system (e.g. Durand, 1980; Tissot and Welte, 1984; Prauss and Riegel, 1989; Langford and Blanc-Valleron, 1990).

A decrease in surface primary productivity through this facies with time is suggested by a decrease in bioclast and planktonic foraminiferal counts upwards from the stratigraphic base to the top of the wackestone facies, such as that observed between 1491.81-1490.7 m in Chittim-2H (Table 3.2). This possibly demonstrates high primary productivity, at the base of the packstone-wackestone couplet, initially led to organic matter supply being dominated by marine sources (Figure 3.17, 3.18 and 3.19). However, as marine primary productivity gradually decreased, terrestrially derived organic matter, became an increasingly dominant source of organic matter flux to the sedimentary reservoir (Figure 3.17, 3.18 and 3.19).

This change in marine primary productivity is endorsed by similar couplets from Val Verde County, where upwardly decreasing globigerinid foraminifer accumulations and bioclastic sediment input, which initially diluted the organic matter of the marine system, indicate a reversion to a low marine primary productivity system (Frebourg et al., 2016). This interpretation of HI profiles is supported in the open literature. Both the T-OAE (e.g. Farrimond et al., 1994; Pancost et al., 2004; Al-Suwaidi et al., 2010) and OAE-2 (Junium et al., 2007; Lenniger et al., 2014; El-Shafeiy et al., 2016) have shown changes in primary productivity, using HI values, on sequence and couplet length time scales.

A decrease in benthic anoxia, indicative of a decrease in primary productivity, stratigraphically upwards through the wackestone facies (Figure 3.18 and 3.19) could be inferred by the high-resolution vertical changes in U_{EF}. Examples of these gradual decreases can be observed between 1498.05-1497.6 m, 1491.8-1491.1 m and 1500.8-1500.2 m in Chittim-2H (Figure 3.16). It would be expected that an enhanced supply of biolimiting nutrients leading to higher levels of primary productivity within the oxic zone would likely have caused an expansion and intensification of the oxygen minimum zone (OMZ) at the sediment-water interface during the deposition of 1498.05-1497.6 m, 1491.8-1491.1 m and 1500.8-1500.2 m in Chittim-2H (Figure 3.16; e.g. Schlanger and Jenkyns, 1976). Towards the upper limit of the couplets mentioned above, a diminished nutrient supply led to a decreased primary productivity and reduced benthic anoxia (Figure 3.17, 3.18 and 3.19). This reduced anoxia

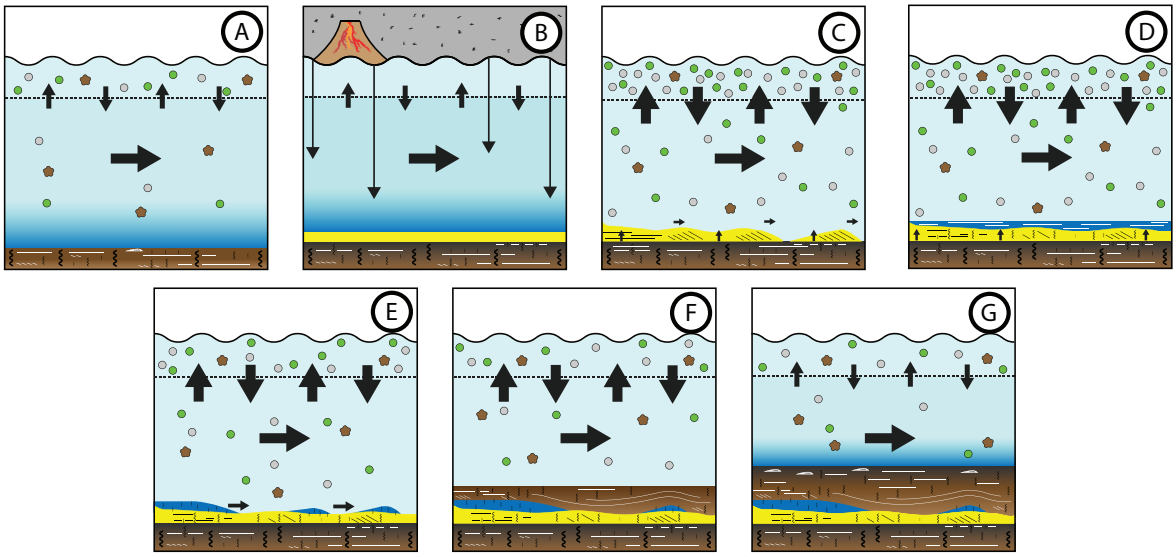

Figure 3.19: Integrated model for sedimentary transport and deposition for the more oxygenated and mixed water column during the deposition of the Upper Eagle Ford. (A) Nutrient depleted oceanic system resulting in low primary productivity leading to little deposition of planktonic foraminifera. (B) Volcanic eruption and ash deposition adding previously depleted nutrients to the system. Increases in atmospheric–ocean thermal gradients as a result of periods of solar insolation maxima lead to greater, more frequent storms and stronger bottom currents resulting in a short term periodic de-stratification of the water column. (C) Increased numbers of primary producers lead to blooms in higher trophic levels in both the euphotic and benthic zone. As in the Upper Eagle Ford the ash fall deposit is reworked by the deep oceanic currents leading to the formation of the Bentonitic Claystone and the unidirectional flow structures seen within this facies. (D) This bloom eventually leads to the deposition of high numbers of planktonic foraminifera and other upper trophic level organisms. (E) These are reworked into laminated and massive foraminiferal packstones and heavily bioturbated by benthic organisms destroying many of the original sedimentary structures. (F) In time a decrease in nutrient availability leads to lower concentrations of planktonic debris and reduces the numbers of benthic organisms bioturbating the sea floor resulting in the deposition of the argillaceous wackestones and higher preservation of organic carbon. Bioturbation of the argillaceous wackestone likely obscures the presence of foraminiferal-rich laminae, making it appear weakly laminated to massive within the Upper Eagle Ford. (G) Over time increasing stratification results in lower euphotic zone nutrient availability and productivity, though more than in the Lower Eagle Ford, and greater preservation of organic carbon.

may have been repeated until a new influx of biolimiting nutrients occurred and the process was repeated.

However, this study finds that on a couplet scale the upwards-trending TOC enrichment profiles bear a much closer relationship to those of Mo_{EF}, which displays an opposing trend to U_{EF}, such as those observed between 1498.05-1497.7 m, 1491.8-1490.05 m and 1500.9-1500.2 m in Chittim-2H (Figure 3.18). Mo has been widely used as a proxy for euxinic, oxygen-depleted, sulphide-rich conditions (e.g. Algeo and Lyons, 2006). Euxinia is intensified, and Mo is enriched, in restricted to semi-enclosed basins like the Black Sea or the Cariaco Basin (e.g. Tribovillard et al.,

2006). In this study area Mo_{EF} increases from the stratigraphic base to the top of wackestone beds indicating an increase in euxinia, basinal restriction and water column stratification (Figure 3.17, 3.18 and 3.19; Algeo and Lyons, 2006; Tribovillard et al., 2006; Algeo and Tribovillard, 2009; Algeo and Rowe, 2012). This is shown to occur between 1498.05-1497.75 m, 1491.85-1491 m and 1500.85-1500.3 m in Chittim-2H (Figure 3.16).

Comparatively, the packstone beds show low Mo_{EF} values suggesting weaker euxinia and stratification (Figure 3.17, 3.18 and 3.19). Recent studies have shown that increasing stratification inhibits primary productivity (Bopp et al., 2002; Boyd and Doney, 2002; Sarmiento et al., 2004) as the photosynthetic production of organic matter is critically dependent on the supply of nutrient from the subsurface ocean to the euphotic zone (Falkowski et al., 1988; Gruber et al., 2002). Therefore, it may be likely that primary productivity became grossly lowered due to an increase in water column stratification (Figure 3.18 and 3.19).

Stratification in the Western Interior Seaway possibly broke down during the deposition of the bentonite beds due to an increase in regional or global thermal gradients and subsequent larger and more frequent storms leading to mixing of the water column and stronger bottom currents (e.g. Research on Cretaceous Cycles Group, 1986; Sageman et al., 1996, 1997; Flogel et al., 2005; Meyers et al., 2001; Berger, 2013; van Helmond et al., 2014). This may be due to increases in atmospheric–ocean thermal gradients and associated climate systems as a result of either: 1. enhanced latitudinal distribution of solar insolation maxima (i.e. maxima in Milankovitch periodicities; e.g. Flogel et al., 2005, Eldrett et al., 2015a); 2. enhanced global or regional atmospheric temperatures due to increased volcanic greenhouse gas emissions; 3. a mixture of the two in which glacial deloading, as a result of solar insolation maxima, on the Cordilleran orogenic resulted in increased volcanic greenhouse gas emissions (see section 3.5.3). Based on the arguments offered here an idealised depositional model is presented in Figure 3.17. In this model a bentonitic claystone is followed by a foraminiferal packstone. This in turn is followed by a laminated argillaceous foraminiferal wackestone which grades into

an argillaceous wackestone. These changes occur due to increases in atmospheric and ocean thermal gradients as a result of periods of solar insolation maxima which lead to greater, more frequent storms and stronger bottom currents resulting in de-stratification of the water column.

The deposition of the bentonitic claystone dramatically increases the euphotic zone nutrient availability stimulating increased primary productivity. With time euphotic zone primary productivity decreases in line with increasing water column stratification which occurs as a result of reduced latitudinal energy gradients and increasing solar insolation minima. This leads to a decrease in the marine kerogen fraction but an increase in organic carbon preservation.

Longer term variations in sedimentology also exist between the Lower and Upper Eagle Ford (Figure 3.18 and 3.19). The Lower Eagle Ford shows few occurrences of bioturbation, molluscs or inoceramids except for the Mid-Cenomanian Event and Jukes-Browne Event indicating a better mixed water column and more oxygenated benthic zone during these carbon isotope events. One particular section, 1507.02-1507.24 m in Chittim-2H (Figure 3.3, 3.11 and 3.18), shows heavy bioturbation most likely from a large benthic organism transported in high energy currents or sediment flows.

In comparison, regularly bioturbated facies as well as greater occurrences of mollusc, inoceramid and unidentifiable shell fragments in the Upper Eagle Ford (Figure 3.3) likely indicate a significantly more oxygenated sediment-water interface and a more mixed water column during the deposition of the Upper Eagle Ford (Figure 3.19). Furthermore, as previously suggested the prevalence of the argillaceous wackestone in the Upper Eagle Ford indicates both a reduction in primary productivity and energy of flow regime throughout this section of core (see section 3.1.2; Figure 3.19).

In the Upper Eagle Ford higher levels of water column mixing and benthic oxygenation likely leads to less water column stratification, slower decrease in nutrient availability and lower preservation of organic matter.

3.5.2.1 Critical Assessment of the Mechanisms causing Cyclic Sedimentation

A number of models have been proposed to account for the deposition of rhythmically bedded strata in the KWIS including: i) primary productivity (productivity model); ii) input of terrigeneous sediments (dilution model); iii) the intensity of bottom currents (scour model); iv) benthic oxygenation and hence, the extent and preservation of organic matter (redox model); and v) climatic response to changes in solar insolation driven by Milankovitch cycles.

A number of interacting processes have been suggested to drive models (i) to (v). These include: 1) large eustatic oscillations; 2) changes in depositional regime relating to global climatic and hydrological cycle shifts; 3) changes in prevalent wind directions leading to shifts in oceanic currents; 4) latitudinal fluctuations of the intertropical convergence zone (ITCZ) and climatic changes driven by Milankovitch cyclicity.

These models all have weaknesses summarised as follows:

a) Large enough eustatic oscillations to shift storm wave base and create alternating wackestone-packstone structures are unlikely over such short time periods (e.g. Haq, 2014), in particular there is little evidence that sea level fluctuations occurred in the Western Interior Seaway on 100 kyr cycles (Gale et al., 2008).

b) Changes in depositional regime are also unlikely. Facies distributions in eastern sections of the Mowry and Western Interior Seaway lack evidence for drastic changes in major depocentres and drainage patterns from the Cordilleran fold and thrust belt (e.g. Winker and Buffler,1988; Ewing, 1991; McFarlan and Menes, 1991; Dean and Arthur, 1988, 1998; Goldhammer and Johnson, 2001; Phelps et al., 2013). As such, studies of the East Texas Basin suggest that the dominant regional depocentre remained east of the San Marcos arch throughout the Cenomanian-Turonian (e.g. Goldhammer and Johnson, 2001; Ruppel et al., 2012; Fairbanks et al., 2016).

c) Recent oceanographic and climatic studes suggest a relatively constant, westerly prevailing wind direction around the Western Interior Seaway throughout the Cenomanian and the Turonian (Trabucho Alexandre et al., 2010). Though wind direction and strength may have changed over shorter timescales, it is unlikely to have changed so extensively and so often over such extended periods of time (Elder, 1988; Sageman et al., 1997; Ledwell et al., 2000; Trabucho Alexandre et al., 2010). However, caution must be taken in using a single climate model as justification for a stable wind-field through the time interval and further work must be undertaken to investigate the impact of wind strength and direction during this time period.

d) Today, the ITCZ extends over the Atlantic Ocean from South America to the west coast of Africa with latitudinal seasonal variations between 10N and 20N (July) and the equator (January; e.g. Peterson and Haug, 2006). Similar ITCZ latitudinal variations are expected to have existed during the Cenomanian to early Turonian (e.g. Pettke et al., 2002; Friedrich et al., 2008). As the study area is largely above 25N it is unlikely to have been affected by cyclical variations of the ITCZ. However, significantly different global climate conditions existed during the mid-Cretaceous (e.g. Hay, 2008; Hay and Floegel, 2012) which possibly resulted in an expanded subtropical-tropical Hadley Cell (Wagner et al., 2013). This has been linked to changes in organic matter quality and quantity in Cretaceous Atlantic sediments as a result of significant change in depositional conditions off NW-Africa (Wagner et al., 2013). Hofmann et al. (1999) showed that at ODP Site 369 the deposition of black shales with enhanced organic matter quality and higher TOC occurred during humid periods which resulted in enhanced supply of nutrients via continental runoff and water column stratification. Furthermore, Wagner et al. (2013) suggest the existing data supports the assumption that the shales were deposited with an assumed southern limit between 25S and 30S, and possibly a similar northern limit. Therefore, further work may be required to disentangle the impact of orbital scale fluctuations in low latitude wind and oceanographic patterns in lithological cycles.

Certain aspects of previous models may still hold true. The model presented in Fig. 3.17, 3.18 and 3.19 suggests changes in solar insolation as a result of Milankovitch

forcings somehow affected volcanism rates and frequency (discussed further in section 3.5.3), leading to the common association of bentonites immediately prior to foraminiferal packstones. As such this model presents a modification of the Eldrett et al. (2015b) work which suggests that insolation maxima led to limestone deposition following increased surface temperatures, evaporation, precipitation, enhanced storms and terrestrial input at high latitudes being coeval with greater carbonate dilution of organic matter at lower latitude. The model presented here provides a mechanism for the cyclical changes which requires nutrient enhancement as a result of Milankovitch-driven bentonite deposition.

3.5.3 Potential Causes for and Consequences of Bentonite Cyclicity

Based on the astronomical timescale of the Iona-1 core (Eldrett et al., 2015a) previous studies have suggested that the lithological couplets in the Iona-1 core may reflect climatic forcing driven by solar insolation resulting from integrated Milankovitch periodicities (Eldrett et al., 2015b). Differences in environmental energy, water column stratification and water column stability led to periods of 'limestone' (interpreted here as massive foraminiferal packstones and laminated foraminiferal packstones) and 'marlstone' (interpreted here as laminated argillaceous wackestones and foraminiferal argillaceous wackestones) deposition with individual 'limestone' beds being the product of integrated precession-obliquity cycles modulated by eccentricity (Eldrett et al., 2015b).

However, when plotting the occurrence of the bentonitic claystones of Iona-1 to depth their stratigraphical occurrences appear to follow a similar cyclicity to the wackestone-packstone alternations (Figure 3.20). Further to this using the recently published Iona-1 timescale (Eldrett et al., 2015a) the frequency of their occurrences suggests that they may follow Milankovitch timescales (Figure 3.20). In particular, the cyclicity of bentonites in the bottom 30 m of the Lower Eagle Ford correspond well to 100, 50, 25, 20 and 15 kyr (Figure 3.20) which are very similar to the proposed Cenomanian-Turonian short eccentricity of 97 kyr, obliquity of 50 kyr and precession cycles of 24 kyr and 19kyr (Eldrett et al., 2015b).

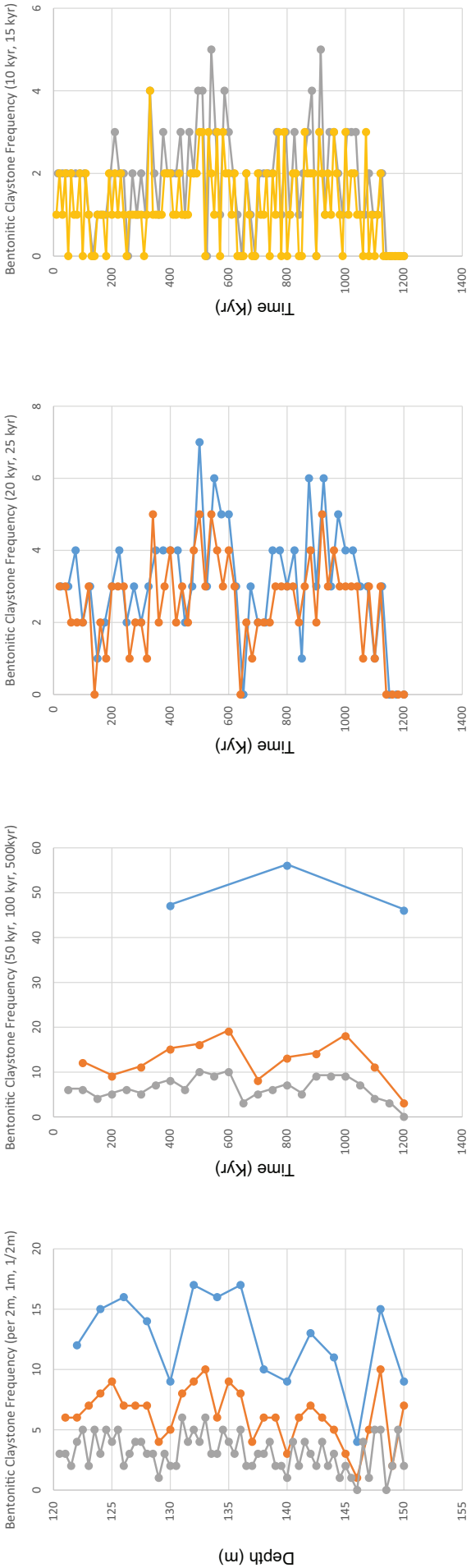

Figure 3.20: Graphs showing the occurrence of bentonitic claystones in the lower 30 m of the Iona-1 core in relation to depth (m) and time (Kyr) based on the astronomical timescale of Eldrett et al., 2015a. The depth and time categories into which the bentonitic claystone facies have been divided are indicative of the Milankovitch cycles. Based on Eldrett et al., 2015a, 2 m of core should correspond to the Long Eccentricity cycle, 1 m the Short Eccentricity cycle and 0.5 m the 50,000 year obliquity cycle. These graphs show that the bentonitic claystones appear to occur on the same timescales as the couplets.

There are a number of mechanisms that result in bentonites occurring on astronomical timescales. The first, preservation bias due to eustasic changes, is unlikely as the Cretaceous was a greenhouse climate and large enough eustatic fluctuations to move the storm wave base are unlikely over such short (103-104 Kyr) periods (e.g. Haq, 2014). The second, shifting depositional regimes relating to hydrological cycles or prevailing wind directions, is possible but also unlikely. Recent oceanographic and climatic studies suggest a relatively constant, westerly prevailing wind direction around the Western Interior Seaway throughout the Cenomanian-Turonian (Trabucho Alexandre et al., 2010); however, this may not necessarily mean the wind direction and strength was constant over shorter timescales i.e. precessional frequencies. A third potential reason may be that volcanic eruptions occurred on astronomical frequencies.

It has long been postulated that ice and glacier growth is linked to orbital cyclicities (Denton and Hughes, 1983; Gildor, 2000; Gale et al., 2002; Berger, 2013). Periods of solar insolation minima (i.e. minima in Milankovitch periodicities) lead to reduced latitudinal thermal-energy gradients and a stratified water column (e.g. Research on Cretaceous Cycles Group, 1986; Berger, 2013). These intervals, which occur mainly during the deposition of the wackestones in the KWIS (Eldrett et al., 2015b), would allow glacier and ice sheets to grow. Comparatively, periods of solar insolation maxima, which occur mainly during the deposition of the packstones in the KWIS (Eldrett et al., 2015b), result in increases in the atmospheric-ocean thermal gradients, rapid deglaciation and associated climate system elements (e.g. Research on Cretaceous Cycles Group, 1986; Berger, 2013). These include more energetic environments e.g. greater, more frequent storms, stronger bottom currents, and de-stratification of the water column (Research on Cretaceous Cycles Group, 1986).

An interesting question to consider may be why every limestone-marlstone couplet does not start with a bentonite. The more energetic environments discussed above-may in turn result in erosion of some bentonitic claystone beds. Furthermore, this would also allow for movement of essential trace metals from deeper parts of the

water column during these periods.

Over long time scales it has been suggested that glacial growth and subsequent ice loading has influenced volcanism (Hall, 1982; Paterne et al., 1990; Sigvaldson et al., 1992; Nakada and Yokose, 1992; Paterne and Guichard, 1993; Jull and Mackenzie, 1996; Glazner et al., 1999). Recent evidence for regional volcanic responses to variations in glaciation suggests that subaerial volcanism increased with deglaciation (e.g. Jellinek et al., 2004; Bacon and Lanphere, 2006; Rawson et al., 2016). Such an increase can be understood as a consequence of deglaciation depressurising volcanoes, and the lower pressure leading to a greater probability of eruption because of increased magmatic melt (Maclennan et al., 2002) and reduced confining pressure (Jellinek et al., 2004).

The above suggests that the waxing and waning of ice masses on the nearby cordillera on the timescale of the cyclicity of bentonites in the Eagle Ford may therefore be possible. Empirical data on arc eruption rates and volumes through time remain ambiguous, and attempts to identify exactly how subduction-related volcanoes respond to ice-unloading remain inconclusive (e.g., McGuire et al., 1997; Singer et al., 2008; Watt et al., 2013). However, the loss of 10% of the Vatnajokull glacier in Iceland over the last century is indicated to have resulted in a volume of 0.014 km^3/yr being produced in response to current ice thinning (Pagli and Sigmundsson, 2008).

Quarternary examples suggest that glacial growth occurs on eccentricity, obliquity and precession timescales (Hays et al., 1976; Tiedemann et al., 1994; Shackleton, 2000). However, the idea of Mid-to-Late Cretaceous glaciation is debated. Most geochemical proxies point to a long term warming trend from the late Aptian to the Cenomanian-Turonian (Clarke and Jenkyns, 1999; Pucat et al., 2003). Estimates of Cretaceous climates, compared to today, reach up to 5℃ warmer inland and oceanic temperatures at low latitudes (Wilson and Norris, 2001; Wilson et al., 2002) and 15℃ at high latitudes (Jenkyns et al., 2004). Furthermore, continental configurations do not favour ice sheet inception (Ladant and Donnadieu, 2016).

There are a number of arguments in favour of glacial episodes during the Cenomanian-Turonian including the interpretation of oxygen isotope records (Bornemann et al., 2008; Stoll and Schrag, 2000) and sequence stratigraphy (Miller et al., 2004; Galeotti et al., 2009). In addition, the downward revision of atmospheric pCO_2 for the Late Cretaceous (Fletcher et al., 2005, 2008; Barclay et al., 2010) to levels significantly lower than those from the major Eocene-Oligocene Antarctic glaciation (Coxall et al., 2005; Pagani et al., 2011; Ladant et al., 2014; Heureux et al., 2015) increases the likelihood of Cenomanian-Turonian glacial events. As such though the occurrence of glacial events in the Late Cretaceous are a possibility, further work is required to investigate glacial growth on the proposed source of these bentonites, the West Cordillera margin of North America (estimated maximum altitude of 3000-4000 m above sea level; Burchfiel et al., 1992), and whether it is possible to replicate these findings in other areas of the world.

3.5.4 Lateral Variations

Marine mudrocks have traditionally been assumed to only accumulate in low-energy settings due to their fine-grain size (Potter, 2003; Boggs, 2005). However, recent studies have suggested that when suspended in the water column mud-sized particles can accumulate under relatively high-energy current conditions and even create bedforms (Stow, 1994; Honjo, 1997; Schieber et al., 2007, 2013; Macquaker et al., 2010). Furthermore, oceanographic studies have shown that the seafloor is commonly subjected to bottom currents and is not the quiescent environment it was long thought to be (e.g. Stow et al., 2002). As such it must be expected that mudrocks can accumulate under a range of water depths and energy conditions.

Isolated clay-sized particles require current velocities of greater than 0.1 mm/sec to remain in suspension (Hjulstrom, 1935). As such, oceanic settings rarely have currents slow enough to allow the suspension settling of clay- sized particles. Instead fine-grained particles reach the seafloor through flocculation and settling (Ghadeer and Macquaker, 2011). Flocculation results in fine particles being bound together into aggregates, by chemical, physical, and/or biological processes, known as ma-

rine snow (e.g., Stow, 1994; Honjo, 1997; Loucks and Ruppel, 2007; Schieber et al., 2007, 2013; Macquaker et al., 2010).

These larger particles have settling velocities of up to a few hundred metres per day (Alldredge and Silver, 1988; Riebesell, 1992) and are more resistant to shear (Alldredge et al., 1990). Modern flume experiments have shown that mud floccules can settle at speeds of up to 30 cm/sec for phyllosilicate mud (Schieber et al., 2007) and 50 cm/sec for carbonate mud (Schieber et al., 2013). In modern shelf environments bottom current velocities range from a few cm/sec (e.g. Nelson et al., 1999; Lobo et al., 2000) to 150 cm/sec (Menanteau et al., 1983). Additionally, on modern slopes bottom currents reach 100 cm/sec and up to 200 cm/sec when topographically confined (Stow et al., 2002).

Accumulations of mud- and silt- sized particles result in the formation of highly cohesive sediments that require high velocities to be eroded (Hjulstrom, 1935). Dewatering of these sediments such as pelagic clays and calcareous oozes (pelagic sand to silt-sized sediments) cause an increase in their erosional speed threshold (Lonsdale and Southard, 1974; Southard et al., 1971). Additionally, flume experiments show that the accumulation of fine-grained sediments occur in the form of large polygenic particles (up to 75 mm; Lonsdale and Southard, 1974; Alldredge and Gotschalk, 1989). The resulting rocks from these experiments displayed a fine grained texture, giving the false impression of low-energy deposition (Lonsdale and Southard, 1974; Alldredge and Gotschalk, 1989).

Low density, coarse-grained carbonate sediment can have unexpectedly low settling velocities (e.g. Jorry et al., 2006). For example, planktonic foraminifera have been shown to have settling velocities of less than 2 mm/sec (Berger and Piper, 1972). As such, foraminiferal packstones or grainstones can be misinterpreted to have been deposited under high energy conditions if the pelagic material has accumulated in a mud-rich environment.

In the Western Interior Seaway bentonites typically form thin (mm to meters thick) beds present over a wide lateral extent of 100s to 1000s of kms (Eaton, 1963).

Smectite-rich bentonites have the ability to swell 2-8 times their original volume when hydrated and can form easily deformable plastic beds prone to flow (e.g. Gens and Alonso, 1992). Comparatively, kaolinite-rich bentonites, which lack smectite enrichment, do not expand and form durable, hardground beds (e.g. Gens and Alonso, 1992). The bentonites of the Innes-1, Iona-1 and Chittim-2H cores contain high concentrations of smectite and display a wide variety of sedimentary features associated with subaqueous transport. Features such as low-angle cross stratification and current ripples indicate deposition under unidirectional currents (Figure 3.11), therefore demonstrating that many of the bentonitic claystones have been reworked (Figure 3.18 and 3.19).

Cretaceous bentonites have previously been suggested to be responsible for subaqueous current and debris flow deposits in Northern Alaska (Anderson et al., 1969). In this area the hydration and expansion of montmorillonite-rich bentonites led to slopes of 5 degrees upwards forming glide planes for sediment (Anderson et al., 1969). Within the Maverick basin bentonites may have had a similar affect. The expansion and hydration of smectite-rich bentonites is likely to lead to local slope instability. This reduces the friction between the bentonitic claystone and the overlying sediment. Minor evidence for mass flow deposits exists in the Chittim-2H, Innes-1 and Iona-1 cores including the heavily bioturbated 1507.02-1507.24 m of Chittim-2H where it is likely a large bottom feeder was transported to deeper sections of the Maverick Basin by high energy currents or mass flows.

Evidence for mass flow deposits have previously been suggested to exist in the basal third of the Lower Eagle Ford of Iona-1 (Eldrett et al., 2017). Additionally, a reduction in shear strength as caused by the expansion of bentonitic claystones is likely to have promoted reworking and migration of the sediment into barchan and transverse dunes such as those found at Carnegie Ridge (Lonsdale and Malfait, 1974).

Within the laminated foraminiferal argillaceous wackestones and argillaceous wackestone facies this reduction in shear strength may have little effect, as the higher concentrations of clays, mud and silt potentially had sufficient cohesive ef-

fect against hydrodynamic forces associated with critical shear stress (Mitchener and Torfs, 1996; Van Ledden et al., 2004). However, due to lower clay, mud and silt concentrations in the foraminiferal packstone facies, this decrease in shear strength may have resulted in these facies being controlled by cohesionless behaviour. Such a reduction in shear strength would mean these facies are more susceptible to reworking and down-slope movement by bottom currents, eventually creating discrete sediment accumulations (Figure 3.18 and 3.19; Flemming, 1980; Shanmugam et al., 1993; Endo et al., 2005).

Based on the arguments offered here an integrated model for sedimentary transport and deposition is presented in Figures 3.18 and 3.19. Initially, a nutrient depleted oceanic system results in low primary productivity leading to little deposition of planktonic foraminifera. Following this a volcanic eruption and ash deposition add previously depleted nutrients to the system. This increased the numbers of primary producers led to blooms in higher trophic levels. The ash fall deposit was then reworked by the deep oceanic currents leading to the formation of the Bentonitic Claystone and the unidirectional flow structures seen within this facies. This bloom eventually led to the deposition of high numbers of planktonic foraminifera and other upper trophic level organisms, these were then reworked into laminated and massive foraminiferal packstones, which display a range of unidirectional currents structures.

In time a decrease in nutrient availability led to lower concentrations of planktonic debris being deposited resulting in the formation of the laminated argillaceous foraminiferal wackestones and higher preservation of organic carbon. Over time an increase in stratification resulted in lower euphotic zone nutrient availability and productivity, greater preservation of organic carbon and the deposition of the argillaceous wackestone facies. During the MCE an unstable water column or periodic influx of oxygenated waters may have led to periods of higher euphotic nutrient availability and benthic oxygenation resulting in the preservation of higher numbers of inoceramus. In the Upper Eagle Ford bioturbation of the argillaceous wackestone likely obscures the presence of foraminiferal-rich laminae, making it appear weakly

laminated to massive within the Upper Eagle Ford.

3.5.5 Implications

Preliminary work presented in Chapter 3 suggests a strong response to volcanic eruptions in the Western Interior Seaway. As such it is possible to apply the learnings taken from this study to future studies of both:

1. Rhythmically interbedded marl-limestone sequences;

2. Volcanic ash fertilization of ancient oceans and how it's expressed in the geological record.

How long lived and exactly what parts of the marine biogeochemical system have been influenced remain to be investigated. Modelling could help with this, yet important parameters that would go into these are poorly constrained and could limit the usefulness of results obtained (e.g. Boyd and Mackie, 2008). Even modern large scale ash-release experiment (sensu Boyd et al., 2007), which whilst likely being highly informative, could be difficult to realise and would almost certainly still lead to further questions (Boyd et al., 2007).

Predicting phytoplankton community responses to ash supply will likely require a detailed evaluation of the ash being added to the system. For example ash particle size may exert a particularly important control on metal release, as for a given mass of ash addition metal release may be expected to be greater for ash samples with smaller grain sizes and thus larger surface area per bulk ash mass (assuming soluble salts on the ash surface scale positively with surface area). Carefully designed experiments detecting metal release from ash using conditions that best replicate, or ideally utilise, the natural ocean are needed if ash mass fluxes are to be used for projecting total metal (e.g. Fe) input to the surface ocean subsequent to an eruption and thereby attempting to quantify primary production stimulated (c.f. Watson, 1997). For reasons outlined previously, such experiments should pay careful consideration to ash particle size, ash loading, and exposure time to best mimic natural

ash depositions in the oceanic regime of interest (i.e. coastal versus open ocean waters).

Consequently, in the case of ash-driven fertilisation there is the potential for long term stimulation of ecosystems, sedimentary cycles, and carbon export. However, more work is required to understand why it is prevalent in the southern Western Interior Seaway and if these findings can be validated by comparison to other time equivalent sections around the region or world. Formations such as La Luna which are known to contain large numbers of bentonites (Zumberge, 1984), are time equivalent and are relatively close to the Cordilleran orogenic belt may provide an excellent opportunity to confirm this study.

Alternative processes may cause or contribute to the lithological cycles that result in the formation of marl-limestone sequences and mechanisms that relate to the Western Interior Seaway may not be universal. For example, the origin and significance of the limestone beds and nodules in the uppermost Rhaetian (Triassic) to Sinemurian (Jurassic) Blue Lias Formation of Britain, a non-bentonite bearing rhythmite, has long been a subject of interest (Day, 1865; Richardson, 1923; Kent, 1936). One of the reasons the Blue Lias Formation has attracted so much research interest is that it exhibits two styles of sedimentary cyclicity. Visually most obvious are the alternations of limestones and non-limestones, but also present are alternations of homogeneous, organic-carbon-poor strata (grey limestone plus light grey marl) with laminated organic-carbon-rich (e.g. Hallam, 1964; Weedon, 1986; 1987a; Arzani, 2004).

In the offshore hemipelagic facies of the Blue Lias Formation, the spacing of individual limestones within zones and the varying limestone proportions of limestones from zone-to-zone and from site-to-site, can all be related to the bottom-water turbulence (e.g. Weedon, 1986, 2017; Mogadam and Paul, 2000; Barras and Twitchett, 2007; Seilacher, 2007). Initiation of limestone formation is explained by periods of non-deposition causing cementation of the zone of anaerobic methane oxidation by sulphate close to the sediment-water interface (Raiswell, 1988, Bottrell and Raiswell, 1989). Deposition of light marl was associated with a drier climate char-

acterized by much stronger and/or more frequent, though possibly still rare, major storms whereas more tranquil conditions were typical for the deposition of dark marl and laminated shale (Waterhouse, 1999). However, occasionally during deposition of laminated shale, storms did lead to non-deposition and formation of laminated limestone beds and laminated limestone nodule horizons (Radley, 2008).

This shows that the conditions required to form rhythmitic strata are often complicated and extensive in nature. As such though the findings of this study are important in helping us understand rhythmites but caution must be taken as mechanisms related to this study may not be ubiquitous with all bentonite bearing limestone-marl sequences.

3.6 Conclusions

This high-resolution stratigraphic, sedimentological, mineralogical and geochemical study of the Cenomanian-Turonian southern Western Interior Seaway has provided important insights into the depositional dynamics of the Eagle Ford Group. This study spans a transect from the main Comanchean shelf (Innes-1), the slope (Iona-1) and the intra-shelf basin (Chittim-2H). This study identifies five main facies: (1) argillaceous wackestone facies, (2) laminated argillaceous foraminiferal wackestone facies, (3) laminated foraminiferal packstone, (4) massive foraminiferal packstone facies, (5) massive bentonitic claystone.

Evidence from this study suggests the formation of these facies appears to be a function of clay contents, bottom currents and productivity. The argillaceous wackestone and laminated argillaceous foraminiferal wackestone facies form under periods of low primary productivity and low accumulation rates. Differences in current regime and levels of primary productivity lead to the formation of the two different wackestone facies. Comparatively the laminated foraminiferal packstone and massive foraminiferal packstone facies form due to high primary productivity and high accumulation rates. Reworking of the packstone facies by bottom currents has resulted in the creation of carbonate sand ridges/sheets and isolated hydraulic

dunes. Differences in clay concentrations likely played a part in this. Higher concentrations of clay in the laminated foraminiferal packstones created a cohesive effect against hydrodynamic forces preventing the reworked carbonate sand ridges/sheets from forming barchan dunes. Furthermore, the lower concentrations of clay in the massive foraminiferal packstone may have caused greater porosity and permeability compared to the laminated packstone facies. This resulted in diagenesis preferentially affecting and recrystallizing the massive packstone facies obscuring sedimentary structures.

A number of models have previously been proposed to account for the deposition of rhythmically bedded strata in the KWIS: i) primary productivity (productivity model); ii) input of terrigeneous sediments (dilution model); iii) the intensity of bottom currents (scour model); iv) benthic oxygenation and hence, the extent and preservation of organic matter (redox model); and v) climatic response to changes in solar insolation driven by Milankovitch cycles. This study suggests the cyclicity observed in the Eagle Ford Group appears to be a function of nutrient limitation. Periodic ash falls from the Cordilleran Orogenic Belt released iron, nitrates and other nutrients into the system from soluble salts coating the ash particles resulting in periods of high primary productivity and high accumulations of foraminifera and other bioclasts (packstone facies). Over time primary productivity rates decrease resulting in lower accumulations rates of planktonic foraminifera and other bioclasts (wackestone facies). As such this study suggests that control over these alternations is not linked to changes in sea level but highly complex depositional and biogeochemical dynamics that created discontinuous bodies and intricate large-scale sedimentological architecture.

The high concentrations of swelling clays within the bentonitic claystones likely led to slope instability and helped create the lateral sediment accumulations found in southern Western Interior Seaway. Finally, this study tentatively suggests that the deposition of the bentonitic claystones, interpreted to be ash fall deposits, may have occurred on astronomical timescales as a result of glacier loading on the Cordilleran Magmatic Arc.

4 Sedimentary mercury enrichments as a marker for submarine Large Igneous Province volcanism: evidence from the Mid-Cenomanian Event and Oceanic Anoxic Event 2 (Late Cretaceous)

This chapter is modified from **J. D. Scaife**, M. Ruhl, A. J. Dickson, T. A. Mather, H. C. Jenkyns, L. M. E. Percival, S. P. Hesselbo, J. Cartwright, J. S. Eldrett, S. C. Bergman, D. Minisini, 2017. Sedimentary mercury enrichments as a marker for submarine Large Igneous Province volcanism? Evidence from the Mid-Cenomanian Event and Oceanic Anoxic Event 2 (Late Cretaceous). *Geochemistry, Geophysics, Geosystems*.

Abstract

Oceanic anoxic events were major climatic perturbations during which widespread marine anoxia and euxinia developed, and large amounts of organic carbon were buried on the ocean floor and in large lakes. Oceanic Anoxic Event 2 (OAE 2), at the Cenomanian-Turonian boundary ($\sim$94 Ma), is the largest perturbation of the global carbon cycle in the mid-Cretaceous and can be recognized by a characteristic $\sim$3 ‰ positive carbon-isotope excursion in sedimentary strata. Although OAE 2 has been linked to large-scale volcanism, several large igneous provinces (LIPs) were active at this time (e.g. Caribbean, High Arctic, Madagascan and Ontong-Java) and little clear evidence has emerged linking OAE 2 to a specific LIP. The Mid-Cenomanian Event (MCE, 96 Ma), identified by a small, $\sim$1 ‰ positive carbon-isotope excursion, is often referred to as a prelude to Oceanic Anoxic Event 2. However, similarly, no clear underlying cause has yet been demonstrated and its relationship to Oceanic Anoxic Event 2 is poorly constrained. Here, this study reports sedimentary mercury concentration data from four sites, three from the southern margin of the Western Interior Seaway of North America and one from Demerara Rise, in the equatorial proto-North Atlantic Ocean. This study finds that, in both areas, increases in mercury concentrations and Hg/TOC ratios coincide with the MCE and the subsequent OAE 2. However, the increases found in these sites are significantly more subtle than those found in records of many other Mesozoic events, possibly suggesting a marine rather than atmospheric dispersal of mercury for both events. Combined, the new mercury data presented here are consistent with an initial magmatic pulse at the time of the MCE, with a second and greater, pulse at the onset of OAE 2, possibly related to the emplacement of LIPs in the Pacific Ocean and/or the High Arctic.

4.1 Introduction

The mid-Cretaceous was a period characterized by major perturbations in the global carbon cycle, associated with the widespread development of anoxic-euxinic con-

ditions in the global ocean, termed Oceanic Anoxic Events (OAEs) (Schlanger and Jenkyns, 1976; Jenkyns, 1980; Arthur et al., 1987; Schlanger et al., 1987; Jenkyns, 2010). One such widely studied anoxic event, Oceanic Anoxic Event 2 (OAE 2, Cenomanian-Turonian, circa 94 Ma) is marked by an organic-rich mudstone, often referred to as 'black shale'. It is recorded in many parts of the world's oceans and marked by a globally recognized positive carbon-isotope excursion (CIE; Tsikos et al., 2004). This positive CIE is thought to reflect the widespread transfer of relatively ^{12}C-enriched organic matter into marine sediments, and the development of anoxic/euxinic conditions in many marine basins (Schlanger et al., 1987; Jarvis et al., 1988; Sinninghe Damsté and Köster, 1998; Jenkyns, 2010; Dickson et al., 2016, 2017). This study focuses on the southern Western Interior Seaway and Demerara Rise in the proto-North Atlantic (Figure 4.1). However, in contrast to other globally recognized sections that recorded organic-rich deposits developed under anoxic to euxinic conditions during the OAE 2 interval (e.g. Bonarelli Level in Europe), some parts of the southern Western Interior Seaway recorded relatively organic-lean sediments deposited during oxygenated conditions during OAE 2 (e.g. Meyers, 2007; Eldrett et al., 2014). On Demerara Rise 'black shales' occur throughout the Albian-Santonian stages and are not limited to the OAE 2 level (Erbacher et al., 2004; Shipboard Scientific Party, 2004; Meyers et al., 2006).

The Cenomanian-Turonian OAE 2 is globally also marked by changes in assemblages of planktonic and benthonic calcareous microbiota such as foraminifers and ostracods, as well as dinoflagellates, nannofossils and, locally, radiolarians (Jarvis et al., 1988; Erba, 2004; Musavu-Moussavou et al., 2007; Coccioni et al., 2016; Falzoni et al., 2016, Eldrett et al., 2017). In northern Europe, invasion of boreal 'pulse faunas', including the belemnite species *Praeactinocamax plenus*, was a feature of the early to mid-phase of OAE 2, suggesting at least regional cooling; this is also reflected in increases in bulk oxygen-isotope values of enclosing chalks signifying a fall in surface-water temperatures (Lamolda et al., 1994; Gale and Christensen, 1996; Jenkyns et al., 2017). This so-called Plenus Cold Event was also registered in the western Atlantic and at the southern end of the Western Interior Seaway by invasion of boreal dinoflagellates (Eldrett et al., 2014; van Helmond et al., 2014),

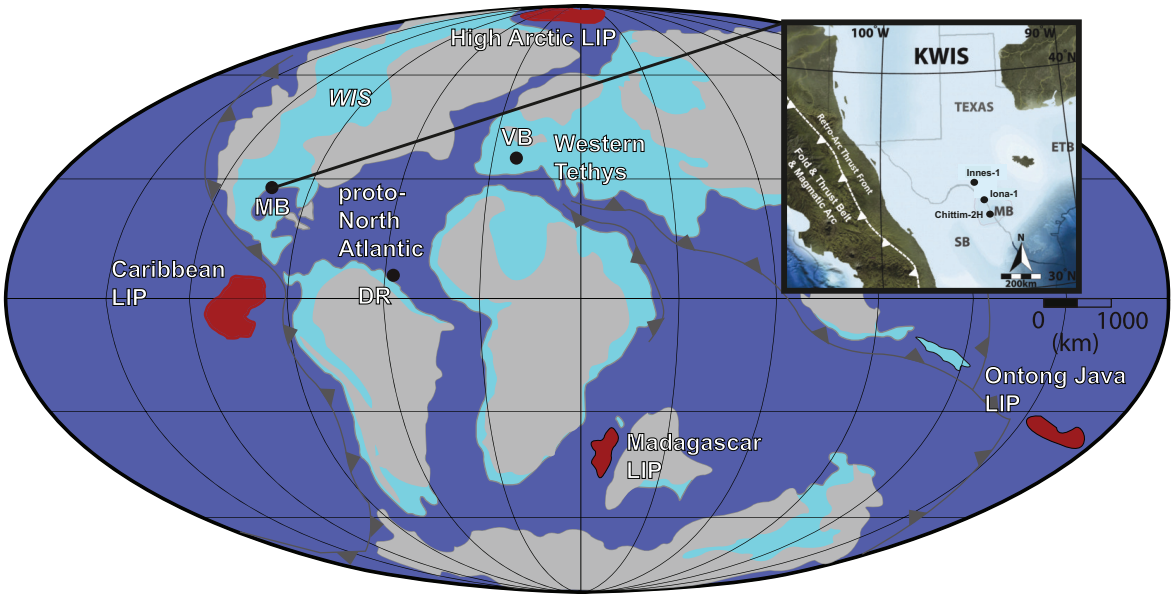

Figure 4.1: Map showing the positions of the Caribbean, High Arctic and Madagascar LIPs during the Cenomanian-Turonian time interval, as well as the Central American Seaway (CAS), Maverick Basin (MB), Demerara Rise (DR) and the Vocontian Basin (VB). Light blue shading indicates shallow marine, dark blue indicates deep-marine and grey indicates terrestrial environments. Dark grey lines with chevrons indicate a convergent margin. This figure includes a close-up of the Cretaceous Western Interior Seaway (top right) displaying the position of the Maverick Basin cores (SB-Sabinas Basin; ETB-East Texas Basin; Figure modified after Du Vivier et al., (2014) and Eldrett et al., (2014)).

as well as by falls in temperature in the proto-Atlantic determined by the organic geochemical TEX_{86} proxy (Forster et al., 2007; Sinninghe Damsté et al., 2010). The global nature of the Plenus Cold Event is signified by a drop in pCO_2 reconstructed from organic geochemical proxies, stomatal indices of fossil leaves, and the relative difference between changes in carbonate and organic-carbon isotopes (Kuypers et al., 1999; Barclay et al., 2010; Jarvis et al., 2011). Overall, the pattern of extinctions and originations, also involving macrobiota such as ammonites and bivalves, is significant enough to have originally defined the Cenomanian-Turonian stage boundary (Jarvis et al., 1988).

The global carbon cycle was also perturbed during the Mid-Cenomanian Event (MCE), which is marked by around a 1 ‰ positive carbon-isotope excursion in carbonates. The size of this excursion is slightly smaller, and shorter in duration, than the ∼2-3 ‰ positive CIE recorded during OAE 2 (Jarvis et al., 2006; Joo and Sageman, 2014; Eldrett et al., 2015a; Gambacorta et al., 2015). Integrated astronomical age models from the Western Interior Seaway date the onset of the MCE to 96.57 ± 0.12 Ma, the peak of the first MCE carbon isotope excursion known as MCE 1a at

96.49 $\pm$ 0.15 Ma and the end of the MCE to 96.36 $\pm$ 0.12 Ma (Eldrett et al., 2015a; Batenburg et al., 2016). Comparatively, age models from the Western Interior Seaway for OAE 2 estimate the start of the initial carbon isotope excursion at around 94.65 $\pm$ 0.12 Ma and the duration of the whole OAE between 0.52 Myr and 0.71 Myr. This duration can, however, be extended to 0.92 Ma following a more inclusive interpretation of the isotopic onset of the event (Sageman et al., 2006; Ma et al., 2014; Eldrett et al., 2015a).

Sections of mid-Cenomanian age in the Western Interior Seaway and equatorial Atlantic show a modest increase in values of total organic carbon (TOC) during the MCE, suggesting that accelerated global organic-matter burial also drove the positive carbon-isotope excursion during this event (Figure 4.2; cf. Friedrich et al., 2009). Like OAE 2, the MCE was also typified by changes in assemblages of benthic and planktonic foraminifers and radiolarians (Coccioni and Galeotti, 2003). Equally, carbonate sections recording the MCE show the presence, in brachiopod calcite, of relatively heavy oxygen-isotope ratios that suggest cooling, and are locally accompanied by boreal 'pulse faunas' including the belemnite *Praeactinocamax primus*, the form ancestral to *Praeactinocamax plenus* (Paul et al., 1994; Gale and Christensen, 1996; Mitchell and Carr, 1998; Voigt et al., 2004). Nd-isotope evidence suggests a climatically controlled reorganization of water masses during both the MCE and OAE 2, at least in northern European and adjacent areas (Zheng et al., 2016). Detailed geochemical studies (iodine:calcium ratios of pelagic carbonates and iron-speciation studies of interbedded organic-rich black shales) of one section in Marche-Umbria, Italy, suggest that both subsurface and bottom waters were characterized by relatively low dissolved oxygen contents in the interval between the MCE and OAE 2 (Owens et al., 2017), but there are no significant carbon-cycle events except for a minor positive CIE recorded in the English Chalk named the 'Jukes-Browne Event'. This event can be correlated with a similar small-scale feature in the Western Interior Seaway (Jarvis et al., 2006; Joo and Sageman, 2014).

Extensive volcanic activity and the subaqueous emplacement of Large Igneous Provinces (LIPs) (Caribbean, High Arctic, Madagascar and Ontong-Java LIPs: Fig-

ure 4.1) have previously been suggested to be responsible for the initiation of OAE 2 and the MCE. The most significant evidence for volcanism during OAE-2 is a distinct shift towards unradiogenic osmium-isotope ratios, which predates the onset of the Cenomanian-Turonian positive CIE by c. 100 kyr and suggests that a major pulse of volcanism and associated seafloor hydrothermal weathering began just prior to its onset (Figure 4.6; Orth et al., 1993; Snow et al., 2005; Turgeon and Creaser, 2008; Tegner et al., 2011; Du Vivier et al., 2014, 2015; Jenkyns et al., 2017)). The associated, potentially large-scale, release of greenhouse gases and other compounds is suggested to have resulted in the initiation of a number of catastrophic and interconnected oceanographic and climatic changes (Erbacher et al., 2001; Blättler et al., 2011; Pogge von Strandmann et al., 2013; van Helmond et al., 2013). However, the dynamic nature and spatial heterogeneity of the responses to volcanism at the time of OAE 2 are poorly constrained. For example, decreases in redox sensitive trace metals throughout large areas of the Western Interior Seaway indicate it may have become de-stratified and ventilated during OAE 2 despite water column stratification and stagnation occurring in many other parts of the global oceans (Eldrett et al., 2014; 2016). Furthermore, palynological assemblages display increases in gymnosperms through the Plenus Cold Event interval, possibly reflecting a transition from mega-thermal to meso-thermal vegetation and potentially indicating a period of climatic cooling rather than an increased hydrological cycle (Van Helmond et al., 2014; Eldrett et al., 2017).

Thus far, linking the initiation of OAE 2 to a specific magmatic event has relied on the temporal coincidence of LIP emplacement (Caribbean, High Arctic, Madagascar and Ontong-Java LIPs: Figure 4.1) with proposed environmental changes. However, tentatively changing lead-isotopic ratios in marine strata that record OAE 2 at Gorgo a Cerbara (Marche-Umbria, Italy) show a shift towards values associated with the Caribbean and Madagascar LIPs, in addition to mid-ocean ridge basalts (MORB) (Kuroda et al., 2007). Alternatively, if the invasion of boreal biota during the Plenus Cold Event involved the southward movement of water masses, the Arctic LIP may have been an important source for observed geochemical changes in marine sediments (Zheng et al., 2013).The High Arctic LIP (HALIP) formed between 130-80

Ma, after the Jurassic opening of the Canada Basin (tholeiitic; 130-80 Ma) and prior to the continental rift magmatism of the Lincoln Sea (alkaline; 85-60 Ma) (Brown et al., 1987; Bailey and Rasmussen, 1997; Estrada and Henjes-Kunst, 2004; Estrada, 2015; Evenchick et al., 2015; Davis et al., 2017). The magmatic successions of the HALIP are observed in the Canadian Arctic Islands, Svalbard, Franz Josef Land, Chukchi, Barents Shelf, Alpha-Mendeleev Rise and in North Greenland (also see Maher, 2001; Tarduno et al., 1998; Buchan and Ernst, 2006).

Mercury (Hg) enrichments in sedimentary successions are increasingly showing promise as a tracer for major volcanic events in the past. Events studied include the end-Permian, end-Triassic, Early Toarcian and end-Cretaceous global environmental perturbations, with Hg spikes linked to the Siberian Traps, the Central Atlantic Magmatic Province, the Karoo-Ferrar igneous province and the Deccan Traps, respectively as well as some Palaeozoic LIPs (e.g., Sanei et al., 2012; Grasby et al., 2013; Sial et al., 2013; Percival et al., 2015; 2016; 2017; Thibodeau et al., 2016). Mercury is strongly enriched in volcanic emissions, which are one of the major natural sources of Hg to the troposphere and stratosphere (Pyle and Mather, 2003). Volcanic Hg is mostly emitted as gaseous elemental mercury (GEM) with other forms of gaseous Hg and particulate Hg representing a minor component (Bagnato et al., 2007; Witt et al., 2008). The atmospheric residence time of GEM is 0.5-2 years (Slemr et al., 1995; Lindqvist and Rodhe, 1985), significantly longer than many other volcanic metals emitted as aerosols and particles, which typically have residence times on the order of a few weeks (Jaenicke, 1980; Schroeder and Munthe, 1998; Hinkley et al., 1999; Mather et al., 2003). Volcanic Hg therefore has a greater likelihood of global dissemination in the atmosphere than most other volcanic trace metals.

In the modern environment Mercury (Hg) is a ubiquitous environmental contaminant that originates from natural and anthropogenic sources (Fitzgerald et al., 2007). Direct atmospheric deposition is the primary source of Hg to the ocean whereas riverine discharge, mobilization from sediments, groundwater and submarine hydrothermal inputs contribute lesser amounts (Mason et al., 2012). The majority of atmo-

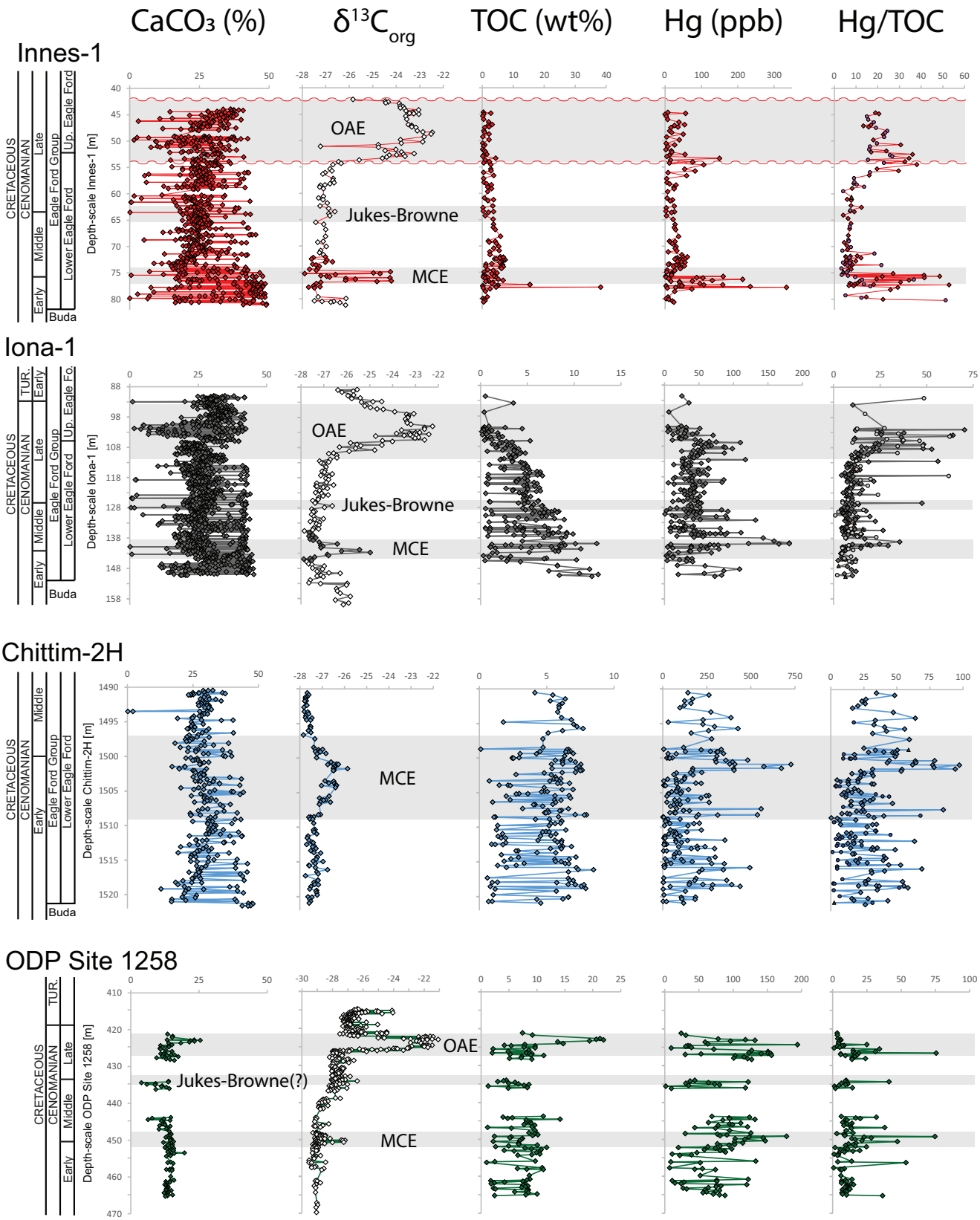

Figure 4.2: Data from the Western Interior Seaway and Demerara Rise: Innes-1, Iona-1, Chittim-2H and Site 1258. Ca (%; this study), $\delta^{13}C_{org}$ (‰; full colour markers indicate results from this study; Innes-1 empty markers indicate data from Eldrett et al., (2015a) and Eldrett et al., (2017); Innes-1 undulating red lines indicate unconformity following Eldrett et al., (2017); Iona-1 empty markers indicate data from Eldrett et al., (2014); Site 1258 empty markers indicate data from Erbacher et al., (2005), TOC (wt%; this study), Hg (ppb; this study) and Hg/TOC (ppb/wt%; this study; circle markers indicate limestones, diamond markers indicate marlstones and triangle markers indicate bentonites).

spheric emissions are anthropegenic (Fitzgerald et al., 1998; Amos et al., 2013) and emissions are hypothesized to increase during the next century (Hammerschmidt, 2011; Kocman et al., 2013; Pirrone et al., 2010; Streets et al., 2009). Mercury exists as four primary chemical species in seawater: mercuric ion (Hg(II)) and monomethylmercury (MMHg, CH3Hg+) in complexes with onorganic and organic ligands as well as elemental Hg (Hg0) and dimethylmercury (DMHg, (CH3)2Hg), which are dissolved gases. Each of these species are hypothesized to be linked through the Hg(II) pool (Hg(II) reduction occurs to such an extent that Hg0 estuarine and marine surface waters is usually supersaturated with respect to the atmosphere, leading to evasion (Andersson et al., 2011). Moreover, in situ methylation of Hg(II) is an important source of MMHg and DMHg in many marine ecosystems (Balcom et al., 2004; Hammerschmidt and Fitzgerald, 2006a; Sunderland et al., 2009; Hollweg et al., 2010; Cossa et al., 2011). MMHg is the bioacumulative species of Hg that is present throughout the marine water column (Hammerschmidy and Bowman, 2012; Heimburger et al., 2010).

In modern marine environments, hydrothermal inputs constitute comparitively small fluxes, ¡20% modern atmospheric inputs, and can be dispersed in plumes 10-100s km in lateral extent, with their size and shape dependent on the prevailing oceanic currents (Mason et al., 2012; Bowman et al., 2015). Nearfield removal of Hg from vents also may occur due to precipitation of sulfides and/or oxides, as found for Fe, Mn and other metals that complex strongly with sulfide (German and Von Damm, 2004). Such removal is also supported by local enrichment of Hg in hydrothermal associated deposits and sediments (e.g. Dekov, 2007). If elemental Hg (Hg0) were released from hydrothermal vents it might be transported over longer distances due to a slower rate of oxidation in cold, dark waters (Stoffers et al., 1999; Amyot et al., 2005).

Once mercury has entered the ocean a number of biotic and abiotic processes may affect it, often resulting in the formation of organic-Hg complexes. Consequently, mercury is typically adsorbed onto organic matter when deposited in sediments. In modern environments this relationship results in a roughly constant Hg/TOC ratio

(Benoit et al., 2001; Outridge et al., 2007; Gehrke et al. 2009; Liu et al., 2012; Ruiz and Tomiyasu, 2015). In sulphide-rich waters, the precipitation of Hg-sulphide complexes may result in rapid burial of Hg on a scale of weeks to months (Benoit et al., 1999; Niessen et al., 2003).

Due to the relative infancy of Hg as a proxy there are limits to our current understanding of it. Little is presently known about a number of factors which may effect the expulsion of Hg from volcanoes and its concentration in organic sediments. These factors include: 1. the difference between mercury expulsion from explosive versus effusive volcanic events; 2. the impact of magmatic intrusions through organic rich sediments on mercury expulsion during volcanic events; and 3. the effects of thermal maturation of organic sediments on mercury concentrations in sedimentary successions.

Here this study examines Hg concentrations in sedimentary successions spanning the Mid-Cenomanian to Early Turonian interval, to further constrain the role of LIP volcanism in initiating climatic and oceanographic change during the Mid-Cenomanian Event and the Cenomanian-Turonian OAE 2. To this end, this study presents the first Hg data for these time intervals, from three sedimentary archives in the Southern Western Interior Seaway and one in the equatorial North Atlantic Ocean (Demerara Rise). This study compares the Hg/TOC data with published neodymium-isotope data (εNd(t)) from Demerara Rise and osmium isotope data ($^{187}Os/^{188}Os$) from the Vocontian Basin, NW Tethys Ocean, as well as with palaeoceanographic models reconstructing dominant palaeo-current directions. This study uses these various lines of evidence to assess the most likely volcanic source of the Hg, its timing and its mode of transport.

4.2 Geological Setting

This study presents data from samples from four marine mudstone successions spanning the Mid-Cenomanian to Early Turonian interval. Three of the sequences are cores (Innes-1, Iona-1 and Chittim-2H) which sample the Eagle Ford Group (Bo-

quillas Formation) in the Southern Western Interior Seaway (Maverick Basin, Texas, USA, Figure 4.1). The sequences comprise metre-scale marlstone-limestone couplets deposited in a distal, clastic-sediment starved, intra-shelf basin along the retro-arc foreland basin of western North America (with a suggested palaeowater depth of around 50-100 m) (Pessagno, 1969; Eldrett et al. 2014; Denne et al., 2014; Lowery et al., 2014; Eldrett et al., 2015b). Bentonites occur commonly throughout the sedimentary succession of the Western Interior Seaway cores (Eldrett et al., 2014; Figure 4.2) and are thought to represent geologically instantaneous massive Plinian eruptions from the Western Cordilleran convergent margin, a site of abundant Late Cretaceous felsic magmatism that resulted in intrusive batholiths and plutons (e.g. Burchfiel et al., 1992; Allmendinger, 1992; Bird, 1998; Dickinson, 2001; Desmares et al., 2007), as well as extrusive features that injected 10s to 100s km^3 of ash into the atmosphere (Sellards et al., 1932). This ash was transported downwind to the east and eventually covered large portions of North America and the adjacent oceans (e.g. Sellards et al., 1932; Burchfiel et al., 1992; Allmendinger, 1992). The bentonites typically form thin beds (mm to cm thick) correlatable for 100s to 1000s km (Eldrett et al., 2015a) and their contacts tend to be sharp although biological reworking and sea currents have led to some modification.

The fourth core (from ODP Site 1258) is located on the northwest-facing slope of the Demerara Rise, off Suriname (South America; Figure 4.1), where the sediments were deposited at the southern edge of the proto-North Atlantic Ocean, a semi-enclosed basin with its long axis roughly perpendicular to the direction of the persistent trade winds (Trabucho Alexandre et al., 2010). The proto-North Atlantic was connected to the Pacific Ocean through the Central American Seaway, which separated North and South America (Figure 4.1). The stratigraphy of this core is represented by laminated high-TOC mudstones, characterized by TOC values of 5-10% (and up to 29% around the OAE 2), phosphatic nodules and well-preserved fish-debris (Erbacher et al., 2005; Friedrich et al., 2006, 2009; Hetzel et al., 2009).

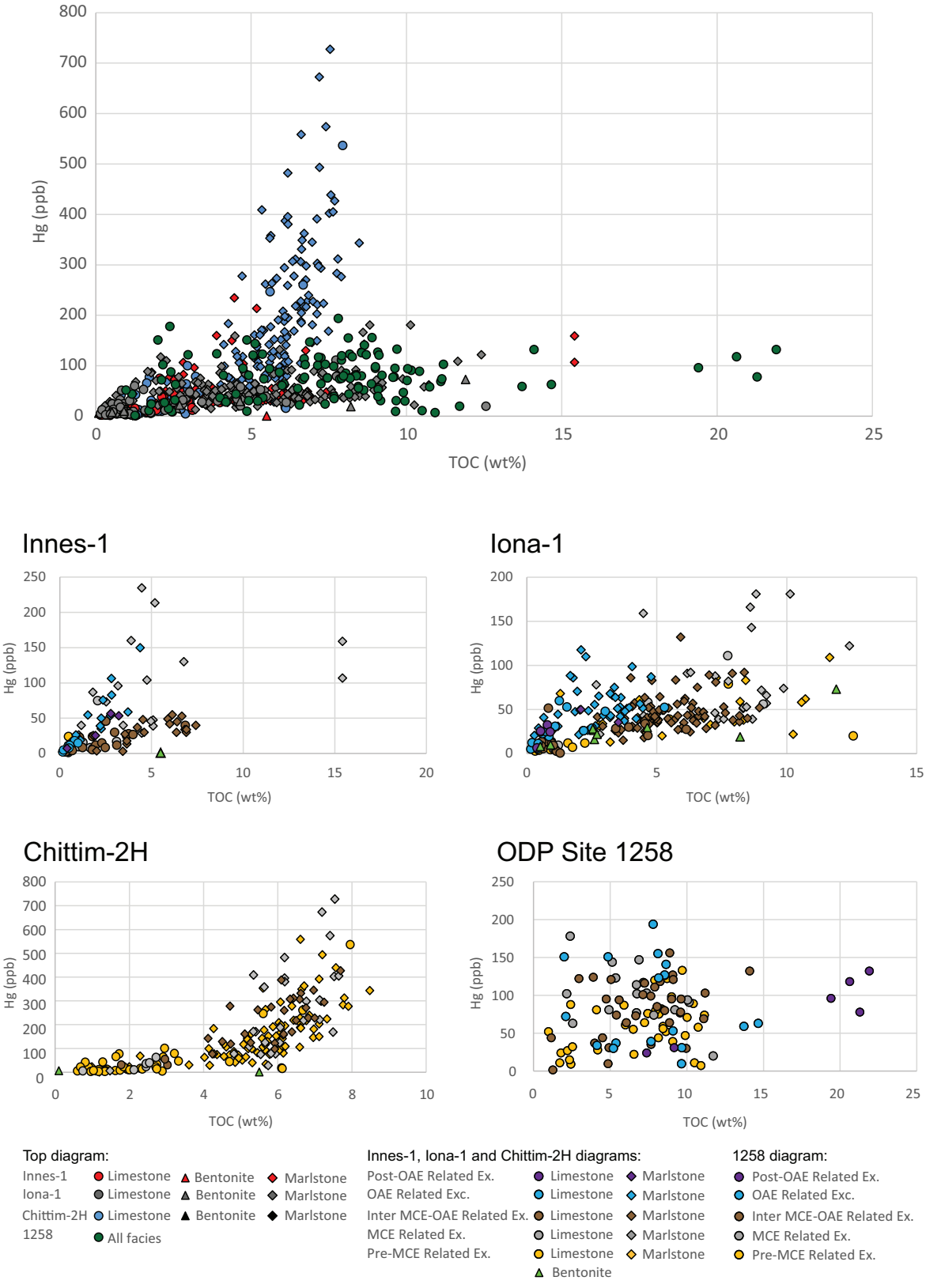

Figure 4.3: Data from the Western Interior Seaway and Demerara Rise plotting Hg (ppb) against TOC (wt%). Top figure shows data from Innes-1, Iona-1, Chittim-2H and ODP Site 1258. Bottom four figures show Hg (ppb) against TOC (wt%) for each individual core and separated for the stratigraphic intervals spanning the Pre-MCE, MCE, Inter-Excursion Period, OAE 2, and Post-OAE 2.

4.3 Analytical Methods

4.3.1 Mercury Analyses

Sedimentary mercury concentrations (Figure 4.2) were measured using 50±5 mg of powdered sample with a Lumex RA-915 Portable Mercury Analyzer coupled to the PYRO-915 Pyrolyzer (as described by Bin et al. 2001). Fifteen peat-standard samples (NIMT/UOE/FM/001 - Inorganic Elements in Peat) with a Hg concentration of 169±7 ppb, were used to calibrate the Lumex prior to each run and to estimate external reproducibility. Mercury concentrations were then subsequently normalized against % TOC to correct for the efficient complexation of Hg to organic matter.

4.3.2 Organic-Carbon Isotope Analysis ($\delta^{13}C_{org}$)

Previous studies on the Innes-1 and Iona-1 cores generated well-defined $\delta^{13}C_{org}$ records for OAE 2, but only low-resolution signatures across the Mid-Cenomanian Event (MCE) (Eldrett et al., 2014, 2015a, 2016). Additional measurements were undertaken to increase the data resolution across the MCE interval for these cores (Figures 4.2 and 4.3). Furthermore, a new $\delta^{13}C_{org}$ curve is presented from the Chittim-2H core. This core was drilled and recovered from the central part of the Maverick Basin and records the MCE in a more expanded section than those in the Innes-1 and Iona-1 cores. Sample density in these three cores varies between 10 and 20 cm. One gram aliquots of homogenized sample powder were decarbonated with 40 ml cold 3M HCl and were subsequently rinsed four times with distilled water to reach neutral pH. About 1 to 15 mg, depending on TOC concentration, of oven-dried and powdered decarbonated sample residue was weighed into 8x5 mm tin capsules for $\delta^{13}C_{org}$ analyses. The analyses were performed at the Stable Isotope Laboratory at the Open University, Milton Keynes using a Thermo Flash HT elemental analyzer coupled to a ThermoFinnigan MAT 253. Accuracy of carbon-isotope ratios on the Vienna Pee Dee Belemnite (VPDB) scale were ensured by applying a three-point calibration using IAEA-CH-6 sucrose, NIST8573 glutamic acid and IR-

041 alanine. The reproducibility determined from these standards was $<$0.1 ‰ (1 S.D., n=23).

4.3.3 Rock-Eval and Coulomat TOC analyses

Total carbon (TC) and total inorganic carbon (TIC) were determined for samples from Site 1258 with a Strohlein Coulomat 702 Analyzer (Figure 4.2, 4.3; see details in Jenkyns, (1988)). For TC and TIC analyses, sample aliquots were measured, with one aliquot having been heated overnight at 450℃ to remove organic matter. Total organic carbon (TOC) was calculated as the difference between TC and TIC. The long-term average value and reproducibility of TOC measurements on the in-house SAB134 standard is 2.95 $\pm$0.14 wt% (2 S.D., n = 27).

For all remaining Eagle Ford samples (cores Innes-1, Iona-1 and Chittim-2H), TOC was measured by Rock-Eval pyrolysis on a Rock-Eval VI standard instrument with pyrolysis and oxidation ovens. Laboratory procedures as described in Behar et al. (2001) were used. Quality control was provided by the in-house SAB134 standard and the certified IFP160000 standard, which were regularly run between samples. The reproducibility of TOC analyses of the in-house SAB134 and the reference IFP160000 standards are, respectively, $\pm$0.22% and $\pm$0.08% (2 S.D.). The long-term average TOC values of SAB134 standard and IFP160000 are 2.98 % and 3.27 %, respectively.

4.3.4 ICP-MS

New samples were analysed for major elements and trace metals using Inductively-Coupled Plasma Mass Spectroscopy (ICP MS) and Optical Emission Spectroscopy (OES) at Chemostrat Ltd, UK. To evaluate the redox state (Figure 4.4), the concentrations of redox-sensitive trace metals were determined, in particular, molybdenum (Mo) and vanadium (V), both of which have been widely used to infer paleo-redox conditions in modern and ancient sediments (Brumsack, 2006; Tribovillard et al., 2006; Algeo et al., 2012). These redox-sensitive trace metals show variable solubil-

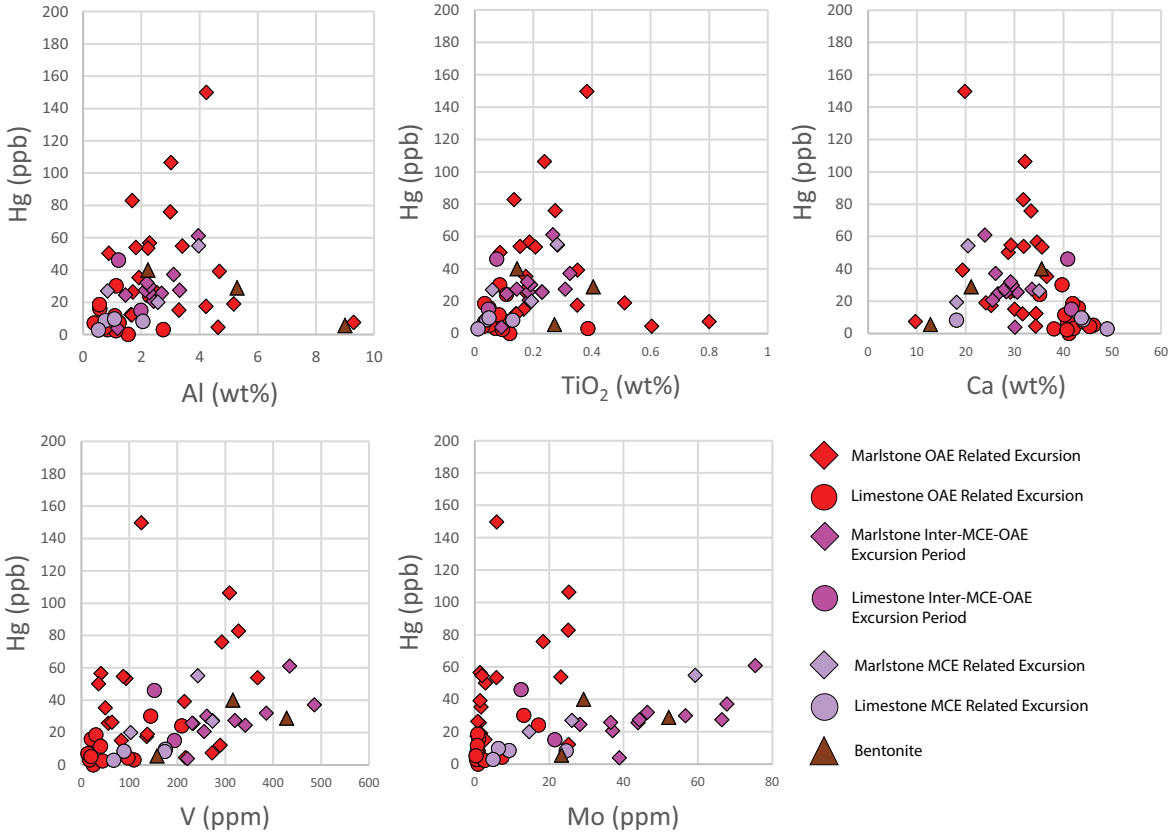

Figure 4.4: Data from Innes-1 showing cross-plots between Hg (ppb; this study) and Al, TiO_2, Ca, V and Mo (Eldrett et al., 2017). Data is split following three stratigraphic intervals spanning the MCE, OAE 2, and the Inter-Excursion Period.

ity with redox state, resulting in authigenic enrichments in oxygen-depleted sedimentary environments. To investigate the influence of changing detrital input, aluminium (Al) and titanium oxide (TiO_2) were used to normalize the data (Figure 4.4), as they are commonly utilised as a proxy for terrigenous detrital material due to their relative chemical inertness and lack of biological uptake (Brumsack, 2006; Tribovillard et al., 2006; Algeo et al., 2012).

4.4 Results

4.4.1 New Carbon-Isotope Stratigraphy of the MCE

This study presents new $\delta^{13}C_{org}$ from the Chittim-2H core and high-resolution data across the Mid-Cenomanian Event for the Innes-1 and Iona-1 cores (Figure 4.2). The $\delta^{13}C_{org}$ isotope record of Chittim-2H is characterized by an overall positive iso-

topic excursion (1508.3-1496.2 m) containing two key positive excursions of circa 1.3 ‰ (1505.77-1503.28 m) and 1.4 ‰ (1503.28-1499.37 m), reflecting MCE 1a and 1b (Figure 4.2). The $\delta^{13}C_{org}$ isotope record of Innes-1 is characterized by a series of positive excursions (between 77.51-72.19 m) specifically two key excursions of ∼1.9 ‰ (at approximately 76.63 m) and 2.1 ‰ (at ∼74.89 m), also reflecting MCE 1a and 1b. The previously published data of Iona-1 (Eldrett et al., 2015a) are similar to the new Innes-1 data, with two clear positive excursions of 1-1.5 ‰ at 142.71 m and 139.86 m which could be interpreted as MCE 1a and 1b, respectively. Further to this, these chemostratigraphic markers match the previously published biostratigraphy of Innes-1 and Iona-1, where the positive CIE of the MCE of both cores are bracketed by the highest occurrence of *Rotalipora brotzeni* and the lowest occurrence of *Helvetoglobotruncana praehelvetica* (Eldrett et al., 2015a, 2017).

4.4.2 Hg/TOC: Eagle Ford

4.4.2.1 Hg/TOC: Eagle Ford MCE Excursion

All three Western Interior Seaway cores show evidence of Hg and Hg/TOC excursions around the same stratigraphic level as the MCE. Chittim-2H, shows the largest Hg/TOC excursion in terms of absolute Hg/TOC magnitude, beginning at 1503.91 m and continuing up to circa 1499.95 m (Figure 4.2). However, it should be noted that these values are above a baseline outside the MCE level stratigraphy with relatively scattered data points. At Chittim-2H the Hg/TOC ratio values reach highs of 94, 97 and 78 ppbHg/wt%TOC at 1500.26, 1500.89 and 1501.45 m, respectively, and the Hg/TOC ratios remain greater than 20 ppbHg/wt%TOC between 1502.12 m and 1499.95 m.

Innes-1 shows the second largest MCE-related Hg/TOC excursion in terms of absolute Hg/TOC magnitude, occuring from 79.63 m to 75.09 m with highs of 53, 30, 36, 41,48, 41 and 27 ppbHg/wt%TOC occurring at 77.51, 77.1, 76.63, 76.28, 75.96, 75.74 and 75.46 m, respectively (Figure 4.2). Between each relative maximum, Hg/TOC values drop by, on average, 17 ppbHg/wt%TOC, giving this excursion a

slightly scattered appearance. Although low TOC values lead to some spikes in Hg/TOC below the sediments associated with the MCE, at 75.09 m Hg/TOC values drop to 5 ppbHg/wt%TOC and remain predominantly lower than 20 ppbHg/wt%TOC up to the level of the OAE-2 Hg/TOC excursion (section 4.4.2.2).

Iona-1 records the smallest MCE-related Hg/TOC excursion of the three studied cores in the southern Western Interior Seaway, beginning at circa 141 m and continuing up to $\sim$135.7 m. Maximum values of 29, 36 and 23 ppbHg/wt%TOC are reached at 140.2, 139.0 and 137.4 m, respectively. Between 139.8 m and 137.8 m Hg/TOC values remain above 20 ppbHg/wt%TOC. Prior to the MCE Hg/TOC excursion, Hg/TOC values remain lower than 12 ppbHg/wt%TOC. Above the MCE-related Hg/TOC excursion, in the interval between the MCE and OAE 2, the signal is more erratic than Innes-1 with at least 2 Hg/TOC spikes $>$30 ppbHg/wt%TOC.

4.4.2.2 Hg/TOC: Eagle Ford OAE 2 Excursion

Although the Iona-1 Hg/TOC signal shows a degree of scatter, both Innes-1 and Iona-1 contain Hg and Hg/TOC excursions which precede and continue through part of the positive CIE of OAE 2 (Figure 4.2; see 4.4.2.3). Iona-1 shows a number of large Hg/TOC excursions beginning at $\sim$112.6 m and persisting up to $\sim$101.6 m (Figure 4.2). Over this 11 m section there are six noteworthy peaks: at 112.4 m, 108.4 m, 107 m, 105.6 m, 104 m and 102.2 m, which reach Hg/TOC ratios of 56, 53, 49, 46, 63 and 71 respectively. Between each of these excursions Hg/TOC ratio values decrease to less than 15 ppbHg/wt%TOC. Stratigraphically above the OAE 2 interval there are few data points, but Hg/TOC ratios generally decrease to less than 10 ppbHg/wt%TOC.

Innes-1 shows a slightly smaller Hg/TOC excursion than Iona-1, which extends from $\sim$56.6 m to $\sim$47.2 m (Figure 4.2). Hg/TOC values increase from $\sim$8 in the interval below OAE-2, remain generally higher than 20 between 55.35 m and 52.13 m, and reach highs of 30, 38, 32, 34, 36 and 30 ppbHg/wt%TOC at 55.74, 54.55, 54.22, 53.33, 52.6 and 50.77 m, respectively. Above OAE-2, Hg/TOC ratios decrease to

approx. 13 ppbHg/wt%TOC, rising to ∼20 from 47.1 m to the 44.62 m.

4.4.2.3 Hg/TOC: Eagle Ford Hg/TOC Lag

The Hg/TOC excursions in the Iona-1 and Innes-1 cores appear to display contrasting behaviour in terms of their stratigraphic relationships with the MCE-related CIEs. The Hg/TOC excursion in Iona-1 occurs ∼4.9 m stratigraphically up-section from the onset of the corresponding CIE, whereas the onset of the MCE-related Hg/TOC excursion in Innes-1 precedes the onset of the CIE by up to 2.8 m of stratigraphy (Figure 4.2). These relationships indicate a significant offset between the start of the Hg/TOC excursions in the Innes-1 and Iona-1 cores.

With regard to OAE 2, the onset of the Hg/TOC excursions in both Innes-1 and Iona-1 stratigraphically precede the CIE by ∼2 m and ∼4 m, respectively, with the Hg/TOC excursions of both cores beginning at the same stratigraphic level. It should be noted that the irregularly defined Hg/TOC baseline between the MCE and OAE 2 in the Iona-1 core data complicate definition of the exact offset, which is further complicated by a stratigraphic unconformity at ∼54 m in Innes-1 (Eldrett et al., 2017).

4.4.2.4 Hg/TOC: Eagle Ford Baseline

Prior to the MCE-related Hg/TOC excursion, between 80.6 m and 79.63 m, Innes-1 has relatively high Hg/TOC values, with 50% of data points over 20 ppb Hg/wt%TOC with a single high data point of 51 ppbHg/wt%TOC recorded at 80.6 m (Figure 4.2). Between the top of the MCE Hg/TOC excursion and the base of the OAE-2 Hg/TOC excursions at 75.09 m and 55.6 m values remain below 20 ppbHg/wt%TOC, with the vast majority of values falling in the range 5-10 ppbHg/wt%TOC (Figures 2, 3 and 5).

In the Iona-1 core, Hg/TOC values remain consistently lower than 12 ppb Hg/wt%TOC below the MCE. Stratigraphically, between the levels recording the end of the MCE and onset of the OAE, Hg/TOC shows increases at 135.7 m and 112.6

m. Here, the curve is more erratic with data points at 135.2, 132.2, 126.2, 123.4, 119.9 and 117.2 m reaching 26, 22, 48, 24, 22 and 62 ppbHg/wt%TOC, respectively (Figure 4.2). However, 70% of Hg/TOC values remain below 10 ppbHg/wt%TOC and 90% remain below 15 ppbHg/wt%TOC (Figure 4.5).

The Hg/TOC curve of Chittim-2H has the most scattered data of the three cores. Stratigraphically above and below the MCE, Hg/TOC values continuously jump between $>$40 ppbHg/wt%TOC and $<$15 ppbHg/wt%TOC. A number of high Hg/TOC values are found at 151.82, 1511.84, 1508.18, 1507.3, 1498.7, 1497.2, 1495.7 and 1494.13 m with values of 69, 63, 68, 86, 59, 59, 56 and 64 ppbHg/wt%TOC, respectively, and lows of 5, 14, 5, 9, 10, 25, 31, 17 and 16 recorded in intervening levels (Figure 4.2).

4.4.3 Hg/TOC: Demerara Rise (ODP Site 1258)

4.4.3.1 Hg/TOC: Site 1258 MCE Excursion

High and variable Hg/TOC values occur stratigraphically below and above the MCE level. Superimposed on the background variability, the Site 1258 data are suggestive of a well-defined Hg/TOC excursion from 452.39-448.59 m, coinciding with the MCE positive CIE. Hg/TOC peaks of 47 and 75 ppbHg/wt%TOC occur at 450.59 and 449.18 m; between these peaks Hg/TOC values drop to 14 ppbHg/wt%TOC (Figure 4.2). The overall peak values occur in direct concert with a shift to more radiogenic εNd(t) values (Figure 4.6; Macleod et al., 2008; Jiménez-Berrocoso et al., 2010; Martin et al., 2012).

4.4.3.2 Hg/TOC: Site 1258 OAE 2 Excursion

The data from Demerara Rise suggest a Hg/TOC excursion around the OAE 2 positive CIE, which extends from 426.97 m to 423.59 m, reaching Hg/TOC highs at 426.62, 426.16 and 425.52 m of 75, 31 and 34 ppbHg/wt%TOC respectively (Figure 4.2). As with the MCE-related Hg/TOC excursion, peak values occur in direct

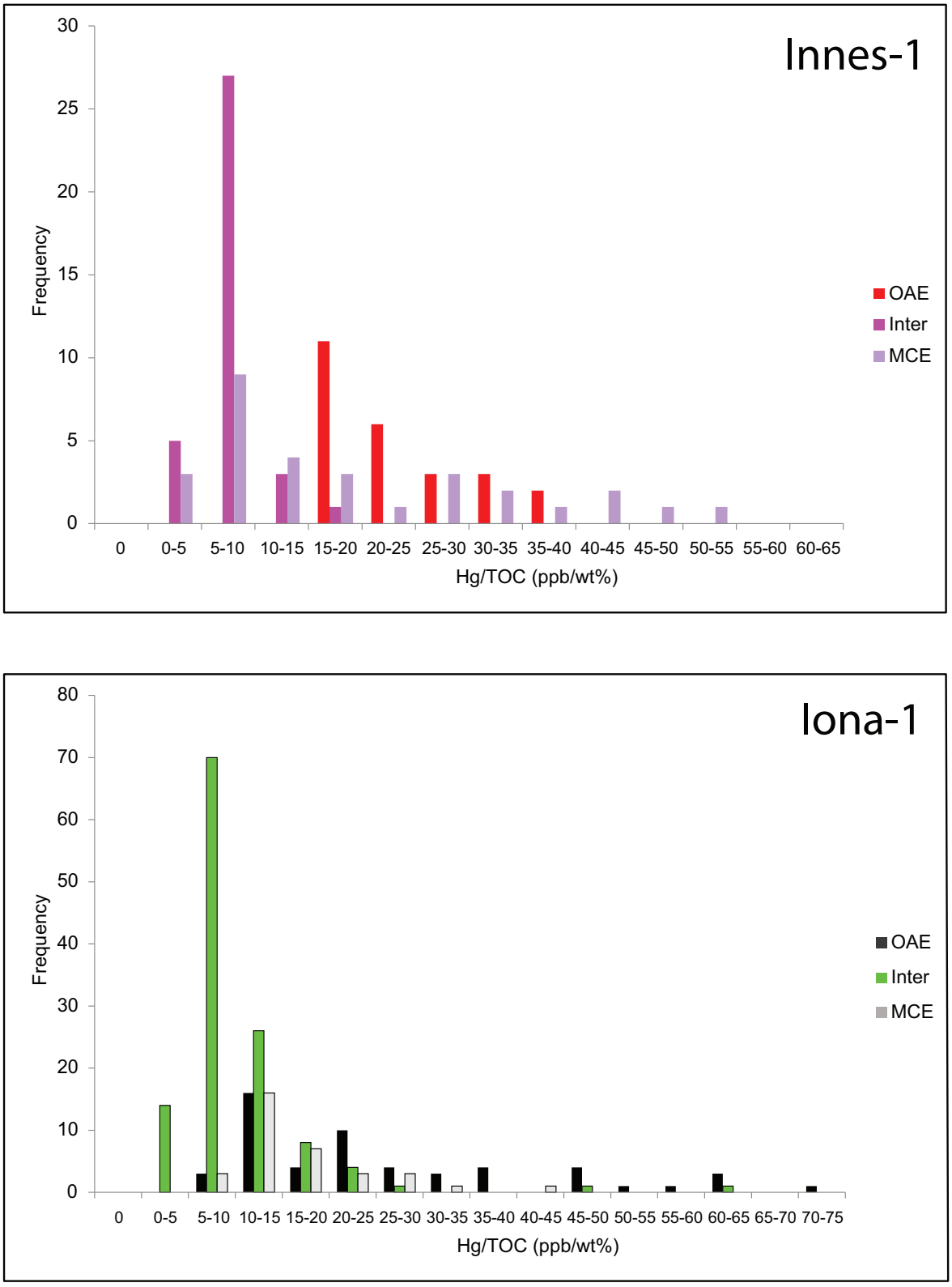

Figure 4.5: Histograms of the number of samples, from the Innes-1 and Iona-1 cores, occurring per succeeding bin of 5 ppbHg/wt%TOC class widths. Data have been split following the stratigraphic intervals spanning the MCE, OAE 2, and the Inter-Excursion Period.

concert with a shift to more radiogenic εNd(t) values (Macleod et al., 2008; Jiménez-Berrocoso et al., 2010; Martin et al., 2012), $\sim$0.7 m below the initiation point of the global positive CIE that characterizes OAE 2 (Figure 4.6).

4.4.3.3 Hg/TOC: Site 1258 Hg/TOC Lag

There is a stratigraphic lag between the peak of the MCE Hg/TOC excursion and the CIE, with peak Hg/TOC values post-dating the onset of the MCE 1b CIE (as defined by Friedrich et al. 2009), by $\sim$0.8 m (Figure 4.2). A stratigraphic lag also exists between the onset of the OAE 2 related Hg/TOC excursion and the onset of the associated positive CIE, the onset of the first preceding the latter by $\sim$0.7 m (Figure 4.2).

4.4.3.4 Hg/TOC: Site 1258 Baseline

Prior to the MCE, over 95% of the Hg/TOC data points at Site 1258 are below 15 ppbHg/wt%TOC with only two data points reaching over 20 ppbHg/wt%TOC. 80% of data points between the MCE and OAE 2 have values less than 15 ppbHg/wt%TOC and 87% less than 20 ppbHg/wt%TOC (Figure 4.2). Three anomalously high points of 38, 31 and 41 ppbHg/wt%TOC occur at 446.79, 443.98 and 434.38 m, respectively.

Importantly, all Hg/TOC excursions discussed here (sections 4.4.2 and 4.4.3) are based on increases in Hg concentrations and increases in Hg concentrations relative to TOC rather than decreases in TOC.

4.5 Discussion

4.5.1 Hg vs Major and Redox-sensitive Trace-Metal Concentrations

Changes in nutrient fluxes to the global ocean can lead to increases in marine primary productivity, enhancing the shuttling of carbon from the atmosphere and surface ocean to the sedimentary carbon reservoir, possibly increasing the preservation of organic matter and the potentially associated sequestration of Hg. Associated changes in the redox state of the water column and sedimentary poor-waters and especially the development of euxinic, H_2S rich water-column conditions may result in Hg sulphide precipitating in marine sediments (Sanei et al., 2012). These processes may have affected the rate of Hg sequestration in the past. In this study, changes in major elements and compounds of detrital sedimentary origin, which possibly broadly reflect changes in nutrient supply from landmasses into the marine realm, show no obvious links to mercury concentrations or their stratigraphic position related to the MCE and OAE 2 CIEs within the Innes-1 core (Figure 4.4). The increased supply of detritus-related minerals due to an intensified hydrological cycle during the MCE and OAE 2 likely accounts for the generally a poor correlation between Hg and Al and TiO_2 concentrations (Figure 4.4; Erbacher et al., 2001; Blättler et al., 2011; Pogge von Strandmann et al., 2013; van Helmond et al., 2013). Under anoxic and euxinic conditions higher concentrations of organic matter are preserved due to lower levels of aerobic biological activity in the water column or in the sedimentary poor-space (e.g. Demaison and Moore, 1980). Both Mo and V become enriched under very low oxygen and sulphidic conditions at the sediment-water interface or in the water column (e.g. Algeo and Maynard, 2004; Tribovillard et al., 2005; Tribovillard et al., 2006). Therefore, in low-oxygen, aquatic depositional environments where organic matter is accumulating, a positive correlation exists between redox-sensitive trace metal and Hg concentrations and TOC. The Hg concentrations throughout the Innes-1 core are generally lower in $CaCO_3$-rich limestone beds, because Hg readily binds with organic-compounds and therefore is more enriched in the relatively TOC-rich more marly facies.

The relative distribution of Hg vs redox-sensitive trace elemental concentrations (e.g. Mo and V) varies throughout the Innes-1 core (Figure 4.4). The OAE 2 interval is marked by relatively low redox-sensitive trace metal concentrations and relative high Hg concentrations, whereas the MCE and the inter-excursion period between the MCE and OAE 2 show reasonably strong positive correlations between Mo and V and Hg. This can be explained by: (a) strongly enhanced volcanogenic fluxes of Hg during OAE 2 relative to the fluxes of Mo and V into the sedimentary realm, (b) the strong facies control on sedimentary molybdenum and vanadium concentrations, with predominantly $CaCO_3$-rich facies during OAE 2 in the Innes-1 core resulting in low Mo and V values (less than 30 ppm V and less than 10 ppm Mo), (c) globally reduced Mo and V seawater concentrations during the MCE and OAE 2 due to global trace metal drawdown and the associated depletion of the marine trace-metal inventory, under conditions of expanding oxygen-depletion in geographically widespread regions (Hetzel et al., 2009; van Bentum et al., 2009; Eldrett et al., 2017; Jenkyns et al., 2017), and (d) relatively reduced sedimentary Mo and V concentrations throughout OAE 2 (Figure 4.4) due to a basinal oxygenation event related to open water-mass exchange (Eldrett et al., 2014; Eldrett et al., 2017).

4.5.2 MCE and OAE 2 Hg/TOC Excursions

Previous studies investigating Hg enrichments during global climatic perturbations have used such data to connect the events to LIP volcanism (Section 4.1). The four cores studied here show elevated Hg and Hg/TOC values in sediments deposited during the MCE and OAE 2. LIP volcanism (coeval LIPs shown in Figure 4.1) has been suggested as the initial trigger for the climatic and palaeoceanographic perturbations associated with OAE 2 (see section 4.5.3; Orth et al., 1993; Snow et al., 2005; Turgeon and Creaser, 2008; Tegner et al., 2011; Du Vivier et al., 2014, Du Vivier et al., 2015; Jenkyns et al., 2017). During past major global-change events, an increased flux of mercury to the global ocean-atmosphere system could also have been achieved by widespread wild res, large-scale volcanism, or release of thermogenic Hg from volcanism, or a bolide impact. Evidence for widespread

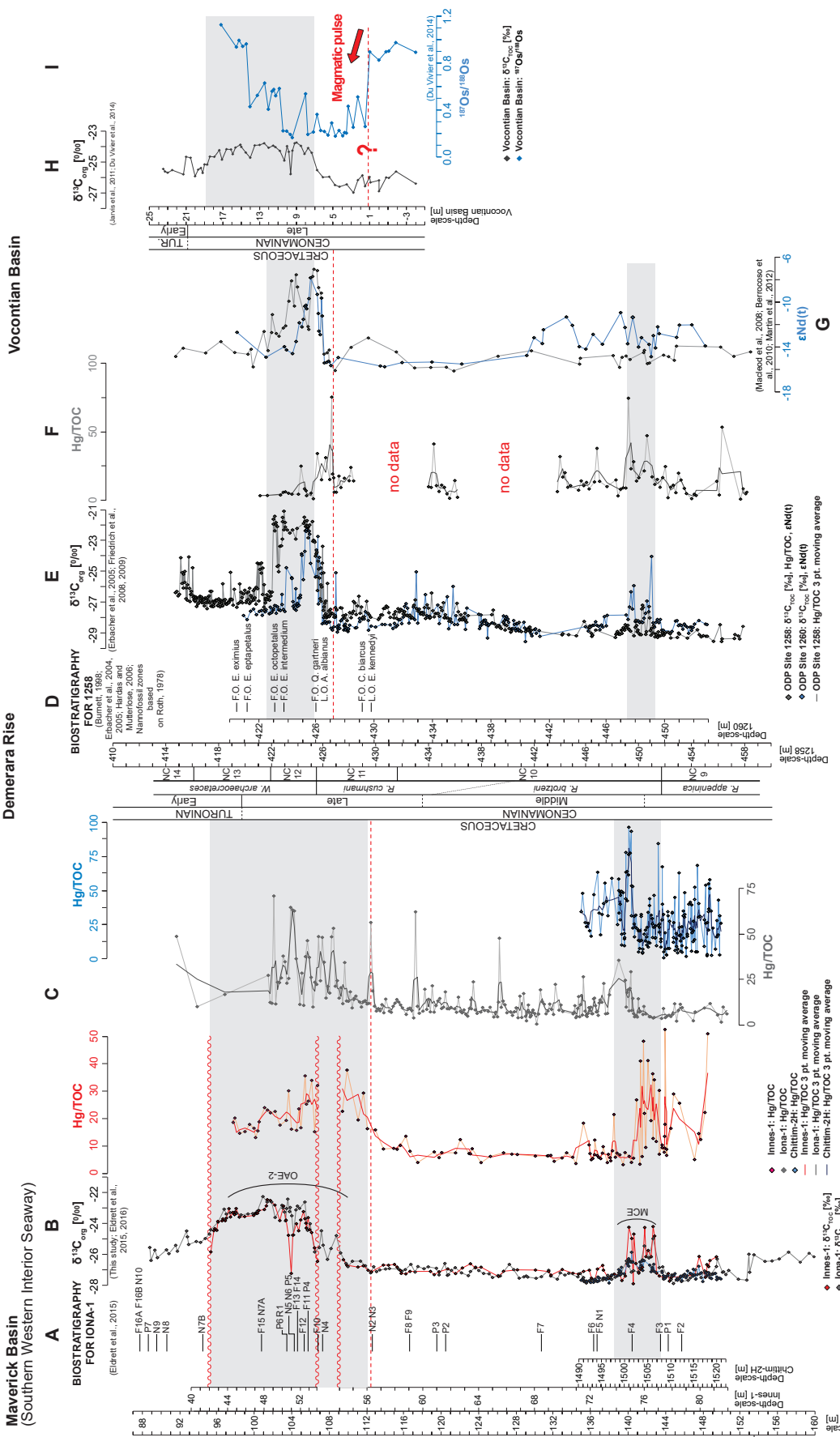

Planktonic Foraminifera Events: LO Rotalipora brotzeni=F2; LO Thalmanninella appenninica=F3; FO Whiteinella aprica=F4; FO Helvetoglobotruncana praehelvetica=F5; FO Rotalipora cushmani=F6; FO Whiteinella archaeocretacea=F7; FO cons. Rotalipora cushmani=F8; FO cons. Whiteinella archaeocretacea=F9; LO Rotalipora deeckei=F10; LO Thalmanninella greenhornensis=F11; LO Rotalipora cushmani=F12; FO Dicarinella hagni=F13; FO Guembelitria cenomana=F14; FAO Heterohelix reussi-moremani ("Heterohelix shift")=F15; FO Marginotruncana renzi=F16a; FO Marginotruncana schneegansi=F16b.
Calcareous Nannoplankton: FO Corollithion kennedyi=N1; ACME Corollithion kennedyi=N2; FO Gartnerago obliquum=N3; LO Axopodorhabdus albianus=N4; LO Corollithion kennedyi=N5; LO Cretarhabdus striatus=N6; LO Helenea chiastia (extrapolated)=N7a; LO Helenea chiastia (extrapolated)=N7b; FO Quadrum gartneri=N8; FO Eprolithus octopetalus=N9; FO ?Eprolithus eptapetalus=N10. Radiolarians: FAO Radiolarians=R1. Dinoflagellate Cysts: FCO Litosphaeridium siphoniphorum=P1; LSAO Bosedinia spp. cf. sp.1 and sp.3 of Prauss (2012b)=P2; LCO Cyclonephelium longispinatum=P3; FO Cyclonephelium membraniphorum=P4; LO Adnatosphaeridium tutulosum=P5; LO cons. Litosphaeridium siphoniphorum=P6; LO Adnatosphaeridium? Chonetum=P7. Where LO=last occurrence; LCO=last common occurrence; FO=first occurrence; FCO=first common occurrence; cons.=consistent occurrence.

Figure 4.6: Data from the Western Interior Seaway Innes-1, Iona-1 and Chittim-2H cores: (A) Biostratigraphy of the Iona-1 core. (B) $\delta^{13}C_{org}$ (this study; Eldrett et al., (2015a, 2017); Innes-1 undulating red lines indicate unconformity as adapted from Eldrett et al., (2017), illustrating a split in the Innes-1 depth scale due to a hiatus relative to Iona-1), (C) Hg/TOC (this study). Data from Demerara Rise ODP Sites 1258 and 1260: (D) Biostratigraphy of ODP Site 1258 (Burnett, 1998; Erbacher et al., 2004, 2005; Hardas and Mutterlose, 2006). Nannofossil zones are based on Roth (1978). (E) $\delta^{13}C_{org}$ [Erbacher et al., 2005; Friedrich et al., 2009], (F) Hg/TOC (this study), (G) εNd [Macleod et al., 2006; Jimnez-Berrocoso et al., 2010; Martin et al., 2012]. Data from the Vocontian Basin: (H) $\delta^{13}C_{org}$ (Jarvis et al., 2011), (I) $^{187}Os/^{188}Os$ (Du Vivier et al., 2014). The red dashed line marks the onset of the $^{187}Os/^{188}Os$ excursion attributed to a magmatic pulse and/or basalt-seawater interaction as recorded in the Vocontian Basin, and possible stratigraphic correlation to the Demerara Rise and Western Interior Seaway sedimentary archives.

wildfires, thermogenic emissions or subaerial LIP emplacement at the MCE and OAE 2 is, however, lacking (e.g. Alvarez et al., 1984; Pegram and Turekian, 1999; Kuroda et al., 2007; Turgeon and Creaser, 2008), and previous estimates of bolide impacts have suggested they would not provide enough Hg to the atmosphere to result in a significant Hg anomaly (Sial et al., 2014). Therefore the Hg/TOC excursions presented here may be taken as new evidence suggesting a significant flux of volcanically derived Hg and associated gasses and (toxic) compounds to the southern proto-North Atlantic (Demerara Rise) and the southern Western Interior Seaway (Maverick Basin) during these periods.

Results from the localities here studied show that Hg/TOC ratios are 10-100 times lower than found in most previous studies of other Mesozoic events (Sanei et al., 2012; Grasby et al., 2013; Percival et al., 2015; Thibodeau et al., 2016; Sial et al., 2016) with the possible exception of OAE 1a (cf. Charbonnier and Föllmi, 2017). There are a number of possible reasons for the differences in the magnitude of MCE and OAE 2 related Hg/TOC ratios described here compared to other Mesozoic events, including: (1) the nature (i.e. subaerial or submarine) and geographical position of the LIP; (2) the intensity, length and type of the volcanic episode(s) (e.g. explosive versus effusive); (3) thermogenic release of Hg from organic-rich records; and (4) muting of Hg/TOC due to high TOC levels and the resulting dampening of Hg/TOC values in the studied sedimentary archives. (1) is duscussed in the section 4.5.3 that follows. Each of these other factors are discussed in turn:

(2) Subaerial LIP volcanism may have resulted in relatively high Hg fluxes directly into the atmosphere, therefore possibly resulting in larger Hg excursions. However, at present the Hg fluxes of past subaerial LIP volcanism are largely unconstrained. Longer and more intense episodes of volcanism might expel more mercury into the ocean-atmosphere system and transfer larger amounts of Hg into the sedimentary realm over shorter periods of time. Differences in past LIP eruption type and their long term effects on Hg expulsion have not been widely studied, although most LIPs are thought to have been predominantly effusive with underlying sill and feeder complexes (e.g. Bryan and Ernst, 2008). Nearly all modern volcanic Hg studies

have assessed Hg fluxes derived from non-explosive eruptions as well as mid-ocean ridges and oceanic hydrothermal vents where Hg is released passively during the degassing of CO_2 (e.g. Schuster et al., 2002; Bowman et al., 2015). The most commonly used modern analogue to LIP volcanism is the Laki eruption on Iceland in the 18th century although there are no Hg measurements from this event (Thordarson and Self, 2003). More work is needed to understand the differences in expulsion of gaseous Hg between explosive and effusive eruptions. Bentonites make up around 5% of the Western Interior Seaway cores ($>$300 in Iona-1: Eldrett et al., 2015a) and are possibly derived from silicic caldera eruptions. The bentonites in the studied records show low Hg/TOC ratios of between 5 and 15 ppbHg/wt%TOC, values comparable to low sedimentary background values in the Innes-1 core (Figures 2 and 3). Furthermore, the strata above and below the bentonites do not appear to be geochemically impacted by proximity to these deposits (see Appendix B) as the underlying and overlying sediments display values comparable to sediments in other parts of the core. Hence, it is unlikely that the Hg in this study area is sourced from the Western Cordilleran convergent margin or that Hg migrated from the bentonites. Therefore, Hg has not become diagenetically enriched in under- and overlying sediments.

(3) The thermogenic release of Hg due to the intrusion of dykes and/or sills into organic-rich strata could potentially release large fluxes of Hg to the ocean-atmosphere system due to its volatility. This mechanism has been suggested for other global change events, such as the Toarcian Oceanic Anoxic Event (T-OAE) where dykes and sills from the Karoo-Ferrar LIP are known to have penetrated organic-rich sedimentary basins (Percival et al., 2015). It is possible that one of the LIPs known to be active during this period penetrated an organic-rich sedimentary basin. However, further work is required to quantify the effect of its mechanism.

(4) As TOC contents are highest before and after the MCE and then gradually drop to lower values around OAE 2 (Figure 4.2) it is unlikely that high levels of organic matter resulted in a muting effect.

In summary, it may be reasonable to suggest that the most likely cause of the ob-

served increases in sedimentary Hg and Hg/TOC was LIP volcanism and its nature and its proximity to the here studied sedimentary archives during deposition.

4.5.3 Submarine LIPs and Hg Dispersal Mechanism

Submarine magmatic activity and associated basalt-seawater interaction has been suggested as the initial trigger for the climatic and palaeoceanographic perturbations associated with OAE 2 (i.e. Rampino and Strothers, 1988; Courtillot and Renne, 2003; Turgeon and Creaser, 2008; Jenkyns et al., 2017). A globally observed shift in the $^{187}Os/^{188}Os$ ratio of organic-rich mudstones, to unradiogenic values (Turgeon and Creaser, 2008; du Vivier et al., 2014, 2015), and a change in seawater strontium-isotope ratios to less radiogenic values coinciding with OAE 2, supports this interpretation (Jones and Jenkyns, 2001). Equivalent negative excursions in lithium and calcium isotope ratios during OAE 2, taken to represent changes in seawater values, imply increases in weathering of silicates (Blättler et al., 2011; Pogge von Strandmann et al., 2013), which may indicate subaerial basalt emplacement followed by weathering of an exposed landmass in addition to alteration of submarine basalts.

Of the four LIPs thought to have been active throughout the Cenomanian and Turonian (Figure 4.1) the only potentially direct evidence that links OAE 2 with the Caribbean Plateau and/or Madagascar (subaerial) Flood Basalt is based on lead-isotope signatures (Kuroda et al., 2007): however, this study did not incorporate data from the High Arctic and Ontong Java LIPs). The Madagascar LIP has been $^{40}Ar/^{39}Ar$ (Storey et al., 1995) and U-Pb (Torsvik et al., 1998) radio-isotopically dated to have formed between 91.6-83.7 Ma, significantly later than the onset of OAE-2. However, The volcanic basement of the extensive submarine Madagascar Ridge (Sinha et al., 1981) remains unsampled and undated. The initiation of OAE 2 does correspond well with $^{40}Ar/^{39}Ar$ radio-isotopic ages for the Caribbean LIP (95.1 Ma to 92.2 Ma; Snow et al., 2005), although paired U-Pb analyses are still required to rule out potential bias of the $^{40}Ar/^{39}Ar$ dates towards a younger age due to post depositional alteration or overprinting by a younger metamorphic event.

Submarine LIP emplacement during the MCE and OAE 2 may represent an alternative source for elevated oceanic Hg concentrations. Such a mechanism could have featured intense release of hydrothermal Hg during rapid emplacement of mafic rocks, similar to that observed on mid-ocean ridge systems today; potentially accompanied by additional Hg-rich fluids expelled during subsequent basalt-seawater interactions. In such a situation, the amount and pattern of sedimentary Hg enrichments observed at any location would have depended on the direction and intensity of the palaeo-ocean currents transporting Hg from source to sink, in addition to the position of the volcanic centre, the flux size and the global oceanic Hg residence time. As mercury has a short ($<$1.5 kyr) residence time in the modern ocean, it might be expected that sites located more distally from a LIP would show less sedimentary enrichment in Hg than those in more proximal positions.

Neodymium-isotope records (εNd; Figure 4.6) for the mid-Cretaceous at Demerara Rise show a shift from extremely unradiogenic values to more radiogenic values during both the MCE (MCE 1b) and OAE 2, which are akin to Pacific, Tethyan and eastern proto-North Atlantic signatures (MacLeod et al., 2008; Jiménez-Berrocoso et al., 2010; Martin et al., 2012). The change in εNd likely reflects a switch in the source and circulation of intermediate-depth waters at these times (Zheng et al., 2013). Palaeo-ocean models suggest that the palaeogeography and persistent palaeo-trade winds in the south-western proto-North Atlantic resulted in a net flow of surface waters through the Central American Seaway into the Pacific Ocean (Trabucho Alexandre et al., 2010). A sub-surface counter-current has been suggested to have moved in the opposite direction, entering the western proto-North Atlantic at depth and upwelling along the northern and southern continental margins (Trabucho Alexandre et al., 2010). This sub-surface counter current could have acted as a transport mechanism to move Hg-enriched waters from the Pacific Caribbean LIP into the southern Western Interior Seaway and the western and southern proto-North Atlantic (Figure 4.7). A similar model has recently been proposed to explain the occurrence of mafic chromium-isotope signatures in the Western Interior Seaway during OAE 2, which were argued to originate from the Caribbean LIP (Holmden et al., 2016). The Hg data presented here may, therefore, tie the timing of environ-

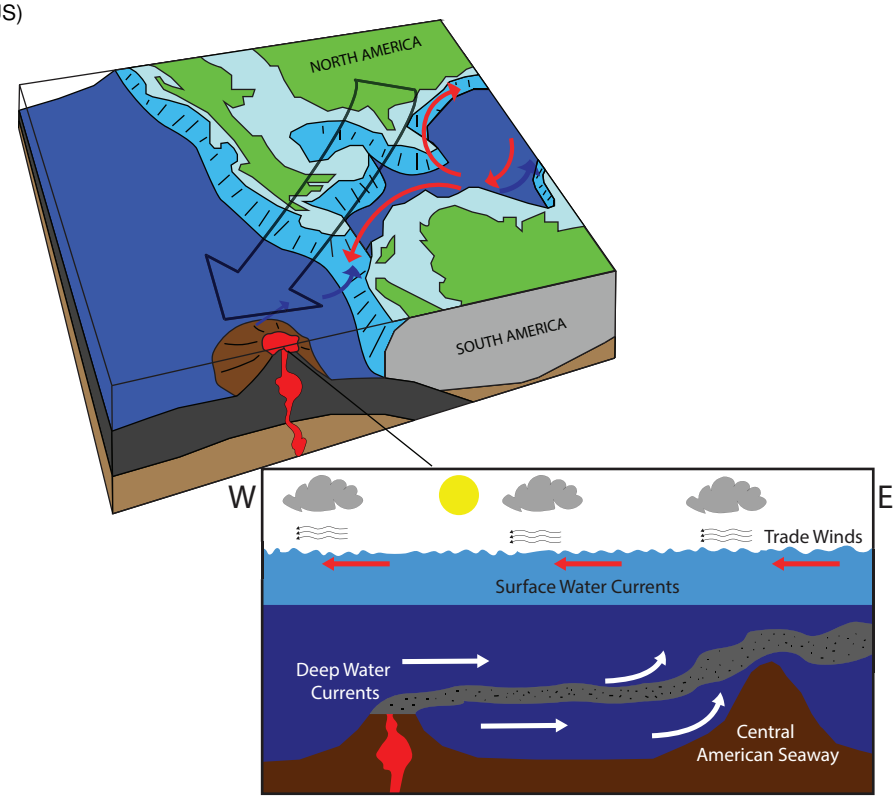

Figure 4.7: Palaeoceanographic model of the Cenomanian-Turonian Pacific and Atlantic Oceans and Western Interior Seaway, showing reconstructed palaeo-currents in the proto-North Atlantic region (modified from Trabucho Alexandre et al., 2010). The trade winds (largest arrow) are credited with causing a dominant westward surface-water flow and circulation (red arrows) leading to upwelling on the southern margins of the Western Interior Seaway. Bottom figure: Schematic diagram showing intermediate/deep waters entering the proto-North Atlantic Basin, acting as a possible conduit for Hg-enriched water masses.

mental changes observed during the MCE and during OAE 2 directly to magmatism associated with the Caribbean LIP via a submarine plume of Hg-enriched intermediate to deeper waters. If correct, sedimentary Hg concentrations at sites located outside of the proto-North Atlantic Ocean and the Western Interior Seaway should exhibit small, or undetectable peaks in Hg consistent with a lack of direct atmospheric Hg dispersal.

Alternatively, periodic incursions by boreal dinoflagellate cyst taxa shown in both Canada and the Eagle Ford Group of the Western Interior Seaway during OAE 2 (Eldrett et al., 2014, 2016; Van Helmond et al., 2016) indicate a southward flow of boreal water and therefore may provide a pathway for a second or alternative mercury source from the High Arctic Large Igneous Province. The equatorial flow of boreal water at this time may be associated with a more complex oceanographic system whereby a strong cyclonic gyre developed in the central Western Interior

Seaway drawing both Tethyan waters northward along the eastern margin and boreal waters southward along the western margin of the seaway (Slingerland et al., 1996; Kump and Slingerland, 1999; Elderbak and Leckie, 2016). Importantly, both models do not rule out the possibility of multiple LIPs having erupted at the same time.

It therefore is plausible that the sedimentary Hg enrichments observed during the MCE and OAE 2, in contrast to other Mesozoic OAEs, were sourced from localized Hg plumes in subsurface waters. The alternative suggestion remains that volcanogenic trace metals, including Hg, may have entered the atmosphere through the water-column (Bagnato et al., 2017) or directly by explosive/subaerial volcanic activity associated with submarine LIP emplacement. The release and dissolution of volcanogenic gases within the water column would in turn have resulted in smaller fluxes of Hg entering the global atmosphere than would otherwise have been the case. Such a mechanism could explain the reduced sedimentary Hg and more subtle and variable Hg/TOC excursions at the MCE and OAE 2, relative to the signals associated with other Mesozoic global change events proposed to originate from subaerial LIP emplacement.

Possible evidence against atmospheric mediation of the signal is the decreasing trend in the magnitude of Hg/TOC ratios along a south-to-north transect of the Western Interior Seaway (Chittim-2H $\rightarrow$ Iona-1 $\rightarrow$ Innes-1, respectively; Figures 4.1 and 4.2), tentatively explained by decreasing concentrations of mercury in the water column due to the increasing distance the sub-aqueous source. The longer atmospheric lifetime of Hg means that such differences would have been significantly less marked had the dispersal mechanism been subaerial. Future studies of other marine, but especially also continental sedimentary records from the proto-North Atlantic region and elsewhere, spanning the Cenomanian-Turonian transition, will help to determine the dominant dispersal pathway for Hg at this time.

Irrespective of the dominant dispersal mechanism for Hg during the MCE and OAE 2, the multiple excursions in Hg and Hg/TOC values at these time intervals, observed in the sedimentary records from four different cores, spread over 2 geo-

graphically separated regions, strongly suggests a temporal link between increased magmatic activity and major perturbations in global biogeochemical cycles, climate and the palaeo-environment at those times.

4.5.4 Comparisons to OAE 1a

Throughout the Early Cretaceous, the Greater Ontong Java episode of LIP activity led to the formation of the Ontong Java, Manihiki and Hikurangi Plateaus in the Pacific Ocean (e.g. Méhay et al., 2009; Tejada et al., 2009; Kuroda et al., 2011; Bottini et al., 2012). Although the establishment of an exact temporal relationship between OAE 1a and LIP activity remains a major challenge, several lines of evidence, such as age correlations to changes in the marine sedimentary lead isotopic composition, a change in volcanogenic trace-element concentrations and an $\sim$880 kyr interval during OAE 1a marked by an exceptionally unradiogenic Os-isotopic composition of the global ocean, suggest that OAE 1a may have been triggered by the emplacement of the Ontong Java Plateau in the central Pacific Ocean (e.g. Tarduno et al.,1991; Erba, 1994; Larson and Erba, 1999; Jones and Jenkyns, 2001; Méhay et al., 2009; Tejada et al., 2009; Kuroda et al., 2011; Bottini et al., 2012; Erba et al., 2015).

Three coeval sedimentary records from the western Tethyan region, across OAE 1a, which were separated by 100-300 km and were 4000-7000 km away from the Ontong Java Plateau, showed only limited increases in sedimentary mercury enrichments (Charbonnier and Föllmi, 2017). These Hg/TOC enrichments were suggested to be partly related to supposed changes in primary productivity, redox conditions and TOC preservation rates (Charbonnier and Föllmi, 2017). However, increased emission of gaseous Hg^0 during LIP formation was suggested to be the principal source of increased sedimentary mercury enrichment (Charbonnier and Föllmi, 2017). The sedimentary Hg/TOC values associated with OAE 1a show comparable values to the results for OAE 2 shown in this study and were explained by the muting effects of high sedimentary TOC contents in the studied record (Charbonnier and Föllmi, 2017).

As the emplacement of the Ontong Java Plateau was largely deep-sea submarine (Tarduno et al., 1991; Méhay et al., 2009; Tejada et al., 2009; Kuroda et al., 2011; Bottini et al., 2012; Erba et al., 2015) unlike the shallow subaqueous or subaerial eruptive history of the Manihiki and Hikurangi Plateaus (Tarduno et al., 1991), the Ontong Java LIP is suggested to have introduced reactive metals directly into the ocean (Bottini et al., 2012; Erba et al., 2015) rather than dispersing particulates and gases predominantly through the atmosphere.

Palaeo-ocean models suggest that the palaeogeography and palaeo-trade winds in the Tethys and Pacific oceans resulted in a net flow of waters from the Ontong Java LIP to the proto-North Atlantic in a clockwise fashion (Hay, 2009; Erba et al., 2015). A sub-surface oceanic counter current has been suggested to result in upwelling along the western Tethyan margins (Hay, 2009). This counter current could have acted as a transport mechanism for the movement of a volcanogenically derived plume from the central Pacific Ontong Java LIP to the sites of these cores in the western Tethys. Alternatively, if the distance from the source was too great for a submarine plume to hold a significant Hg concentration then it may suggest that the Ontong Java LIP temporarily became periodically emerged, as suggested by the local presence of pyroclastic sediments (Thordason, 2004), thereby providing an atmospheric dispersal mechanism for Hg.

The deep-submarine and geographic position for the formation of the Ontong-Java Plateau have therefore potentially directly impacted mercury distributions in the studied sedimentary records spanning OAE 1a. Similar to OAE 1a, the lower Hg/TOC ratios observed across the MCE and OAE 2 may have resulted from localized submarine Hg plumes or the release and dissolution of volcanogenic gases within the water column resulting in smaller fluxes of Hg entering the global atmosphere, relative to levels observed for continental LIP emplacements at other global change events.

4.5.5 Minor Cenomanian carbon-cycle perturbations: *Jukes-Browne Event*

A small positive CIE of 0.8 ‰ is visible both in Iona-1 (between 128.36 m to 126.1 m) and in Innes-1 (between 65.49 and 62.39 m). Within the ODP Site 1258 core on Demerara Rise a period of erratic carbon-isotope fluctuation occurs between 435.34 m and 432.66 m. However, between these limits there are three particularly high positive CIEs of around 0.5, 1 and 0.7 ‰ at 435.11, 434.21 and 432.97 m respectively, which may correspond to the minor CIE found in the Western Interior Seaway cores. The CIEs observed in Iona-1 and at Site 1258 fall within the relatively narrow occurrence-range of the planktonic foraminiferal marker species *Rotalipora cushmani* (Shipboard Scientific Party, 2004; Eldrett et al., 2015a). and the position of the CIE in each core fits a similar position within a chemostratigraphical and biostratigraphical framework (Figure 4.2 and 4.6; Eldrett et al., 2017). As such, this study hypothesizes that these CIEs are equivalent to the Jukes-Browne Event, first recognized in the English Chalk (Jarvis et al., 2006) where it spans the correlative upper *A. jukesbrownei* and the lower *C. guerangeri zones* (Hardenbol et al., 1998), and subsequently in central areas of the Western Interior Seaway (Joo and Sageman, 2014). Consequently, this small positive excursion may provide a marker for the base of the Upper Cenomanian in Innes-1, Iona-1 and 1258. A combined astronomical and geochronological age model for the Iona-1 core calibrates the Jukes-Browne Event (128.36-126.1 m) to between 95.79 - 95.69 Ma $\pm$0.12 Ma (Eldrett et al., 2015a) therefore potentially assigning a numerical age to both the *Jukesbrownei*-related CIE and more tentatively the Middle-Upper Cenomanian substage boundary of 95.79 $\pm$0.12 Ma (Eldrett et al., 2015a).

Anomalously high Hg/TOC values of 48 ppbHg/wt%TOC and 41 ppbHg/wt%TOC accompany the Iona-1 and Site 1258 CIEs at 126.2 m and 434.38 m, respectively. The CIE of Innes-1 is also accompanied by a Hg/TOC excursion, which although of smaller absolute magnitude (12 ppbHg/wt%TOC), is significantly away from the lower stable baseline values in this part of the Innes-1 core (Figure 4.2). It is possible that these excursions implicate volcanism and the potentially accompanying release of CO^2 and other greenhouse gasses and compounds, and associated changes in

global carbon burial rates, as drivers for this relatively minor perturbation to the global carbon cycle. However, the true nature of the observed Hg/TOC excursions at this time, defined only by a single data point, albeit in all three cores, needs further study as it also coincides with low TOC values (Figure 4.2). This suggests elevated Hg/TOC values may be to some extend an artefact of a change in the deposition and preservation of organic matter during these periods. If the event were caused by volcanic activity, the much smaller size of the CIE found in all three cores indicates that the volcanic event responsible for it would most likely have been significantly smaller in volume or shorter in duration than those responsible for the geochemical anomalies observed for the MCE and OAE 2.

4.6 Conclusions

New sedimentary Hg concentration data from three sites in the Western Interior Seaway and one from the south-western proto-North Atlantic Ocean (Demerara Rise) demonstrate elevated Hg and Hg/TOC values at the stratigraphic levels of the Mid-Cenomanian Event (MCE) and the Cenomanian-Turonian Oceanic Anoxic Event 2 (OAE 2). Values are, however, muted in comparison to signals found during other Mesozoic intervals marked by OAEs and/or global change events that are associated with coeval subaerial LIP emplacement. The smaller Hg signals associated with OAE 2 and the MCE possibly resulted from Hg dispersal by a submarine plume, following a subaqueous LIP emplacement rather than resulting from atmospheric dispersion. The transmission of this plume by sub-surface palaeo-currents moving either from the Pacific, through the Central American Seaway into the south-western proto-North Atlantic Ocean or from the Arctic via the Canadian sector of the Western Interior Seaway are consistent with previous palaeoceanographic reconstructions of water mass movements. This study finds no causal link between the enrichment of redox-sensitive trace metals and the MCE- or OAE 2-related Hg/TOC excursions. In addition, a possible short-term Hg/TOC enrichment, in tandem with a carbon-isotope excursion, is recognized at the level of the Jukes-Browne Event, occurring stratigraphically in-between the MCE and OAE 2 in the Innes-1, Iona-1

and Site 1258 cores.

5 Environmental and Climatic Evolution of the Cenomanian-Turonian Southern Western Interior Seaway

This chapter is modified from **J. D. Scaife** et al., Environmental and Climatic Evolution of the Cenomanian-Turonian Southern Western Interior Seaway. *Cretaceous Research*, in prep. Micha Ruhl performed the Iona-1 XRF analysis.

Abstract

The Late Cretaceous Epoch was characterized by a number of large-scale global perturbations in the global carbon cycle, the most prominent occurring at the Cenomanian-Turonian Boundary marked by Oceanic Anoxic Event 2 (OAE 2). This event is discernible in many areas of the world by a large positive carbon-isotope excursion, the development of a 'black-shale' record, and evidence of anoxic-euxinic conditions in the water-column. However, in the southern Western Interior Seaway, the onset of OAE 2 is marked by significant reductions in concentrations of redox sensitive trace metals, and organic-lean sediments. This study integrates high-resolution geochemical, sedimentological and mineralogical data from a $>$300 km transect, comprising 4 cores from the Comanche shelf to the Hawksville sub-basin, in order to understand the hydrodynamic, climatic and depositional environment of the southern Western Interior Seaway. The results of this study show four distinct stages in the deposition of the Eagle Ford Group, termed depositional units and defined herein. Phase A, corresponding to the lowermost stratigraphical third of the Lower Eagle Ford, occurred under a humid climate with high continental runoff, anoxic/euxinic benthic conditions in the water column and exchange with a nutrient-rich water mass resulting in resupply of the trace metal inventory. Phase B, the upper stratigraphical two thirds of the Lower Eagle Ford, took place within a more arid climate, with lower continental runoff, a highly restricted anoxic benthic zone with some periods of euxinia, and little siliciclastic input. Phase C, the lowermost stratigraphical half of the Upper Eagle Ford, occurred during a mostly humid climate with high continental runoff and the presence of a suboxic benthic zone that experienced multiple periods of oxygenation related to a more open water mass exchange. This phase contains the Plenus Cold Event (PCE) interval which exhibits a brief switch to a more arid climate and the potential influx of a volcanically derived, nutrient-rich, water-mass. Phase D, the upper stratigraphical half of the Upper Eagle Ford, occurred under a more arid climate with lower continental runoff, reduced benthic oxygen content, and enhanced concentration of organic matter due to a reduction in detrital and siliciclastic input.

5.1 Introduction

The mid-to-late Cretaceous was a time characterized by major perturbations in the global carbon cycle, termed Oceanic Anoxic Events (OAEs), sustained global warming, emplacement of marine Large Igneous Provinces, and global sea-level highstands, leading to the development of several epicontinental seaways (Schlanger and Jenkyns, 1976; Jenkyns, 1980; Arthur et al., 1987; Schlanger et al., 1987; Jenkyns, 2010). The most pronounced global carbon cycle perturbation at this time, termed Oceanic Anoxic Event 2 (OAE 2), occurred at the Cenomanian-Turonian transition (circa 94 Ma), and is discernible by a globally recognized $\sim$3 ‰ positive, carbon-isotope excursion (CIE; Tsikos et al., 2004; Jarvis et al., 2006; Sageman et al., 2006; Ma et al., 2014; Eldrett et al., 2015a; Gambacorta et al., 2015; Jenkyns et al., 2017). This excursion is thought to reflect the widespread transfer of relatively ^{12}C-enriched organic matter into marine sediments. In many areas of the world's oceans, OAE 2 is indeed marked by a organic carbon-rich 'black shale' record and the development of anoxic/euxinic conditions (Schlanger et al., 1987; Jarvis et al., 1988; Sinninghe Damsté and Köster, 1998; Tsikos et al., 2004; Turgeon and Creaser, 2008; Jenkyns, 2010). The global carbon cycle was also perturbed during the Mid-Cenomanian Event (MCE), which is marked by a $\sim$1 ‰ positive carbon-isotope excursion in carbonates (Scaife et al., 2017). In the interval between the MCE and OAE 2 (Owens et al., 2017) there are no significant carbon-cycle events except for a minor positive CIE recorded in the English Chalk named the 'Jukes-Browne Event'. This event can be correlated with a similar small-scale feature in the Western Interior Seaway (Jarvis et al., 2006; Joo and Sageman, 2014) and is recorded in both the Innes-1 and Iona-1 core (Scaife et al., 2017).

Proposed hypotheses for enhanced carbon sequestration and ocean anoxia during these events include triggers such as changes in ocean circulation and eustatic sea level rise, flooding large areas of continental shelves promoting global stratification and stagnation under greenhouse climates (Erbacher et al. 2001). Extensive volcanic activity and the subaqueous emplacement of Large Igneous Provinces (LIPs) (Caribbean, High Arctic, Madagascar and Ontong-Java LIPs) have been suggested

to be responsible for the initiation of OAE 2 and the MCE, with evidence suggesting that the High Arctic and Caribbean LIPs were active at the time of OAE 2 (Orth et al., 1993; Snow et al., 2005; Tegner et al., 2011; Holmden et al., 2016; Jenkyns et al., 2017; Scaife et al., 2017). The associated, large-scale, release of greenhouse gases and toxic compounds is suggested to have resulted in catastrophic oceanographic and climatic changes, which impacted on and initiated a number of processes resulting in enhanced carbon burial and, in geographically widespread areas of the world, ocean anoxia.

To understand the underlying causal mechanisms of oceanic anoxic events and OAE 2 as well as to accurately calculate the rate of biogeochemical processes robust and high-resolution mineralogical and geochemical frameworks are required. Recently, debate over the modulation of organic-rich sediment deposition by local and regional processes (i.e. basin restriction, water stratification, bottom currents) during perturbations to the carbon cycle has called into question the relative influence of global processes (i.e. sea level change, orbital forcing) (e.g. Trabucho-Alexandre et al., 2010). This is particularly relevant to (parts of) shallow epicontinental seaways, such as the southern part of the Western Interior Seaway, where in contrast to other globally recognized sections that record organic-rich sediments during the OAE 2 interval (e.g. the Bonarelli interval in Italy), the onset of OAE 2 is marked by significant drops in concentrations of redox sensitive trace metals and the occurrence of organic-lean sediments (Eldrett et al., 2014, 2017). This is accompanied in many areas of the southern and central Western Interior Seaway by a change in lithology from laminated, organic carbon-rich shales to interbedded limestone and marlstone/calcareous shales (e.g. Stephenson, 1929; Adkins and Lozo, 1951; Charvat, 1985; Jiang, 1989; Dawson, 1997, 2000; Chapter 3 of this thesis).

Previous studies have proposed that the Cretaceous Western Interior Seaway (WIS) was restricted during the Cenomanian, promoting anoxia, due to a sill in the southern gateway (i.e. Texas/Mexico); and that only late Cenomanian sea-level rise (Greenhorn cyclothem of Kauffman, 1977, 1984) was sufficient to reach a critical sill depth allowing a breach of the southern end of the seaway allowing the

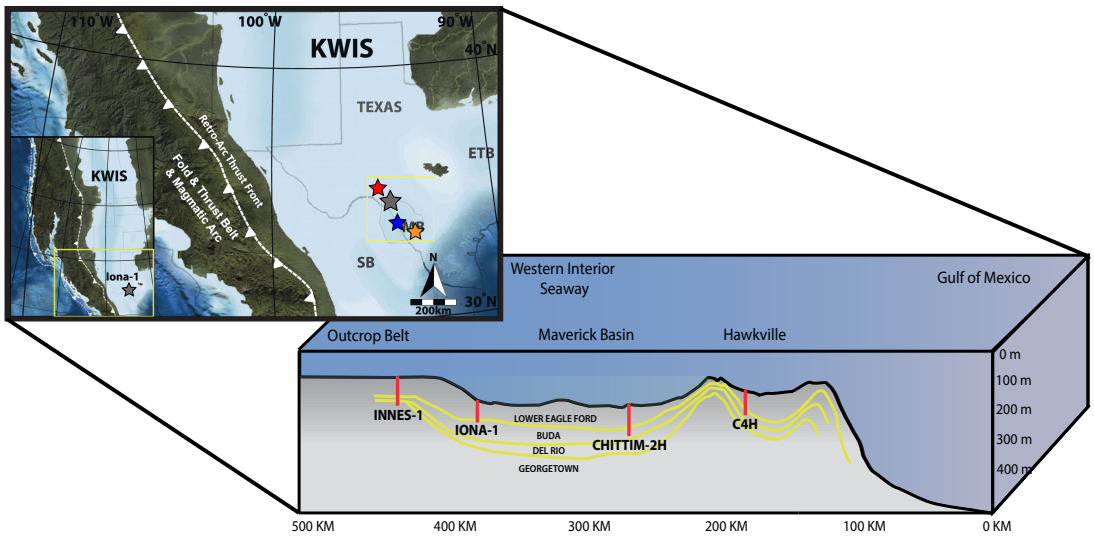

Figure 5.1: A 3D diagram displaying the position of the Innes-1, Iona-1, Chittim-2H and C4H cores in the southern Western Interior Seaway including the positions of the Maverick Basin, Hawkville Basin and Gulf of Mexico. Subsurface stratigraphy shows the position of the Lower Eagle Ford, Buda Limestone, Del Rio Clay and Georgetown formations at the time of the Cenomanian-Turonian boundary. Water depth estimations are taken from Eldrett et al. (2014, 2017). This figure includes a close-up of the Cretaceous Western Interior Seaway (top left) displaying the Maverick Basin cores (SB-Sabinas Basin; ETB-East Texas Basin; Figure modified after Eldrett et al., 2014).

rapid incursion of warm, saline Tethyan waters (Arthur and Sageman, 2005). An inflow of Tethyan waters at this time is suggested by the i) improved environmental conditions as indicated by the sharp increase in abundance and diversity of foraminiferal/molluscan, in particular ammonite, assemblages reaching far north into the WIS (McNeil and Caldwell, 1981; Kauffman, 1984, 1985; Eicher and Diner, 1985; Elder, 1985; Leckie et al., 1998; Caldwell et al., 1993; Kauffman and Caldwell, 1993, Elderbak and Leckie, 2016) and ii) the lithologic transition from organic-rich mudrocks to a highly bioturbated limestone dominated facies in southern and central parts of the Western Interior Seaway (Corbett et al. 2014; Lowery et al. 2014).

Some studies indicate a more complex oceanographic system existing in the Western Interior Seaway during the Cenomanian-Turonian, with strong cyclonic gyres developing and drawing in both Tethyan and Boreal water-masses (Slingerland et al., 1996; Kump and Slingerland, 1999; Elderbak and Leckie, 2016). Changes in assemblages of planktonic and benthonic calcareous microbiota associated with OAE 2 (e.g. Jarvis et al., 1988; Erba, 2004) do register in the Western Interior Seaway as well as an invasion of Boreal dinoflagellates (Keller and Pardo, 2004; Eldrett et al.,

2014; van Helmond et al., 2014; Eldrett et al., 2015a). These changes in biota also occur during a period when boreal fauna also migrated into northern Europe, which was accompanied by increases in bulk oxygen-isotope values of chalks, signifying a fall in surface-water temperatures (Lamolda et al., 1994; Gale and Christensen, 1996; Jenkyns et al., 2017), as well as by falls in temperature in the proto-Atlantic determined by the organic geochemical TEX_{86} proxy (Forster et al., 2007; Sinninghe Damsté et al., 2010). This stratigraphic interval is commonly known as the 'Plenus Cold Event' (PCE).

These observations possibly imply more complex oceanographic and climatic changes operating in the southern Western Interior Seaway than previously suggested. In order to better understand the nature and timing of palaeoenvironmental and palaeoclimatic processes this study uses a high resolution, cm-scale, dataset from four cores along a $>$300 km transect of cores that represent a range of palaeobathymetric settings, in order to constrain and differentiate between local and global controls on both water-column conditions (as reflected by inorganic water-column geochemical proxies) and organic matter enrichment of the Eagle Ford Group. The primary objectives of this study then are to: 1) produce a high-resolution palaeoenvironmental interpretation of the southern Western Interior Seaway throughout the deposition of the Eagle Ford Group; 2) constrain the palaeoclimatic controls on the deposition of the Eagle Ford Group; 3) determine potential changes in water mass exchange, and; 4) evaluate the hydrographic evolution of the southern Western Interior Seaway.

5.2 Geological Setting

This study investigates the Eagle Ford Group of the southern Western Interior Seaway (Figure 5.1). The group comprises a 60-130 m thick sequence of metre-scale organic-rich marl-limestone bed couplets, deposited in a distal, clastic-sediment starved, intra-shelf basin, along the retro-arc foreland basin of western North America (suggested palaeowater depth of $\sim$50-100 m) (Pessagno, 1969; Eldrett et al. 2014; Denne et al., 2014; Lowery et al., 2014; Eldrett et al., 2015b). Four marine

mudrock successions were studied spanning the Mid-Cenomanian to Early Turonian interval in the Maverick Basin and surrounding Comanche shelf. The Maverick basin initially developed as one of a number of fault-bounded Jurassic rift basins in the southern KWIS and is thought to represent a failed rift arm of the Late Jurassic opening of the Gulf Coast basin (Scott, 2004).

The Eagle Ford Group is unconformably underlain by the Early to Mid-Cenomanian Buda Formation, a bioclastic limestone comprising calcispheral wackestone and skeletal packstone). In the study area, the Buda-Eagle Ford contact is an irregular surface with subtle incisions and rip-up clasts of Buda encased in the lowermost Eagle Ford Group (Chapter 3). The Eagle Ford Group is comprises five dominant facies: 1) argillaceous wackestone; 2) laminated argillaceous foraminiferal wackestone; 3) laminated foraminiferal packstone; 4) massive foraminiferal packstone; 5) bentonitic claystone (Chapter 3). The Eagle Ford shows abundant unidirectional flow features throughout much of both the Upper and Lower Eagle Ford members including scours, asymmetrical ripples, planar cross-bedding, and discontinuous laminae (Chapter 3).

The wackestone beds of the Lower Eagle Ford are generally dark in colour and rich in TOC (Chapter 3). In most Eagle Ford literature these are lithologies commonly known as marlstones (e.g. Eldrett et al., 2015a), and will be so referred to in this study. The packstone beds are much lighter in colour, and largely composed of planktonic foraminifer and bioclasts, with low TOC (Chapter 3). In most Eagle Ford literature these are commonly known as limestones (e.g. Eldrett et al., 2015a) and will be so referred to in this study. The Lower Eagle Ford is dominated by laminated argillaceous foraminiferal wackestones containing 3-12 % TOC, and laminated foraminiferal packstones containing 1-3% TOC. Though minor bioturbation occurs in parts of the Lower Eagle Ford, burrowing is relatively rare and small scale, except for minor-to-moderate bioturbation around the Jukes-Browne Event and moderate-to-intense bioturbation around the Mid-Cenomanian Event which both coincide with an influx of *Inoceramus* (Chapter 3). Comparatively, moderate bioturbation occurs throughout much of the Upper Eagle Ford, onsetting at around

54 m in Innes-1 and 106 m in Iona-1, which contains much paler lithologies, and generally lower TOC,1-3 %. The Upper Eagle Ford is dominated by argillaceous wackestones, containing 1-4 % TOC, as well as laminated and massive foraminiferal packstones, containing 1-2 % TOC. Calcite recrystallisation is apparent in both the Lower Eagle Ford and the Upper Eagle Ford, and often obscures sedimentary structures and textures in the packstone lithologies.

In this study area the Eagle Ford is unconformably overlain by the Coniacian-Santonian Austin Chalk and the contact is gradational and coincides with an abrupt change in gamma ray values (Driskell et al., 2012; Chapter 3). The total duration of the preserved Eagle Ford sedimentary record is less than 8 Myr (Eldrett et al., 2015a) and comprises a number of sedimentary cycles, including a major transgression of the Upper Comanche Shelf of the Gulf Coast Margin within the southern portion of the Epicontinental Seaway of western North America (Dawson and Almon, 2010).

5.3 Analytical methods

5.3.1 Sampling

The methodology for the XRD, Rock-Eval/Coulomat, and organic-carbon isotopes measurements of Innes-1, Iona-1 and Chittim-2H have been discussed in chapters 3 and 4. The methodology in this chapter focuses on the whole core XRF of the Innes-1, Iona-1, C4H and Chittim-2H cores, increased resolution of organic-carbon isotope measurements of the Innes-1 and Iona-1 cores, as well as new organic-carbon isotope and TOC stratigraphic profiles for C4H, and finally whole core XRD for the Iona-1 and Chittim-2H cores. Previous studies on the Innes-1 and Iona-1 cores showed well-defined δ^{13}_{org} records for OAE 2, but only low-resolution, $>$30 cm, signatures across the smaller scale so-called Mid-Cenomanian Event (MCE) and Jukes-Browne Event (Eldrett et al., 2014, 2015, 2016). New measurements were undertaken in order to increase the stratigraphic resolution of data across these intervals for the Iona-1 and Innes-1 cores. In addition, a new δ^{13}_{org} curve

is presented from the C4H core, drilled on the southern edge of the Maverick Basin. For this study, the sample spacing in Innes-1 and Iona-1 was increased to 10 cm from the ∼0.5 m resolution employed by Eldrett et al. (2014). Sample density in core C4H is more varied depending on sample availability and tends to be ∼30 cm (Figure 5.2, 5.3, 5.4 and 5.5).

5.3.2 X-Ray Diffraction

Powdered 50 mg samples were analyzed by powder X-ray diffraction (XRD) using a Siemens D500 X-ray diffractometer with a Co Ka source, operated at 40 kV and 25 mA, and scanned between 5 and 80 degrees 2Q. Powders were back loaded into sample holders in the anaerobic chamber. To prevent any oxidation during preparation and analysis, powders were coated with a thin layer of glycerol in the anaerobic chamber, which maintains stability well beyond the data collection period. Final X-ray diffractograms are shown (see Appendix C) with ”background” patterns removed after subtracting several analyses performed on sample holders with identical amounts of glycerol. External standards were used to ascertain reproducibility, an error margin of 5% (1 S.D.) was found. Clay mineralogical analysis is based on methods developed by Kübler (1987) and Adatte et al. (1996). The intensities of the identified minerals are measured for a semi-quantitative estimate of the proportion of clay minerals, which is therefore given in relative percent without correction factors.

5.3.3 X-Ray Fluorescence (XRF)

High-resolution (10-15 cm) elemental concentrations (e.g. Ca, Ti, Fe, Rb, Zr) were obtained by hand-held X-ray fluorescence (XRF) analyses on the slabbed archive halves of the Innes-1, Iona-1, Chittim-2H and C4H cores. XRF analyses were conducted with a Thermo Scientific Niton XL3 instrument, with a 120-sec measurement window. Long-term drift in measurement values was counteracted by regular internal calibration. Internal measurement uncertainty, partly due to internal calibration

and Compton normalization, differs between elements. Long-term drift in analyses was further checked by repeated analysis of the NIST 2780 and NIST2709 international reference standards. Repeated analysis of the NIST 2780 standard gave an average of 1426 $\pm$ 205 ppm (1 S.D.), for Ca and 28395 $\pm$ 240 ppm (1 S.D.) for Fe. Repeated analysis of the NIST 2709 standard showed for calcium an average of 21130 $\pm$ 362 ppm, and for Fe an average of 34678 $\pm$ 382 ppm. Reproducibility of XRF-based calcium concentration data was further confirmed by comparison to calcium carbonate content calculated from total mineral carbon measurements obtained using a Rock Eval 6.

5.3.4 Organic-Carbon Isotope Analyses (δ^{13}_{org})

One gram aliquots of homogenized sample powder were decarbonated with 40 ml cold 3M HCl and were subsequently rinsed four times with distilled water to reach neutral pH. 1-15 mg of oven-dried and powdered decarbonated sample residue was weighed into 85 mm tin capsules to obtain $\sim$25 μg organic C for δ^{13}_{org} analyses. The analyses were performed at the Stable Isotope Laboratory at the Open University, Milton Keynes, using a Thermo Flash HT elemental analyzer coupled to a ThermoFinnigan MAT 253. Accuracy of carbon-isotope ratios on the Vienna Pee Dee Belemnite (VPDB) scale were ensured by applying a three-point calibration using IAEA-CH-6 sucrose, NIST8573 glutamic acid and IR-041 alanine. The reproducibility determined from these standards was $<$0.1% (1 S.D., n=23).

5.3.5 Coulomat TOC analyses

Total carbon (TC) and total inorganic carbon (TIC) were determined for samples from core C4H with a Strohlein Coulomat 702 Analyzer (see details in Jenkyns, 1988). For TC and TIC analyses, sample aliquots were measured, with one aliquot having been heated overnight at 450°C to remove organic matter. Total organic carbon (TOC) was calculated as the difference between TC and TIC. The long-term average value and reproducibility of TOC measurements based on the in-house

SAB134 standard is 2.95 $\pm$0.14 wt% (2 S.D., n = 27).

5.4 Results

5.4.1 Carbon Isotopes

Presented here are new δ^{13}_{org} from the C4H core and high-resolution, $\sim$10 cm, data across the Mid-Cenomanian and Jukes-Browne Event for the Innes-1 and Iona-1 cores (Figure 5.2). The δ^{13}_{org} isotope record of C4H core is characterized by an overall positive isotopic excursion from 2792.7 m to 2779 m of 1.7 ‰. This positive isotope excursion contains a drop between 2782.5 m and 2780.4 m of 1 ‰. The new MCE δ^{13}_{org} record of Iona-1 is characterized by a series of positive isotopic excursions (between 136.4 and 144.4 m) containing two key excursion periods of where values increase by circa 1.9 ‰ (at $\sim$142.71 m) and 2.1 ‰ (at $\sim$137.5 m). The Jukes-Browne Excursions of Innes-1 and Iona-1 are characterised by three individual excursions of circa 1, 1.3 and 0.9 ‰ at 62.6, 63.46 and 64.32 m in Innes-1, and 126.6, 127.31 and 127.77 m in Iona-1 (Figure 5.2).

5.4.2 Total Organic Carbon

New data from C4H shows high TOC values ($>$6 wt%) in the stratigraphically lowest part of the core (Fig. 2). However, these values are largely dependent on lithology, as marl-mudstone beds display on average 5.7 wt% TOC, whilst limestone beds only average 2 wt% TOC. There is a gradual, marginal decline in the amount of TOC present in the marls from 6.11 wt% at 2795.82 m to 5.2 wt% at 2781.08 m (Figure 5.2). At which point TOC values drop to 2.2 wt% and do not reach more than 3.45 wt% to the top of the core.

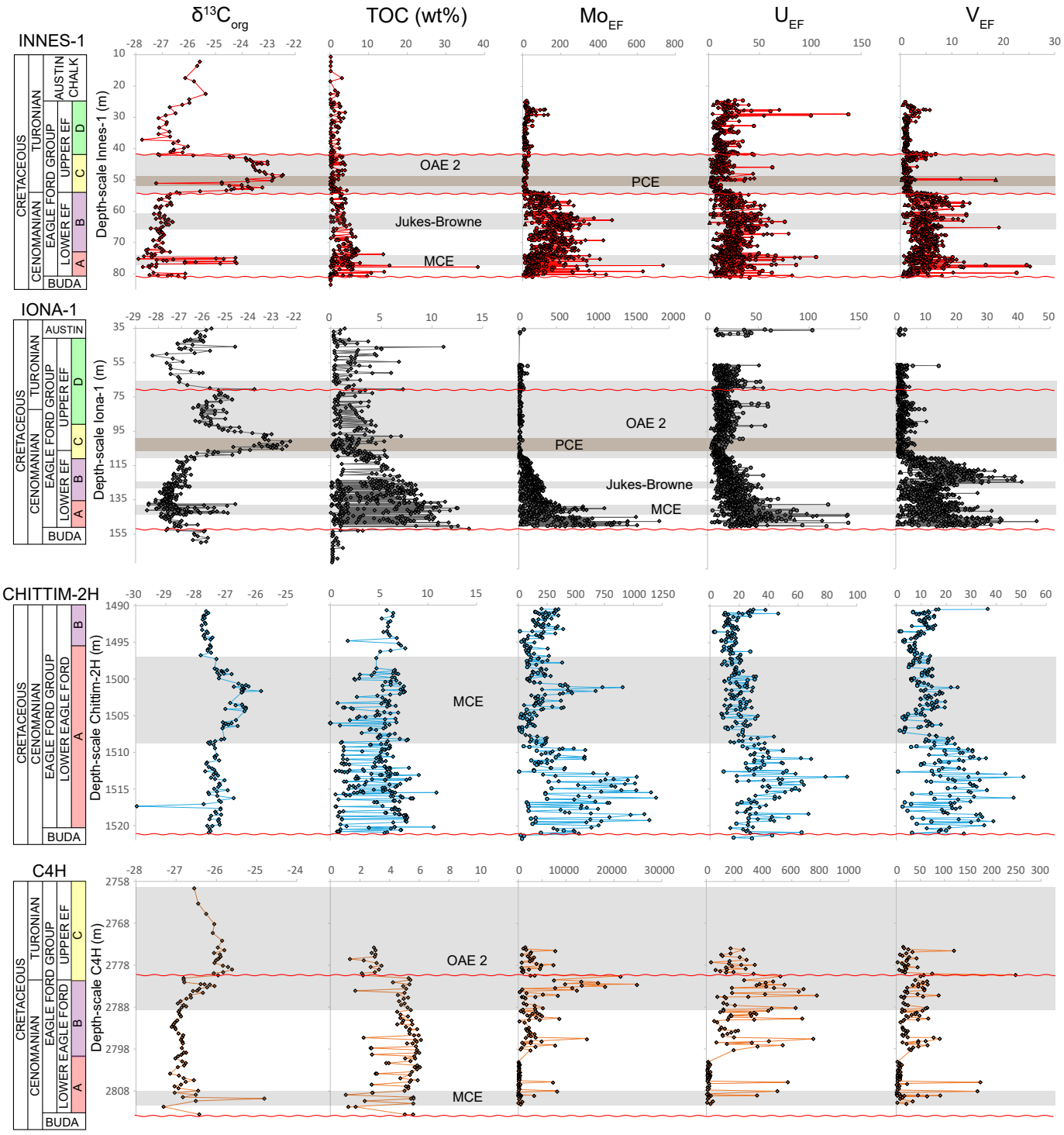

Figure 5.2: Data from the Western Interior Seaway cores including Innes-1, Iona-1, Chittim-2H and C4H. ($\delta^{13}C_{org}$) (‰ ; this study; Eldrett et al., 2015a; Eldrett et al., 2016; Eldrett et al., 2014), TOC (wt%; this study; Scaife et al., 2017), Mo_{EF} (this study), U_{EF} (this study) and V_{EF} (this study). Enrichments factors are calculated by dividing the samples trace metal concentration by its aluminium concentration and then the constituent average shales. Average shale values are taken from Brumsack, 2006. For Innes-1, Iona-1 and Chittim-2H circles denote limestones (red in Innes-1, grey in Iona-1 and blue in Chittim-2H, diamonds denote marlstones (red in Innes-1, grey in Iona-1 and blue in Chittim-2H) and triangles denote bentonites (red in Innes-1, grey in Iona-1 and blue in Chittim-2H). For C4H diamonds represent all facies. Includes a stratigraphic column that contains corresponding depositional units (A-D) of the Eagle Ford discussed in this study.

5.4.3 Geochemistry

Concentrations of redox sensitive trace metals are often used to evaluate the redox state of depositional environments. Elements such as Molybdenum (Mo), Uranium (U), Copper (Cu), Nickel (Ni), Vanadium (V), Iron (Fe) and Manganese (Mn) have been widely used to infer paleo-redox conditions in modern and ancient sediments (e.g. Brumsack, 2006; Tribovillard et al. 2006; Algeo et al. 2012; Fig. 2). These redox-sensitive trace metals show variable behaviour with redox state, typically resulting in authigenic enrichments in oxygen-depleted sedimentary environments. In particular, Mo has been widely used as a proxy for benthic redox potential because of its generally strong enrichment in organic-rich marine facies deposited under oxygen-depleted, sulfide-rich conditions (Algeo and Lyons, 2006; Tribovillard et al., 2006; Algeo and Tribovillard, 2009). To investigate the influence of changing detrital input, Aluminium (Al), Zirconium (Zr) and Titanium (Ti) are commonly utilised as proxies for terrigenous detrital material due to their relative chemical inertness (e.g. Brumsack, 2006; Calvert and Pederson, 2007; Fig. 4). Copper (Cu), iron (Fe) and manganese (Mn) can be used as important indicators for hydrothermal activity due to their release during subaqueous volcanism (Morford et al., 2005).

Due to the biogeochemical cycling of elements such as U, V, Mo, Ni and Cu in the water column and their affinity to organic matter and sulphides, trace metals often show large differences between facies. For example, U abundance usually shows a good correlation with both organic carbon rain rate in present-day water column conditions (McManus et al., 2005) and with the organic-carbon content in anoxic (non-sulfidic) facies (Algeo and Maynard, 2004). However, trace metals that are deposited with detrital sediments can be differentiated from those that are precipitated under anoxic conditions by comparison with Al, Ti or Zr. A commonly used technique for interpreting trace element data is to calculate the enrichment factor (EF) by normalizing the ratio of the trace element to Al within a given sample to the ratio of trace element to Al in the ”average shale” (Wedepohl, 1971, 1991). Elements possessing an EF greater than one are considered to be ’enriched’, whilst those with an EF of less than one are considered to be ’depleted’.

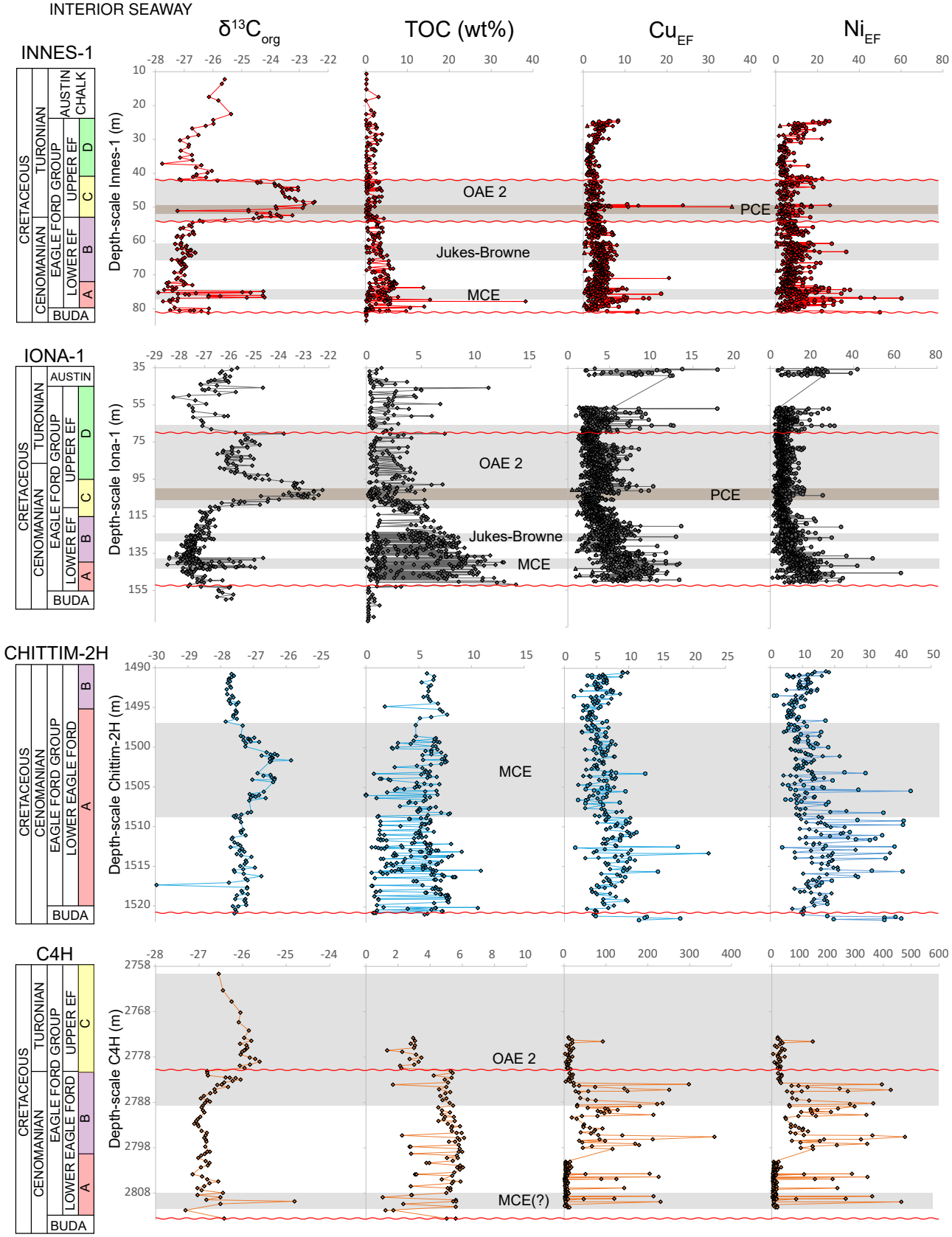

Figure 5.3: Data from the Western Interior Seaway cores including Innes-1, Iona-1, Chittim-2H and C4H. ($\delta^{13}C_{org}$) (‰ ; this study; Eldrett et al., 2014; Eldrett et al., 2015a; Eldrett et al., 2016), TOC (wt%; this study; Scaife et al., 2017), Cu_{EF} (this study) and Ni_{EF} Ni_{EF} (this study). For Innes-1, Iona-1 and Chittim-2H circles denote limestones (red in Innes-1, grey in Iona-1 and blue in Chittim-2H, diamonds denote marlstones (red in Innes-1, grey in Iona-1 and blue in Chittim-2H) and triangles denote bentonites (red in Innes-1, grey in Iona-1 and blue in Chittim-2H). For C4H diamonds represent all facies. Includes a stratigraphic column that contains corresponding depositional unit (A-D) of the Eagle Ford discussed in this study.

Mo, U, V, Cu, Ni, Fe and Mn enrichment factors are plotted stratigraphically in Figures 5.2, 5.3, 5.4 and 5.5. The cores are divided into four depositional units that were identified based on stratigraphic changes in their trace metal enrichment factors. As previously suggested in section 3.1 enrichment factors appear to be strongly dependent on lithology with marlstones displaying significantly higher enrichments.

5.4.4 Depositional units

Depositional unit A comprises the lowermost part of the Lower Eagle Ford (Figures 5.2, 5.3, 5.4 and 5.5) and displays high TOC, and the most highly enriched concentrations of redox sensitive trace metals compared to average shale. Within this stratigraphic interval trace metal enrichments decline at the base of the MCE (circa. 77 m in Innes-1, 144 m in Iona-1 and 1507 m in Chittim-2H). Redox sensitive trace metals then increase and become highly enriched again towards the end of the Mid-Cenomanian Event. In Innes-1, Iona-1 and Chittim-2H this section records combined trace metal enrichment factor averages of Mo_{EF}=107, U_{EF}=35 and V_{EF}=7 for limestones, and Mo_{EF}=356, U_{EF}=30 and V_{EF}=13 for marls. The detritus-related trace metals show high concentrations in depositional unit A. For Innes-1, Iona-1 and Chittim-2H this records trace metal averages of Zr=82 ppm, Al=21935 ppm and Ti=1390 ppm in the marlstones and Zr=38 ppm, Al=11180 ppm and Ti=920 ppm in the limestones.

Enrichments in Mo, Ni, V and Fe of up to 1000, 25, 30 and 20000, respectively, occur in this depositional unit, relative to global average shale, and largely coincide with the upper half of the MCE (Figures 5.2, 5.3 and 5.5). These are particularly obvious in Chittim-2H where they peak around 1502.5 m.

Depositional unit B accounts for the remainder of the Lower Eagle Ford (Figures 5.2, 5.3, 5.4 and 5.5), and displays high TOC and highly enriched concentrations of redox sensitive trace metals compared to average shale, although less so than in unit A. A large increase in vanadium is particularly evident in the Innes-1 and Iona-1 cores

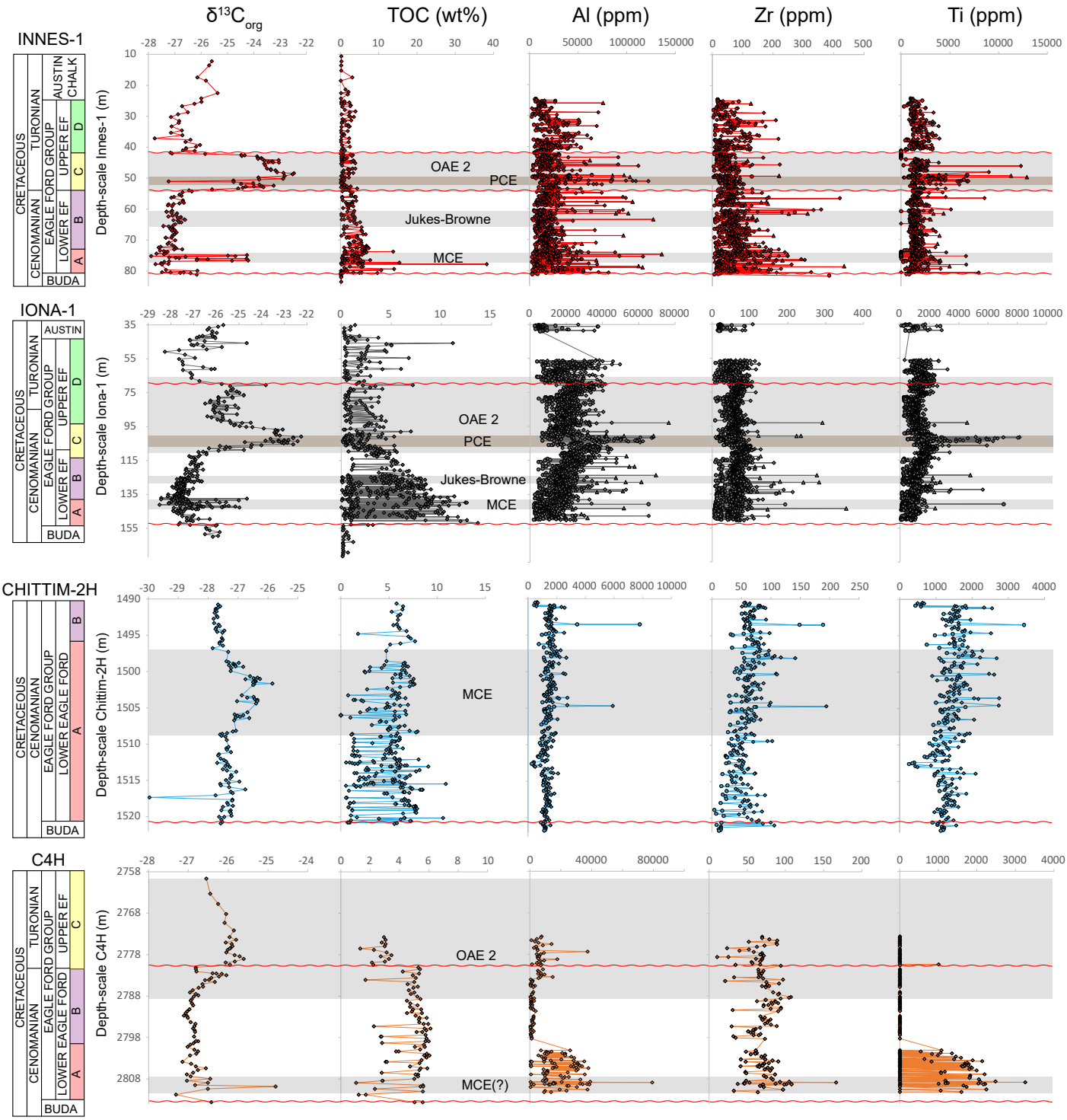

Figure 5.4: Data from the Western Interior Seaway cores including Innes-1, Iona-1, Chittim-2H and C4H. ($\delta^{13}C_{org}$) (‰; this study; Eldrett et al., 2014; Eldrett et al., 2015a; Eldrett et al., 2016), TOC (wt%; this study; Scaife et al., 2017), Ti (ppm; this study, see Appendix C) and Al (this study) and Zr (ppm; this study). For Innes-1, Iona-1 and Chittim-2H circles denote limestones (red in Innes-1, grey in Iona-1 and blue in Chittim-2H, diamonds denote marlstones (red in Innes-1, grey in Iona-1 and blue in Chittim-2H) and triangles denote bentonites (red in Innes-1, grey in Iona-1 and blue in Chittim-2H). For C4H diamonds represent all facies. Includes a stratigraphic column that contains corresponding depositional unit (A-D) of the Eagle Ford discussed in this study.

from 61 m and 124.3 m respectively, coinciding with the end of the Jukes-Browne Event. At the base of depositional unit B redox sensitive trace metals start to decline below the boundary between the Lower Eagle Ford and Eagle Ford Groups. For Innes-1, Iona-1 and Chittim-2H this section records combined trace metal enrichment factor averages of Mo_{EF}=91, U_{EF}=24 and V_{EF}=5 for limestone beds, and Mo_{EF}=193, U_{EF}=22 and V_{EF}=10 for marlstone beds.

In comparison to depositional unit A, the concentration of detritus-related trace metals in depositional unit B decrease slightly in the marlstone beds and increase in the limestone beds (Figures 5.4). For Innes-1, Iona-1, and Chittim-2H this section records combined trace metal averages of Zr=70 ppm, Al=19368 ppm and Ti=1408 ppm in the marlstone beds and Zr=55 ppm, Al=14320 ppm and Ti=1494 ppm in the limestone beds. Iona-1 observes an increase in Zr, Al and Ti towards the end of the depositional unit B from 124.3 m onwards. Minor Cu, Mn and Fe enrichments of 2, 10 and 5000 respectively occur between 60-64 m in Innes-1 and 125-128 m in Iona-1 occurring in conjunction with the Jukes-Browne Event.

Depositional unit C comprises the lower part of the Upper Eagle Ford (Figures 5.2, 5.3, 5.4 and 5.5), and is characterized by a significant drop to very low redox sensitive trace metal enrichments, with lowest values being found at the onset of OAE 2 (circa. 53 m in Innes-1 and 109 m in Iona-1) and a slight recovery from 51 m in Innes-1 and 105 m in Iona-1 upwards. For Innes-1, Iona-1 and Chittim-2H this unit records combined trace metal enrichment factor averages of Mo_{EF}=25, U_{EF}=14 and V_{EF}=2 for limestones, and Mo_{EF}=23, U_{EF}=12 and V_{EF}=3 for marls. Al and Ti concentrations increase substantially from depositional units B to C and a $\sim$20,000 ppm and $\sim$5000 ppm excursion can be observed between 104 m and 100 m in Iona-1 and 51 m and 48 m in Innes-1. Furthermore, significant Fe, Mn and Cu enrichments relative to global average shale are also recorded between 104 m and 100 m in Iona-1 and 51 m and 48 m in Innes-1, a section corresponding to the 'benthonic foraminiferal zone' (Eldrett et al., 2014). For Innes-1 and Iona-1 this section records trace metal averages of Zr=63 ppm, Al=2753 ppm and Ti=1988 ppm in the marlstone beds and Zr=36 ppm, Al=19264 ppm and Ti=1828 ppm in the limestone

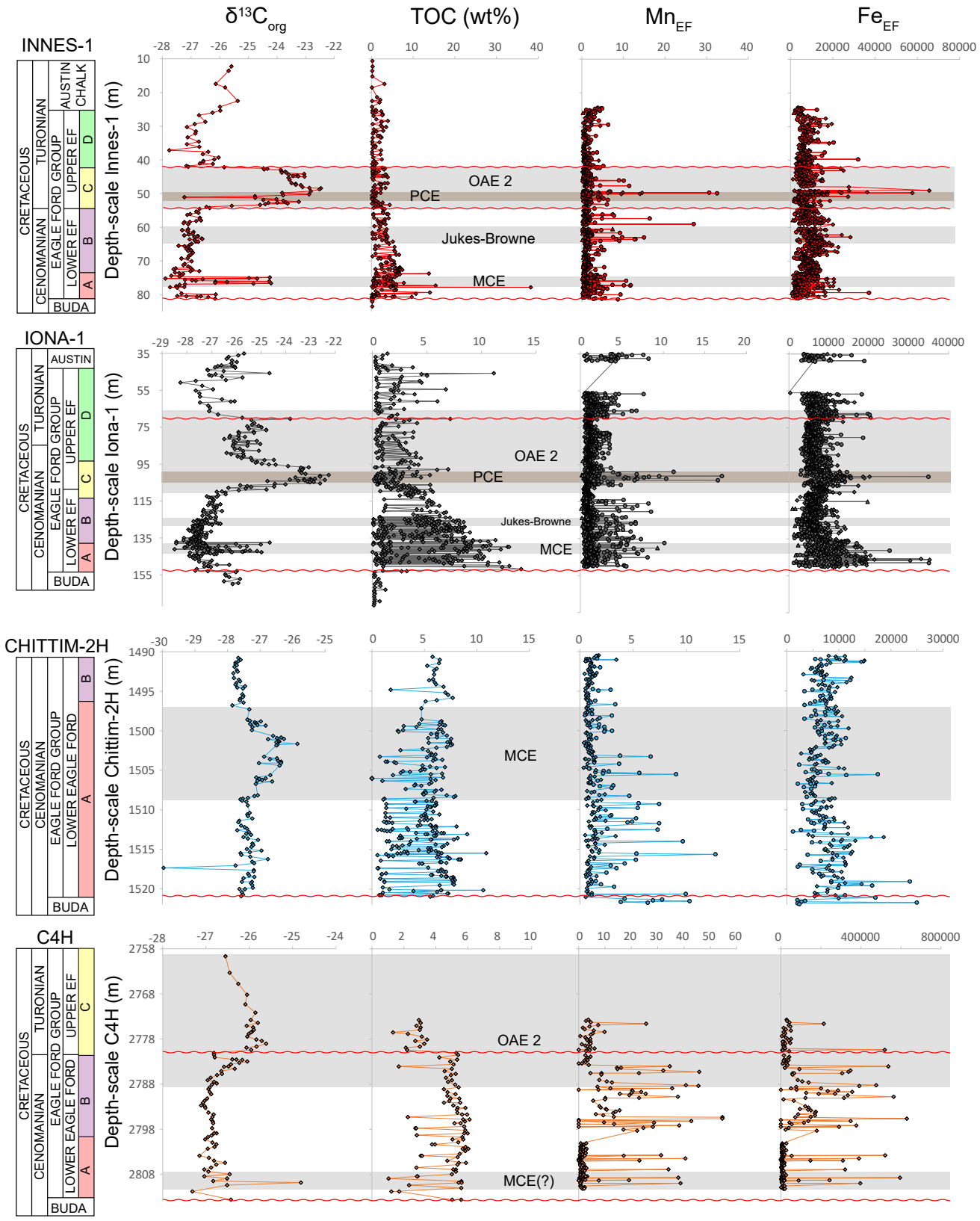

Figure 5.5: Data from the Western Interior Seaway cores including Innes-1, Iona-1, Chittim-2H and C4H. ($\delta^{13}C_{org}$) (‰ ; this study; Eldrett et al., 2015a; Eldrett et al., 2016; Eldrett et al., 2014), TOC (wt%; this study; Scaife et al., 2017), Fe_{EF} (this study) and Mn_{EF} (this study). For Innes-1, Iona-1 and Chittim-2H circles denote limestones (red in Innes-1, grey in Iona-1 and blue in Chittim-2H, diamonds denote marlstones (red in Innes-1, grey in Iona-1 and blue in Chittim-2H) and triangles denote bentonites (red in Innes-1, grey in Iona-1 and blue in Chittim-2H). For C4H diamonds represent all facies. Includes a stratigraphic column that contains corresponding depositional unit (A-D) of the Eagle Ford discussed in this study.

beds.

Depositional unit D coincides with the upper part of the Upper Eagle Ford (Figures 5.2, 5.3, 5.4 and 5.5), characterized by low redox sensitive trace metal enrichments, but slightly higher than depositional unit C. For Innes-1, Iona-1 and Chittim-2H this section records combined trace metal enrichment factor averages of Mo_{EF}=30, U_{EF}=24 and V_{EF}=2 for limestones, and Mo_{EF}=48, U_{EF}=10 and V_{EF}=2 for marls. This depositional unit has higher concentrations of detrital-related trace metals in comparison to A and B, however, slightly lower than C. Both Innes-1 and Iona-1 show slight decreases in the concentrations of Al, Ti and Zr at the base of depositional unit C ($\sim$42.1 m in Innes-1 and $\sim$66.3 m in Iona-1) before increasing again to higher concentrations at around 40.5 m in Innes-1 and 60 m in Iona-1. For Innes-1 and Iona-1 this section records trace metal averages of Zr=65 ppm, Al=23635 ppm and Ti=1557 ppm in the marlstones and Zr=36 ppm, Al=13505 ppm and Ti=1101 ppm in the limestones.

5.4.5 Mineralogy

5.4.5.1 Bulk Mineralogy

Calcite, quartz and clays are the dominant minerals in both Iona-1 and Chittim-2H with minor amounts of plagioclase, dolomite and pyrite (Figure 5.6 and 5.7). Depositional units A and B are dominated by high concentrations of calcite (60-80%), quartz (10-15%) and clays (15-40%). Clay and quartz concentrations increase (10%) and calcite concentrations decrease (15%) during the MCE (1508-1495 m in Chittim-2H, 143-137 m in Iona-1), minor spikes in plagioclase ($\sim$5%), pyrite ($\sim$4%) and dolomite ($\sim$1.5%) also occur throughout this interval. Depositional unit C shows a general decrease in calcite of between 20-30%, an increase of clays of up to 20%, and an increase of quartz of up to 15%. Pyrite, marcasite, dolomite and plagioclase also show minor incursions throughout this section. Between 104m and 100 m in Iona-1, a 15% increase in clay and quartz concentration accompanies a 20-30% decrease in calcite concentration. These data cover the start of depositional unit D

which generally displays a decrease in total clays and quartz (10% each), and an increase in calcite (20%).

5.4.5.2 Clay Mineralogy

Clay assemblages of Iona-1 and Chittim-2H are composed of kaolinite, smectite, illite, and illite-smectite mixed layer (I/S mixed layer; Figure 5.8 and 5.9). Depositional units A and B are dominated by kaolinite (15-20%) and smectite (30-40%) with smaller amounts of illite (∼10%) and I/S mixed layer (10%). Between 1508 m and 1495 m in Chittim-2H and 143 m and 137 m in Iona-1, kaolinite concentrations increase by ∼15% and smectite concentrations decreases by ∼10%; there is also

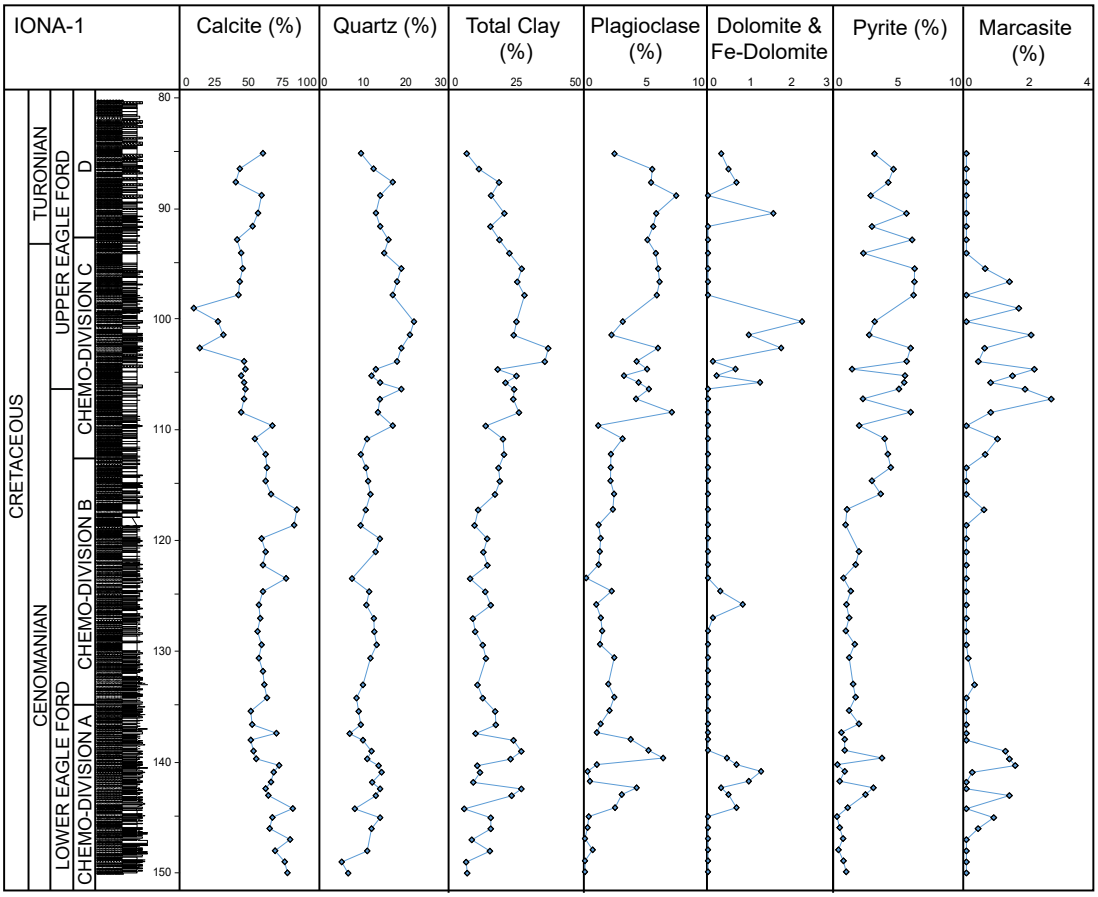

Figure 5.6: Bulk rock analysis of the mineralogy of the Iona-1 core including calcite (%), quartz (%), total clay (%), plagioclase (%), dolomite and Fe-dolomite (%), pyrite (%) and marcasite (%). Includes a stratigraphic column modified from Chapter 3 and corresponding depositional unit (A-D) of the Eagle Ford discussed in this study.

a minor increase in illite concentrations of 5%. In depositional unit C, smectite concentrations decrease by 15-20% and kaolinite concentrations decrease by ∼15%. Between 104 m and 100 m, around the benthonic foraminiferal zone (Eldrett et al., 2014), kaolinite concentrations decrease by up to 20% and smectite concentrations increase by 20-25%. A decrease in illite concentrations of 5-10% between 102-98 m, lags the increasing abundance of smectite. The kaolinite/smectite ratio is a humidity index (Chamley, 1989; Pardo et al., 1999; Adatte et al., 2002) which shows high ratios in depositional units A and C around the MCE and OAE 2 (Figure 5.8 and 5.9).

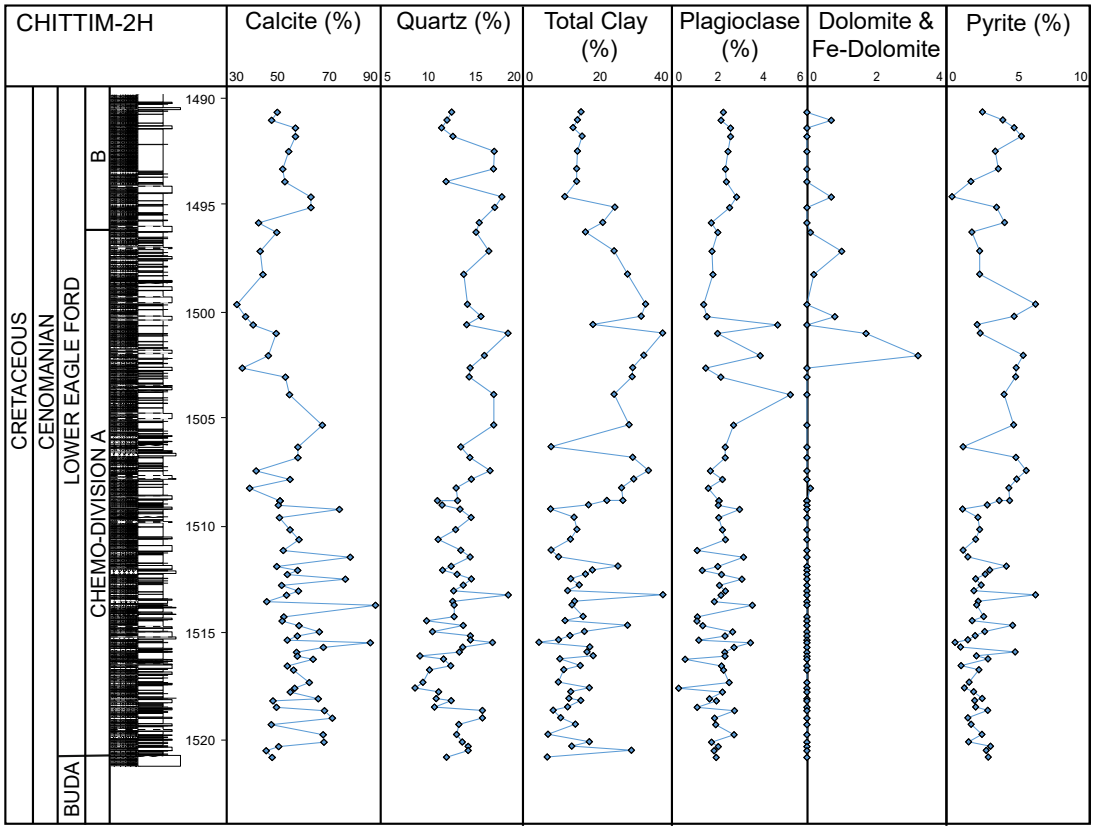

Figure 5.7: Bulk rock analysis of the mineralogy of the Chittim-2H core including calcite (%), quartz (%), total clay (%), plagioclase (%), dolomite and Fe-dolomite (%) and pyrite (%). Includes a stratigraphic column modified from Chapter 3 and corresponding depositional unit (A-D) of the Eagle Ford discussed in this study.

5.5 Discussion

5.5.1 Principal Component Analysis (PCA)

In order to provide additional understanding into the main controls on organic matter composition and paleoenvironmental significance, PCA was

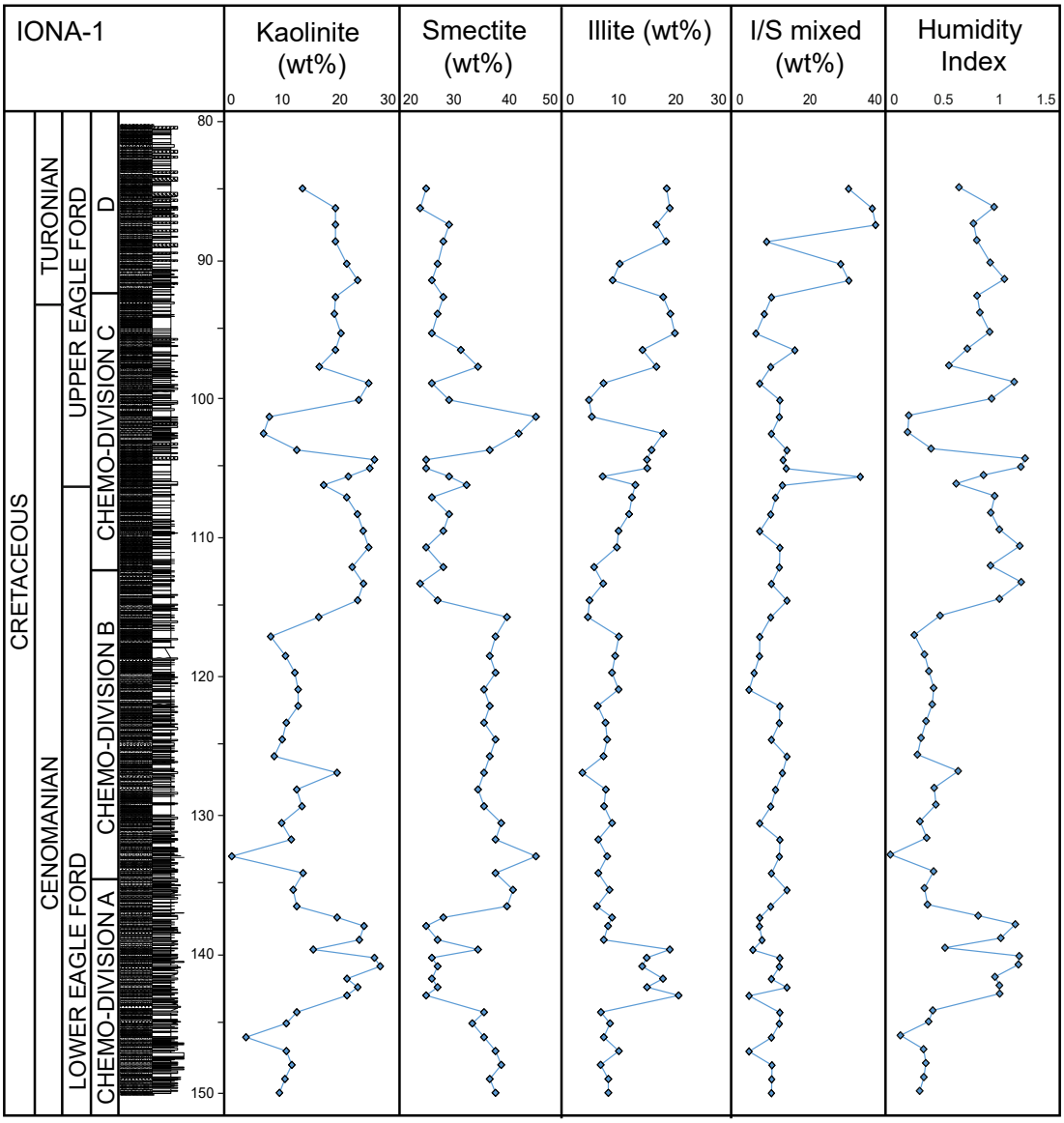

Figure 5.8: Clay mineralogical analysis of the Iona-1 core including kaolinite (%), smectite (%), illite (%), illite-smectite mixed layer (%), humidity index (kaolinite:smectite ratio). Includes a stratigraphic column modified from Chapter 3 and corresponding depositional unit (A-D) of the Eagle Ford discussed in this study.

conducted on the geochemical datasets. PCA was run on each core that had multiple detailed analyses from the same core sample/depth, including Innes-1, Iona-1 and Chittim-2H using the statistical software C2 (http://www.staff.ncl.ac.uk/stephen.juggins/software/C2Home.htm). Variables within the dataset include major and trace elements, δ^{13}_{org} and TOC. The PCA results show a clear grouping of samples along the two primary axes (Figure 5.11). All three cores analysed showed similar principal components and clusters and in support of the discussion only the PCA results run on the combined dataset are presented.

Four groups were identified and stratigraphically defined: depositional unit A = lowermost lower Eagle Ford; depositional unit B = uppermost lower Eagle Ford; depo-

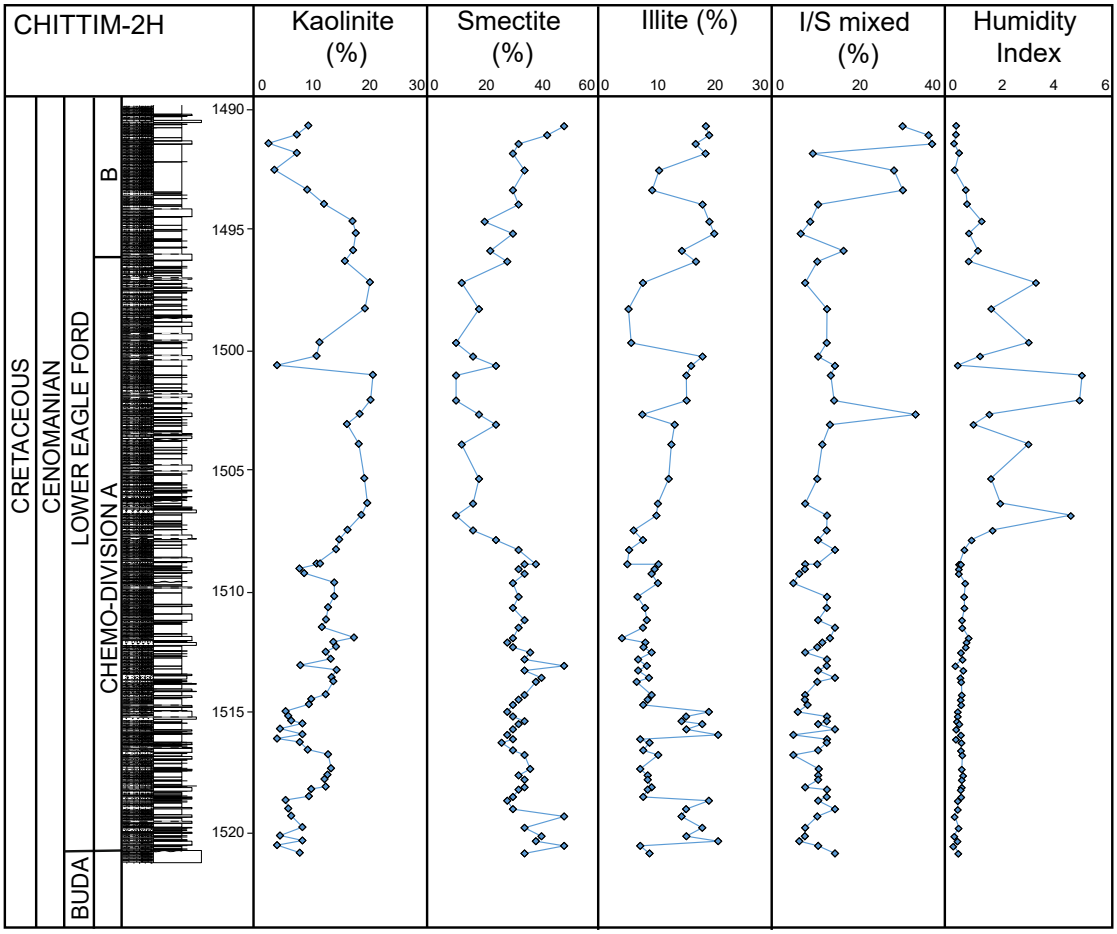

Figure 5.9: Clay mineralogical analysis of the Chittim-2H core including kaolinite (%), smectite (%), illite (%), illite-smectite mixed layer (%), humidity index (kaolinite:smectite ratio). Includes a stratigraphic column modified from Chapter 3 and corresponding depositional unit (A-D) of the Eagle Ford discussed in this study.

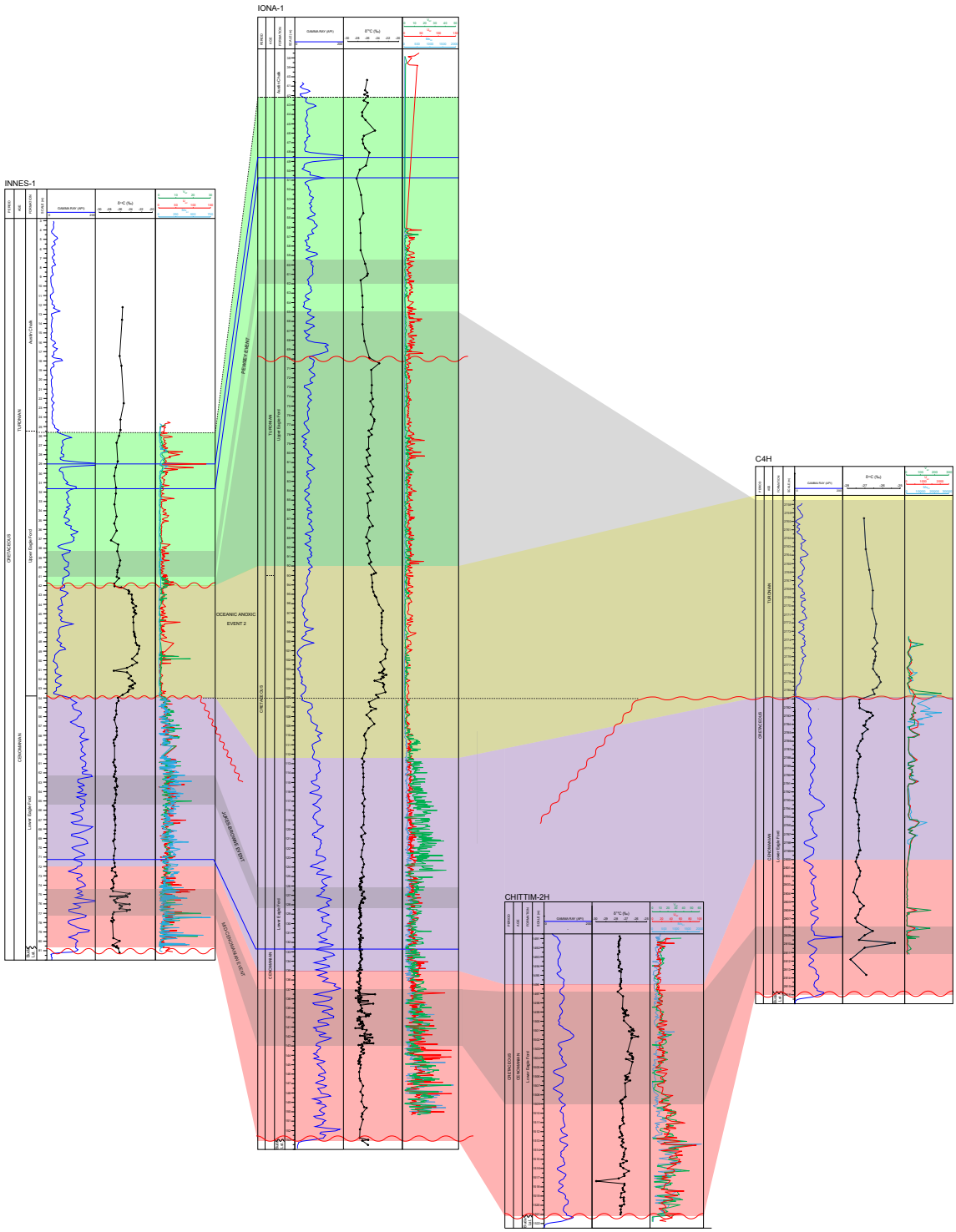

Figure 5.10: Correlatable transect of gamma ray, ($\delta^{13}C_{org}$), and overlain redox sensitive trace metal enrichment factor data (Mo_{EF}, U_{EF} and V_{EF}) from the Western Interior Seaway Innes-1, Iona-1, Chittim-2H and C4H. This figure includes the correlation of depositional units A-D across the study area as well as a base correlation from Chapter 3.

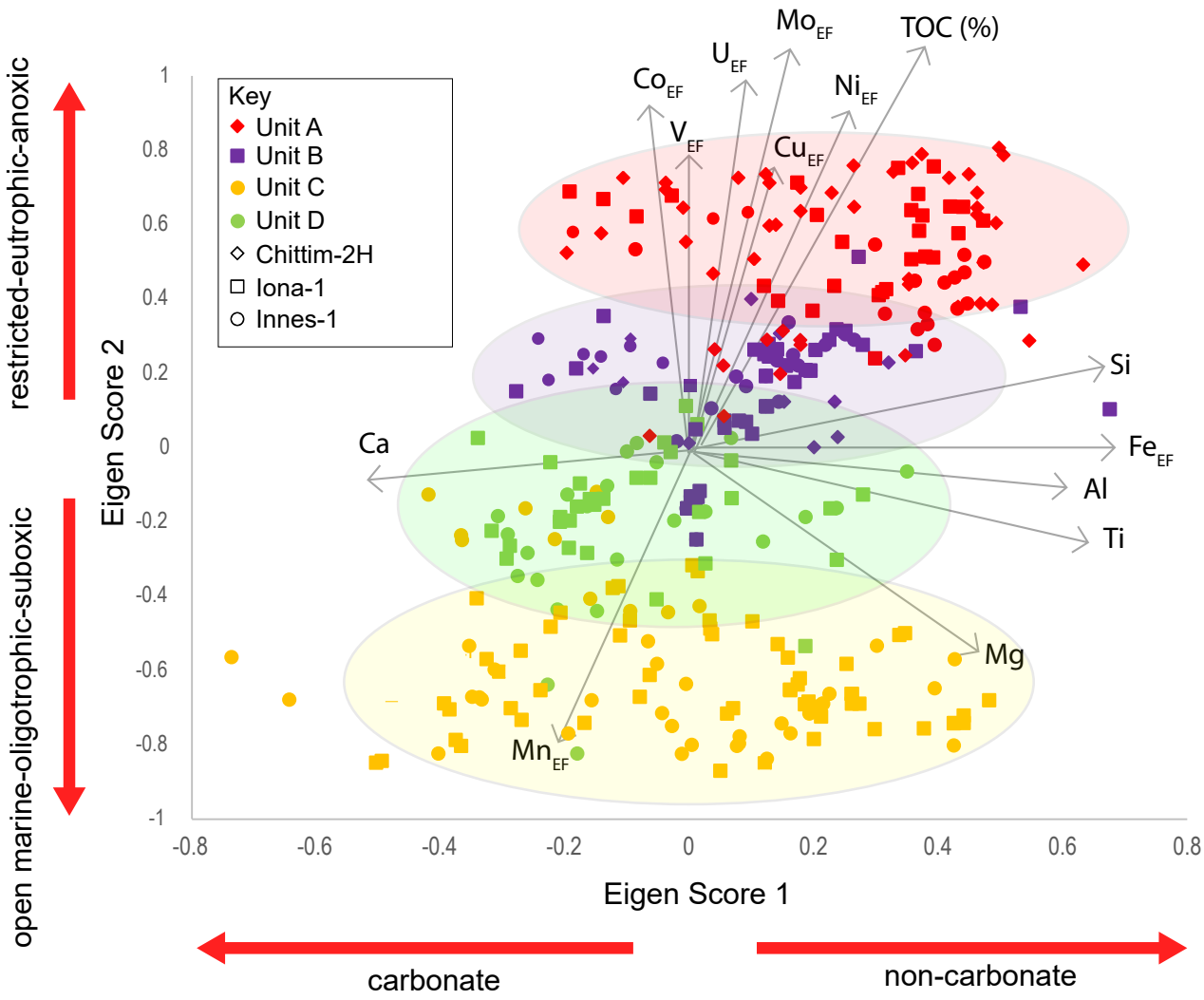

Figure 5.11: PCA results showing principle axis/eigen scores; selected environmental variables. Samples plotted as a function of site location (see insert) and lithostratigraphic interval (colours; groups in figure).

sitional unit C = lowermost upper Eagle Ford; and depositional unit D = uppermost upper Eagle Ford. Along the y-axis/ eigen score 1, samples with high negative scores comprise high Ca contents, whereas positive scores correspond with high concentrations of Si, Fe, Al and Ti. As such these are likely to indicate increased terrigenous contributions , i.e. terrestrial/ detrital riverine dilution, or possible diagenetic alteration of volcanic ash into clays (Eldrett et al., 2015b). Therefore, the clustering of the environmental variables along Eigen score 1 is interpreted as representing the carbonate - non carbonate mixing trend.

Eigen score 2 is interpreted to represent a restricted/anoxic/eutrophic to olig-

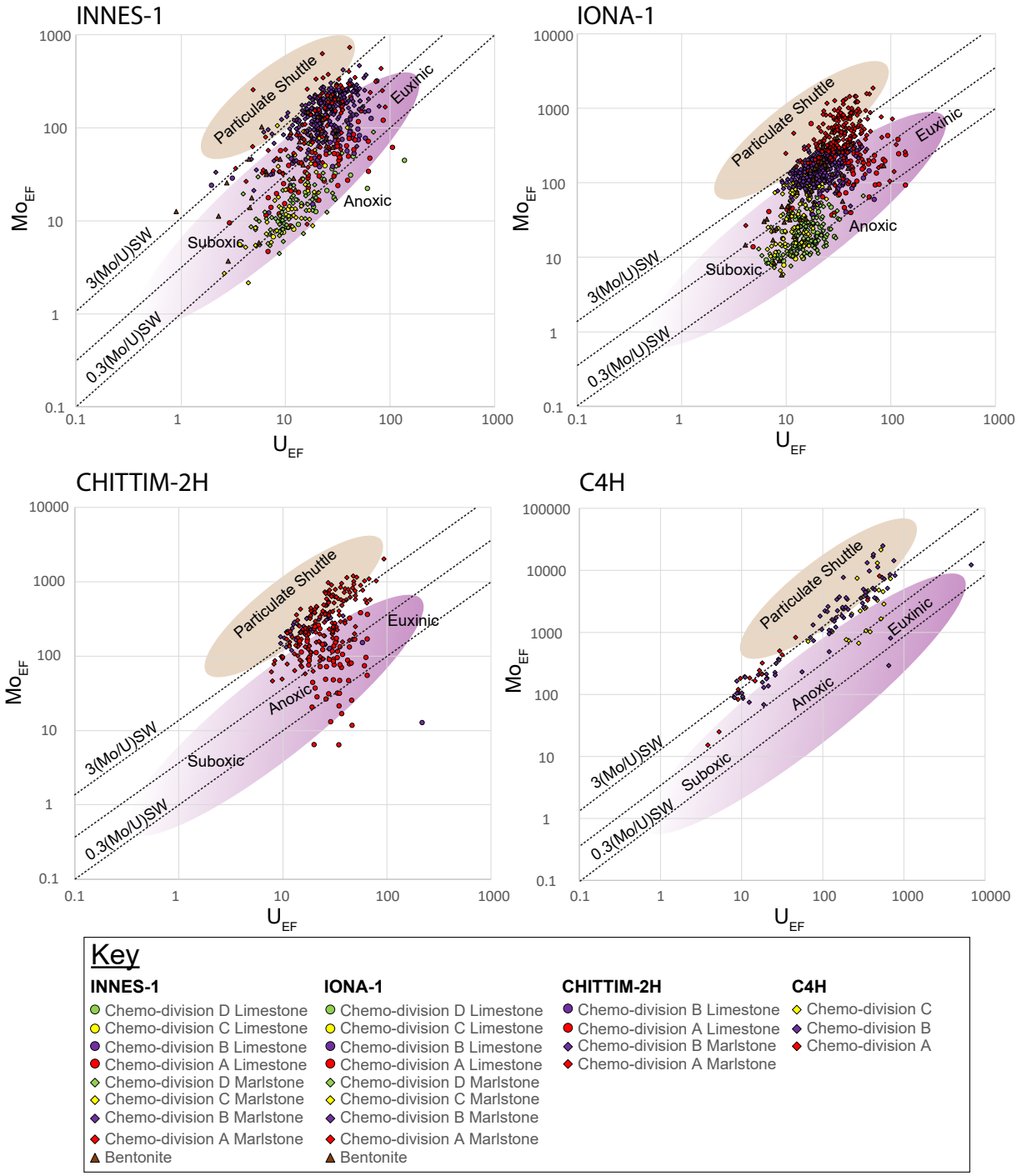

Figure 5.12: Logarithmic plots of Mo_{EF}:U_{EF} covariance for Innes-1, Iona-1, Chittim-2H and C4H. Diagonal dashed lines represent multiples (0.3, 1, and 3) of Mo_{EF}:U_{EF} ratio (3) of present-day seawater (SW). Values greater than x3 SW are generally associated with the particulate shuttle; whereas those trending with modern day sea water reflect an unrestricted marine trend. Cores are divided into depositional units: A is represented by green symbols, B is represented by yellow symbols, C is represented by purple symbols and D is represented by red symbols. For Innes-1, Iona-1, Chittim-2H and C4H circles denote limestones, diamonds denote marlstones and triangles denote bentonites in all three cores. For C4H diamonds represent all facies. Relative enrichment of Mo_{EF} compared to U_{EF} suggest an active cycling of Mn-Fe particulates (especially Mn-oxyhydroxides) between the water column and sediment water interface, characteristic of a "particulate shuttle" (Algeo and Tribovillard, 2009; Tribovillard et al. 2012).

otrophic/suboxic marine trend with high positive scores associated with high values in TOC and redox sensitive trace metal concentrations. High negative eigen scores are associated with proxies indicative of more oxygenated water conditions such as lower concentrations in redox sensitive trace metals. The negative eigen scores are therefore interpreted as representing more open marine, oxygenated and oligotrophic depositional environments. Trace metal enrichment factors are plotted against depth for each of the sites in Figures 5.1 to 5.4 and section 5.5.2.1 to further support the paleoenvironmental interpretation discussed below.

5.5.2 Geochemical proxies as an environmental index

Depositional units A, B, C and D are representative of different depositional conditions during the development of the Eagle Ford Group (Figure 5.10). Based on the strong relative enrichments of Mo, U and V compared to average shale, it can be interpreted that the water column and sediment pore waters were anoxic during significant parts of depositional unit A. The Mo enrichment is indicative of the presence of H_2S suggesting that the bacterial degradation of organic matter occurred at least partly by sulfate reduction, and therefore euxinia is highly likely. Furthermore, the relative enrichment of Mo_{EF} compared to U_{EF} (Figure 5.12) in depositional unit A and the high concentrations of pyrite at 139.7 m and 142.4 m in Iona-1 (Figure 5.6) suggest an active cycling of Mn-Fe particulates (especially Mn-oxyhydroxides) between the water column and sediment water interface, characteristic of a ”particulate shuttle” (Algeo and Tribovillard, 2009; Tribovillard et al. 2012).

Mn-Fe cycling accelerates the transfer of Mo_{auth} to the sediment relative to other redox-sensitive trace metals (e.g., U) that do not participate in this particulate shuttle, leading to elevated $(Mo/U)_{auth}$ ratios. Particulate MnFe-oxyhydroxides form at the chemocline indicating periods of water column stratification during the deposition of depositional unit A. The importance of MnFe redox cycling for authigenic Mo accumulation is dependent on the vertical position of the chemocline. Such redox cycling has little influence on Mo_{auth} accumulation where the chemocline is located (1) within the sediment, as in oxicsuboxic facies, or (2) high within a stably stratified

anoxic water column, as in the Black Sea or Framvaren Fjord, where molybdate is reductively released back into the water column (Jacobs et al., 1985; Skei et al., 1996; Crusius et al., 1996). Comparatively, in environments which are subject to redox variations over short timescales, MnFe redox cycling may be a major factor in enhancing Mo transfer to the sediment (Murray, 1975; Crusius et al., 1996). In such settings, vertical fluctuations in the position of the chemocline alternately promote (1) Mo scavenging, by suplhides, in the water column when the chemocline recedes below the sediment/water interface and oxidizing (albeit suboxic) deepwaters catalyze precipitation of solid-phase MnFe-oxyhydroxides, and (2) Mo release at the sediment/water interface when the chemocline rises into the water column and sulfidic bottomwaters catalyze reductive dissolution of MnFe-oxyhydroxides in surficial sediments (Algeo and Lyons, 2006). This process represents a Mo pump that may be responsible for the exceptionally large Mo_{auth} burial fluxes in marine systems such as the Cariaco Basin and Saanich Inlet (Algeo and Lyons, 2006).

The drop in redox sensitive and other trace metal concentrations at the onset of the MCE in depositional unit A is likely related to global trace metal drawdown through sedimentation (Algeo and Lyons, 2006). This is similar to the recorded depletion of sedimentary redox sensitive trace metals during the onset of OAE 2 which has been proposed to reflect the draw-down of the global trace metal sea-water inventory due to sequestration in sediments under expanded anoxic/euxinic conditions (Hetzel et al. 2009; Dickson et al. 2016, 2017; Goldberg et al. 2016; Owens et al., 2016). There are fewer the potential sinks for these trace metals around the onset of the MCE compared to the black shales deposited in the Tethys and in the proto-North Atlantic Ocean of OAE 2 (e.g. Kuhnt et al., 1990). Nevertheless, evidence for mid-Cenomanian organic-rich facies is widespread, including the occurrence of potential sinks in the North Atlantic at Site 367 (Cape Verde Basin), Site 398 (Vigo Seamount), and Site 386 (Bermuda Rise) (Cool, 1982; Arthur and Dean, 1986; Summerhayes, 1987). Moreover, a thin, laminated organic-rich layer of early mid-Cenomanian age also occurs in the Vocontian Trough (Jenkyns et al., 1994). Even in the absence of a global occurrence of organic-carbon-rich beds, the MCE marks a distinct lithological change to darker coloured sediments in both the Scaglia

Bianca Formation of the Umbria-Marche Basin and the Cenomanian Lower Chalk Formation in East Kent (Southeastern England; Coccioni and Galeotti, 2002).

The strong enrichments of redox sensitive trace metals Mo, U and V relative to average shale indicate that depositional unit B was also deposited under anoxic to euxinic conditions (Figure 5.2 and 5.10). However, the decrease in Mo enrichments may indicate decreased H_2S availability and therefore a change from euxinic to anoxic conditions (Figure 5.12). Furthermore, the decrease of Mo_{EF} relative to U_{EF} as seen in depositional unit B compared to A (Iona-1; Figure 5.12) may be due to the relative decrease of water column Fe and subsequent end to the particulate shuttle removing Mo in the form of pyrite (Figure 5.8 and 5.9).

The onset of depositional unit C coincides with the large positive carbon isotope excursion of OAE 2 and a decrease in TOC values in both Innes-1 and Iona-1 (Figure 5.10). The decrease in Mo_{EF}, U_{EF} and V_{EF}, as well as the relative concentrations of Mo_{EF} to U_{EF}, may indicate a shift to suboxic depositional conditions (Figure 5.12). Previous studies have suggested that global drawdown of Mo and other redox sensitive trace metals may be responsible for drops in their concentrations around the onset OAE 2 (Hetzel et al. 2009; Owens et al., 2016). Furthermore, negative $\delta^{15}N$ values found around the Cenomanian-Turonian boundary of the Eagle Ford Group from outcrop studies in the Waco area have been suggested to indicate a fixation of N from the atmosphere by cyanobacteria (Boling and Dworkin, 2016). The need for increased fixation of atmospheric N may have arisen from the removal of dissolved inorganic N by bacterial denitrification and anaerobic oxidation of ammonia (Sachs and Repeta, 1999; Kuypers et al., 2004). An ecosystem that would favour the fixation of atmospheric N would be one in which N is the bio-limiting nutrient, while other nutrients such as P were readily available (Karl et al., 2002). In the present day, this only occurs in areas of upwelling in the presence of oxygen minimum zones. This suggests that oxygen levels were still very low in this depositional environment at that time (Boling and Dworkin, 2016). However, marcasite is present between 106 m and 95 m in Iona-1 (Figure 5.6). Marcasite may form from pyrite as a result of oxygen in overlying sea water diffusing downward through the sediment

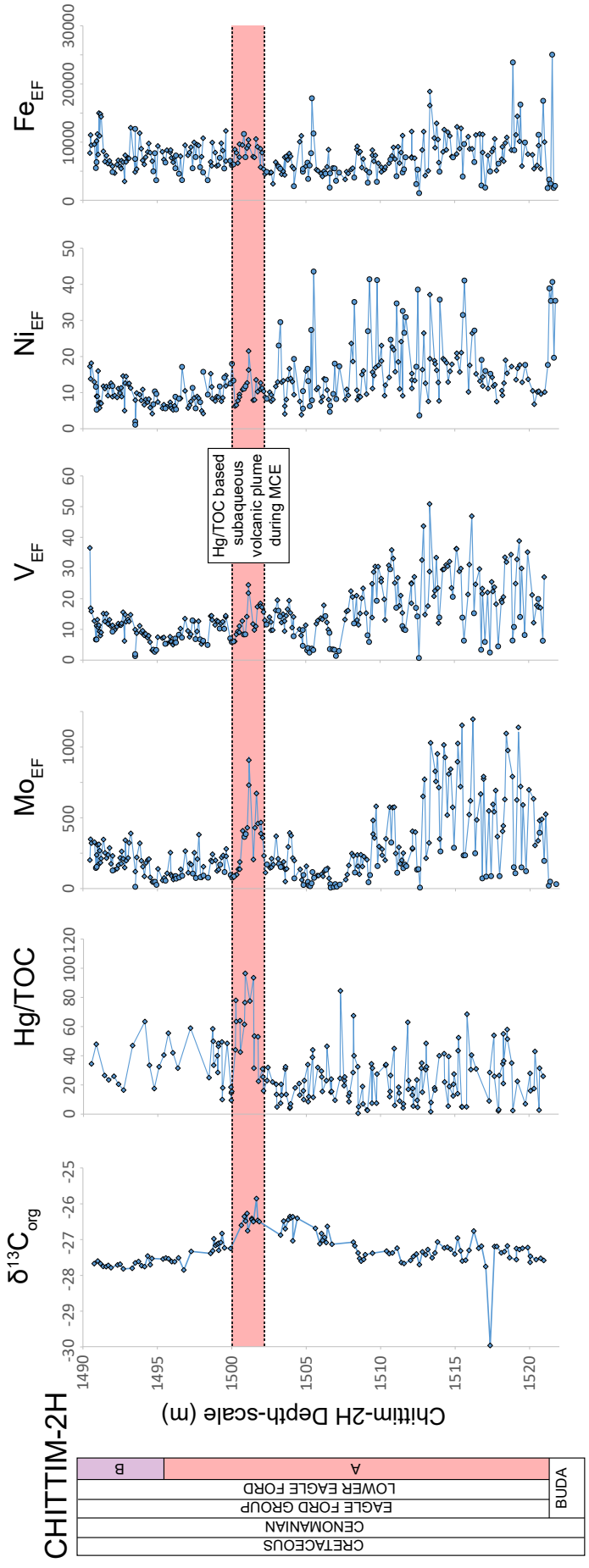

Figure 5.13: Data from Chittim-2H. ($\delta^{13}C_{org}$) (‰; this study), Hg/TOC (this study; Scaife et al., 2017), Mo_{EF} (this study), V_{EF} (this study), Ni_{EF} (this study) and Fe_{EF} (this study). Displaying a coincidence between the Hg/TOC excursion during the MCE and trace metal enrichments in the southern Western Interior Seaway. This possibly indicates a genetic relationship between the occurrence of a subaqueous volcanic plume and trace metal enrichments at this time. Circles denote limestones, diamonds denote marlstones and triangles denote bentonites in all cores. Includes a stratigraphic column that contains corresponding depositional units (A-D) of the Eagle Ford discussed in this study.

as a migrating oxidation front (Schieber, 2011). Therefore, this suggests that multiple oxygenation events may have occurred during the deposition of the sedimentary sequences within depositional unit C. These re-oxygenation events may indicate a dynamic ocean circulation system during the deposition of depositional unit C, such as that proposed by Trabucho Alexandre (2010), or alternatively may be indicative of variations in eustasy related to regional tectonic and/or mantle plume-lithosphere dynamics associated with the emplacement of LIPs (i.e. High Arctic or Caribbean; Eldrett et al., 2017; Scaife et al., 2017) .

The base of depositional unit D coincides with the end of the large positive carbon isotope excursion of OAE 2 in Innes-1 and a 1.5 ‰ decrease in the carbon-isotope excursion of OAE 2 in Iona-1 (Figure 5.10). A slight recovery in the concentrations of redox sensitive trace metals relative to average shale in depositional unit D possibly indicates a minor decrease in water column and pore water oxygenation during deposition following the end of the major carbon cycle perturbation or alternatively an increase in the global trace-metal seawater inventory (Figure 5.2).

5.5.2.1 Trace metal anomalies as an indicator for water-mass incursions

Many trace metals in the Innes-1, Iona-1 and Chittim-2H cores display clear enrichments relative to average shale corresponding to both the MCE and OAE 2. Chittim-2H and Iona-1 both display enrichments of Cu, Mo and Ni, and Innes-1 and Iona-1 display enrichments of V, Cu and Ni, coinciding with the latter half of the MCE (Figure 5.2, 5.3). Stratigraphically higher, between 60 m and 64 m in Innes-1 and 125m and 128 m in Iona-1, significant enrichments in Cu, Mn and Fe relative to average shale occur, and positive excursions in concentrations of Ti and Al are also observed (Figures 5.3, 5.4 and 5.5). Possible sources of trace metals, particularly mafic trace metals such as copper, to the Western Interior Seaway include: (1) basalt hydrothermal alteration, enhanced by accelerated seafloor spreading or emplacement of LIPs (Snow et al., 2005; Jenkyns et al., 2017); (2) changes in the redox or productivity state of the water column or at the sediment-water interface (e.g. Brumsack, 2006; Tribovillard et al. 2006; Algeo et al. 2012); (3) local-scale re-

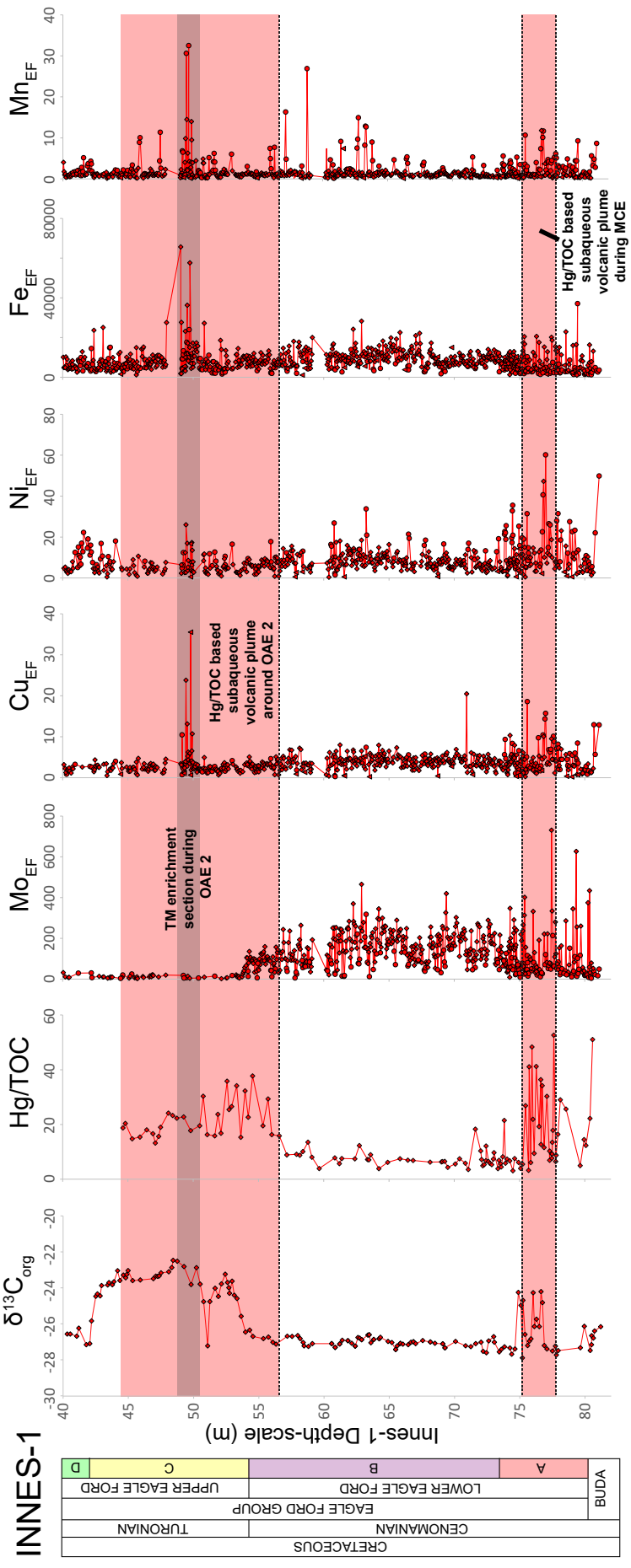

Figure 5.14: Data from Innes-1. ($\delta^{13}C_{org}$) (‰; this study; Eldrett et al., 2016), Hg/TOC (this study; Scaife et al., 2017), Mo_{EF} (this study), Cu_{EF} (this study), Ni_{EF} (this study), Fe_{EF} (this study) and Mn_{EF} (this study). Displaying a coincidence between the Hg/TOC excursion and Mo, Cu and Ni enrichments during the MCE in the southern Western Interior Seaway. This possibly indicates a genetic relationship between the occurrence of a subaqueous volcanic plume and trace metal enrichments at this time. Comparatively, trace metal enrichments during OAE 2 do not coincide with the volcanically derived Hg/TOC excursion. Instead Ni, Fe, Mn, and Cu enrichments indicate an influx of trace metals during the Plenus Cold Event. Circles denote limestones, diamonds denote marlstones and triangles denote bentonites in all cores. Includes a stratigraphic column that contains corresponding depositional units (A-D) of the Eagle Ford discussed in this study.

mobilization within the sediment column or into the overlying water-column (Owens et al., 2012; Jenkyns et al., 2017); (4) detrital flux from the adjacent Sevier orogenic belt (Meyers et al., 2012; van Helmond et al., 2013); (5) Plinian volcaniclastic deposits, which are abundant in the Western Interior Seaway cores, and/or; (6) an extraterrestrial impact (Orth et al., 1993). The MCE trace metal anomalies coincide with a strong mercury enrichment relative to TOC (Hg/TOC; Figure 5.13, 5.14 and 5.15), an enrichment suggested to derive from a hydrothermal subaqueous plume (Scaife et al., 2017). The increased sedimentary concentration of these trace metals around the main volcanically derived Hg peak, points towards a volcanic source for the elevated oceanic trace metal concentrations at this time. This subaqueous volcanic plume has been argued to originate from either the High Arctic Large Igneous Province or Caribbean Plateau (Scaife et al., 2017) and may indicate an incursion by either a northern or southern water-mass during the MCE.

Comparatively, the Mn, Fe, Ti, Al and Cu trace metal excursions in Innes-1 and Iona-1 occur around the Plenus Cold Event (PCE) and do not correspond to a specific Hg/TOC excursion (Figure 5.14 and 5.15). Mn can become concentrated in stratified water columns as it displays an active biogeochemical cycle across redox boundaries at or above the sediment-water interface (Canfield et al., 1993). Mn redox cycling is of primary importance for trace-metal enrichment in suboxic-anoxic systems because it can trigger and/or accelerate the transfer of trace elements from seawater to the sediment as well as diagenetically remobilize trace elements within the sediment (e.g., Morford et al., 2005 and references therein). However, the iron enrichment relative to average shale and other mafic elements such Cu supports subaqueous LIP emplacement over other potential sources (Figure 5.14 and 5.15). This may further support the incursion of a water-mass during the PCE, from either Tethyan or, more likely, Boreal sources, due to evidence of the incursion of boreal fauna in the southern Western Interior Seaway at this time (Eldrett et al., 2014). Alternatively, the trace metal peaks during the PCE may result from globally reduced anoxic conditions, leading to remobilization of metals from the sedimentary reservoir into the global ocean subsequently increasing global ocean, and basinal, inventories allowing for enrichments in anoxic/euxinic depositional environments (Jenkyns

et al., 2017).

5.5.2.2 Mineralogy as a climatic index

Bulk rock and clay mineralogy, including the clay contents and detrital index, have the potential to provide an environmental and climatic index. High clay influxes inferred for depositional unit A, around the MCE, and depositional unit C, throughout OAE 2, suggesting increased weathering of silicates and high continental runoff (Figure 5.6 and 5.7), whereas low clay concentrations within depositional unit B and the base of depositional unit D suggest low continental runoff and lesser weathering of silicates (Figure 5.6 and 5.7).

Clay minerals form in a number of ways: (1) in terrestrial soils that are eroded and transported to the oceans; (2) from the degradation of ash fall deposits (bentonites; Chamley, 1989); and (3) recrystallisation of new minerals during diagenetic processes or tectonic activity (authigenesis; Chamley, 1989). However, the impact of authigenesis can be assumed to be minor as sedimentological thin section analysis indicates only very minor concentrations of authigenic kaolinite in Innes-1, Iona-1 and Chittim-2H (see Appendix A), and there is little evidence for tectonic activity in the Western Interior Seaway during the Cenomanian-Turonian. Furthermore, bentonites occur relatively evenly throughout the cores rather than concentrated in particular stratigraphical intervals and so degradation of these are unlikely to preferentially effect only one interval of the core. Therefore, changes in continentally derived clay may best explain the observations for increases in clays concentrations in the studied Western Interior Seaway cores.

Depositional unit A and C are dominated by the major clay minerals illite, kaolinite and smectite as well as displaying a low humidity index (Figure 5.8 and 5.9). Kaolinite forms under humid conditions in tropical soils, whereas smectite forms in tropical soils in dry, seasonal climate conditions or from the alteration of basalts (Chamley, 1989; Gertsch et al., 2010). In comparison, illite and IS mixed layers are largely products of mechanical erosion (Chamley, 1989). Distribution of clay

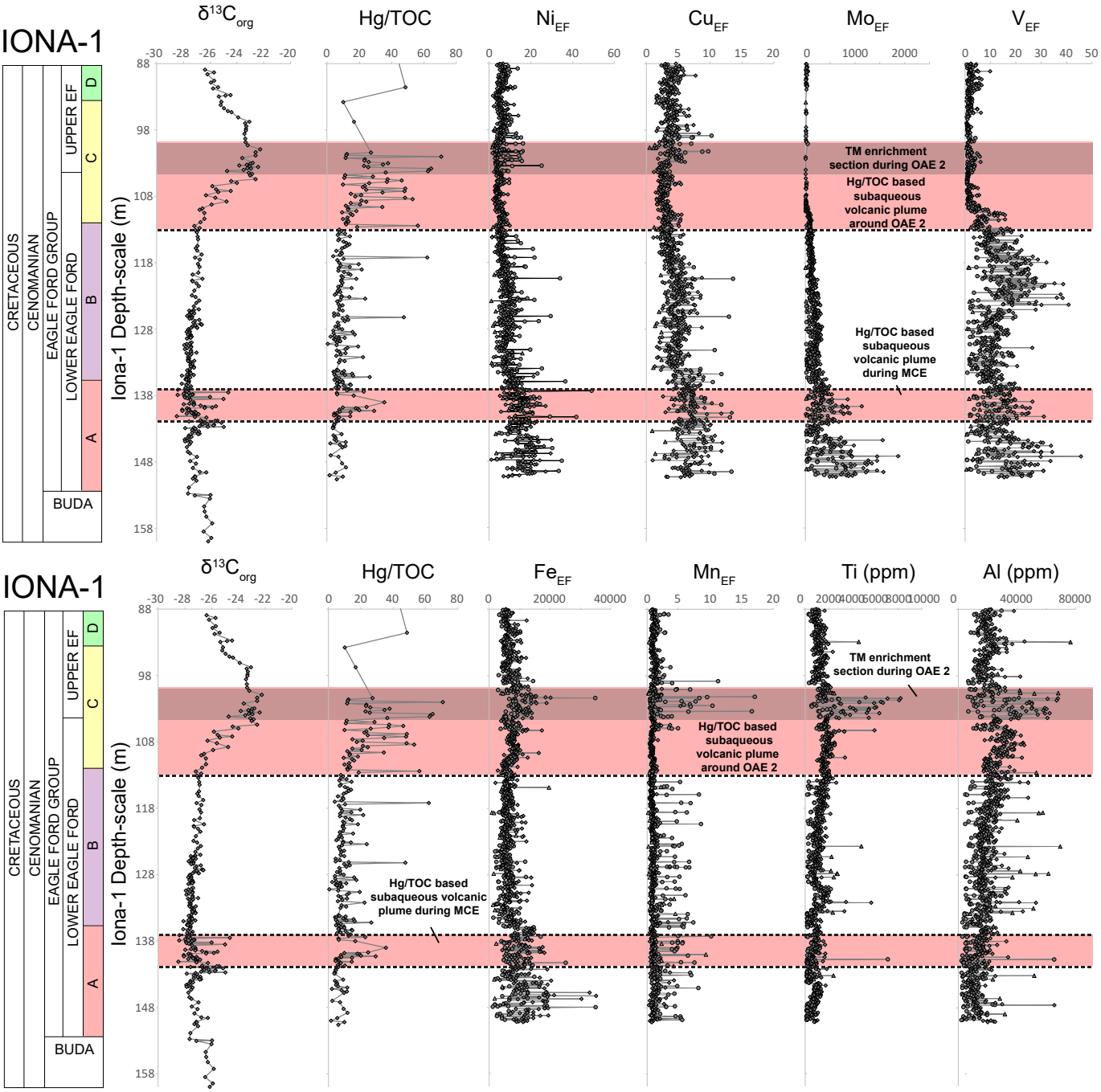

Figure 5.15: Data from Iona-1. ($\delta^{13}C_{org}$) (‰; this study; Eldrett et al., 2014), Hg/TOC (this study; Scaife et al., 2017), Ni_{EF} (this study), Cu_{EF} (this study), Mo_{EF} (this study), V_{EF} (this study), Fe_{EF} (this study), Mn_{EF} (this study), Ti (ppm; this study) and Al (ppm; this study). Displaying a coincidence between the Hg/TOC excursion and Mo, V, Fe, Cu and Ni enrichments during the MCE in the southern Western Interior Seaway. This possibly indicates a genetic relationship between the occurrence of a subaqueous volcanic plume and trace metal enrichments at this time. Comparatively, trace metal enrichments during OAE 2 do not coincide with the volcanically derived Hg/TOC excursion. Instead Fe, Mn, Cu and V enrichments as well as large excursions in the concentrations of Ti and Al indicate an influx of trace metals during the Plenus Cold Event. Circles denote limestones, diamonds denote marlstones and triangles denote bentonites in all cores. Includes a stratigraphic column that contains corresponding depositional unit (A-D) of the Eagle Ford discussed in this study.

minerals in sediments can also be influenced by the differential settling of kaolinite versus smectite and illite in the water column (Chamley 1989; Kubler and Jaboyedoff, 2000; Godet et al., 2008). However, Iona-1 and the deeper water section of Chittim-2H show comparable results suggesting a similar forcing mechanism (Figure 5.8 and 5.9). Due to the formation of kaolinite in soils under humid conditions and smectite in soils under dry conditions a kaolinite/smectite ratio has been used to indicate relative humidity (Chamley, 1989; Pardo et al., 1999; Adatte et al., 2002).

Within these constraints, and based on the relatively high smectite and low kaolinite concentrations, arid climate conditions existed throughout much of depositional units A and B (Figure 5.8 and 5.9). However, low smectite, high kaolinite and high humidity ratio sections bracketing the MCE, between 143 m and 137 m in Iona-1 and 1508 m and 1495 m in Chittim-2H, and much of OAE 2, 116-84 m in Iona-1, indicate a largely humid climate during these periods of deposition (Figure 5.8 and 5.9). Low kaolinite and high smectite abundance between 100 m and 105 m in Iona-1, coinciding with the PCE indicates a period of deposition under arid climate conditions. The increase in bulk clay concentrations in this stratigraphic interval may indicate high continental runoff (Figure 5.8) or alternatively may be due to a reduced carbonate supply. However, high illite and kaolinite at the base of the Lower Eagle Ford, in depositional unit A, and from 93-84 m in Iona-1 indicate periods where products are largely derived from mechanical erosion and therefore indicate that high continental runoff was the more likely explanation (Figure 5.8 and 5.9).

The differences in climate signals inferred from clay mineral assemblages in the Western Interior Seaway cores can be explained by an accelerated hydrological cycle and global increase in weathering rates in response to volcanism around the MCE and OAE 2 (Jenkyns, 2003; Scaife et al., 2017).

Latitudinal shifts of the Intertropical Convergence Zone (ITCZ), the dynamic boundary between south-east and north-east trade winds associated with a well-organized zonal band of low pressure and high precipitation that occurs predominantly over the ocean basin (Peterson and Haug, 2006), may offer an alternative explanation. Its latitudinal position and variations are controlled mainly by eccentricity, precession,

insolation and the percentage of continents per hemisphere (Peterson and Haug, 2006). High eccentricity during the MCE and OAE 2 has previously been suggested to cause high latitudinal variations of the ITCZ (Floegel and Wagner, 2006). However, during the Cenomanian–Turonian the latitude of the study area was greater than 25°N (e.g. Eldrett et al., 2014) and the northern ITCZ boundary varies seasonally between 0°N and 15°N (Floegel and Wagner, 2006). Modelling results have previously suggested that during OAE 2 and the MCE the importation of humidity from south to north resulted in tropical humid conditions between 0°N and 10°N and subtropical humid conditions between 10°N and 20°N in North America (Chumakov et al., 1995; Floegel and Wagner, 2006; Fluteau et al., 2007). Therefore this explanation is unlikely.

The isotopic ratios of $^{87}Sr/^{86}Sr$ and $^{187}Os/^{188}Os$, due to their concentration in continental crust as opposed to the mantle, act as fingerprints for the relative importance of fluvial supply of these elements from the continents to the marine environment versus seawater ocean–crust interaction (Elderfield, 1986; PeuckerEhrenbrink and Ravizza, 2000). For the MCE and OAE 2, a correlation of the event (as defined by the δ^{13}_{org}) with the onset of a decline in the Sr isotope curve (derived from skeletal and bulk carbonate) is observed, implying a relative increase in the supply of mantlederived strontium from hydrothermal or other mafic igneous sources (Bralower et al., 1997; Jones and Jenkyns, 2001). The Os isotope record of the Livello Bonarelli in UmbriaMarche, Italy supports this interpretation by illustrating a dramatic drop in values just below the base of the black shale (Turgeon and Creaser, 2008). However, very detailed Sr isotope analysis of primary bivalve (rudist) calcite in Italian shallow water limestones defines an interval of more radiogenic values where carbon isotope ratios, defining the onset of the OAE, rise into the positive excursion (Frijia and Parente, 2008). These critical data suggest the existence of an interval when global weathering rates increased enough to override the nonradiogenic trend in $^{87}Sr/^{86}Sr$ ratios during both the OAE 2 and the MCE.

There are three potential source areas for detrital clays in the study area. The first is the Cordilleran orogenic belt to the west. During the mid-to-late Cretaceous major

marine transgressions occurred in the distal part of the Cordilleran foreland basin due to accommodation created by rapid flexural subsidence in central Utah, western Wyoming and southwestern Montana (Gardner and Cross, 1994; Gardner, 1995). This was filled by up to 1,600 meters of fluvial sediment that built a broad coastal plain hundreds of kilometers eastward from the topographic front of the Cordilleran thrust belt (Gardner and Cross, 1994; Gardner, 1995; White et al., 2002). The second, to the east sedimentation in the Woodbine delta system resulted in deposition of the coeval Tuscaloosa and Woodbine Formations in a fluvial and deltaic setting (Sohl et al., 1991; Dubiel et al., 2010), as well as incised-valley-fill, nearshore marine, and wave-dominated-delta deposits (Hentz et al., 2014). During the Cretaceous, much of the riverborne detritus included illite (Pratt, 1984), this has also been suggested to have contributed a substantial clay mineral component within the Eagle Ford facies east of and around the San Marcos arch area (Fairbanks et al., 2016). However, large areas of the southern Western Interior Seaway were shielded from significant detrital fluxes from the eastern North American continent by the San Marcos arch (e.g. Goldhammer and Johnson, 2001). The third, is made apparent by an influx of clays to the southern Western Interior Seaway coinciding with the Plenus Cold Event. The Plenus Cold Event was registered at the southern end of the Western Interior Seaway by invasion of boreal dinoflagellates (Eldrett et al., 2014; van Helmond et al., 2014). Furthermore, Nd-isotope evidence suggests a climatically controlled reorganization of water masses during both the MCE and OAE 2, at least in northern European and adjacent areas (Zheng et al., 2016). As such it appears strongly suggestive that a detrital pathway exists during this period from the boreal realm.

5.5.2.3 Mo-TOC Relationships as an indicator for hydrographic dynamics

Stratigraphic variations in Mo-TOC relationships within an environment can yield information about the dynamics of basin hydrography (Algeo and Maynard, 2004). This can be used to test high-resolution chemostratigraphic data for both spatial and temporal changes in all four cores (Figure 5.15). The high but variable Mo/TOC

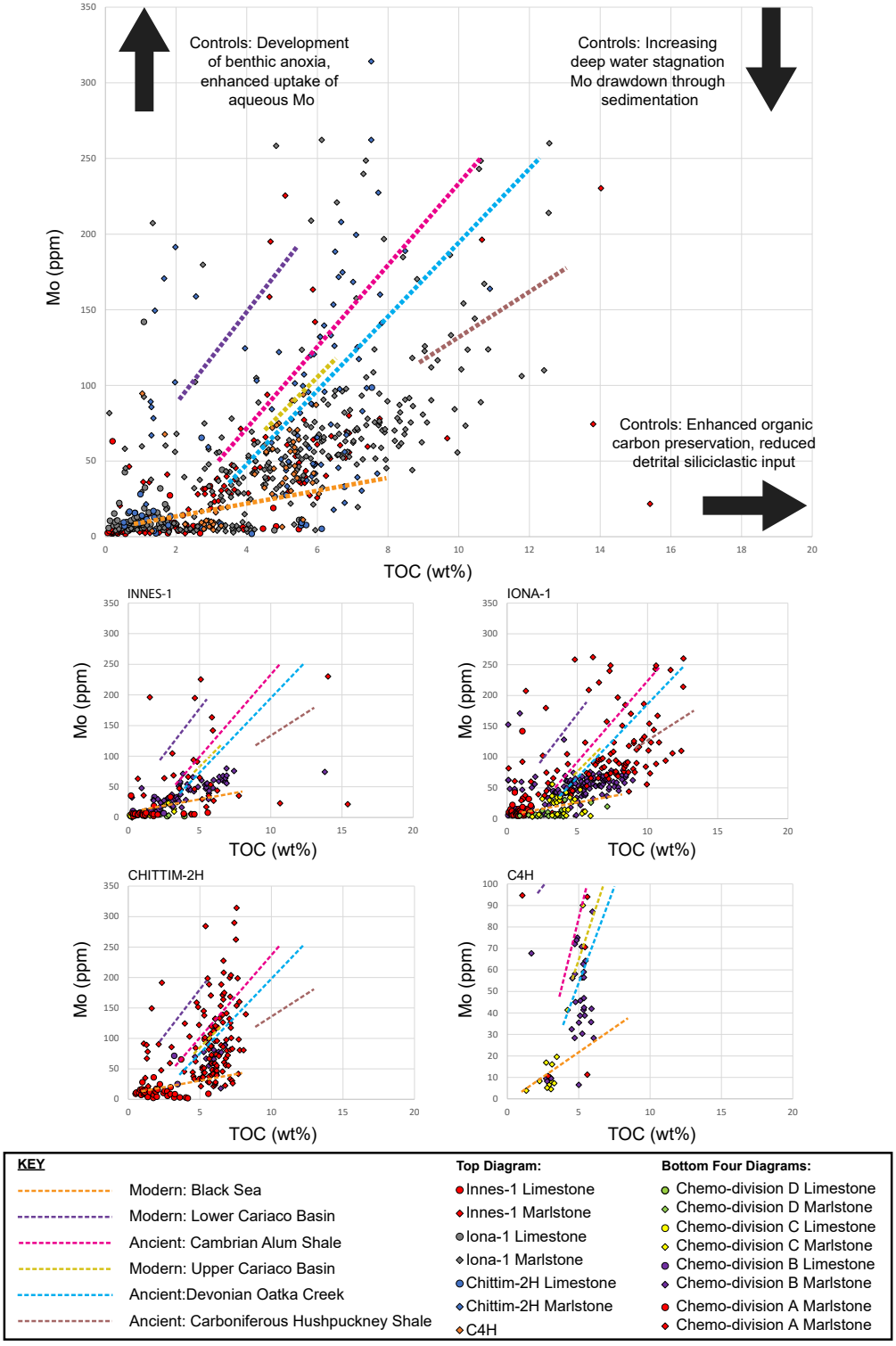

Figure 5.16: Total Organic Carbon (TOC) versus Mo concentrations from the Innes-1, Iona-1, Chittim-2H and C4H cores. TOC vs. Mo tend to show a general covariance between higher Mo concentrations and higher TOC values. Coloured bars representing modern and ancient molybdenum and TOC values (Lyons et al., 2009). Generalized controls for sedimentary Mo-TOC covariation associated with deepwater renewal in silled anoxic basins from Algeo and Lyons, 2006. For Innes-1, Iona-1, Chittim-2H and C4H circles denote limestones, diamonds denote marlstones and triangles denote bentonites in all three cores. For C4H diamonds represent all facies. The XRF and TOC measurements compared in this diagram all correspond in sample depth or the Coulomat/Rock-Eval sample depth is within 1 cm vertical depth, upwards or downwards, of the XRF measurement taken on the slabbed archive core.

ratios in depositional unit A indicates development of benthic anoxia, enhanced uptake of aqueous Mo, fluctuating levels of detrital input and a plentiful resupply of Mo through deepwater renewal (Figure 5.16; Algeo and Lyons, 2006). Depositional unit A was therefore likely deposited during a period in which the southern Western Interior Seaway was influenced by repeated deepwater renewal events whereby enhanced exchange with nutrient-rich waters occurred resulting in resupply of the trace metal inventory. Variable values of Mo_{EF} and Mo to TOC ratios suggest that water-column redox change (towards anoxia) and increased preservation is only partly responsible for the high concentrations of TOC through this stratigraphic interval in the southern Western Interior Seaway (Figure 5.16; see Appendix D).

A shift toward significantly less variable, higher TOC, and lower Mo concentrations in depositional unit B may be indicative of increasing deepwater stagnation, and Mo-drawdown through sedimentation (Figure 5.15; Algeo and Lyons, 2006). A decline in aqueous Mo concentration likely occurred as a result of removal to the sediment without adequate resupply through deepwater renewal. This denotes a period of high restriction in the southern Western Interior Seaway. The strong positive correlation between Mo and TOC, as well as Mo_{EF} and TOC (Figure 5.16; see Appendix D) is suggestive of a strong reliance on preservation of organic carbon through anoxia for the high concentrations of TOC at this time.

The younger sediments of depositional unit C generally show positive covariance but significantly lower Mo and TOC values are observed compared to depositional unit A and B (Figure 5.16). This protracted shift towards lower values likely indicates the development of increased benthic oxygenation, as also suggested by the increased occurrence of benthic foraminifera and intense bioturbation (Eldrett et al., 2014, 2015a; Chapter 3). Comparatively, the sediments of depositional unit D show little covariance between Mo and TOC (Figure 5.16). The relatively low Mo/TOC ratios indicate enhanced organic carbon concentration, most likely due to reduced detrital siliciclastic input relative to depositional unit C.

5.5.3 Depositional and environmental control on deposition of the Eagle Ford Group

The southern Western Interior Seaway provides an ideal area for studying the relative influences of global and local processes including water-mass exchange, climate, anoxia and hydrodynamics during OAE 2 in a shallow epicontinental seaway (Figure 5.17). For much of the deposition of depositional unit A, particularly during the MCE, a humid climate prevailed, with high continental runoff. During this time the southern Western Interior Seaway had developed benthic anoxia, with high levels of free H_2S in the water column and an active cycling of Mn-Fe particulates. Frequent exchange with nutrient-rich water masses repeatedly renewed the trace metal inventory including a possible volcanically derived subaqueous plume during the MCE.

Later, through the deposition of depositional unit B, a more arid climate prevailed with much lower continental runoff. Anoxia prevailed in the benthic zone of the Western Interior Seaway and high Mo-enrichment likely indicates at least some periods of euxinia. During this interval, the southern Western Interior Seaway was highly restricted with little to no exchange or renewal with other nutrient-rich water masses and little siliciclastic input.

Depositional unit C appears to have been deposited under a mostly humid climate with an increasingly high continental runoff. Throughout this period of deposition the benthic zone of the southern Western Interior Seaway is likely to have been suboxic with high relative influxes of detrital and siliciclastic material. Though some evidence from Lake Waco sections, central Texas, suggests periods of impingement by an oxygen minimum zone (Bolin and Dworkin, 2016), the presence of marcasite from this study suggests a dynamic ocean system with multiple oxygenation events. Data from the PCE, indicates a possible transient switch to a less humid, more arid climate at this time. Simultaneously, iron and mafic trace metal enrichments potentially indicate the influx of a volcanically derived nutrient-rich subaqueous plume or alternatively the remobilization of trace metals into the global ocean inventory

and subsequent deposition in the southern Western Interior Seaway. Furthermore, the high clay concentrations of the PCE indicate either a detritus-rich source or increased weathering and high continental runoff at this time.

Depositional unit D is characterized by a return to a more arid climate with lower continental runoff. Marginally higher trace metal enrichments indicate a period of deposition under lower benthic oxygen content and enhanced concentration of organic matter due to a reduction in detrital and siliciclastic input.

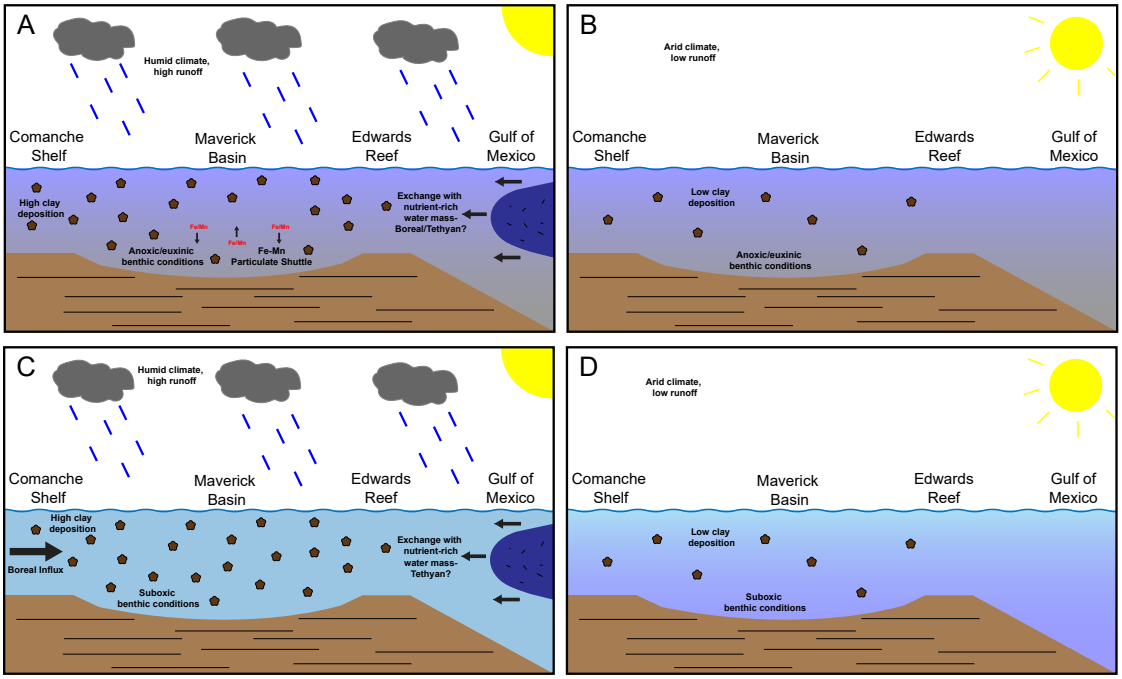

Figure 5.17: The depositional and environmental evolution of the study area. Depositional phase A is defined by a mostly warm, humid climate resulting in high continental runoff and the deposition of relatively high clay abundances (brown globular shapes). The study area was marked by an anoxic-euxinic benthic zone where a Fe-Mn particulate shuttle was prevalent and exchanges with a nutrient-rich water-mass occur. Phase B has a more arid, dry climate resulting in lower runoff and the deposition of less clay. The study area is anoxic, most likely with periods of euxinia and is hydrographically isolated. Phase C was defined by a warm, humid climate resulting in high continental runoff and the deposition of relatively high clay abundances (brown globular shapes). The benthic zone was most likely suboxic during this phase of deposition, possibly due to the impingement of an oxygen minimum zone, with possible periods of oxygenation from a nutrient-rich water-mass, including a large incursion during the Plenus Cold Event. Depositional phase D was defined by a return to a more arid climate with lower continental runoff. The oxygen levels of the benthic zone likely decreased but were still relatively suboxic. During this phase there is an enhanced preservation of organic matter due to a reduction in detrital and siliciclastic input.

5.6 Conclusions

To understand the underlying causal mechanisms of oceanic anoxic events and OAE 2 as well as to accurately calculate the rate of biogeochemical processes robust and high-resolution mineralogical and geochemical frameworks are required. This high-resolution mineralogical and geochemical study of the southern Western Interior Seaway has provided insights into the depositional environment of the Cenomanian-Turonian Eagle Ford Group as well as helped unravel the causal mechanisms and biogechemical processes that have occurred during OAE 2. As such these analyses provide a reliable framework for interpreting the dynamics of environmental change throughout a period of major perturbations to the global carbon cycle as well as providing insights into the nature of the associated Greenhouse conditions in a mid-latitude, shelf platform setting.The main findings are:

1. Anoxic/euxinic benthic conditions existed for much of the Lower Eagle Ford with active Fe-Mn cycling in the lower third. Comparatively the Upper Eagle Ford experienced mostly suboxic benthic conditions.

2. Climatic changes during the MCE and OAE 2 greatly affected the sedimentology of the Eagle Ford Group. Humid climates and enhanced runoff greatly increased the concentration of clays and other siliciclastic sediments during these periods. Comparatively, the Plenus Cold Event and the upper two thirds of the Lower Eagle Ford experienced relatively arid climates and subsequently low runoff.

3. Two clear periods of large scale water mass incursion or exchange have been identified in this study based on their geochemical signatures: (a) during the Plenus Cold Event; (b) during the second half of the Mid-Cenomanian Event.

4. High but variable Mo/TOC ratios in the bottom third of the Lower Eagle Ford indicate the possibility of exchange with a nutrient rich water source resulting in resupply of the trace metal inventory. The southern Western Interior Seaway then becomes increasingly restricted in the upper two thirds of the Lower Eagle

Ford preventing further exchange. A dramatic decrease in Mo and TOC values at the onset of OAE 2 likely indicates an increase in benthic oxygenation. This is followed by a minor decrease in benthic oxygen in the upper section of the Upper Eagle Ford and the enhanced concentration of organic matter due to a reduction in detrital and siliciclastic input.

6 Overall Conclusions and Future Directions

6.1 Overall Conclusions

As set out in the introduction, the aim of this thesis has been to improve understanding of organic-rich carbonate- and clastic-mixed mudrock systems by investigating the sedimentology and sedimentary geochemistry of the Eagle Ford Group. This has been achieved by using a multidisciplinary study employing high resolution geochemistry, stratigraphy and sedimentology on four cores from the Cretaceous southern Western Interior Seaway.

This study presents a new high resolution spatial and temporal understanding of the couplet-scale cyclicity found in the Eagle Ford Group (Chapter 3) as well as investigating the longer term core-scale geochemical and sedimentological evolution of the Eagle Ford Group. Chapter 5 investigated the evidence for and modulating effects of regional depositional, hydrographic and climatic changes, whereas Chapter 4 investigated Cenonamian and Turonian global forcing factors including the key drivers behind the Mid-Cenomanian Event (MCE) and Cenomanian-Turonian Oceanic Anoxic Event 2 (OAE 2).

This study found five dominant facies in the Eagle Ford Group of Innes-1, Iona-1 and Chittim-2H: (1) argillaceous wackestone; (2) laminated argillaceous foraminiferal wackestone; (3) laminated foraminiferal packstone; (4) massive foraminiferal packstone; (5) massive bentonitic claystone.

These facies were found to form rhythmically interbedded packstone-wackestone couplets on the scale of tens of centimeters. Evidence from this study suggests periods of high productivity and high accumulation rates led to the formation of the packstone facies, whereas periods of low primary productivity and low accumulation rates resulted in the formation of the argillaceous wackestone and laminated argillaceous foraminiferal wackestone facies.

This study suggests that the cyclicity observed in the Eagle Ford Group is a function of the fertilization of a nutrient limited system by ash falls from the Cordilleran Orogenic Belt. Release of iron, nitrates and other nutrients from soluble salts coat-

ing the ash particles promoted periods of high primary productivity resulting in the high accumulations of foraminifera and other bioclasts, packstones facies. With time the availability of nutrients decreased resulting in periods of low primary productivity and low accumulation rates, wackestones facies. Differences in current regime and levels of primary productivity lead to the sedimentological differences between the two wackestone facies.

Further modulation of the packstone facies occurred at couplet scale by bottom currents and as a function of clay contents. Reworking of the packstone facies by bottom currents resulted in the creation of carbonate sand ridges/sheets and isolated hydraulic dunes. Differences in clay concentrations likely played a part in this. Higher concentrations of clay in the laminated foraminiferal packstones created a cohesive effect against hydrodynamic forces preventing the reworked carbonate sand ridges/sheets from forming barchan dunes. Furthermore, the lower concentrations of clay in the massive foraminiferal packstone may have resulted in greater porosity and permeability compared to the laminated packstone facies. This resulted in diagenesis preferentially affecting and recrystallizing the massive packstone facies obscuring sedimentary structures.

Evidence from this study also suggests that lateral variabilities in lateral continuity of the packstone and wackestone bodies may have been a function of the high concentrations of swelling clays within the bentonitic claystones. These swelling clays likely led to slope instability and helped create the lateral sediment accumulations found in southern Western Interior Seaway.

Core-scale, rather than couplet-scale, analysis of the Eagle Fords mineralogy, sedimentology and geochemistry (Chapter 5) suggests that regional changes in water-mass exchange, climate, anoxia and hydrodynamics played a longer-term role in the formations evolution. These regional forcing factors also partly modulating the expression of the couplets in the Lower and Upper Eagle Ford as discussed in Chapters 3 and 5 (discussed in Figures 3.19 and 3.20).

This study finds that the bottom third of the Lower Eagle was deposited under highly

euxinic-anoxic benthic conditions with active Fe-Mn cycling and some open water mass exchange with a nutrient rich source resulting in the replenishment of the trace metal inventory. Comparatively the top two thirds of the Lower Eagle Ford were deposited in a highly restricted environment where no water mass exchange occurred and anoxic/euxinic benthic conditions prevailed.

The Upper Eagle Ford experienced mostly suboxic benthic depositional conditions during OAE 2 with high relative levels of detrital and siliciclastic input. However, post-OAE 2 benthic oxygen decreases slightly, or there is a replenishment of the global trace metal inventory following the end of OAE 2, and a large reduction in detrital and siliciclastic input resulting in enhanced concentration of organic matter.

Alternative mechanisms to explain the cyclicity, such as an expanded subtropical-tropical Hadley cell during the mid-Cretaceous (e.g. Wagner et al., 2013) or climate-driven mechanisms resulting from Milankovitch cyclicity (e.g. Eldrett et al., 2015b) may have impacted the depositional conditions under which the Upper and Lower members of the Eagle Ford Group were deposited. Further work is required to disentangle the influence of the mechanisms suggested in this thesis.

Global forcing factors are also shown to have an important role in the formation and evolution of the Eagle Ford Group (Chapters 4 and 5). Sedimentary mercury (Hg) concentration data was presented from three sites in the Western Interior Seaway and one from the south-western proto-North Atlantic Ocean (Demerara Rise). The results demonstrate elevated Hg and Hg/TOC values at the stratigraphic levels of the Mid-Cenomanian Event (MCE) and the Cenomanian-Turonian Oceanic Anoxic Event 2 (OAE 2). These Hg/TOC values are, however, muted in comparison to signals found at other Mesozoic OAE sections proposed to be associated with co-eval subaerial LIP emplacement. This possibly indicates that Hg dispersal occurred via a submarine plume, following a subaqueous LIP erupting directly into the water column rather than resulting from atmospheric dispersion.

This study suggests that transmission of this plume by sub-surface palaeo-currents moving either from the Pacific, through the Central American Seaway into the south-

western proto-North Atlantic Ocean or from the Arctic via the Canadian sector of the Western Interior Seaway are consistent with previous palaeoceanographic reconstructions of water mass movements and with εNd constraints on water-mass evolution. This palaeoceanographic model is consistent with major volcanic activity in the Caribbean during both the MCE and OAE 2 and possibly that of the High Arctic.

Large-scale release of greenhouse gases and other compounds during a major pulse of Caribbean or High Arctic LIP volcanism during the MCE and OAE 2 most likely resulted in an accelerated hydrological cycle. Large increases in clays and siliciclastics shown during these periods, documented in Chapter 5, indicate a humid climate and enhanced runoff. Strongly suggesting that both core-scale sedimentology and geochemistry was effected by global forcing factors at this time. Finally, two periods of large scale incursion by a boreal or tethyan water mass during the Plenus Cold Event and the Mid Cenomanian Event are suggested by the excursions of trace metal enrichments coinciding with large Hg/TOC enrichments. The impact of these incursions on couplet-scale sedimentology is discussed further in Figure 3.19.

6.2 Implications

This study has broad implications for a number of different applications:

1. OAEs: It has been proposed that the major forcing behind OAEs was an abrupt rise in temperature induced by the rapid influx of CO2 into the atmosphere from volcanogenic or methanogenic sources associated with the formation of LIPs (Figure 2.6; e.g. Coffin and Eldholm, 1994; Ernst et al., 2005). Not only does this study provides further evidence to this hypothesis but the smaller Hg signals associated with OAE 2 and the MCE, indicating Hg dispersal by a submarine plume, suggest that both subaqueous and subaerial LIP emplacement can result in these catastrophic oceanographic and climatic changes.

2. Unconventional reservoirs: Understanding depositional and sedimentological

variations of unconventional plays is essential to enable success throughout the production lifecycle of the unconventional hydrocarbon reservoir rocks. Knowledge of the geological processes that control the deposition of a mudrock sequence is fundamental to understanding mudrock variability, both temporally and spatially, and to facilitate the development of process-based predictive models for organic rich source rocks and unconventional reservoirs. The approach taken to assess the sedimentology and cyclicity of the TOC-rich wackestones and the TOC-poor packstones as well as the lateral continuity of these bodies provides a methodology to better understand the vertical and lateral variabilities that can exist in an unconventional reservoir. Geographic and stratigraphic sweet spots for well productivity can then be predicted by understanding how and where different parts of a cycle are stacked (Driskell et al., 2012). As each unconventional play is unique, what works for reservoir characterization and risk mapping in one play is not necessarily applicable to another (Driskell et al., 2012). However, developing an understanding of the interaction of the main reservoir properties should lead to less uncertainty, particularly in areas of the play with few existing wells (Driskell et al., 2012).

3. Local versus regional versus global forcing factors: The detailed analysis of the deposition of the Eagle Ford Group has been conducted to better understand its subsurface lateral and vertical variabilities. The results appear to suggest that regional and local factors dominated the deposition of the Eagle Ford. However, global controls have clearly exerted an effect as well. Further work is required to validate whether regional controls tend to dominate the deposition of similar formations also.

The Cretaceous La Luna Formation would be one such option due to its many similarities with the Eagle Ford. The early deposition of the black shales of La Luna has long been considered a combination of rapid sea-level rise and presence of upwelling currents (Perez-Infante et al., 1996) but modulation by local tectonics (Parra et al., 2003; Macsotay et al., 2003) and other regional factors such deepwater currents is apparent (Macsotay et al., 2003). As such further study of La Luna may present an excellent opportunity to help disentangle the relative effects of regional and global forcing factors.

4. Bentonite occurrence on orbital timescales: In Chapter 4 this study discusses how rapid changes in climate have long been suggested to cause volcanic eruptions due to ice loading and sea level changes (e.g. Rampino et al., 1979; Denton and Hughes, 1983; Gale et al., 2002; Berger, 2013). Furthermore, regional studies have connected climate and volcanism over broader timescales (e.g., Jellinek et al., 2004; McGuire et al., 1997; Nowell et al., 2006; Paterne et al., 1990; see section 3.6.4). However, a lack of literature exists connecting climate forcings as a cause for volcanism past the Cenozoic.

The Cordilleran Orogenic Belt is believed to be the origin of the bentonites of the southern Western Interior Seaway (Burchfiel et al., 1992). Deglaciation would result in depressurisation of volcanoes or increased flux melting (e.g. Grove et al., 2012), leading to a greater probability of eruption because of increased magmatic melt (Maclennan et al., 2002) and reduced confining pressure (Jellinek et al., 2004). The work presented here may therefore present initial evidence for glacial growth during the greenhouse world of the Cenomanian-Turonian (Elder et al., 1994; Sageman et al., 1998; Stoll and Schrag, 2001; Laurin et al., 2001).

5. Ash fertilization of nutrient limited ocean systems: The ash fertilization mechanism has been hypothesized to drive large-scale perturbations in biogeochemical cycles and large scale sedimentary cycles observed in geological records (Bay et al., 2004; Cather et al., 2009). However, previously little has been presented in way of evidence about the long term influence (thousands to millions of years) of ash fertilization on Cretaceous ecosystems. This study suggests a strong, long-term response to volcanic eruptions in the Western Interior Seaway and provides a basis for future work on ash fertilization in the geological record.

How long lived and exactly what parts of the marine biogeochemical system have been influenced remain to be investigated. Further to this, the relative influences of eruption type, rate and size are still poorly constrained in the modern ocean (e.g. Scasso et al., 1994; Stern, 2008; Narcisi et al., 2012; Watt et al., 2013).

6.3 Future Work and Directions

Whilst the work presented in Chapters 3-5 contributes to understanding the deposition of the Eagle Ford Group in the southern Western Interior Seaway many important questions remain to be answered. Some of these questions are considered below.

How do the relative effects of global and local controls modulate the deposition of other Cenomanian-Turonian organic-rich mudrocks?

Phanerozoic source rocks are not randomly distributed in time and space but are concentrated within specific time intervals and palaeogeographic positions that relate to major earth system events and palaeotectonic framework (Bishop et al., 2014). The Cenomanian-Turonian boundary interval represents one of the most profound global perturbations in the carbon cycle of the last 140 million years (Arthur et al., 1987; Turgeon and Creaser, 2008). This interval is characterized by the widespread deposition of organic-rich fine grained sediment and marked by a globally recognized positive carbon isotope excursion that reflects the widespread removal of ^{12}C-enriched organic matter in marine sediments under global anoxic greenhouse conditions (Schlanger and Jenkyns, 1976; Arthur and Schlanger, 1979; Jenkyns, 1980; Scholle and Arthur, 1980; Herbin et al., 1986; Arthur et al., 1987, 1988; Weissert and Lini, 1991; Jenkyns et al., 1994). As such this interval is characterized by the widespread occurrence of many petroleum source rocks such the Natih (van Buchem et al., 1996), La Luna (Zumberge, 1984), Tarfaya (Kuhnt et al., 1997), Abu Roash (El Beialy et al., 2010) and Shilaif formations (Burchette et al., 1993). However, the lateral and temporal variability as well as the relative timing of the deposition of many of these formations is very poorly constrained (Figure 6.1). Further research is required to better understand the geographic and internal variability of these systems as well as their timing in an effort to better understand their occurrence and how their characteristics vary as a result of their depositional profile.

This detailed analysis of the deposition of the Eagle Ford Group has been conducted to better understand its subsurface lateral and vertical variabilities. It appears that

regional and local factors dominated the deposition of the Eagle Ford. However, global controls have clearly exerted an effect as well. In all this study suggests that paleogeographic, paleoclimatic and palaeotectonic events in North America combined to produce the rock record of the Eagle Ford Group. Nevertheless, this data only provides a detailed record of deposition in a restricted area of an epicontinental seaway, the Western Interior Seaway. The study of other Cenomanian-Turonian intervals would provide an excellent opportunity to validate the findings of this study. The Cretaceous La Luna Formation would be one such option due to its many similarities with the Eagle Ford. Cenomanian to Campanian in age it is composed of interbedded dark-grey calcareous ”black shales” and limestones (Zumberge, 1984). These are largely composed of abundant calcareous planktonic foraminifera (Zumberge, 1984) and its trace metal enrichments suggest restricted bottom water circulation (Mongenot et al., 1996; Rangel et al., 2000). Furthermore, it appears that both ”black shale deposition, or at least its most organic carbon-rich portions, and oxygen-depleted bottom water conditions are diachronous with OAE 2 prevailing well before the Cenomanian-Turonian boundary and continuing until the Santonian (Perez-Infante et al., 1996; Sliter et al., 1999; Tribovillard et al., 2004).

The early deposition of the ”black shales” of La Luna has long been considered a combination of rapid sea-level rise and presence of upwelling currents (Perez-Infante et al., 1996) but modulation by local tectonics (Parra et al., 2003; Macsotay et al., 2003) and other regional factors such deepwater currents is apparent (Macsotay et al., 2003). High resolution, multidisciplinary studies on facies variabilities and their depositional environments is lacking in the literature. Therefore this would be an excellent place to not only validate and confirm the findings of this study but further constrain the relative effects of global and local controls on organic-rich mudrocks during the Cenomanian and Turonian or Late Cretaceous.

What are the biogeochemical consequences of volcanic eruptions in the Cretaceous Western Interior Seaway? Does ash fertilization cause a forcing effect on sedimentary records at a regional scale and other periods of the earths history?

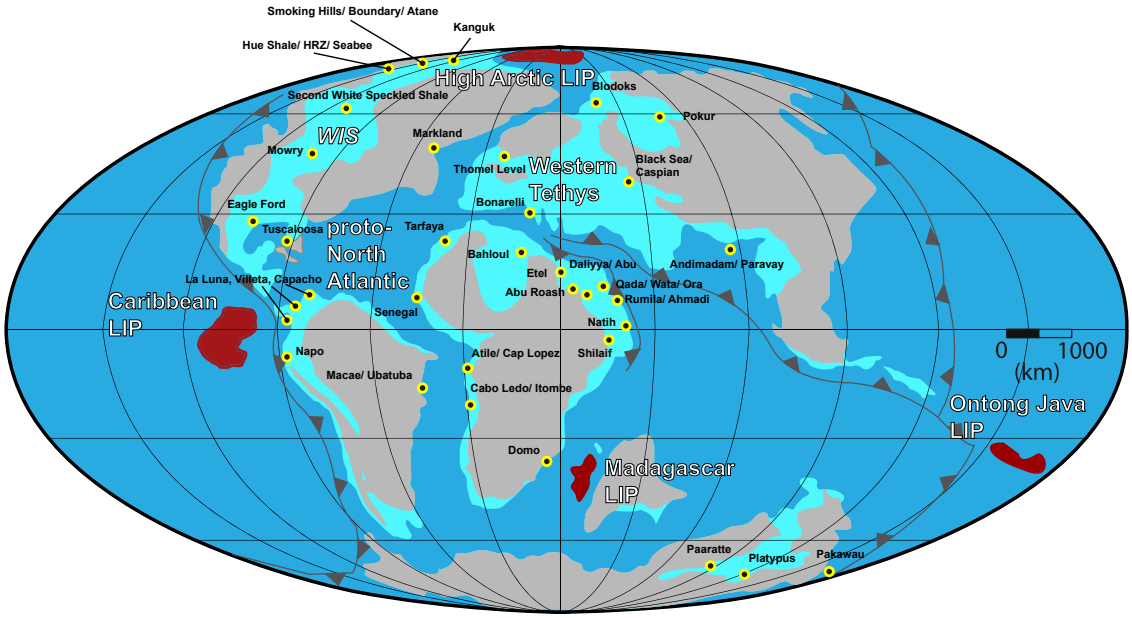

Figure 6.1: Palaeogeographic map showing the spatial distribution of known organic-rich sediments deposited between 100 and 90 Ma (Cenomanian Turonian). Adapted from Bishop and Bergman (2014).

Phytoplankton and other organisms across the majority of the worlds oceans are thought to be limited by the availability of the 'macronutrient' nitrate, the essential trace-metal 'micronutrient' iron and a number of other nutrients (Morel and Price, 2003; Olgun et al., 2011; Browning et al., 2014). Due to the fundamental role of Fe and other nutrients in regulating many organisms such as phytoplankton across large areas of the worlds oceans, there has been much interest in investigating potential sources of bioavailable Fe to the ocean. In recent years many studies have investigated the release of nutrients from ash and attempted to identify phytoplankton blooms (e.g. Frogner et al., 2001; Olgun et al., 2011, 2013; Duggen et al., 2007; Achterberg et al., 2013). This fertilization mechanism has been hypothesized to drive large-scale perturbations in biogeochemical cycles and large scale sedimentary cycles observed in geological records (Bay et al., 2004; Cather et al., 2009). However, at present little is understood about the long term influence (thousands to millions of years) of ash fertilization on ecosystems. Further to this, the relative influences of eruption type, rate and size are still poorly constrained in the modern ocean (e.g. Scasso et al., 1994; Stern, 2008; Narcisi et al., 2012; Watt et al., 2013).

Preliminary work presented in Chapter 3 suggests a strong response to volcanic

eruptions in the Western Interior Seaway. How long lived and exactly what parts of the marine biogeochemical system have been influenced remain to be investigated. Modelling could help with this, yet important parameters that would go into these are poorly constrained and could limit the usefulness of results obtained (e.g. Boyd and Mackie, 2008). Even modern large scale ash-release experiment (sensu Boyd et al., 2007), which whilst likely being highly informative, could be difficult to realise and would almost certainly still lead to further questions (Boyd et al., 2007).

Predicting phytoplankton and community responses to ash supply will likely require a detailed evaluation of the ash being added to the system. For example ash particle size may exert a particularly important control on metal release, as for a given mass of ash addition metal release may be expected to be greater for ash samples with smaller grain sizes and thus larger surface area per bulk ash mass (assuming soluble salts on the ash surface scale positively with surface area). Carefully designed experiments detecting metal release from ash using conditions that best replicate, or ideally utilise, the natural ocean are needed if ash mass fluxes are to be used for projecting total metal (e.g. Fe) input to the surface ocean subsequent to an eruption and thereby attempting to quantify primary production stimulated (c.f. Watson, 1997). For reasons outlined previously, such experiments should pay careful consideration to ash particle size, ash loading, and exposure time to best mimic natural ash depositions in the oceanic regime of interest (i.e. coastal versus open ocean waters).

Consequently, in the case of ash-driven fertilisation there is the potential for long term stimulation of ecosystems, sedimentary cycles, and carbon export. However, more work is required to understand why it is prevalent in the southern Western Interior Seaway and if these findings can be validated by comparison to other time equivalent sections around the region or world. Formations such as La Luna which are known to contain large numbers of bentonites (Zumberge, 1984), are time equivalent and are relatively close to the Cordilleran orogenic belt may provide an excellent opportunity to confirm this study.

Do volcanic eruptions occur on Milankovitch periodicities during the

Cenomanian-Turonian and what is the forcing factor for this?

In Chapter 4 this study discusses how rapid changes in climate have long been suggested to cause volcanic eruptions due to ice loading and sea level changes (e.g. Rampino et al., 1979; Denton and Hughes, 1983; Gale et al., 2002; Berger, 2013). Furthermore, regional studies have connected climate and volcanism over broader timescales (e.g., Jellinek et al., 2004; McGuire et al., 1997; Nowell et al., 2006; Paterne et al., 1990; see section 3.6.4). However, a lack of literature exists connecting climate forcings as a cause for volcanism past the Cenozoic.

Despite the greenhouse world of the Cenomanian-Turonian, glacier growth has been suggested to exist (Elder et al., 1994; Sageman et al., 1998; Stoll and Schrag, 2001; Laurin et al., 2001). The Cordilleran Orogenic Belt is believed to be the origin of the bentonites of the southern Western Interior Seaway (Burchfiel et al., 1992). Deglaciation would result in depressurisation of volcanoes or increased flux melting (e.g. Grove et al., 2012), leading to a greater probability of eruption because of increased magmatic melt (Maclennan et al., 2002) and reduced confining pressure (Jellinek et al., 2004). By compiling a dated, regional eruptive archive in the southern Western Interior Seaway it may be possible to understand the feedbacks between climate and rates of volcanism. However, this may be a monumental task as arc volcanoes present particular challenges when compiling regional eruption archives. Records of effusive eruptions from long-lived systems are difficult to reconstruct and date, and deposits from the explosive eruptions that dominate arc records are prone to erosion and reworking (Fontijn et al., 2014). Furthermore, eruption frequency records are prone to temporal bias (as preservation potential typically declines with time), and consider different sized eruptions to be equally significant. Detailed characterization of preserved eruptive products is essential to reconstruct a sufficiently complete eruptive history to investigate arc-scale volcanic responses to deglaciation.

Further research into glacier formation in the North American continent during the Cenomanian and Turonian may also provide potential answers to this question but also presents its own problems. The comparison of extremely high resolution (cm-

scale) $\delta^{18}O$ and TEX_{86} on a continuous core such as Iona-1 may provide controls on glacioeustasy and temperature changes in the southern Western Interior Seaway. By comparing these to other sections around the world it may be possible to discern high resolution climatic and glacioeustatic changes.

Are mercury concentrations influenced by the thermal maturation of organic-rich rocks?

Due to large quantities of mercury being degassed in volcanic emissions (Pyle and Mather, 2003) mercury (Hg) enrichments in sedimentary successions are increasingly being used as a tracer for major volcanic events in the past (e.g. Sanei et al., 2012; Grasby et al., 2013; Sial et al., 2013; Percival et al., 2015; Thibodeau et al., 2016). Chapter 4 sets out the main processes that lead to the formation of mercury enrichments within sedimentary successions. However, due to its relatively recent discovery as a geochemical tracer for volcanism, little is actually known about the physical and biogeochemical processes that may affect mercury when it is being or has been deposited such as diagenesis or thermal maturation.

Mercury is a highly volatile element and as such metamorphism of organic-rich lithologies during large scale volcanism may have produced thermogenic mercury gas. As a result in areas such as the Karoo Basin where the Karoo Province is believed to have intruded into organic-rich shales and coals (McElwain et al., 2005; Svensen et al., 2007) significant concentrations of thermogenic mercury gas may have been produced potentially increasing Hg output to the atmosphere during the Toarcian Oceanic Anoxic Event. Similarly, long term thermal maturation of organic matter in rocks may result in mobilization of mercury and subsequent thermogenic release causing unreliable results.

Preliminary work in Chapter 4 (see Appendix B) indicates that despite a higher T_{max} ($\sim$30 ℃) and vitrinite reflectance data (0.4 R_o; see Appendix B) Chittim-2H has significantly higher Hg concentrations and enrichments than Innes-1. This points toward a complicated system. Therefore, predicting changes in mercury enrichments as a result of thermal maturation will likely require both a detailed lab and core based

evaluation. By heating thermally immature organic-rich samples of known TOC and Hg in standardized atmospheres to different temperatures it would be possible to measure loss of mercury. However, like many of these experiments whilst this would be highly informative it would almost certainly still lead to further questions.

A core based study would most likely require multiple cores of the same formation and increasing thermal maturities with good age constraints that have been deposited during the emplacement of a large igneous province. Preferably the sedimentary successions would be largely homogenous and it would be relatively easy to correlate between different sections of each core. The effects of diagenesis in this core would have to be evaluated to minimise the likelihood of mercury mobilisation due to through flowing hydrothermal fluids. Mercury enrichments could then be evaluated stratigraphically and each core could be compared.

7 References

Achterberg, E.P., Moore, C.M., Henson, S.A., Steigenberger, S., Stohl, A., Eckhardt, S., Avendano, L.C., Cassidy, M., Hembury, D., Klar, J.K. and Lucas, M.I., 2013. Natural iron fertilization by the Eyjafjallajökull volcanic eruption. Geophys. Res. Let., 40(5), 921-926.

Adams, T.L., Strganac, C., Polcyn, M.J. and Jacobs, L.L., 2010. High resolution three-dimensional laser-scanning of the type specimen of Eubrontes (?) glenrosensis Shuler, 1935, from the Comanchean (Lower Cretaceous) of Texas: implications for digital archiving and preservation. Palaeontologia Electronica, 13(3), p.11.

Adatte, T. Stinnesbeck, W. and Keller, G., 1996. Lithostratigraphic and mineralogic correlations of near K/T boundary clastic sediments in northeastern Mexico: implications for origin and nature of deposition. Geol. Soc. Am. Spec. Pap, 307, 211-226.

Adkins, W.S. and Lozo, F.E., 1951. Stratigraphy of the Woodbine and Eagle Ford, Waco area, Texas. Southern Methodist Univ., Fondren Sci. Ser., 4, 105-161.

Alexander, M., 2014. A New Look at Maverick Basin Basement Tectonics. Gulf Coast Ass. of Geol. Soc.

Algeo, T.J. and Lyons, T.W., 2006. Mo-total organic carbon covariation in modern anoxic marine environments: Implications for analysis of paleoredox and paleohydrographic conditions. Paleoceanog., 21(1).

Algeo, T.J. and Maynard, J.B., 2004. Trace-element behavior and redox facies in core shales of Upper Pennsylvanian Kansas-type cyclothems. Chem. Geol., 206(3), 289-318.

Algeo, T.J. and Rowe, H., 2012. Paleoceanographic applications of trace-metal concentration data. Chem. Geol., 324, 6-18.

Algeo, T.J. and Tribovillard, N., 2009. Environmental analysis of paleoceanographic systems based on molybdenum-uranium covariation. Chem. Geol., 268(3), 211-225.

Alldredge, A. L., Granata, T. C., Gotschalk, C. C. and Dickey, T. D., 1990. The physical strength of marine snow and its implications for particle disaggregation in the ocean: Limnology and Oceanography, 35, 1415- 1428.

Alldredge, A. L. and Gotschalk, C. C., 1989. Direct observations of the mass flocculation of diatom blooms: Characteristics, settling velocities and formation of diatom aggregates: Deep-Sea Research. Part I, Oceanographic Research Papers, 36, 2, 159-171.

Alldredge, A. L. and Silver, M. W., 1988. Characteristics, dynamics and significance of marine snow. Progress in Oceanography, 20, 41-82.

Allen, J. R. L., 1984. Sedimentary structures, their character and physical basis: Amsterdam, Elsevier, 663.

Allmendinger, R.W., 1992. Fold and thrust tectonics of the western United States exclusive of the accreted terranes. The Cordilleran orogen: Conterminous US: Boulder, Colorado, Geol. Soc. Am., Geology of North America, 3, 583-607.

Alsharhan, A.S. and Nairn, A.E.M., 1993. Carbonate platform models of Arabian Cretaceous reservoirs. In: Cretaceous Carbonate Platforms (Eds J.A.T. Simo, R.W. Scott and J.P. Masse), AAPG Mem., 56, 173-184.

Alvarez, W., Alvarez, L.W., Asaro, F. and Michel, H.V., 1984. The end of the Cretaceous: sharp boundary or gradual transition. Science, 223, 1183-1187. Anderson, D.L., 2005. Large igneous provinces, delamination, and fertile mantle. Elements, 1(5), 271-275.

Anderson, D.M., Reynolds, R.C. and Brown, J., 1969. Bentonite debris flows in northern Alaska. Science, 164(3876), 173-174.

Ando, A., Nakano, T., Kaiho, K., Kobayashi, T., Kokado, E. and Khim, B.K., 2009. Onset of seawater $^{87}Sr/^{86}Sr$ excursion prior to Cenomanian-Turonian Oceanic Anoxic Event 2? New Late Cretaceous strontium isotope curve from the central Pacific Ocean. J. Foram. Res., 39(4), 322-334.

Arthur, M.A. and Sageman, B.B., 2005. Sea-level control on source-rock development: perspectives from the Holocene Black Sea, the mid-Cretaceous Western Interior Basin of North America, and the Late Devonian Appalachian Basin, in The Deposition of Organic Carbon-Rich Sediments: Models, Mechanisms and Consequences, edited by N. B. Harris, Spec. Publ. SEPM Soc. Sed. Geol., 82, 35-59.

Arthur, M.A. and Schlanger, S.O., 1979. Cretaceous. AAPG Bull., 63(6), 870-885.

Arthur, M.A., Dean, W.E. and Pratt, L.M., 1988. Geochemical and climatic effects of increased marine organic carbon burial at the Cenomanian/Turonian boundary. Nature, 335(6192), 714-717.

Arthur, M.A., Dean, W.E. and Schlanger, S.O., 1985. Variations in the global carbon cycle during the Cretaceous related to climate, volcanism, and changes in atmospheric CO2. The Carbon Cycle and Atmospheric CO: Natural Variations Archean to Present, 504-529.

Arthur, M.A., Dean, W.E. and Stow, D.A.V., 1984. Models for the deposition of Mesozoic-Cenozoic fine-grained organic-carbon-rich sediment in the deep sea. Geol. Soc., Lon., Spec. Publ., 15(1), 527-560.

Arthur, M.A. and Dean, W.E., 1991. A holistic geochemical approach to cyclomania examples from Cretaceous pelagic limestone sequences. In: Einsele, G., Ricken, W., Seilacher, A. (Eds.), Cycles and Events in Stratigraphy. Springer-Verlag, Berlin, Heidelberg, New York, 126-166.

Arthur, M.A., Dean, W.E., Pollastro, R.M., Scholle, P.A. and Claypool, G.E., 1985. A comparative geochemical study of two transgressive pelagic limestone units, Cre-

taceous Western Interior basin. In: Pratt, L.M., Kauffman, E.G., Zelt, F.B. (Eds.), Fine-Grained Deposits and Biofacies of the Cretaceous Western Interior Seaway: Evidence of Cyclic Sedimentary Processes. SEPM Field Trip Guidebook 4, 16-27.

Arthur, M.A., Schlanger, S.T. and Jenkyns, H.C., 1987. The Cenomanian-Turonian Oceanic Anoxic Event, II. Palaeoceanographic controls on organic-matter production and preservation. Geol. Soc., Lon., Spec. Publ., 26(1), 401-420.

Atchison, D.E., 1954. Geology of the Bushy Creek Quadrangle, Williamson County, Texas. Masters Thesis: University of Texas at Austin, 1954. Austin, Texas, United States.

Bacon, C.R., Lanphere, M.A., 2006. Eruptive history and geochronology of Mount Mazama and the Crater Lake region, Oregon. Geol. Soc. Am. Bull., 118 (11-12), 1331-1359.

Bagnato, E., Aiuppa, A., Parello, F., Calabrese, S., D'Alessandro, W., Mather, T.A., McGonigle, A.J.S., Pyle, D.M. and Wängberg, I., 2007. Degassing of gaseous (elemental and reactive) and particulate mercury from Mount Etna volcano (Southern Italy). Atm. Environ., 41(35), 7377-7388.

Bagnato, E., Oliveri, E., Acquavita, A., Covelli, S., Petranich, E., Barra, M., Italiano, F., Parello, F. and Sprovieri, M., 2017. Hydrochemical mercury distribution and air-sea exchange over the submarine hydrothermal vents off-shore Panarea Island (Aeolian arc, Tyrrhenian Sea). Mar. Chem.,194, 63-78.

Balcom, P.H., Fitzgerald, W.F., Vandal, G.M., Lamborg, C.H., Rolfhus, K.R., Langer, C.S. and Hammerschmidt, C.R., 2004. Mercury sources and cycling in the Connecticut River and Long Island Sound. Mar. Chem., 90(1), 53-74.

Barclay, R.S., McElwain, J.C. and Sageman, B.B., 2010. Carbon sequestration activated by a volcanic CO2 pulse during Ocean Anoxic Event 2. Nature Geo., 3(3), 205-208.

Barron, E.J., Arthur, M.A. and Kauffman, E.G., 1985. Cretaceous rhythmic bedding sequences: a plausible link between orbital variations and climate. Earth Planet. Sci. Lett., 72(4), 327-340.

Batenburg, S.J., De Vleeschouwer, D., Sprovieri, M., Hilgen, F.J., Gale, A.S., Singer, B.S., Koeberl, C., Coccioni, R., Claeys, P. and Montanari, A., 2016. Orbital control on the timing of oceanic anoxia in the Late Cretaceous. Climate of the Past, 12(10), 1995-2009.

Bay, R.C., Bramall, N. and Price, P.B., 2004. Bipolar correlation of volcanism with millennial climate change. Proceedings of the National Academy of Sciences of the United States of America, 101(17), 6341-6345.

Behar, F., Beaumont, V. and Penteado, H.D.B., 2001. Rock-Eval 6 technology: performances and developments. Oil & Gas Science and Technology, 56(2), 111-134.

Beier, C., Haase, K.M., Abouchami, W., Krienitz, M.S. and Hauff, F., 2008. Magma genesis by rifting of oceanic lithosphere above anomalous mantle: Terceira Rift,

Azores. Geochem., Geophys., Geosyst., 9(12).

Benoit, J.M., Gilmour, C.C., Mason, R.P. and Heyes, A., 1999. Sulfide controls on mercury speciation and bioavailability to methylating bacteria in sediment pore waters. Environmental Science & Technology, 33(6), 951-957.

Benoit, J.M., Mason, R.P., Gilmour, C.C. and Aiken, G.R., 2001. Constants for mercury binding by dissolved organic matter isolates from the Florida Everglades. Geochim. Cosmochim. Acta, 65(24), 4445-4451.

Berger, A., 2013. Milankovitch and climate: understanding the response to astronomical forcing, 126.

Berger, W. H. and Piper, D. J., 1972, Planktonic foraminifera: Differential settling, dissolution, redeposition: Limnology and Oceanography, 17, 2, 275-287, Bertani, R.T. and Carozzi, A.V., 1985. Lagoa Feia Formation (Lower Cretaceous), Campos Basin, Offshore Brazil: Rift Valley Stage lacustrine Carbonate reservoirs - I. J. Petrol. Geol., 8(1), 37-58.

Bin, C., Xiaoru, W. and Lee, F.S., 2001. Pyrolysis coupled with atomic absorption spectrometry for the determination of mercury in Chinese medicinal materials. Analytica Chimica Acta, 447(1), 161-169.

Bird, P., 1998. Kinematic history of the Laramide orogeny in latitudes 35-49 N, western United States. Tectonics, 17(5), 780-801.

Bishop, A., Ross, M. and Bergman, S., 2014. April. Earth system controls on the temporal occurrence of petroleum source rocks. In: AAPG Convention.

Blain, S., Quéguiner, B., Armand, L., Belviso, S., Bombled, B., Bopp, L., Bowie, A., Brunet, C., Brussaard, C., Carlotti, F. and Christaki, U., 2007. Effect of natural iron fertilization on carbon sequestration in the Southern Ocean. Geophys. Res. Let., 446(7139), 1070.

Blättler, C.L., Jenkyns, H.C., Reynard, L.M. and Henderson, G.M., 2011. Significant increases in global weathering during Oceanic Anoxic Events 1a and 2 indicated by calcium isotopes. Earth Planet. Sci. Lett., 309(1), 77-88.

Boling, K.S. and Dworkin, S.I., 2015. Origin of organic matter in the Eagle Ford Formation. Interpretation, 3(1), 27-39.

Bonadonna, C. and Phillips, J.C., 2003. Sedimentation from strong volcanic plumes. J. Geophys. Res.: Solid Earth, 108(B7), 2340-2368.

Bopp, L., Le Quéré, C., Heimann, M., Manning, A.C. and Monfray, P., 2002. Climateinduced oceanic oxygen fluxes: Implications for the contemporary carbon budget. Global Biogeochemical Cycles, 16(2).

Bornemann, A., Norris, R.D., Friedrich, O., Beckmann, B., Schouten, S., Sinninghe Damsté, J.S., Vogel, J., Hofmann, P. and Wagner, T., 2008. Isotopic evidence for glaciation during the Cretaceous supergreenhouse. Science, 319(5860), 189-192.

Bottini, C., Cohen, A.S., Erba, E., Jenkyns, H.C. and Coe, A.L., 2012. Osmium-

isotope evidence for volcanism, weathering, and ocean mixing during the early Aptian OAE 1a. Geology, 40(7), 583-586.

Bowman, K.L., Hammerschmidt, C.R., Lamborg, C.H. and Swarr, G., 2015. Mercury in the North Atlantic Ocean: The US GEOTRACES zonal and meridional sections. Deep Sea Research Part II: Topical Studies in Oceanography, 116, 251-261.

Boyd, P.W. and Doney, S.C., 2002. Modelling regional responses by marine pelagic ecosystems to global climate change. Geophys. Res. Let., 29(16), 1806.

Boyd, P.W., Jickells, T., Law, C.S., Blain, S., Boyle, E.A., Buesseler, K.O., Coale, K.H., Cullen, J.J., De Baar, H.J., Follows, M. and Harvey, M., 2007. Mesoscale iron enrichment experiments 1993-2005: Synthesis and future directions. Science, 315(5812), 612-617.

Browning, T.J., Bouman, H.A., Henderson, G.M., Mather, T.A., Pyle, D.M., Schlosser, C., Woodward, E.M.S. and Moore, C.M., 2014. Strong responses of Southern Ocean phytoplankton communities to volcanic ash. Geophys. Res. Let., 41(8), 2851-2857.

Browning, T.J., Bouman, H.A., Moore, C.M., Schlosser, C., Tarran, G.A., Woodward, E.M.S. and Henderson, G.M., 2014. Nutrient regimes control phytoplankton ecophysiology in the South Atlantic. Biogeosciences (BG), 11(2), 463-479.

Brumsack, H.J., 2006. The trace metal content of recent organic carbon-rich sediments: implications for Cretaceous black shale formation. Palaeogeogr. Palaeoclimatol. Palaeoecol., 232(2), 344-361.

Bryan, S.E. and Ernst, R.E., 2008. Revised definition of large igneous provinces (LIPs). Earth Sci. Rev., 86(1), 175-202.

Bryan, S.E., Peate, I.U., Peate, D.W., Self, S., Jerram, D.A., Mawby, M.R., Marsh, J.G. and Miller, J.A., 2010. The largest volcanic eruptions on Earth. Earth-Science Rev., 102(3), 207-229.

Burchette, T.P., 1993. Mishrif Formation (Cenomanian-Turonian), Southern Arabian Gulf. In: Simo, J. A. T., Scott, R. W. and Masse, J. P.. Cretaceous carbonate platforms: AAPG Memoir 56, p. 185199.

Burchfiel, B.C. and Lipman, P.W., 1992. The Cordilleran orogen: conterminous US (No. 1). Geol. Soc. Am.

Burchfiel, B.C., Cowan, D.S. and Davis, G.A., 1992. Tectonic Overview of the Cordilleran Orogen in the Western United States. In: (Eds) B.C. Burchfiel, P.W. Lipman, and M.L. Zoback. The Cordilleran orogen: conterminous US (No. 1). Boulder, Colorado. Geol. Soc. Am., 407-480.

Burke, K., 2011. Plate tectonics, the Wilson Cycle, and mantle plumes: geodynamics from the top. Annual Rev. Earth Planet. Sci., 39, 1-29.

Burnett, J.A., Gallagher, L.T. and Hampton, M.J., 1998. Upper cretaceous. Calcareous nannofossil biostratigraphy, 132-199.

Caldwell, W.G.E., Diner, R., Eicher, D.L., Fowler, S.P., North, B.R., Stelck, C.R. and von Holdt Wilhelm, L., 1993. Foraminiferal biostratigraphy of Cretaceous marine cyclothems. Evolution of the Western Interior Basin: Geol. Ass. Can., Spec. Pap., 39, 477-520.

Calvert, S.E. and Pedersen, T.F., 1993. Geochemistry of recent oxic andanoxic sediments: implications for the geological record. Mar. Geol. 113, 67-88.

Campbell, I.H., 2005. Large igneous provinces and the mantle plume hypothesis. Elements, 1(5), 265-269.

Campbell, I.H., 2007. Testing the plume theory. Chem. Geol., 241(3), 153-176.

Caron, M., Robaszynski, F., Amedro, F., Baudin, F., Deconinck, J.F., Hochuli, P.A., Nielsen, K.V.S.P. and Tribovillard, N., 1999. Estimation de la duree de l9evenement anoxique global au passage Cenomanien/Turonien; approche cyclostratigraphique dans la formation Bahloul en Tunisie centrale. Bull. Soc. Géolog. Fran., 170(2), 145-160.

Cather, S.M., Dunbar, N.W., McDowell, F.W., McIntosh, W.C. and Scholle, P.A., 2009. Climate forcing by iron fertilization from repeated ignimbrite eruptions: The icehouse-silicic large igneous province (SLIP) hypothesis. Geosphere, 5(3), 315-324.

Chamley, H., 1989. Clay formation through weathering. In: Clay Sedimentology (21-50). Springer Berlin Heidelberg.

Charbonnier, G. and Föllmi, K.B., 2017. Mercury enrichments in lower Aptian sediments support the link between Ontong Java large igneous province activity and oceanic anoxic episode 1a. Geology, 45(1), 63-66.

Charbonnier, G., Morales, C., Duchamp-Alphonse, S., Westermann, S., Adatte, T. and Föllmi, K.B., 2017. Mercury enrichment indicates volcanic triggering of Valanginian environmental change. Sci. Rep., 7.

Charvat, W.A., 1985. The nature and origin of the bentonite rich Eagle Ford rocks, central Texas.

Chumakov, N.M., Zharkov, M.A., Herman, A.B., Doludenko, M.P., Kalandadze, N.N., Lebedev, E.L., Ponomarenko, A.G. and Rautian, A.S., 1995. Climatic belts of the mid-Cretaceous time. Stratigraphy and Geological Correlation, 3(3), 42-63. Church, J.A., Gregory, J.M., Huybrechts, P., Kuhn, M., Lambeck, K., Nhuan, M.T., Qin, D. and Woodworth, P.L., 2001. Changes in sea level. In: JT Houghton, Y. Ding, DJ Griggs, M. Noguer, PJ Van der Linden, X. Dai, K. Maskell, and CA Johnson (eds.): Climate Change 2001: The Scientific Basis: Contribution of Working Group I to the Third Assessment Report of the Intergovernmental Panel, 639-694.

Clarke, L.J. and Jenkyns, H.C., 1999. New oxygen isotope evidence for long-term Cretaceous climatic change in the Southern Hemisphere. Geology, 27(8), 699-702.

Coccioni, R. and Galeotti, S., 2003. The mid-Cenomanian Event: prelude to OAE 2. Palaeogeogr. Palaeoclimatol. Palaeoecol., 190, 427-440.

Coccioni, R., Catanzariti, R., Frontalini, F., Galbrun, B., Jovane, L., Montanari, A., Savian, J.F. and Sideri, M., 2016. Integrated magnetostratigraphy, biostratigraphy, and chronostratigraphy of the Paleogene pelagic succession at Gubbio (central Italy). Geol. Soc. Am. Spec. Pap., 524, 139-160.

Coccioni, R., Sideri, M., Frontalini, F. and Montanari, A., 2016. The Rotalipora cushmani extinction at Gubbio (Italy): Planktonic foraminiferal testimonial of the onset of the Caribbean large igneous province emplacement? Geol. Soc. Am. Spec. Pap., 524, 79-96.

Coffin, M.F. and Eldholm, O., 1991. Large igneous provinces: JOI/USSAC workshop report.

Coffin, M.F. and Eldholm, O., 1994. Large igneous provinces: crustal structure, dimensions, and external consequences. Rev. Geophys., 32(1), 1-36.

Coltice, N., Phillips, B.R., Bertrand, H., Ricard, Y. and Rey, P., 2007. Global warming of the mantle at the origin of flood basalts over supercontinents. Geology, 35(5), 391-394.

Coogan, A.H., 1977. Early and Middle Cretaceous Hippuritacea (rudists) of the Gulf Coast. In: Cretaceous Carbonates of Texas and Mexico: Applications to Subsurface Exploration (Eds) D.G. Bebout and R.G. Loucks, Bur. Econ. Geol. Univ. Tex. Austin Rep. Inv., 89, 32-70

Cool, T.E., 1982. Sedimentological evidence concerning the palaeoceanography of the Cretaceous western North Atlantic Ocean. Palaeogeogr. Palaeoclimatol. Palaeoecol., 39(1-2), 1-35.

Corbett, M.J., Watkins, D.K. and Pospichal, J.J., 2014. A quantitative analysis of calcareous nannofossil bioevents of the Late Cretaceous (Late Cenomanian-Coniacian) Western Interior Seaway and their reliability in established zonation schemes. Mar. Micropaleontol., 109, 30-45.

Courtillot, V., 1994. Mass extinctions in the last 300 million years: one impact and seven flood basalts. Israel J. Earth Sci., 43(255), 66.

Courtillot, V.E. and Renne, P.R., 2003. On the ages of flood basalt events. Comptes Rendus Geoscience, 335(1), 113-140.

Coxall, H.K., Wilson, P.A., Palike, H., Lear, C.H. and Backman, J., 2005. Rapid stepwise onset of Antarctic glaciation and deeper calcite compensation in the Pacific Ocean. Nature, 433(7021), 53.

Cronin, T.M., 2009. Paleoclimates: understanding climate change past and present. Columbia University Press.

Dawson, W.C., 1986. Austin Chalk and Buda Limestone (Cretaceous) Petroleum Reservoirs in Caldwell County, Texas–A Case History. Energy exploration & exploitation, 4(5), 377-389.

Dawson, W.C., 1997. Limestone microfacies and sequence stratigraphy: Eagle Ford Group (Cenomanian-Turonian) north-central Texas outcrops. GCAGS Trans.

Dawson, W.C., 2000. Shale microfacies: Eagle Ford Group (Cenomanian-Turonian) north-central Texas outcrops and subsurface equivalents. GCAGS L, 607-622.

Dawson, W.C., Almon, W.R., 2010. Eagle Ford Shale variability: Sedimentologic influences on source and reservoir character in an unconventional resource unit.

Dean, W.E., and Arthur, M.A., 1988, Cretaceous Western Interior Seaway drilling project: an overview. In: (Eds) Dean, W.E., and Arthur, M.A.. Stratigraphy and Paleoenvironments of the Cretaceous Western Interior Seaway, USA: SEPM, Concepts Sedimentol. Paleontol., 6, 1-10.

Dean, W.E., Arthur, M.A. and Claypool, G.E., 1986. Depletion of ^{13}C in Cretaceous marine organic matter: Source, diagenetic, or environmental signal? Mar. Geol., 70(1-2), 119-157.

Dean, W.E. and Arthur, M.A., 1998. Geochemical expressions of cyclicity in Cretaceous pelagic limestone sequences: Niobrara Formation, Western Interior Seaway. SEPM Concepts Sedimentol. Paleontol. 6, 227-255.

Deckart, K., Féraud, G., Marques, L.S. and Bertrand, H., 1998. New time constraints on dyke swarms related to the Parané-Etendeka magmatic province, and subsequent South Atlantic opening, southeastern Brazil. J. Volcanol. Geotherm. Res., 80(1-2), 67-83.

Demaison, G.J. and Moore, G.T., 1980. Anoxic environments and oil source bed genesis. Organic Geochemistry, 2(1), 9-31.

Denne, R.A., Hinote, R.E., Breyer, J.A., Kosanke, T.H., Lees, J.A., Engelhardt-Moore, N., Spaw, J.M. and Tur, N., 2014. The Cenomanian-Turonian Eagle Ford Group of South Texas: Insights on timing and paleoceanographic conditions from geochemistry and micropaleontologic analyses. Palaeogeogr. Palaeoclimatol. Palaeoecol., 413, 2-28.

Denton, G.H. and Hughes, T.J., 1983. Milankovitch theory of ice ages: Hypothesis of ice-sheet linkage between regional insolation and global climate. Quat. Res., 20(2), 125-144.

Desmares, D., Grosheny, D., Beaudoin, B., Gardin, S. and Gauthier-Lafaye, F., 2007. High resolution stratigraphic record constrained by volcanic ash beds at the Cenomanian-Turonian boundary in the Western Interior Basin, USA. Cretac. Res., 28(4), 561-582.

Dickinson, W.R. and Lawton, T.F., 2001. Carboniferous to Cretaceous assembly and fragmentation of Mexico. Geol. Soc. Am. Bull., 113(9), 1142-1160.

Dickinson, W.R., 2004. Evolution of the North American cordillera. Annu. Rev. Earth Planet. Sci., 32, 13-45.

Dickson, A.J., Jenkyns, H.C., Porcelli, D., van den Boorn, S. and Idiz, E., 2016. Basin-scale controls on the molybdenum-isotope composition of seawater during Oceanic Anoxic Event 2 (Late Cretaceous). Geochim. Cosmochim. Acta, 178, 291-306.

Donovan, A., Staerker, S., Pramudito, A., Li, W., Corbett, M. J., Lowery, C.M., Miceli A., Romero, R. and Gardner, D., 2012, The Eagle Ford outcrops of West Texas: A laboratory for understanding heterogeneities within unconventional mudstone reservoirs: GCAGS Journal, 1, 162-185.

Donovan, A.D. and Staerker, T.S., 2010. Sequence stratigraphy of the Eagle Ford (Boquillas) Formation in the subsurface of South Texas and outcrops of West Texas. GCAGS Transactions, 60, 861-899.

Driskill, B., Suurmeyer, N., Rilling-Hall, S., Govert, A.M. and Garbowicz, A., 2012, January. Reservoir description of the subsurface Eagle Ford Formation, Maverick Basin area, South Texas, USA. In SPE Europec/EAGE Annual Conference. Soc. of Petroleum Engineers.

Du Vivier, A.D., Jacobson, A.D., Lehn, G.O., Selby, D., Hurtgen, M.T. and Sageman, B.B., 2015. Ca isotope stratigraphy across the Cenomanian-Turonian OAE 2: links between volcanism, seawater geochemistry, and the carbonate fractionation factor. Earth Planet. Sci. Lett., 416, 121-131.

Du Vivier, A.D., Selby, D., Sageman, B.B., Jarvis, I., Gröcke, D.R. and Voigt, S., 2014. Marine 187 Os/188 Os isotope stratigraphy reveals the interaction of volcanism and ocean circulation during Oceanic Anoxic Event 2. Earth Planet. Sci. Lett., 389, 23-33.

Du Vivier, A.D.C., Selby, D., Condon, D.J., Takashima, R. and Nishi, H., 2015. Pacific 187 Os/188 Os isotope chemistry and U-Pb geochronology: Synchroneity of global Os isotope change across OAE 2. Earth Planet. Sci. Lett., 428, 204-216.

Duggen, S., Croot, P., Schacht, U. and Hoffmann, L., 2007. Subduction zone volcanic ash can fertilize the surface ocean and stimulate phytoplankton growth: Evidence from biogeochemical experiments and satellite data. Geophys. Res. Let., 34(1).

Dunham, R. J., 1962, Classification of carbonate rocks according to depositional texture, in W. E. Ham, ed., Classifications of carbonate rocksa symposium: AAPG Mem. 1, 108-121.Durand, B., 1980. Sedimentary organic matter and kerogen. Definition and quantitative importance of kerogen. Kerogen-Insoluble organic matter from sedimentary rocks, 13-34.

Eaton, G.P., 1963. Volcanic ash deposits as a guide to atmospheric circulation in the geologic past. J. Geophys. Res., 68(2), 521-528.

Eaton, J.P., 1963. Crustal structure from San Francisco, California, to Eureka, Nevada, from seismicrefraction measurements. J. Geophys. Res., 68(20), 5789-5806.

Eberli, G.P., Bernoulli, D., Sanders, D. and Vecsei, A., 1993. From aggradation to progradation; the Maiella Platform, Abruzzi, Italy. In: Cretaceous carbonate platforms (Eds J.A.T. Simo, R.W. Scott and J.P. Masse), AAPG Mem., 56, 213-232.

Eicher, D.L. and Worstell, P., 1970. Cenomanian and Turonian foraminifera from the great plains, United States. Micropaleontol., 269-324.

Eicher, D.L., and Diner, R., 1985. Foraminifera as indicators of watermass in the Cretaceous Greenhorn Sea, Western Interior. In: (Eds.) Pratt, L., Kauffman, E.G., Zelt, F.B. Fine-grained deposits and biofacies of the Cretaceous Western Interior Seaway: evidence of cyclic depositional processes. SEPM Annual Mid-year Meeting, Field Trip, 4, 122-134.

Eicher, D.L. and Diner, R., 1989. Origin of the Cretaceous Bridge Creek cycles in the Western Interior, United States. Palaeogeogr. Palaeoclimatol. Palaeoecol.74, 127-146.

Eicher, D.L. and Diner, R., 1991. Environmental factors controlling Cretaceous limestone-marlstone rhythms. In: Einsele, G., Ricken, W., Seilacher, A. (Eds.), Cycles and Events in Stratigraphy. Springer, Berlin, 79-93.

Einsele, G., Ricken, W., Seilacher, A., (Eds.) 1991, Cycles and events in stratigraphy. Springer, Berlin.

El Beialy, S.Y., El Atfy, H.S., Zavada, M.S., El Khoriby, E.M. and Abu-Zied, R.H., 2010. Palynological, palynofacies, paleoenvironmental and organic geochemical studies on the Upper Cretaceous succession of the GPTSW-7 well, North Western Desert, Egypt. Marine and Petroleum Geology, 27(2), 370-385.

Elder, W.P., 1985. Biotic patterns across the Cenomanian-Turonian extinction boundary near Pueblo, Colorado. In: Pratt, L.M., Kauffman, E.G., Zelt, F.B. (Eds.), Field Trip Guidebook, 4, 157-169.

Elder, W.P., 1987. The paleoecology of the Cenomanian-Turonian (Cretaceous) stage boundary extinctions at Black Mesa, Arizona. Palaios, 24-40.

Elder, W.P., 1991. Molluscan paleoecology and sedimentation patterns of the Cenomanian-Turonian extinction interval in the southern Colorado Plateau region. Geol. Soc. Am. Spec. Pap., 260, 113-138.

Elder, W.P., Gustason, E.R., Sageman, B.B., 1994. Correlation of basinal carbonate cycles to nearshore parasequences in the Late Cretaceous Greenhorn seaway, Western Interior USA. Geol. Soc. Am. Bull., 106(7), 892-902.

Elderbak, K. and Leckie, R.M., 2016. Paleocirculation and foraminiferal assemblages of the Cenomanian-Turonian Bridge Creek Limestone bedding couplets: Productivity vs. dilution during OAE2. Cretac. Res., 60, 52-77.

Eldrett, J.S., Dodsworth, P., Bergman, S.C., Wright, M. and Minisini, D., 2017. Water-mass evolution in the Cretaceous Western Interior Seaway of North America and Equatorial Atlantic. Climate of the Past, 13(7), 855.

Eldrett, J.S., Ma, C., Bergman, S.C., Lutz, B., Gregory, F.J., Dodsworth, P., Phipps, M., Hardas, P., Minisini, D., Ozkan, A. and Ramezani, J., 2015a. An astronomically calibrated stratigraphy of the Cenomanian, Turonian and earliest Coniacian from the Cretaceous Western Interior Seaway, USA: Implications for global chronostratigraphy. Cretac. Res., 56, 316-344.

Eldrett, J.S., Ma, C., Bergman, S.C., Ozkan, A., Minisini, D., Lutz, B., Jackett, S.J.,

Macaulay, C. and Kelly, A.E., 2015b. Origin of limestone-marlstone cycles: astronomic forcing of organic-rich sedimentary rocks from the Cenomanian to early Coniacian of the Cretaceous Western Interior Seaway, USA. Earth Planet. Sci. Lett., 423, 98-113.

Eldrett, J.S., Minisini, D. and Bergman, S.C., 2014. Decoupling of the carbon cycle during Ocean Anoxic Event 2. Geology, 42(7), 567-570.

Elkins-Tanton, L.T., 2005. Continental magmatism caused by lithospheric delamination. Geol. Soc. Am.Spec. Pap., 388, 449-461.

Elkins-Tanton, L.T., 2007. Continental magmatism, volatile recycling, and a heterogeneous mantle caused by lithospheric gravitational instabilities. J. Geophys. Res.: Solid Earth, 112(B3).

Elkins-Tanton, L.T.E. and Hager, B.H., 2000. Melt intrusion as a trigger for lithospheric foundering and the eruption of the Siberian flood basalts. Geophys. Res. Let., 27(23), 3937-3940.

Emerson, S.R. and Huested, S.S., 1991. Ocean anoxia and the concentrations of molybdenum and vanadium in seawater. Mar. Chem., 34(3-4), 177-196.

Endo, N., Sunamura, T. and Takimoto, H., 2005. Barchan ripples under unidirectional water flows in the laboratory: Formation and planar morphology: Earth Surface Processes and Landforms, 30, 13, 1675-1682.

Erba, E., 1994. Nannofossils and superplumes: the early Aptian ”nannoconid crisis”. Paleoceanog., 9(3), 483-501.

Erba, E., Bartolini, A. and Larson, R.L., 2004. Valanginian Weissert oceanic anoxic event. Geology, 32(2), 149-152.

Erba, E., Duncan, R.A., Bottini, C., Tiraboschi, D., Weissert, H., Jenkyns, H.C. and Malinverno, A., 2015. Environmental consequences of Ontong Java Plateau and Kerguelen Plateau volcanism. Geol. Soc. Am. Spec. Pap., 511, SPE511-15.

Erbacher, J., Friedrich, O., Wilson, P.A., Birch, H. and Mutterlose, J., 2005. Stable organic carbon isotope stratigraphy across Oceanic Anoxic Event 2 of Demerara Rise, western tropical Atlantic. Geochem., Geophys., Geosyst., 6(6).

Erbacher, J., Huber, B.T., Norris, R.D. and Markey, M., 2001. Increased thermohaline stratification as a possible cause for an ocean anoxic event in the Cretaceous period. Nature, 409(6818), 325. Erickson, B.E. and Helz, G.R., 2000. Molybdenum(VI) speciation in sulfidic waters: stability and lability of thiomolybdates. Geochim. Cosmochim. Acta 64, 1149-1158.

Ernst, R.E. and Buchan, K.L., 2001. The use of mafic dike swarms in identifying and locating mantle plumes. Geol. Soc. Am. Spec. Pap., 352, 247-265.

Ernst, R.E., 2005. Large igneous provinces. Cambridge University Press.

Ernst, R.E., and Bleeker W., 2010. Large igneous provinces (LIPs), giant dyke swarms, and mantle plumes: significance for breakup events within Canada and

adjacent regions from 2.5 Ga to the Present. Can. J. Earth Sci., 47, 695-739.

Ernst, R.E., Buchan, K.L. and Campbell, I.H., 2005. Frontiers in large igneous province research. Lithos, 79(3), 271-297.

Estrada, S., 2015. Geochemical and SrNd isotope variations within Cretaceous continental flood-basalt suites of the Canadian High Arctic, with a focus on the Hassel Formation basalts of northeast Ellesmere Island. Int. J. Earth Sci., 104(8), 1981-2005. Evenchick, C.A., Davis, W.J., Bédard, J.H., Hayward, N. and Friedman, R.M., 2015. Evidence for protracted High Arctic large igneous province magmatism in the central Sverdrup Basin from stratigraphy, geochronology, and paleodepths of saucer-shaped sills. Geol. Soc. Am. Bull., B31190-1. Ewing, T.E. and Caren, C.S., 1982. Late Cretaceous volcanism in south and central Texas: stratigraphic, structural and seismic models. Gulf Coast Assoc. Geol. Soc. Trans, 32, 137-145.

Ewing, T.E. and Lopez, R.F., 1991. Principle structural features. In: Salvador, A. (Ed.) The Gulf of Mexico Basin. Geol. Soc. Am., The Geology of North America.

Ewing, T.E., 1985. Westward extension of the Devils River uplift-Implications for the Paleozoic evolution of the southern margin of North America. Geology, 13(6), 433-436.

Ewing, T.E., 1991. Structural framework. In: Salvador, A. (Ed.) The Gulf of Mexico Basin. Geol. Soc. Am., The Geology of North America. 31-52.

Ewing, T.E., 2009. The ups and downs of the Sabine Uplift and the Northern Gulf of Mexico Basin: Jurassic basement blocks, Cretaceous thermal uplifts, and Cenozoic flexure.

Fairbanks, M.D., 2012. High resolution stratigraphy and facies architecture of the upper Cretaceous (Cenomanian-Turonian) Eagle Ford Group, central Texas (Doctoral dissertation).

Fairbanks, M.D., Ruppel, S.C. and Rowe, H., 2016. High-resolution stratigraphy and facies architecture of the Upper Cretaceous (Cenomanian-Turonian) Eagle Ford Group, Central Texas. AAPG Bull., 100(3), 379-403.

Falkowski, P.G., Flagg, C.N., Rowe, G.T., Smith, S.L., Whitledge, T.E. and Wirick, C.D., 1988. The fate of a spring phytoplankton bloom: export or oxidation?. Cont. Shelf. Res., 8(5-7), 457-484.

Falzoni, F., Petrizzo, M.R., Clarke, L.J., MacLeod, K.G. and Jenkyns, H.C., 2016. Long-term Late Cretaceous oxygen-and carbon-isotope trends and planktonic foraminiferal turnover: A new record from the southern midlatitudes. Geol. Soc. Am. Bull., 128(11-12), 1725-1735.

Falzoni, F., Petrizzo, M.R., Jenkyns, H.C., Gale, A.S. and Tsikos, H., 2016. Planktonic foraminiferal biostratigraphy and assemblage composition across the Cenomanian-Turonian boundary interval at Clot Chevalier (Vocontian Basin, SE France). Cretac. Res., 59, 69-97.

Fischer, A.G., 1980. Gilbert-bedding rhythms and geochronology. In: Yochelson,

E.I. (Ed.), The Scientific Ideas of G.K. Gilbert. In: Geol. Soc. Am. Spec. Pap., 183, 93-104.

Fischer, A.G., Herbert, T. and PremoliSilva, I., 1985. Carbonate bedding cycles in Cre-taceous pelagic and hemipelagic sequences. In: Pratt, L.M., Kauffman, E.G., Zelt, F.B. (Eds.), Fine Grained Deposits and Biofacies of the Cretaceous Western In-terior Seaway: Evidence of Cyclic Sedimentary Processes. Soc. of Economic Paleontologists and Mineralogists Field Trip Guidebook, 4, 1-10.

Fisher, R.V. and Schmincke, H.U., 1984. Pyroclastic rocks, 472 Springer, Berlin, 10, 978-3.

Flawn, P.T., 1959. Devils River Uplift. West Texas Geol. Soc. Guidebook, 74-78.

Flawn, P.T., 1961. The Subsurface Ouchita Structural Belt in Texas and Southeast Oklahoma. University of Texas, Bureau of Economic Geology, 65-81.

Flemming, B. W., 1980. Sand transport and bedform patterns on the continental shelf between Durban and Port Elizabeth (southeast African continental margin). Sed. Geol., 26, 1-3, 179-205.

Fletcher, B.J., Beerling, D.J., Brentnall, S.J. and Royer, D.L., 2005. Fossil bryophytes as recorders of ancient CO2 levels: experimental evidence and a Cretaceous case study. Global Biogeochemical Cycles, 19(3).

Fletcher, B.J., Brentnall, S.J., Anderson, C.W., Berner, R.A. and Beerling, D.J., 2008. Atmospheric carbon dioxide linked with Mesozoic and early Cenozoic climate change. Nature Geoscience, 1(1), 43-48.

Flexer, A., Rosenfeld, A., Lipson-Benitah, S. and Honigstein, A., 1986. Relative sea level changes during the Cretaceous in Israel. AAPG Bull., 70(11), 1685-1699.

Floegel, S., Wagner, T., 2006. Insolation-control on the Late Cretaceous hydrological cycle and tropical African climateglobal climate modelling linked to marine climate records. Palaeogeography, Palaeoclimatology, Palaeoecology, 235(1-3), 288-304.

Fluteau, F., Ramstein, G., Besse, J., Guiraud, R. and Masse, J.P., 2007. Impacts of palaeogeography and sea level changes on Mid-Cretaceous climate. Palaeogeography, Palaeoclimatology, Palaeoecology, 247(3-4), 357-381. Fontijn, K., Lachowycz, S.M., Rawson, H., Pyle, D.M., Mather, T.A., Naranjo, J.A. and Moreno-Roa, H., 2014. Late Quaternary tephrostratigraphy of southern Chile and Argentina. Quaternary Science Rev., 89, 70-84.

Forster, A., Kuypers, M.M., Turgeon, S.C., Brumsack, H.J., Petrizzo, M.R. and Sinninghe Damsté, J.S., 2008. The Cenomanian/Turonian oceanic anoxic event in the South Atlantic: New insights from a geochemical study of DSDP Site 530A. Palaeogeogr. Palaeoclimatol. Palaeoecol., 267(3), 256-283.

Forster, A., Schouten, S., Baas, M. and Sinninghe Damsté, J.S., 2007. Mid-Cretaceous (Albian-Santonian) sea surface temperature record of the tropical Atlantic Ocean. Geology, 35(10), 919-922.

Forster, A., Schouten, S., Moriya, K., Wilson, P.A. and Sinninghe Damsté, J.S., 2007. Tropical warming and intermittent cooling during the Cenomanian/Turonian oceanic anoxic event 2: Sea surface temperature records from the equatorial Atlantic. Paleoceanog., 22(1).

Foulger, G.R., 2007. The ”plate” model for the genesis of melting anomalies. Geol. Soc. Am.Spec. Pap., 430, 1-28.

Frakes, L.A., Francis, J.E. and Syktus, J.I., 1992. Climate modes of the Phanerozoic. Cambridge University Press.

Frébourg, G., Ruppel, S.C., Loucks, R.G. and Lambert, J., 2016. Depositional controls on sediment body architecture in the Eagle Ford/Boquillas system: Insights from outcrops in west Texas, United States. AAPG Bull., 100(4), 657-682.

Friedrich, O., Erbacher, J. and Mutterlose, J., 2006. Paleoenvironmental changes across the Cenomanian/Turonian boundary event (oceanic anoxic event 2) as indicated by benthic foraminifera from the Demerara Rise (ODP Leg 207). Revue de micropaléontologie, 49(3), 121-139.

Friedrich, O., Erbacher, J., Moriya, K., Wilson, P.A. and Kuhnert, H., 2008. Warm saline intermediate waters in the Cretaceous tropical Atlantic Ocean. Nature Geoscience, 1(7), p.453. Friedrich, O., Erbacher, J., Wilson, P.A., Moriya, K. and Mutterlose, J., 2009. Paleoenvironmental changes across the Mid Cenomanian Event in the tropical Atlantic Ocean (Demerara Rise, ODP Leg 207) inferred from benthic foraminiferal assemblages. Mar. Micropaleontol., 71(1), 28-40.

Frogner, P., Gslason, S.R. and Óskarsson, N., 2001. Fertilizing potential of volcanic ash in ocean surface water. Geology, 29(6), 487-490.

Gadd, P. E., Lavelle, J. W. and Swift, D. J. P., 1978, Estimates of sand transport on the New York shelf using near bottoöm current meter observations. J. Sed. Res., 48, 1, 239-252.

Gale, A.S. and Christensen, W.K, 1996. Occurrence of the belemnite Actinocamax plenus in the Cenomanian of SE France and its significance. Bull. Geol. Soc. Denmark, 43, 68-77.

Gale, A.S., 2000. The cretaceous world. Biotic response to global change. 145, 4-19.

Gale, A.S., Christensen, W.K. and Gale, A.S., 1996. Occurrence of the belemnite Actinocamax plenus in the Cenomanian of SE France and its significance. Bull. Geol. Soc. of Denmark.

Gale, A.S., Hardenbol, J., Hathway, B., Kennedy, W.J., Young, J.R. and Phansalkar, V., 2002. Global correlation of Cenomanian (Upper Cretaceous) sequences: Evidence for Milankovitch control on sea level. Geology, 30(4), 291-294.

Galeotti, S., Rusciadelli, G., Sprovieri, M., Lanci, L., Gaudio, A. and Pekar, S., 2009. Sea-level control on facies architecture in the Cenomanian-Coniacian Apulian margin (Western Tethys): A record of glacio-eustatic fluctuations during the Cretaceous

greenhouse?. Palaeogeogr. Palaeoclimatol. Palaeoecol., 276(1), 196-205.

Gambacorta, G., Jenkyns, H.C., Russo, F., Tsikos, H., Wilson, P.A., Faucher, G. and Erba, E., 2015. Carbon-and oxygen-isotope records of mid-Cretaceous Tethyan pelagic sequences from the Umbria-Marche and Belluno Basins (Italy). Newsletters on Stratigraphy, 48(3), 299-323.

Gehrke, G.E., Blum, J.D. and Meyers, P.A., 2009. The geochemical behavior and isotopic composition of Hg in a mid-Pleistocene western Mediterranean sapropel. Geochim. Cosmochim. Acta, 73(6), 1651-1665.

Gens, A. and Alonso, E.E., 1992. A framework for the behaviour of unsaturated expansive clays. Canadian Geotechnical Journal, 29(6), 1013-1032.

Gertsch, B., Keller, G., Adatte, T., Berner, Z., Kassab, A.S., Tantawy, A.A.A., El-Sabbagh, A.M. and Stueben, D., 2010. Cenomanian-Turonian transition in a shallow water sequence of the Sinai, Egypt. Int. J. Earth Sci., 99(1), 165-182.

Ghadeer, S. G. and Macquaker, J. H., 2011. Sediment transport processes in an ancient mud-dominated succession: A comparison of processes operating in marine offshore settings and anoxic basinal environments: J. Geol. Soc., 168, 5, 1121-1132.

Gilbert, G.K., 1895. Sedimentary measurement of Cretaceous time. J. Geol., 3(2), 121-127.

Gildor, H. and Tziperman, E., 2000. Sea ice as the glacial cycles' climate switch: Role of seasonal and orbital forcing. Paleoceanog., 15(6), 605-615.

Glazner, A.F., Manley, C.R., Marron, J.S. and Rojstaczer, S., 1999. Fire or ice: Anticorrelation of volcanism and glaciation in California over the past 800,000 years. Geophys. Res. Let., 26(12), 1759-1762.

Godet, A., Bodin, S., Adatte, T. and Fèöllmi, K.B., 2008. Platform-induced clay-mineral fractionation along a northern Tethyan basin-platform transect: implications for the interpretation of Early Cretaceous climate change (Late Hauterivian-Early Aptian). Cretac. Res., 29(5), 830-847.

Goldberg, T., Poulton, S.W., Wagner, T., Kolonic, S.F. and Rehkämper, M., 2016. Molybdenum drawdown during Cretaceous Oceanic Anoxic Event 2. Earth Planet. Sci. Lett., 440, 81-91.

Goldhammer, R.K. and Johnson, C.A., 1999. Mesozoic sequence stratigraphy and paleogeographic evolution of northeast Mexico. Spec. Pap. Geol. Soc. Am., 1-58.

Goldhammer, R.K., and Johnson, C.A., 2001. Middle Jurassic-Upper Cretaceous Paleogeographic Evolution and Sequence-stratigraphic Framework of the Northwest Gulf of Mexico Rim. AAPG Mem. 75.

Gong, Q., Wang, X., Zhao, L., Grasby, S.E., Chen, Z.Q., Zhang, L., Li, Y., Cao, L. and Li, Z., 2017. Mercury spikes suggest volcanic driver of the Ordovician-Silurian mass extinction. Sci. Rep., 7.

Gradstein, F. and Ogg, J., 2004. Geologic time scale 2004-why, how, and where next!. Lethaia, 37(2), 175-181.

Grasby, S.E., Sanei, H., Beauchamp, B. and Chen, Z., 2013. Mercury deposition through the Permo-Triassic biotic crisis. Chem. Geol., 351, 209-216.

Griffin, W.R., Foland, K.A., Stern, R.J. and Leybourne, M.I., 2010. Geochronology of bimodal alkaline volcanism in the Balcones Igneous Province, Texas: Implications for Cretaceous intraplate magmatism in the northern Gulf of Mexico magmatic zone. J. Geol., 118(1), 1-21.

Grosjean, E., Adam, P., Connan, P. and Albrecht, P., 2004. Effects of weathering on nickel and vanadyl porphyrins of a Lower Toarcian shale of the Paris basin. Geochim. Cosmochim. Acta 68, 789-804.

Grove, T.L., Till, C.B. and Krawczynski, M.J., 2012. The role of H2O in subduction zone magmatism. Annual Rev. Earth Planet. Sci., 40, 413-439.

Gruber, N. and Sarmiento, J.L., 2002. Large-scale biogeochemical-physical interactions in elemental cycles. The sea, 12, 337-399.

Hales, T.C., Abt, D.L., Humphreys, E.D. and Roering, J.J., 2005. A lithospheric instability origin for Columbia River flood basalts and Wallowa Mountains uplift in northeast Oregon. Nature, 438(7069), 842.

Hall, K., 1982. Rapid deglaciation as an initiator of volcanic activity: an hypothesis. Earth Surface Processes and Landforms, 7(1), 45-51.

Hamme, R.C., Webley, P.W., Crawford, W.R., Whitney, F.A., DeGrandpre, M.D., Emerson, S.R., Eriksen, C.C., Giesbrecht, K.E., Gower, J.F., Kavanaugh, M.T. and Peña, M.A., 2010. Volcanic ash fuels anomalous plankton bloom in subarctic northeast Pacific. Geophys. Res. Let., 37(19).

Hammerschmidt, C.R. and Fitzgerald, W.F., 2006. Methylmercury cycling in sediments on the continental shelf of southern New England. Geochim. Cosmochim. Acta, 70(4), 918-930.

Haq, B.U., 2014. Cretaceous eustasy revisited. Global and Planetary Change, 113, 44-58.

Haq, B.U., Hardenbol, J. and Vail, P.R., 1987. Chronology of fluctuating sea levels since the Triassic. Science, 235(4793), 1156-1167.

Haq, B.U., Hardenbol, J. and Vail, P.R., 1988. Mesozoic and Cenozoic chronostratigraphy and cycles of sea-level change. Soc. of Economic Palaeontologists and Mineralogists, 42, 71-108.

Hardas, P. and Mutterlose, J., 2006. Calcareous nannofossil biostratigraphy of the Cenomanian/Turonian boundary interval of ODP Leg 207 at the Demerara Rise. Revue de micropaléontologie, 49(3), 165-179.

Hardenbol, J.A.N., Thierry, J., Farley, M.B., Jacquin, T., De Graciansky, P.C. and Vail, P.R., 1998. Mesozoic and Cenozoic sequence chronostratigraphic framework

of European basins.

Hattin, D.E., 1971. Widespread synchronously deposited burrow-mottled limestone beds in the Greenhorn Limestone (Upper Cretaceous) of Kansas and southeastern Colorado. AAPG Bull. 55, 412-431.

Hattin, D.E., 1975. Petrology and origin of fecal pellets in Upper Cretaceous strata of Kansas and Saskatchewan. J. Sed. Res., 45(3).

Hattin, D.E., 1975. Stratigraphy and depositional environment of the Greenhorn Limestone (Upper Cretaceous) of Kansas. Kansas State Geol. Surv. Bull. 209, 128.

Hattin, D.E., 1986. Carbonate substrates of the Late Cretaceous Sea, central Great Plains and southern Rocky Mountains. Palaios 1, 347-367.

Hattin, D.E., 1986. Interregional model for deposition of Upper Cretaceous pelagic rhythmites, US Western Interior. Paleoceanog., 1(4), 483-494.

Hay, W.W. and Leslie, M.A., 1990. Could possible changes in global groundwater reservoir cause eustatic sea-level fluctuations. Sea-Level Change. National Academy Press, Washington, DC, 161-170.

Hay, W.W., 2008. Evolving ideas about the Cretaceous climate and ocean circulation. Cretaceous Research, 29(5-6), 725-753.

Hay, W.W., 2009. Cretaceous oceans and ocean modeling. SEPM, 91, 243-271.

Hay, W.W. and Floegel, S., 2012. New thoughts about the Cretaceous climate and oceans. Earth-Science Reviews, 115(4), 262-272. Hays, J.D., Imbrie, J. and Shackleton, N.J., 1976. Variations in the Earth's orbit: pacemaker of the ice ages. Science, 194(4270), 1121-1132.

Helz, G.R., Miller, C.V., Charnock, J.M., Mosselmans, J.L.W., Pattrick, R.A.D., Garner, C.D. and Vaughan, D.J., 1996. Mechanisms of molybdenum removal from the sea and its concentration in black shales: EXAFS evidences. Geochim. Cosmochim. Acta 60, 3631-3642.

Henry, C.D. and Price, J.G., 1984. Variations in caldera development in the Tertiary volcanic field of TransPecos Texas. J. Geophys. Res.: Solid Earth, 89(B10), 8765-8786.

Hentz, T.F. and Ruppel, S.C., 2010. Regional lithostratigraphy of the Eagle Ford Shale: Maverick Basin to East Texas Basin. GCAGS Trans., 60, 325-337.

Herbin, J.P., Montadert, L., Müller, C., Gomez, R., Thurow, J. and Wiedmann, J., 1986. Organic-rich sedimentation at the Cenomanian-Turonian boundary in oceanic and coastal basins in the North Atlantic and Tethys. Geol. Soc., Lon., Spec. Publ., 21(1), 389-422.

Hetzel, A., Böttcher, M.E., Wortmann, U.G. and Brumsack, H.J., 2009. Paleo-redox conditions during OAE 2 reflected in Demerara Rise sediment geochemistry (ODP Leg 207). Palaeogeogr. Palaeoclimatol. Palaeoecol., 273(3), 302-328.

Heureux, A.M. and Rickaby, R.E., 2015. Refining our estimate of atmospheric CO 2 across the Eocene-Oligocene climatic transition. Earth Planet. Sci. Lett., 409, 329-338.

Hill, R.T., 1887. The topography and geology of the Cross Timbers and surrounding regions in northern Texas. Am. J. Sci., (196), 291-303.

Hinkley, T.K., Lamothe, P.J., Wilson, S.A., Finnegan, D.L. and Gerlach, T.M., 1999. Metal emissions from Kilauea, and a suggested revision of the estimated worldwide metal output by quiescent degassing of volcanoes. Earth Planet. Sci. Lett., 170(3), 315-325.

Hjulstrom, F., 1935, Studies of the morphological activity of rivers as illustrated by the river Fyris, inaugural dissertation, Almqvist & Wiksells, Stockholm, Sweden, 221.

Hofmann, P., Ricken, W., Schwark, L., Leythaeuser, D., 1999. Coupled oceanic effects of climatic cycles from late Albian deep-sea sections of the North Atlantic. In: Barrera, E., Johnson, C. (Eds.), The Evolution of Cretaceous Ocean/Climate Systems. GSA Spec. Pub. 332, Boulder, 143-159. Hoffmann, L.J., Breitbarth, E., Ardelan, M.V., Duggen, S., Olgun, N., Hassellöv, M. and Wängberg, S.., 2012. Influence of trace metal release from volcanic ash on growth of Thalassiosira pseudonana and Emiliania huxleyi. Mar. Chem., 132, 28-33.

Hollweg, T.A., Gilmour, C. and Mason, R.P., 2010. Mercury and methylmercury cycling in sediments of the midAtlantic continental shelf and slope. Limnology and Oceanography, 55(6), 2703-2722.

Holmden, C., Jacobson, A.D., Sageman, B.B. and Hurtgen, M.T., 2016. Response of the Cr isotope proxy to Cretaceous Ocean Anoxic Event 2 in a pelagic carbonate succession from the Western Interior Seaway. Geochim. Cosmochim. Acta, 186, 277-295.

Honjo, S., 1997. Marine snow and fecal pellets: The spring rain of flood to the abyss: Oceanus, 40, 2, 1-3.

Horak, R.L., 1985. Trans-Pecos tectonism and its effect on the Permian basin. Structure and Tectonics of Trans-Pecos Texas: Midland, Texas, West Texas Geol. Soc., 81-87.

Huber, B.T., 1998. Tropical paradise at the Cretaceous poles? Science, 282(5397), 2199-2200.

Huber, B.T., Hodell, D.A. and Hamilton, C.P., 1995. Middle-Late Cretaceous climate of the southern high latitudes: stable isotopic evidence for minimal equator-to-pole thermal gradients. Geol. Soc. Am. Bull., 107(10), 1164-1191.

Huber, B.T., Norris, R.D. and MacLeod, K.G., 2002. Deep-sea paleotemperature record of extreme warmth during the Cretaceous. Geology, 30(2), 123-126.

Huerta-Diaz, M.A. and Morse, J.W., 1990. A quantitative method for determination of trace metal concentrations in sedimentary pyrite. Mar. Chem. 29, 119-144.

Hull, D.C., 2011. Stratigraphic architecture, depositional systems, and reservoir characteristics of the Pearsall shalegas system, lower Cretaceous, south Texas. MS Thesis, University of Texas, Austin, TX, 192.

Ingall, E.D., Bustin, R.M. and Van Cappellen, P., 1993. Influence of water column anoxia on the burial and preservation of carbon and phosphorus in marine shales. Geochim. Cosmochim. Acta, 57(2), 303-316.

Ingle, S. and Coffin, M.F., 2004. Impact origin for the greater Ontong Java Plateau?. Earth Planet. Sci. Lett., 218(1), 123-134.

Isozaki, Y., 2009. Illawarra Reversal: the fingerprint of a superplume that triggered Pangean breakup and the end-Guadalupian (Permian) mass extinction. Gondwana Research, 15(3), 421-432.

Jaenicke, R., 1980. Atmospheric aerosols and global climate. J. Aerosol Sci., 11, 577-588.

Jarvis, I., Carson, G., Hart, M., Leary, P. and Tocher, B., 1988. The Cenomanian-Turonian (late Cretaceous) anoxic event in SW England: evidence from Hooken Cliffs near Beer, SE Devon. Newsletters on Stratigraphy, 147-164.

Jarvis, I., Carson, G.A., Cooper, M.K.E., Hart, M.B., Leary, P.N., Tocher, B.A., Horne, D. and Rosenfeld, A., 1988. Microfossil assemblages and the Cenomanian-Turonian (Late Cretaceous) oceanic anoxic event. Cretac. Res., 9(1), 3-103.

Jarvis, I., Gale, A.S., Jenkyns, H.C. and Pearce, M.A., 2006. Secular variation in Late Cretaceous carbon isotopes: a new δ^{13}C carbonate reference curve for the Cenomanian-Campanian (99.6-70.6 Ma). Geol. Mag., 143(5), 561-608.

Jarvis, I., Lignum, J.S., Gröcke, D.R., Jenkyns, H.C. and Pearce, M.A., 2011. Black shale deposition, atmospheric CO2 drawdown, and cooling during the Cenomanian‐Turonian Oceanic Anoxic Event. Paleoceanog., 26(3).

Jarvis, I., Gale, A.S., Jenkyns, H.C. and Pearce, M.A., 2006. Secular variation in Late Cretaceous carbon isotopes: a new δ 13 C carbonate reference curve for the Cenomanian-Campanian (99.6-70.6 Ma). Geol. Mag., 143(05), 561-608.

Jellinek, A.M., Manga, M. and Saar, M.O., 2004. Did melting glaciers cause volcanic eruptions in eastern California? Probing the mechanics of dike formation. J. Geophys. Res.: Solid Earth, 109(B9).

Jenkyns, H., 1988. The early Toarcian (Jurassic) anoxic event-stratigraphic, sedimentary, and geochemical evidence. Am. J. Sci., 288(2), 101-151. Jenkyns, H.C., 1980. Cretaceous anoxic events: from continents to oceans. J. Geol. Soc., 137(2), 171-188.

Jenkyns, H.C., 2010. Geochemistry of oceanic anoxic events. Geochem., Geophys., Geosyst., 11(3).

Jenkyns, H.C., Dickson, A.J., Ruhl, M. and Boorn, S.H., 2017. Basaltseawater interaction, the Plenus Cold Event, enhanced weathering and geochemical change: deconstructing Oceanic Anoxic Event 2 (Cenomanian-Turonian, Late Cretaceous).

Sedimentol., 64(1), 16-43.

Jenkyns, H.C., Forster, A., Schouten, S. and Sinninghe Damsté, J.S., 2004. High temperatures in the Late Cretaceous Artic Ocean. Nature, 432(7019), 888.

Jenkyns, H.C., Gale, A.S. and Corfield, R.M., 1994. Carbon-and oxygen-isotope stratigraphy of the English Chalk and Italian Scaglia and its palaeoclimatic significance. Geol. Mag., 131(01), 1-34.

Jiang, M.J., 1989. Biostratigraphy and geochronology of the Eagle Ford Shale, Austin Chalk, and lower Taylor marl in Texas based on calcareous nannofossils. PhD Dissertation, Texas A&M University, College Station, TX, 496.

Jiménez-Berrocoso, A., K.G., MacLeod, K.G., Martin, E.E., Bourbon, E., Londoño, C.I. and Basak, C., 2010. Nutrient trap for Late Cretaceous organic-rich black shales in the tropical North Atlantic. Geology, 38(12), 1111-1114.

Jones, A.P., Price, G.D., Price, N.J., DeCarli, P.S. and Clegg, R.A., 2002. Impact induced melting and the development of large igneous provinces. Earth Planet. Sci. Lett., 202(3), 551-561.

Jones, C.E. and Jenkyns, H.C., 2001. Seawater strontium isotopes, oceanic anoxic events, and seafloor hydrothermal activity in the Jurassic and Cretaceous. Am. J. Sci., 301(2), 112-149.

Jones, D.S., Martini, A.M., Fike, D.A. and Kaiho, K., 2017. A volcanic trigger for the Late Ordovician mass extinction? Mercury data from south China and Laurentia. Geology, 45(7), 631-634.

Jones, M. T. and Gislason, S. R., 2008. Rapid releases of metal salts and nutrients following the deposition of volcanic ash into aqueous environments: Geochim. Cosmochim. Acta, 72, 15, 3661-3680.

Joo, Y.J. and Sageman, B.B., 2014. Cenomanian to Campanian carbon isotope chemostratigraphy from the Western Interior Basin, USA. J. Sed. Res., 84(7), 529-542.

Jorry, S. J., Hasler, C. A. and Davaud, E., 2006. Hydrodynamic behaviour of Nummulites: Implications for depositional models: Facies, 52, 2, 221-235.

Jull, M. and McKenzie, D., 1996. The effect of deglaciation on mantle melting beneath Iceland. J. Geophys. Res.: Solid Earth, 101(B10), 21815-21828.

Karl, D.M., 2002. Nutrient dynamics in the deep blue sea. Trends in Microbiology, 10(9), 410-418.

Katz, B. (Ed.), 1995. Petroleum source rocks. Springer Science & Business Media.

Kauffman, E.G. and Caldwell, W.G.E., 1993. The Western Interior Basin in space and time. Evolution of the Western Interior Basin: Geol. Ass. Can., Spec. Pap., 39, 1-30.

Kauffman, E.G. and Hart, M.B., 1996. Cretaceous bio-events. In Global events and

event stratigraphy in the Phanerozoic, 285-312. Springer Berlin Heidelberg.

Kauffman, E.G. and Johnson, C.C., 1988. The morphological and ecological evolution of Middle and Upper Cretaceous reef-building rudistids. Palaios, 194-216.

Kauffman, E.G., 1977. Geological and biological overview: Western Interior Cretaceous basin. The Mountain Geologist.

Kauffman, E.G., 1984. Paleobiogeography and evolutionary response dynamic in the Cretaceous Western Interior Seaway of North America. Jurassic-Cretaceous biochronology and paleogeography of North America: Geol. Ass. Can. Spec. Pap., 27, 273-306.

Kauffman, E.G., 1985. Cretaceous evolution of the Western Interior basin of the United States. Fine-Grained Deposits and Biofacies of the Cretaceous Western Interior Seaway: Evidence of Cyclic Sedimentary Processes: SEPM, Field Trip Guidebook, 4.

Kauffman, E.G., 1995. Global change leading to biodiversity crisis in a greenhouse word: the Cenomanian-Turonian (Cretaceous) mass extinction. In: Stanley, S.M. (Ed.), Effects of Past Global Change on Life. In: Studies in Geophysics. National Academy Press, 47-71.

Kauffman, E.G., Hattin, D.E. and Powell, J.D., 1977. Stratigraphic, paleontologic, and paleoenvironmental analysis of the Upper Cretaceous rocks of Cimarron County, northwestern Oklahoma, 149. Geol. Soc. Am.

Kauffman, E.G., Sageman, B.B., Kirkland, J.I., Elder, W.P., Harries, P.J. and Villamil, T., 1993. Molluscan biostratigraphy of the Cretaceous western interior basin, North America. Evolution of the Western Interior Basin: Geol. Ass. Can. Spec. Pap., 39, 397-434.

Kearns, T.J., 2012. Chemostratigraphy of the Eagle Ford formation.

Keller, G. and Pardo, A., 2004. Age and paleoenvironment of the Cenomanian-Turonian global stratotype section and point at Pueblo, Colorado. Marine Micropaleontol., 51(1), 95-128.

Keller, G., 2008. Cretaceous climate, volcanism, impacts, and biotic effects. Cretac. Res., 29(5), 754-771.

Kennedy, W.J., Walaszczyk, I. and Cobban, W.A., 2005. The global boundary stratotype section and point for the base of the Turonian stage of the Cretaceous: Pueblo, Colorado, USA. Episodes-Newsmagazine of the Int. Union of Geological Sciences, 28(2), 93-104.

Keppie, J.D., Nance, R.D., Murphy, J.B. and Dostal, J., 2003. Tethyan, Mediterranean, and Pacific analogues for the Neoproterozoic-Paleozoic birth and development of peri-Gondwanan terranes and their transfer to Laurentia and Laurussia. Tectonophysics, 365(1), 195-219.

Kerr, A.C., 1998. Oceanic plateau formation: a cause of mass extinction and black shale deposition around the Cenomanian-Turonian boundary? J. Geol. Soc.,

155(4), 619-626.

Kidder, D.L. and Worsley, T.R., 2010. Phanerozoic large igneous provinces (LIPs), HEATT (haline euxinic acidic thermal transgression) episodes, and mass extinctions. Palaeogeogr. Palaeoclimatol. Palaeoecol., 295(1), 162-191.

King, S.D. and Anderson, D.L., 1998. Edge-driven convection. Earth Planet. Sci. Lett., 160(3), 289-296.

Kirkland, J.I., 1991. Lithostratigraphic and biostratigraphic framework for the Mancos Shale (Late Cenomanian to Middle T uronian) at. Stratigraphy, Depositional Environments, and Sedimentary Tectonics of the Western Margin, Cretaceous Western Interior Seaway, 260, 85.

Klinkhammer, G.P. and Palmer, M.R., 1991. Uranium in the oceans: where it goes and why. Geochim. Cosmochim. Acta 55, 1799-1806.

Kolonic, S., Wagner, T., Forster, A., Sinninghe Damsté, J.S., WalsworthBell, B., Erba, E., Turgeon, S., Brumsack, H.J., Chellai, E.H., Tsikos, H. and Kuhnt, W., 2005. Black shale deposition on the northwest African Shelf during the Cenomanian/Turonian oceanic anoxic event: Climate coupling and global organic carbon burial. Paleoceanog., 20(1).

Kübler, B. and Jaboyedoff, M., 2000. Illite crystallinity. Comptes Rendus de l'Académie des Sciences-Series IIA-Earth and Planetary Science, 331(2), 75-89.

Kübler, B., 1987. Cristallinité de l'illite, méthodes normalisées de préparations, méthodes normalisées de mesures. Cahiers Institut Géologie de Neuchtel, Suisse, série ADX.

Kuhnt, W., Herbin, J.P., Thurow, J. and Wiedmann, J., 1990. Distribution of Cenomanian-Turonian organic facies in the western Mediterranean and along the adjacent Atlantic margin. In Deposition of organic facies, 30, 133-160. AAPG Studies in Geology Tulsa, Oklahoma.

Kuhnt, W., Nederbragt, A. and Leine, L., 1997. Cyclicity of Cenomanian-Turonian organic-carbon-rich sediments in the Tarfaya Atlantic coastal basin (Morocco). Cretac. Res., 18(4), 587-601.

Kumar, N., Anderson, R.F. and Biscaye, P.E., 1996. Remineralization of particulate authigenic trace metals in the Middle Atlantic Bight: Implications for proxies of export production. Geochim. Cosmochim. Acta, 60(18), 3383-3397.

Kump, L.R., Slingerland, R.L., 1999. Circulation and stratification of the early Turonian Western Interior Seaway: sensitivity to a variety of forcings. In: Evolution of Cretaceous Ocean-Climate System, Barrera, E., C., Johnson (eds.), Geol. Soc. Am. Spec. Pap., 332, 181-190.

Kuroda, J., Ogawa, N.O., Tanimizu, M., Coffin, M.F., Tokuyama, H., Kitazato, H. and Ohkouchi, N., 2007. Contemporaneous massive subaerial volcanism and late cretaceous Oceanic Anoxic Event 2. Earth Planet. Sci. Lett., 256(1), 211-223.

Kuroda, J., Tanimizu, M., Hori, R.S., Suzuki, K., Ogawa, N.O., Tejada, M.L., Cof-

fin, M.F., Coccioni, R., Erba, E. and Ohkouchi, N., 2011. Lead isotopic record of Barremian-Aptian marine sediments: Implications for large igneous provinces and the Aptian climatic crisis. Earth Planet. Sci. Lett., 307(1), 126-134.

Kuypers, M.M., Blokker, P., Hopmans, E.C., Kinkel, H., Pancost, R.D., Schouten, S. and Sinninghe Damsté, J.S., 2002. Archaeal remains dominate marine organic matter from the early Albian oceanic anoxic event 1b. Palaeogeogr. Palaeoclimatol. Palaeoecol., 185(1), 211-234.

Kuypers, M.M., Pancost, R.D. and Sinninghe Damsté, J.S., 1999. A large and abrupt fall in atmospheric CO2 concentration during Cretaceous times. Nature, 399(6734), 342.

Kuypers, M.M., Pancost, R.D., Nijenhuis, I.A. and Sinninghe Damsté, J.S., 2002. Enhanced productivity led to increased organic carbon burial in the euxinic North Atlantic basin during the late Cenomanian oceanic anoxic event. Paleoceanog., 17(4).

Kuypers, M.M., van Breugel, Y., Schouten, S., Erba, E. and Sinninghe Damsté, J.S., 2004. N2-fixing cyanobacteria supplied nutrient N for Cretaceous oceanic anoxic events. Geology, 32(10), 853-856.

Ladant, J.B. and Donnadieu, Y., 2016. Palaeogeographic regulation of glacial events during the Cretaceous supergreenhouse. Nature Comm., 7.

Ladant, J.B., Donnadieu, Y., Lefebvre, V. and Dumas, C., 2014. The respective role of atmospheric carbon dioxide and orbital parameters on ice sheet evolution at the EoceneOligocene transition. Paleoceanog., 29(8), 810-823.

Lamolda, M.A., Gorostidi, A. and Paul, C.R.C., 1994. Quantitative estimates of calcareous nannofossil changes across the Plenus Marls (latest Cenomanian), Dover, England: implications for the generation of the Cenomanian-Turonian Boundary Event. Cretac. Res., 15(2), 143-164.

Langford, F.F. and Blanc-Valleron, M.M., 1990. Interpreting Rock-Eval pyrolysis data using graphs of pyrolizable hydrocarbons vs. total organic carbon (1). AAPG Bull., 74(6), 799-804.

Langmann, B., Zakek, K., Hort, M. and Duggen, S., 2010. Volcanic ash as fertiliser for the surface ocean. Atmospheric Chemistry and Physics, 10(8), 3891-3899.

Larson, R.L. and Erba, E., 1999. Onset of the MidCretaceous greenhouse in the BarremianAptian: Igneous events and the biological, sedimentary, and geochemical responses. Paleoceanog., 14(6), 663-678.

Larson, R.L. and Pitman, W.C., 1972. World-wide correlation of Mesozoic magnetic anomalies, and its implications. Geol. Soc. Am. Bull., 83(12), 3645-3662.

Larson, R.L., 1991. Geological consequences of superplumes. Geology, 19(10), 963-966.

Laurin, J. and Sageman, B.B., 2001. Tectono-sedimentary evolution of the western margin of the Colorado Plateau during the latest Cenomanian and Early Turonian.

Lechler, M., von Strandmann, P.A.P., Jenkyns, H.C., Prosser, G. and Parente, M., 2015. Lithium-isotope evidence for enhanced silicate weathering during OAE 1a (Early Aptian Selli event). Earth Planet. Sci. Lett., 432, 210-222.

Leckie, R.M., Yuretich, R.F., West, O.L.O., Finkelstein, D. and Schmidt, M.G., 1998. Paleo-ceanography of the southwestern Western Interior Sea during the time of the Cenomanian-Turonian boundary (Late Cretaceous). In: Arthur, M.A., Dean, W.E. (Eds.), Stratigraphy and Paleoenvironments of the Cretaceous Western Interior Seaway. In: Soc. of Economic Paleontologists and Mineralogists. Concepts Sedimentol. Paleontol., 6, 101-126.

Lehnherr, I., St Louis, V.L., Hintelmann, H. and Kirk, J.L., 2011. Methylation of inorganic mercury in polar marine waters. Nature Geo., 4(5), 298.

Lewan, M.D., Maynard, J.B., 1982. Factors controlling the enrichment of vanadium and nickel in the bitumen of organic sedimentary rocks. Geochim. Cosmochim. Acta 46, 2547-2560.

Lindqvist, O. and Rodhe, H., 1985. Atmospheric mercurya review. Tellus B, 37(3), 136-159.

Liro, L. M., Dawson, W. C., Katz, B. J., and Robison, V. D., 1994. Sequence stratigraphic elements and geochemical variability within a ”condensed section”: Eagle Ford Group, east-central Texas: Trans. Atm. Environ. GCAGS., 44, 393-402.

Littler, K., Robinson, S.A., Bown, P.R., Nederbragt, A.J. and Pancost, R.D., 2011. High sea-surface temperatures during the Early Cretaceous Epoch. Nature Geo., 4(3), 169.

Liu, X., Xu, L., Chen, Q., Sun, L., Wang, Y., Yan, H., Liu, Y., Luo, Y. and Huang, J., 2012. Historical change of mercury pollution in remote Yongle archipelago, South China Sea. Chemosphere, 87(5), 549-556.

Lobo, F. J., Hernandez-Molina, F. J., Somoza, L., Rodero, J., Maldonado, A. and Barnolas, A., 2000. Patterns of bottom current flow deduced from dune asymmetries over the Gulf of Cadiz shelf (southwest Spain): Mar. Geol., 164, 3-4, 91-117.

Lock, B. E. and Peschier, L., 2006. Boquillas (Eagle Ford) upper slope sediments, West Texas: Outcrop analogs for potential shale reservoirs: GCAGS. Trans., 56, 491-508.

Lonsdale, P. and Malfait, B., 1974. Abyssal dunes of foraminiferal sand on the Carnegie Ridge. Geol. Soc. Am.Bull., 85, 11, 1697-1712.

Lonsdale, P. and Southard, J. B., 1974. Experimental erosion of North Pacific red clay. Mar. Geol., 17, 1, M51-M60.

Loucks, R. G. and Ruppel, S. C., 2007. Mississippian Barnett shale: Lithofacies and depositional setting of a deep-water shale-gas succession in the Fort Worth Basin, Texas: AAPG Bull., 91, 4, 579-601.

Lowell, J.D., 1985. Structural styles in petroleum exploration. Tulsa, Oil and Gas Consultants Int.

Lowery, C.M., Corbett, M.J., Leckie, R.M., Watkins, D., Miceli Romero, A. and Pramudito, A., 2014. Foraminiferal and nannofossil paleoecology and palaeoceanography of the Cenomanian-Turonian Eagle Ford Shale of southern Texas. Palaeogeogr. Palaeoclimatol. Palaeoecol. 413, 49-65.

Luther, G. W., Ma, S., Trouwborst, R., Glazer, B., Blickley, M., Scarborough, R.W., and Mensinger, M., 2004. The roles of anoxia, H2S, and storm events in fish kills of dead-end canals of Delaware inland bays: Estuaries, 27, 3, 551-560.

Lyons, T.W., Anbar, A.D., Severmann, S., Scott, C. and Gill, B.C., 2009. Tracking euxinia in the ancient ocean: a multiproxy perspective and Proterozoic case study. Annual Rev. Earth Planet. Sci., 37, 507-534.

Ma, C., Meyers, S.R., Sageman, B.B., Singer, B.S. and Jicha, B.R., 2014. Testing the astronomical time scale for oceanic anoxic event 2, and its extension into Cenomanian strata of the Western Interior Basin (USA). Geol. Soc. Am. Bull., 126(7-8), 974-989.

Maclennan, J., Jull, M., McKenzie, D., Slater, L., Grönvold, K., 2002. The link between volcanism and deglaciation in Iceland. Geochem., Geophys., Geosyst., 3(11), 1-25.

MacLeod, K.G., Martin, E.E. and Blair, S.W., 2008. Nd isotopic excursion across Cretaceous ocean anoxic event 2 (Cenomanian-Turonian) in the tropical North Atlantic. Geology, 36(10), 811-814.

Macquaker, J. H. S., Keller, M. A. and Davies, S. A., 2010. Algal blooms and "marine snow": Mechanisms that enhance preservation of organic carbon in ancient fine grained sediments: J. Sed. Res., 80, 934-942.

Macsotay, O., Erlich, R.N. and Peraza, T., 2003. Sedimentary Structures of the La Luna, Navay and Querecual Formations, Upper Cretaceous of Venezuela. Palaios, 18(4-5), 334-348.

Maher, Jr, H.D., 2001. Manifestations of the Cretaceous High Arctic large igneous province in Svalbard. J. Geol, 109(1), 91-104.

Martin, E.E., MacLeod, K.G., Berrocoso, A.J. and Bourbon, E., 2012. Water mass circulation on Demerara Rise during the Late Cretaceous based on Nd isotopes. Earth Planet. Sci. Lett., 327, 111-120.

Mason, R.P., Choi, A.L., Fitzgerald, W.F., Hammerschmidt, C.R., Lamborg, C.H., Soerensen, A.L. and Sunderland, E.M., 2012. Mercury biogeochemical cycling in the ocean and policy implications. Environmental research, 119, 101-117.

Mather, T.A., Pyle, D.M. and Oppenheimer, C., 2003. Tropospheric volcanic aerosol. Volcanism and the Earth's Atmosphere, 189-212.

Maxwell, R.A., Lonsdale, J., Hazzard, R.T. and Wilson, J.A., 1967. Geology of Big Bend National Park, Brewster County, Texas. The University of Texas at Austin Bureau of Economic Geology, 6711, 320.

McDowell, F.W. and Clabaugh, S.E., 1979. Ignimbrites of the Sierra Madre Occiden-

tal and their relation to the tectonic history of western Mexico. Geol. Soc. Am.Spec. Pap., 180, 113-124.

McElwain, J.C., Wade-Murphy, J. and Hesselbo, S.P., 2005. Changes in carbon dioxide during an oceanic anoxic event linked to intrusion into Gondwana coals. Nature, 435(7041), 479.

McFarlan, E.Jr., and L.S. Menes, 1991. Lower Cretaceous, in A. Salvador, ed., The Gulf of Mexico Basin: Decade of North American Geology: Boulder, Geol. Soc. Am., 181-204.

McGuire, W.J., Howarth, R.J., Firth, C.R. and Solow, A.R., 1997. Correlation between rate of sea-level change and frequency of explosive volcanism in the Mediterranean. Nature, 389(6650), 473.

McManus, J., Berelson, W.M., Klinkhammer, G.P., Hammond, D.E. and Holm, C., 2005. Authigenic uranium: relationship to oxygen penetration depth and organic carbon rain. Geochim. Cosmochim. Acta 69, 95-108.

McNeil, D.H. and Caldwell, W.G.E., 1981. Cretaceous rocks and their foraminifera in the Manitoba escarpment. Geol. Ass. Can. Spec. Pap., 21.

Méhay, S., Keller, C.E., Bernasconi, S.M., Weissert, H., Erba, E., Bottini, C. and Hochuli, P.A., 2009. A volcanic CO2 pulse triggered the Cretaceous Oceanic Anoxic Event 1a and a biocalcification crisis. Geology, 37(9), 819-822.

Mélançon, J., Levasseur, M., Lizotte, M., Delmelle, P., Cullen, J., Hamme, R.C., Pena, A., Simpson, K.G., Scarratt, M., Tremblay, J.E. and Zhou, J., 2014. Early response of the northeast subarctic Pacific plankton assemblage to volcanic ash fertilization. Limnology and Oceanography, 59(1), 55-67.

Melott, A.L., Bambach, R.K., Petersen, K.D. and McArthur, J.M., 2012. An 60-Million-Year Periodicity Is Common to Marine $^{87}Sr/^{86}Sr$, Fossil Biodiversity, and Large-Scale Sedimentation: What Does the Periodicity Reflect? J. Geol., 120(2), 217-226.

Menanteau, L., Vanney, J.-R., and Zazo Cardeña, C., 1983. Belo et son environnement (Detroit de Gibraltar): Etude physique d'un site antique, in Belo II. Historique des fouilles: Paris, Casa de Velazquez, 39-221.

Meyers, P.A., Bernasconi, S.M. and Forster, A., 2006. Origins and accumulation of organic matter in expanded Albian to Santonian black shale sequences on the Demerara Rise, South American margin. Organic Geochemistry, 37(12), 1816-1830.

Meyers, S.R. and Sageman, B.B., 2007. Quantification of deep-time orbital forcing by average spectral misfit. Am. J. Sci., 307(5), 773-792.

Meyers, S.R., 2007. Production and preservation of organic matter: The significance of iron. Paleoceanog., 22(4).

Meyers, S.R., Sageman, B.B. and Arthur, M.A., 2012. Obliquity forcing of organic matter accumulation during Oceanic Anoxic Event 2. Paleoceanog., 27(3).

Meyers, S.R., Sageman, B.B. and Hinnov, L.A., 2001. Integrated quantitative stratigraphy of the Cenomanian-Turonian Bridge Creek Limestone Member using evolutive harmonic analysis and stratigraphic modeling. J. Sed. Res., 71(4), 628-644. Meyers, S.R., Siewert, S.E., Singer, B.S., Sageman, B.B., Condon, D.J., Obradovich, J.D., Jicha, B.R. and Sawyer, D.A., 2012. Intercalibration of radioisotopic and astrochronologic time scales for the Cenomanian-Turonian boundary interval, Western Interior Basin, USA. Geology, 40(1), 7-10.

Miller, E.L., Miller, M.M., Stevens, C.H., Wright, J.E. and Madrid, R., 1992. Late Paleozoic paleogeographic and tectonic evolution of the western US Cordillera. The Cordilleran orogen: Conterminous US: Boulder, Colorado, Geol. Soc. Am., Geology of North America, 3, 57-106. Miller, K.G., Barrera, E., Olsson, R.K., Sugarman, P.J. and Savin, S.M., 1999. Does ice drive early Maastrichtian eustasy? Geology, 27(9), 783-786.

Miller, K.G., Sugarman, P.J., Browning, J.V., Kominz, M.A., Olsson, R.K., Feigenson, M.D. and Hernéndez, J.C., 2004. Upper Cretaceous sequences and sea-level history, New Jersey coastal plain. Geol. Soc. Am. Bull., 116(3-4), 368-393.

Miller, R.W., 1990. The stratigraphy and depositional environment of the Boquillas Formation of southwest Texas (Doctoral dissertation, University of Texas at Arlington).

Millot, G., 2013. Geology of Clays: Weathering, Sedimentology, Geochemistry. Springer Science & Business Media.

Milner, S.C., Le Roex, A.P. and O'Connor, J.M., 1995. Age of Mesozoic igneous rocks in northwesternNamibia, and their relationship to continental breakup. J. Geol. Soc., 152(1), 97-104.

Mitchell, S.F. and Carr, I.T., 1998. Foraminiferal response to mid-Cenomanian (Upper Cretaceous) palaeoceanographic events in the Anglo-Paris Basin (Northwest Europe). Palaeogeogr. Palaeoclimatol. Palaeoecol., 137(1-2), 103-125.

Mitchener, H. and Torfs, H., 1996. Erosion of mud/sand mixtures. Coastal engineering, 29(1-2), 1-25. Mongenot, T., Tribovillard, N.P., Desprairies, A., Lallier-Vergès, E. and Laggoun-Defarge, F., 1996. Trace elements as palaeoenvironmental markers in strongly mature hydrocarbon source rocks: the Cretaceous La Luna Formation of Venezuela. Sed. Geol., 103(1-2), 23-37.

Monnin, C., Jeandel, C., Cattaldo, T. and Dehairs, F., 1999. The marine barite saturation state of the world's oceans. Mar. Chem., 65(3), 253-261.

Monperrus, M., Tessier, E., Amouroux, D., Leynaert, A., Huonnic, P. and Donard, O.F.X., 2007. Mercury methylation, demethylation and reduction rates in coastal and marine surface waters of the Mediterranean Sea. Mar. Chem., 107(1), 49-63.

Moran, L.M., 2013. High resolution geochemistry of the Cretaceous Eagle Ford shale, Bee County, Texas.

Morel, F.M.M. and Price, N.M., 2003. The biogeochemical cycles of trace metals in the oceans. Science, 300(5621), 944-947.

Morford, J.L. and Emerson, S., 1999. The geochemistry of redox sensitive trace metals in sediments. Geochim. Cosmochim. Acta 63, 1735-1750.

Moriya, K., Wilson, P.A., Friedrich, O., Erbacher, J. and Kawahata, H., 2007. Testing for ice sheets during the mid-Cretaceous greenhouse using glassy foraminiferal calcite from the mid-Cenomanian tropics on Demerara Rise. Geology, 35(7), 615-618.

Morse, J.W., Luther III, G.W., 1999. Chemical influences on trace metal-sulfide interactions in anoxic sediments. Geochim. Cosmochim. Acta 63, 3373-3378.

Muehlberger, W.R., Hedge, C.E., Denison, R.E. and Marvin, R.F., 1966. Geochronology of the midcontinent region, United States: 3. Southern area. J. Geophys. Res., 71(22), 5409-5426.

Musavu-Moussavou, B., Danelian, T., Baudin, F., Coccioni, R. and Fröhlich, F., 2007. The Radiolarian biotic response during OAE2. A high-resolution study across the Bonarelli level at Bottaccione (Gubbio, Italy). Revue de micropaléontologie, 50(3), 253-287.

Nakada, M., Yokose, H., 1992. Ice age as a trigger of active Quaternary volcanism and tectonism. Tectonophysics, 212(3-4), 321-329.

Neal, C.R., Coffin, M.F., Arndt, N.T., Duncan, R.A., Eldholm, O., Erba, E., Farnetani, C., Fitton, J.F., Ingle, S.P., Ohkouchi, N. and Rampino, M.R., 2008. Investigating large igneous province formation and associated paleoenvironmental events: a white paper for scientific drilling. Scientific Drilling, 6, 4-18.

Nelson, C. H., Baraza, J., Maldonado, A., Rodero, J., Escutia, C. and Barber Jr., J. H., 1999. Influence of the Atlantic inflow and Mediterranean outflow currents on Late Quaternary sedimentary facies of the Gulf of Cadiz continental margin: Mar. Geol., 155, 99-129.

Nicholas, R. L. and Rozendal, R. A., 1975. Subsurface positive elements within the Ouachita foldbelt in Texas and their relation to Paleozoic cratonic margins: AAPG Bull., 59, 193-216.

Nicholas, R.L., 1983. Devils River uplift. Structure and stratigraphy of the Val Verde basinDevils River uplift, Texas: West Texas Geol. Soc. Publ., 83-77.

Niessen, S., Foucher, D., Clarisse, O., Fischer, J.C., Mikac, N., Kwokal, Z., Fajon, V. and Horvat, M., 2003. Influence of sulphur cycle on mercury methylation in estuarine sediment (Seine estuary, France). In Journal de Physique, IV,107, 953-956.

Nowell, D.A., Jones, M.C. and Pyle, D.M., 2006. Episodic quaternary volcanism in France and Germany. J. Quat. Sci., 21(6), 645-675.

Obradovich, J.D., 1993. A Cretaceous time scale. Evolution of the Western Interior Basin, 39, 379-396.

Ogg, J.G. and Hinnov, L.A., 2012. The geologic time scale 2012. 26, 731-791.

Olgun, N., Duggen, S., Andronico, D., Kutterolf, S., Croot, P.L., Giammanco, S., Censi, P. and Randazzo, L., 2013. Possible impacts of volcanic ash emissions of

Mount Etna on the primary productivity in the oligotrophic Mediterranean Sea: Results from nutrient-release experiments in seawater. Mar. Chem., 152, 32-42.

Olgun, N., Duggen, S., Croot, P.L., Delmelle, P., Dietze, H., Schacht, U., Óskarsson, N., Siebe, C., Auer, A. and GarbeSchönberg, D., 2011. Surface ocean iron fertilization: the role of airborne volcanic ash from subduction zone and hot spot volcanoes and related iron fluxes into the Pacific Ocean. Global Biogeochemical Cycles, 25(4).

Orth, C. J., Attrep, M. J., Quintana, L. R., Elder, W. P., Kauffman, E. G. , Diner, R., and Villamil, T., 1993. Elemental abundance anomalies in the late Cenomanian extinction interval: A search for the source(s), Earth Planet. Sci. Lett., 117, 189-204.

Orth, C.J., Attrep, M. and Quintana, L.R., 1990. Iridium abundance patterns across bio-event horizons in the fossil record. Geol. Soc. Am.Spec. Pap., 247, 45-60.

Orth, C.J., Attrep, M., Quintana, L.R., Elder, W.P., Kauffman, E.G., Diner, R. and Villamil, T., 1993. Elemental abundance anomalies in the late Cenomanian extinction interval: A search for the source (s). Earth Planet. Sci. Lett., 117(1-2), 189-204.

Outridge, P.M., Sanei, H., Stern, G.A., Hamilton, P.B. and Goodarzi, F., 2007. Evidence for control of mercury accumulation rates in Canadian High Arctic lake sediments by variations of aquatic primary productivity. Environmental Science & Technology, 41(15), 5259-5265.

Owens, J.D., Lyons, T.W., Hardisty, D.S., Lowery, C.M., Lu, Z., Lee, B. and Jenkyns, H.C., 2017. Patterns of local and global redox variability during the Cenomanian-Turonian Boundary Event (Oceanic Anoxic Event 2) recorded in carbonates and shales from central Italy. Sedimentol., 64(1), 168-185.

Owens, J.D., Lyons, T.W., Li, X., Macleod, K.G., Gordon, G., Kuypers, M.M., Anbar, A., Kuhnt, W. and Severmann, S., 2012. Iron isotope and trace metal records of iron cycling in the protoNorth Atlantic during the CenomanianTuronian oceanic anoxic event (OAE2). Paleoceanog., 27(3).

Pagani, M., Huber, M., Liu, Z., Bohaty, S.M., Henderiks, J., Sijp, W., Krishnan, S. and DeConto, R.M., 2011. The role of carbon dioxide during the onset of Antarctic glaciation. Science, 334(6060), 1261-1264.

Pang, M. and Nummedal, D., 1995. Flexural subsidence and basement tectonics of the Cretaceous Western Interior basin, United States. Geology, 23(2), 173-176.

Parra, M., Moscardelli, L. and Lorente, M.A., 2003. Late Cretaceous anoxia and lateral microfacies changes in the Tres Esquinas member, La Luna Formation, western Venezuela. Palaios, 18(4), 321-333.

Paterne, M. and Guichard, F., 1993. Triggering of volcanic pulses in the Campanian area, South Italy, by periodic deep magma influx. J. Geophys. Res.: Solid Earth, 98(B2), 1861-1873.

Paterne, M., Labeyrie, J., Guichard, F., Mazaud, A. and Maitre, F., 1990. Fluctuations of the Campanian explosive volcanic activity (South Italy) during the past 190,000 years, as determined by marine tephrochronology. Earth Planet. Sci. Lett.,

98(2), 166-174.

Paul, C.R.C., Lamolda, M.A., Mitchell, S.F., Vaziri, M.R., Gorostidi, A. and Marshall, J.D., 1999. The Cenomanian-Turonian boundary at Eastbourne (Sussex, UK): a proposed European reference section. Palaeogeogr. Palaeoclimatol. Palaeoecol., 150(1), 83-121.

Paul, C.R.C., Mitchell, S., Lamolda, M. and Gorostidi, A., 1994. The Cenomanian-Turonian boundary event in northern Spain. Geol. Mag., 131(6), 801-817.

Paul, C.R.C., Mitchell, S.F., Marshall, J.D., Leafy, P.N., Gale, A.S., Duane, A.M. and Ditchfield, P.W., 1994. Palaeoceanographic events in the middle Cenomanian of Northwest Europe. Cretac. Res., 15(6), 707-738.

Pegram, W.J. and Turekian, K.K., 1999. The osmium isotopic composition change of Cenozoic sea water as inferred from a deep-sea core corrected for meteoritic contributions. Geochim. Cosmochim. Acta, 63(23), 4053-4058.

Percival, L.M.E., Witt, M.L.I., Mather, T.A., Hermoso, M., Jenkyns, H.C., Hesselbo, S.P., Al-Suwaidi, A.H., Storm, M.S., Xu, W. and Ruhl, M., 2015. Globally enhanced mercury deposition during the end-Pliensbachian extinction and Toarcian OAE: A link to the Karoo-Ferrar Large Igneous Province. Earth Planet. Sci. Lett., 428, 267-280.

Perez-Infante, J., Farrimond, P. and Furrer, M., 1996. Global and local controls influencing the deposition of the La Luna Formation (Cenomanian-Campanian), western Venezuela. Chem. Geol., 130(3), 271-288.

Pessagno, E.A., 1969. Upper Cretaceous stratigraphy of the western Gulf Coast area of Mexico, Texas, and Arkansas. Geol. Soc. Am. Mem., 111, 1-139.

Peterson, L.C., Haug, G.H., 2006. Variability in the mean latitude of the Atlantic Intertropical Convergence Zone as recorded by riverine input of sediments to the Cariaco Basin (Venezuela). Palaeogeography, Palaeoclimatology, Palaeoecology, 234(1), 97-113.

Pettke, T., Halliday, A.N. and Rea, D.K., 2002. Cenozoic evolution of Asian climate and sources of Pacific seawater Pb and Nd derived from eolian dust of sediment core LL44GPC3. Paleoceanography, 17(3).

Phelps, R. M., 2011, Middle-Hauterivian to LowerCampanian sequence stratigraphy and stable isotope geochemistry of the Comanche platform, South Texas, Ph.D. dissertation, The University of Texas at Austin, Austin, Texas, 240.

Phelps, R.M., Kerans, C., Loucks, R.G., Da Gama, R.O., Jeremiah, J. and Hull, D., 2013. Oceanographic and eustatic control of carbonate platform evolution and sequence stratigraphy on the Cretaceous (Valanginian-Campanian) passive margin, northern Gulf of Mexico. Sedimentol., 61(2), 461-496.

Pogge von Strandmann, P.A., Jenkyns, H.C. and Woodfine, R.G., 2013. Lithium isotope evidence for enhanced weathering during Oceanic Anoxic Event 2. Nature Geo., 6(8), 668-672.

Potter, P. E., 2003, Mudrocks, in G. V. Middleton, ed., Encyclopedia of sediments and sedimentary rocks: Dordrecht, The Netherlands, Kluwer Scientific, 451-459.

Pratt, L.M., 1984. Influence of paleoenvironmental factors on preservation of organic matter in Middle Cretaceous Greenhorn Formation, Pueblo, Colorado. AAPG Bull., 68(9), 1146-1159.

Pratt, L.M., 1985. Isotopic studies of organic matter and carbonate in rocks of the Greenhorn marine cycle.

Pratt, L.M., Arthur, M.A., Dean, W.E. and Scholle, P.A., 1993. Paleoceanographic cycles and events during the Late Cretaceous in the Western Interior Seaway of North America. In: Caldwell, W.G.E., Kauffman, E.G. (Eds.), Evolution of the Western Interior Basin. In: Geol. Ass. Can. Spec. Pap., 39, 333-354.

Pratt, L.M., Threlkeld, C.N., 1984. Stratigraphic significance of $^{13}C/^{12}C$ ratios in mid-Cretaceous rocks of the Western Interior, U.S.A. In: Stott, D.F., Glass, D.J. (Eds.), The Mesozoic of Middle North America, 9. Can. Soc. Petrol. Geol., 305-312

Prauss, M. and Riegel, W., 1989. Evidence from phytoplankton associations for causes of black shale formation in epicontinental seas. Neues Jahrbuch fär Geologie und Paläontologie, Monatshefte, 11, 671-682.

Price, J.G. and Henry, C.D., 1985. Summary of Tertiary stress orientations and tectonic history of Trans-Pecos Texas. In Structure and tectonics of trans-Pecos Texas: West Texas Geol. Soc. Field Conference, 149-151.

Prokoph, A., El Bilali, H. and Ernst, R., 2013. Periodicities in the emplacement of large igneous provinces through the Phanerozoic: relations to ocean chemistry and marine biodiversity evolution. Geoscience Frontiers, 4(3), 263-276.

Prokoph, A., Shields, G.A. and Veizer, J., 2008. Compilation and time-series analysis of a marine carbonate $\delta\ ^{18}O$, $\delta^{13}C$, $^{87}Sr/^{86}Sr$ and $\delta\ ^{34}$ S database through Earth history. Earth-Science Rev., 87(3), 113-133.

Prokoph, A., Villeneuve, M., Agterberg, F.P. and Rachold, V., 2001. Geochronology and calibration of global Milankovitch cyclicity at the Cenomanian-Turonian boundary. Geology, 29(6), 523-526.

Pucéat, E., Lécuyer, C., Sheppard, S.M., Dromart, G., Reboulet, S. and Grandjean, P., 2003. Thermal evolution of Cretaceous Tethyan marine waters inferred from oxygen isotope composition of fish tooth enamels. Paleoceanog., 18(2).

Pyle, D.M. and Mather, T.A., 2003. The importance of volcanic emissions for the global atmospheric mercury cycle. Atm. Environ., 37(36), 5115-5124.

Rampino, M.R., Self, S. and Fairbridge, R.W., 1979. Can rapid climatic change cause volcanic eruptions?. Science, 206(4420), 826-829.

Rampino, M. and Stothers, R., 1988. Flood basalt volcanism during the past 250 million years. Science, 241(4866), 663-668.

Rangel, A., Parra, P. and Niño, C., 2000. The La Luna formation: chemostratigraphy

and organic facies in the Middle Magdalena Basin. Organic Geochemistry, 31(12), 1267-1284.

Ratcliffe, K.T., Wright, A.M. and Schmidt, K., 2012. Application of inorganic whole-rock geochemistry to shale resource plays: an example from the Eagle Ford Shale Formation, Texas. The Sedimentary Record, 10(2), 4-9.

Rawson, H., Pyle, D.M., Mather, T.A., Smith, V.C., Fontijn, K., Lachowycz, S.M. and Naranjo, J.A., 2016. The magmatic and eruptive response of arc volcanoes to deglaciation: Insights from southern Chile. Geology, 44(4), 251-254.

Raye, U., Anthony, E.Y., Stern, R.J., Kimura, J.I., Ren, M., Qing, C. and Tani, K., 2011. Composition of the mansociettle lithosphere beneath south-central Laurentia: Evidence from peridotite xenoliths, Knippa, Texas. Geosphere, 7(3), 710-723.

Reitz, A., Pfeifer, K., De Lange, G.J. and Klump, J., 2004. Biogenic barium and the detrital Ba/Al ratio: a comparison of their direct and indirect determination. Mar. Geol., 204(3), 289-300.

Research on Cretaceous Cycles (R.O.C.C.) Group, 1986. Rhythmic bedding in Upper Cretaceous pelagic carbonate sequences: varying sedimentary response to climatic forcing. Geology, 14, 153-156.

Ricken, W., 1986. Diagenetic Bedding: A Model for Limestone - Marl Alternations. 33-90, Springer Verlag, Berlin.

Ricken, W., 1993. Variation of sedimentation rates in rhythmically bedded sediments-distinction between depositional types. In: Einsele, G., Ricken, W., Seilacher, A. (Eds.), Cycles and Events in Stratigraphy. Springer-Verlag, Berlin, 167-187.

Ricken, W., 1994. Complex rhythmic sedimentation related to third-order sea-level variations: upper Cretaceous, western Interior Basin, U.S.A. In: deBoer, P.L., Smith, D.G. (Eds.), Orbital Forcing and Cyclic Sequences. In: Int. Ass. Sed. Spec. Publ., 19, 167-193.

Riebesell, U., 1992. The formation of large marine snow and its sustained residence in surface waters: Limnology and Oceanography, 37, 63-76.

Robison, C. R., 1997. Hydrocarbon source rock variability within the Austin Chalk and Eagle Ford Shale (Upper Cretaceous), East Texas, U.S.A.. Int. J. Coal Geol., 34, 287-305.

Rohde, R.A. and Muller, R.A., 2005. Cycles in fossil diversity. Nature, 434(7030), 208.

Ross, D.J. and Skelton, P.W., 1993. Rudist formations of the Cretaceous: a palaeoecological, sedimentological and stratigraphical review. Sedimentol. Rev., 1, 73-91.

Roth, P.H., 1978. Cretaceous nannoplankton biostratigraphy and oceanography of the northwestern Atlantic Ocean. Initial reports of the Deep Sea Drilling project, 44, 759.

Ruiz, W.L.G. and Tomiyasu, T., 2015. Distribution of mercury in sediments from Kagoshima Bay, Japan, and its relationship with physical and chemical factors. Environ. Earth Sci., 74(2), 1175-1188.

Ruppel, S.C., Loucks, R.G. and Frébourg, G., 2012. Guide to field exposures of the Eagle Ford-equivalent Boquillas Formation and related Upper Cretaceous Units in southwest Texas: Austin. Texas, The University of Texas at Austin, Bureau of Economic Geology, Mudrock Systems Research Laboratory Field-Trip Guidebook.

Sachs, J.P. and Repeta, D.J., 1999. Oligotrophy and nitrogen fixation during eastern Mediterranean sapropel events. Science, 286(5449), 2485-2488.

Sageman, B., Rich, J., Savrda, C.E., Bralower, T., Arthur, M.A. and Dean, W.E., 1998. Multiple Milankovitch cycles in the Bridge Creek Limestone (Cenomanian-Turonian), Western Interior basin. In: Arthur, M.A., Dean, W.E. (Eds.), Stratigraphy and Paleoenvironments of the Cretaceous Western Interior Seaway, USA. In: Concepts Sedimentol. Paleontol., 6. Soc. Sed. Geol., 153-171.

Sageman, B.B., 1996. Lowstand tempestites: Depositional model for Cretaceous skeletal limestones, Western Interior basin. Geology, 24(10), 888-892.

Sageman, B.B., Meyers, S.R. and Arthur, M.A., 2006. Orbital time scale and new C-isotope record for Cenomanian-Turonian boundary stratotype. Geology, 34(2), 125-128.

Sageman, B.B., Rich, J., Arthur, M.A., Birchfield, G.E. and Dean, W.E., 1997. Evidence for Milankovitch periodicities in Cenomanian-Turonian lithologic and geochemical cycles, Western Interior U.S. J. Sed. Res. 67, 285-301.

Sageman, B.B., Rich, J., Arthur, M.A., Dean, W.E., Savrda, C.E. and Bralower, T.J., 1998. Multiple milankovitch cycles in the bridge creek limestone (Cenomanian-Turonian), western interior basin.

Saleeby, J., 2003. Segmentation of the Laramide slabEvidence from the southern Sierra Nevada region. Geol. Soc. Am.Bull., 115(6), 655-668.

Sames, B., Wagreich, M., Wendler, J.E., Haq, B.U., Conrad, C.P., Melinte-Dobrinescu, M.C., Hu, X., Wendler, I., Wolfgring, E., Yilmaz, I.Ö. Zorina, S.O., 2016. Short-term sea-level changes in a greenhouse world–A view from the Cretaceous. Palaeogeography, Palaeoclimatology, Palaeoecology, 441, 393-411.

Sanei, H., Grasby, S.E. and Beauchamp, B., 2012. Latest Permian mercury anomalies. Geology, 40(1), 63-66.

Sarmiento, J.É., Gruber, N., Brzezinski, M.A., Dunne, J.P., 2004. High-latitude controls of thermocline nutrients and low latitude biological productivity. Nature, 427(6969), 56-60.

Sass, E. and Bein, A., 1982. The Cretaceous carbonate platform in Israel. Cretac. Res., 3(1-2), 135-144.

Saunders, A. and Reichow, M., 2009. The Siberian Traps and the End-Permian mass extinction: a critical review. Chinese Science Bull., 54(1), 20-37.

Savrda, C.E. and Bottjer, D.J., 1994. Ichnofossils and ichnofabrics in rhythmically bed-ded pelagic/hemi-pelagic carbonates: recognition and evaluation of benthic redox and scour cycles. In: de Boer, P.L., Smith, D.O. (Eds.), Orbital Forcing and Cyclic Sequences, Int. Ass. Sed. Spec. Pub., 19, 195-210.

Schieber, J., 2011. Marcasite in black shalesa mineral proxy for oxygenated bottom waters and intermittent oxidation of carbonaceous muds. J. Sed. Res., 81(7), 447-458.

Schieber, J., Southard, J. B. and Thaisen, K., 2007. Accretion of mudstone beds from migrating floccule ripples: Science, 318, 1760-1763.

Schieber, J., Southard, J. B., Kissling, P., Rossman, B. and Ginsburg, R., 2013. Experimental deposition of carbonate mud from moving suspensions: Importance of flocculation and implications for modern and ancient carbonate mud deposition: J. Sed. Res., 83, 11, 1025-1031.

Schlanger, S.O. and Jenkyns, H.C., 1976. Cretaceous oceanic anoxic events: causes and consequences. Geol. Mijnb., 55(3-4), 179-184.

Schlanger, S.O., Arthur, M.A., Jenkyns, H.C. and Scholle, P.A., 1987. The Cenomanian-Turonian Oceanic Anoxic Event, I. Stratigraphy and distribution of organic carbon-rich beds and the marine δ^{13}C excursion. Geol. Soc., Lon., Spec. Publ., 26(1), 371-399.

Schlanger, S.O. and Jenkyns, H.C., 1976. Cretaceous oceanic anoxic events: causes and consequences. Geol. Mijnb., 55(3-4), 179-184.

Schmincke, H.U. and Van Den Bogaard, P., 1991. Tephra layers and tephra events. Cycles and events in stratigraphy: Berlin, Springer-Verlag, 392-429.

Scholle, P.A. and Arthur, M.A., 1980. Carbon isotope fluctuations in Cretaceous pelagic limestones: potential stratigraphic and petroleum exploration tool. AAPG Bull., 64(1), 67-87.

Schroeder, W.H. and Munthe, J., 1998. Atmospheric mercuryan overview. Atm. Environ., 32(5), 809-822.

Schuster, P.F., Krabbenhoft, D.P., Naftz, D.L., Cecil, L.D., Olson, M.L., Dewild, J.F., Susong, D.D., Green, J.R. and Abbott, M.L., 2002. Atmospheric mercury deposition during the last 270 years: a glacial ice core record of natural and anthropogenic sources. Environ. Sci. Tech., 36(11), 2303-2310.

Scopelliti, G., Bellanca, A., Neri, R., Baudin, F. and Coccioni, R., 2006. Comparative high-resolution chemostratigraphy of the Bonarelli Level from the reference Bottaccione section (Umbria-Marche Apennines) and from an equivalent section in NW Sicily: Consistent and contrasting responses to the OAE2. Chem. Geol., 228(4), 266-285.

Scopelliti, G., Bellanca, A., Erba, E., Jenkyns, H.C., Neri, R., Tamagnini, P., Luciani, V. and Masetti, D., 2008. Cenomanian-Turonian carbonate and organic-carbon isotope records, biostratigraphy and provenance of a key section in NE Sicily, Italy:

Palaeoceanographic and palaeogeographic implications. Palaeogeogr. Palaeoclimatol. Palaeoecol., 265(1), 59-77.

Scott, R. J., 2004. The Maverick basin: New technology—new success: GCAGS. Trans., 54, 603-620.

Scott, R.W., 2002. Albian caprinid rudists from Texas re-evaluated. J. Paleontol., 76(3), 408-423.

Scott, R.W., Benson, D.G., Morin, R.W., Shaffer, B.L. and Oboh-Ikuenobe, F.E., 2002. Integrated Albian-lower Cenomanian chronostratigraphy standard, Trinity River section, Texas. In US Gulf Coast Cretaceous stratigraphy and paleoecology: Gulf Coast Section, Soc. of Economic Paleontologists and Mineralogists, Bob F. Perkins Memorial Conference, 23, 277-334.

Scott, R.W., Franks, P.C., Stein, J.A., Bergen, J.A. and Evetts, M.J., 1994. Graphic correlation tests the synchronous Mid-Cretaceous depositional cycles: Western Interior and Gulf Coast. In: Unconformity-Related Hydrocarbons in Sedimentary Sequences (Eds. J.C. Dolson, M.L. Hendricks and W.A. Westcott), 89-98. Rocky Mountain Ass. of Geol., Denver, Colorado.

Scott, R.W., Molineux, A.M., Loeser, H. and Mancini, E.A., 2007. Lower Albian sequence stratigraphy and coral buildups; Glen Rose Formation, Texas, U.S.A. In: Cretaceous Rudists and Carbonate Platforms: Environmental Feedback (Ed R.W. Scott) SEPM Spec. Publ., 87, 181-191.

Selin, N.E., 2009. Global biogeochemical cycling of mercury: a review. Annual Review of Environment and Resources, 34. 43-63.

Sellards, E.H., 1932. The geology of Texas: stratigraphy. University of Texas at Austin.

Seton, M., Gaina, C., Müller, R.D. and Heine, C., 2009. Mid-Cretaceous seafloor spreading pulse: Fact or fiction?. Geology, 37(8),687-690.

Shackleton, N.J., 2000. The 100,000-year ice-age cycle identified and found to lag temperature, carbon dioxide, and orbital eccentricity. Science, 289(5486), 1897-1902.

Shanmugam, G., Spalding, T. D. and Rofheart, D. H., 1993. Process sedimentology and reservoir quality of deepmarine bottom-current reworked sands (sandy contourites): An example from the Gulf of Mexico: AAPG Bull., 77, 7, 1241-1259.

Shipboard Scientific Party, 2004. Site 1258. In Erbacher, J., Mosher, D.C., Malone, M.J., et al., Proc. ODP, Init. Repts., 207: College Station, TX (Ocean Drilling Program), 1-117. Shipboard Scientific Party, 2004. Site 1260. In: Erbacher, J., D.C., Mosher, M.J., Malone, Proc. ODP, Init. Repts., 207: College Station, TX (Ocean Drilling Program), 113, 1-35.

Sial, A.N., Chen, J., Lacerda, L.D., Frei, R., Tewari, V.C., Pandit, M.K., Gaucher, C., Ferreira, V.P., Cirilli, S., Peralta, S. and Korte, C., 2016. Mercury enrichment and Hg isotopes in Cretaceous-Paleogene boundary successions: Links to volcanism and

palaeoenvironmental impacts. Cretac. Res., 66, 60-81.

Sial, A.N., Chen, J., Lacerda, L.D., Peralta, S., Gaucher, C., Frei, R., Cirilli, S., Ferreira, V.P., Marquillas, R.A., Barbosa, J.A. and Pereira, N.S., 2014. High-resolution Hg chemostratigraphy: A contribution to the distinction of chemical fingerprints of the Deccan volcanism and Cretaceous-Paleogene Boundary impact event. Palaeogeogr. Palaeoclimatol. Palaeoecol., 414, 98-115.

Sial, A.N., Lacerda, L.D., Ferreira, V.P., Frei, R., Marquillas, R.A., Barbosa, J.A., Gaucher, C., Windmöller, C.C. and Pereira, N.S., 2013. Mercury as a proxy for volcanic activity during extreme environmental turnover: The Cretaceous-Paleogene transition. Palaeogeogr. Palaeoclimatol. Palaeoecol., 387, 153-164.

Siebert, C., Nägler, T.F., von Blanckenburg, F. and Kramers, J.D., 2003. Molybdenum isotope records as a potential new proxy for palaeoceanography. Earth Planet. Sci. Lett., 211(1), 159-171.

Sigvaldason, G.E., Annertz, K. and Nilsson, M., 1992. Effect of glacier loading/deloading on volcanism: postglacial volcanic production rate of the Dyngjufjöll area, central Iceland. Bull. of Volcanology, 54(5), 385-392.

Sinha, M.C., Louden, K.E. and Parsons, B., 1981. The crustal structure of the Madagascar Ridge. Geophys. J. Int., 66(2), 351-377.

Sinninghe Damsté, J.S. and Köster, J., 1998. A euxinic southern North Atlantic Ocean during the Cenomanian/Turonian oceanic anoxic event. Earth Planet. Sci. Lett., 158(3), 165-173.

Sinninghe Damsté, J.S., van Bentum, E.C., Reichart, G.J., Pross, J. and Schouten, S., 2010. A CO 2 decrease-driven cooling and increased latitudinal temperature gradient during the mid-Cretaceous Oceanic Anoxic Event 2. Earth Planet. Sci. Lett., 293(1), 97-103.

Sinton, C.W. and Duncan, R.A., 1997. Potential links between ocean plateau volcanism and global ocean anoxia at the Cenomanian-Turonian boundary. Economic Geology, 92(7-8), 836-842.

Sleep, N.H., 1990. Hotspots and mantle plumes: Some phenomenology. J. Geophys. Res.: Solid Earth, 95(B5), 6715-6736.

Sleep, N.H., 2006. Mantle plumes from top to bottom. Earth-Science Rev., 77(4), 231-271.

Slemr, F., Junkermann, W., Schmidt, R.W.H. and Sladkovic, R., 1995. Indication of change in global and regional trends of atmospheric mercury concentrations. Geophys. Res. Let., 22(16), 2143-2146.

Slingerland, R., Kump, L.R., Arthur, M.A., Fawcett, P.J., Sageman, B.B. and Barron, E.J., 1996. Estuarine circulation in the Turonian western interior seaway of North America. Geol. Soc. Am. Bull., 108(8), 941-952.

Sliter, W., Mompart, L. and Mural, B., 1999. Factors influencing organic carbon and trace metal accumulation in the Upper Cretaceous La Luna Formation of the

western Maracaibo Basin, Venezuela. Evolution of the Cretaceous ocean-climate system, 203.

Smetacek, V., Klaas, C., Strass, V.H., Assmy, P., Montresor, M., Cisewski, B., Savoye, N., Webb, A., d'Ovidio, F., Arrieta, J.M. and Bathmann, U., 2012. Deep carbon export from a Southern Ocean iron-fertilized diatom bloom. Nature, 487(7407), 313.

Smith, C.I., 1970a. Lower Cretaceous stratigraphy, northern Coahuila, Mexico. Bureau of Economic Geology, University of Texas.

Smith, C.I., 1970b. Lower Cretaceous sedimentation and tectonics of the Coahuila and West Texas platforms. In: Geologic framework of the Chihuahua tectonic belt: West Texas Geol. Soc.-Univ. Texas, Austin, 75-82.

Smith, C.I., 1981. Review of the geologic setting, stratigraphy, and facies distribution of the Lower Cretaceous in northern Mexico. Lower Cretaceous stratigraphy and structure, northern Mexico: West Texas Geol. Soc. Publ., 81-74.

Smith, C.I., Bloxsom, W.E., 1974. The Trinity division and equivalents of northern Coahuila. Mexico: Geoscience and Man, 8, 67-76.

Snow, L.J., Duncan, R.A. and Bralower, T.J., 2005. Trace element abundances in the Rock Canyon Anticline, Pueblo, Colorado, marine sedimentary section and their relationship to Caribbean plateau construction and oxygen anoxic event 2. Paleoceanog., 20(3).

Stephenson, L.W., 1929. Unconformities in upper Cretaceous series of Texas. AAPG Bull., 13(10), 1323-1334.

Steuber, T. and Rauch, M., 2005. Evolution of the Mg/Ca ratio of Cretaceous seawater: implications from the composition of biological low-Mg calcite. Mar. Geol., 217(3), 199-213.

Stewart, J.H., 1976. Late Precambrian evolution of North America: plate tectonics implication. Geology, 4(1), 11-15.

Stoll, H.M. and Schrag, D.P., 1996. Evidence for glacial control of rapid sea level changes in the Early Cretaceous. Science, 272(5269), 1771.

Stoll, H.M. and Schrag, D.P., 2000. High-resolution stable isotope records from the Upper Cretaceous rocks of Italy and Spain: Glacial episodes in a greenhouse planet?. Geol. Soc. Am.Bull., 112(2), 308-319.

Stoll, H.M. and Schrag, D.P., 2001. Sr/Ca variations in Cretaceous carbonates: relation to productivity and sea level changes. Palaeogeogr. Palaeoclimatol. Palaeoecol., 168(3), 311-336.

Storey, M., Mahoney, J.J., Saunders, A.D., Duncan, R.A., Kelley, S.P. and Coffin, M.F., 1995. Timing of hot spot-related volcanism and the breakup of Madagascar and India. Science, 267, 852-852.

Stow, D. A. V., 1994. Deep sea processes of sediment transport and deposition, in

K. Pye, ed., Sediment transport and depositional processes: Oxford, United Kingdom, Blackwell Scientific, 257-291.

Stow, D. A. V., Faugeres, J. C., Howe, J. A., Pudsey, C. J. and Viana, A. R., 2002. Bottom currents, contourites and deep-sea sediment drifts: Current state-of-the-art: Geol. Soc., Lon., Mem., 22, 1, 7-20.

Summerhayes, C.P., 1987. Organic-rich Cretaceous sediments from the North Atlantic. Geol. Soc., Lon., Spec. Publ., 26(1), 301-316.

Sundby, B., Martinez, P. and Gobeil, C., 2004. Comparative geochemistry of cadmium, rhenium, uranium and molybdenum in continental margin sediments. Geochim. Cosmochim. Acta 68, 2485-2493.

Sunderland, E.M., Krabbenhoft, D.P., Moreau, J.W., Strode, S.A. and Landing, W.M., 2009. Mercury sources, distribution, and bioavailability in the North Pacific Ocean: Insights from data and models. Global Biogeochemical Cycles, 23(2).

Svensen, H., Planke, S., Chevallier, L., Malthe-Sørenssen, A., Corfu, F. and Jamtveit, B., 2007. Hydrothermal venting of greenhouse gases triggering Early Jurassic global warming. Earth Planet. Sci. Lett., 256(3), 554-566.

Tarduno, J.A., Sliter, W.V., Kroenke, L., Leckie, M., Mayer, H., Mahoney, J.J., Musgrave, R., Storey, M. and Winterer, E.L., 1991. Rapid formation of Ontong Java Plateau by Aptian mantle plume volcanism. Science, 254, 399-403.

Tegner, C., Storey, M., Holm, P.M., Thorarinsson, S.B., Zhao, X., Lo, C.H. and Knudsen, M.F., 2011. Magmatism and Eurekan deformation in the High Arctic Large Igneous Province: ^{40}Ar-^{39}Ar age of Kap Washington Group volcanics, North Greenland. Earth Planet. Sci. Lett., 303(3), 203-214.

Tegner, C., Storey, M., Holm, P.M., Thorarinsson, S.B., Zhao, X., Lo, C.H. and Knudsen, M.F., 2011. Magmatism and Eurekan deformation in the High Arctic Large Igneous Province: ^{40}Ar-^{39}Ar age of Kap Washington Group volcanics, North Greenland. Earth Planet. Sci. Lett., 303(3), 203-214.

Tejada, M.L.G., Suzuki, K., Kuroda, J., Coccioni, R., Mahoney, J.J., Ohkouchi, N., Sakamoto, T. and Tatsumi, Y., 2009. Ontong Java Plateau eruption as a trigger for the early Aptian oceanic anoxic event. Geology, 37(9), 855-858.

Tessin, A., Sheldon, N.D., Hendy, I. and Chappaz, A., 2016. Iron limitation in the Western Interior Seaway during the Late Cretaceous OAE 3 and its role in phosphorus recycling and enhanced organic matter preservation. Earth Planet. Sci. Lett., 449, 135-144.

Thibodeau, A.M., Ritterbush, K., Yager, J.A., West, A.J., Ibarra, Y., Bottjer, D.J., Berelson, W.M., Bergquist, B.A. and Corsetti, F.A., 2016. Mercury anomalies and the timing of biotic recovery following the end-Triassic mass extinction. Nature Comm., 7.

Thordarson, T. and Self, S., 2003. Atmospheric and environmental effects of the 1783-1784 Laki eruption: A review and reassessment. J. Geophys. Res.: Atmo-

spheres, 108(D1).

Thordarson, T., 2004. Accretionary-lapilli-bearing pyroclastic rocks at ODP Leg 192 Site 1184: a record of subaerial phreatomagmatic eruptions on the Ontong Java Plateau. Geol. Soc., Lon., Spec. Publ., 229(1), 275-306.

Tibert, N.E., Leckie, R.M., Eaton, J.G., Kirkland, J.I., Colin, J.P., Leithold, E.L. and Mccormic, M.E., 2003. Recognition of relative sea-level change in Upper Cretaceous coal-bearing strata: a paleoecological approach using agglutinated Foraminifera and ostracodes to detect key stratigraphic surfaces.

Tiedemann, R., Sarnthein, M. and Shackleton, N.J., 1994. Astronomic timescale for the Pliocene Atlantic δ^{18}O and dust flux records of Ocean Drilling Program Site 659. Paleoceanog., 9(4), 619-638.

Tissot, B.P. and Welte, D.H., 1984. Diagenesis, catagenesis and metagenesis of organic matter. In Petroleum Formation and Occurrence, 69-73. Springer Berlin Heidelberg.

Torsvik, T.H., Tucker, R.D., Ashwal, L.D., Carter, L.M., Jamtveit, B., Vidyadharan, K.T. and Venkataramana, P., 2000. Late Cretaceous India-Madagascar fit and timing of breakup related magmatism. Terra Nova, 12(5), 220-224.

Torsvik, T.H., Tucker, R.D., Ashwal, L.D., Eide, E.A., Rakotosolofo, N.A. and De Wit, M.J., 1998. Late Cretaceous magmatism in Madagascar: palaeomagnetic evidence for a stationary Marion hotspot. Earth Planet. Sci. Lett., 164(1), 221-232.

Trabucho Alexandre, J., Tuenter, E., Henstra, G.A., van der Zwan, K.J., van de Wal, R.S., Dijkstra, H.A. and de Boer, P.L., 2010. The midCretaceous North Atlantic nutrient trap: Black shales and OAEs. Paleoceanog., 25(4).

Trevino, R.H. and Smith, C.I., 1988. Facies and depositional environments of the Boquillas Formation. Upper Cretaceous of southwest Texas: MS thesis, University of Texas at Arlington.

Tribovillard, N., Algeo, T.J., Lyons, T. and Riboulleau, A., 2006. Trace metals as paleoredox and paleoproductivity proxies: an update. Chem. Geol., 232(1), 12-32.

Tribovillard, N., Riboulleau, A., Lyons, T. and Baudin, F., 2004a. Enhanced trapping of molybdenum by sulfurized organic matter of marine origin as recorded by various Mesozoic formations. Chem. Geol. 213, 385-401.

Tribovillard, N., Trentesaux, A., Ramdani, A., Baudinet, F. and Riboulleau, A., 2004b. Controls on organic accumulation in late Jurassic shales of northwestern Europe as inferred from trace-metal geochemistry. Bull. de la Société géologique de France, 175(5), 491-506.

Tsikos, H., Jenkyns, H.C., Walsworth-Bell, B., Petrizzo, M.R., Forster, A., Kolonic, S., Erba, E., Silva, I.P., Baas, M., Wagner, T. and Sinninghe Damsté, J.S., 2004. Carbon-isotope stratigraphy recorded by the Cenomanian-Turonian Oceanic Anoxic Event: correlation and implications based on three key localities. J. Geol. Soc., 161(4), 711-719.

Turgeon, S. and Brumsack, H.J., 2006. Anoxic vs dysoxic events reflected in sediment geochemistry during the Cenomanian-Turonian Boundary Event (Cretaceous) in the Umbria-Marche Basin of central Italy. Chem. Geol., 234(3), 321-339.

Turgeon, S.C. and Creaser, R.A., 2008. Cretaceous oceanic anoxic event 2 triggered by a massive magmatic episode. Nature, 454(7202), 323.

Underhill, J.R. and Paterson, S., 1998. Genesis of tectonic inversion structures: seismic evidence for the development of key structures along the Purbeck-Isle of Wight Disturbance. J. Geol. Soc., 155(6), 975-992.

Vahrenkamp, V.C., Franssen, R.C.M.W., Grotsch, J. and Munoz, P.J., 1993. Maracaibo Platform (Aptian-Albian), northwestern Venezuela. In: Cretaceous Carbonate Platforms (Eds) T.J.A. Simo, R.W. Scott and J.P. Masse, AAPG Mem. 56, 25-33.

van Beek, P., Reyss, J.L., Bonte, P. and Schmidt, S., 2003. Sr/Ba in barite: a proxy of barite preservation in marine sediments? Mar. Geol., 199(3), 205-220.

van Bentum, E.C., Hetzel, A., Brumsack, H.J., Forster, A., Reichart, G.J. and Sinninghe Damsté, J.S., 2009. Reconstruction of water column anoxia in the equatorial Atlantic during the Cenomanian-Turonian oceanic anoxic event using biomarker and trace metal proxies. Palaeogeogr. Palaeoclimatol. Palaeoecol., 280(3), 489-498.

van Buchem, F.S., Razin, P., Homewood, P.W., Philip, J.M., Eberli, G.P., Platel, J.P., Roger, J., Eschard, R., Desaubliaux, G.M., Boisseau, T. and Leduc, J.P., 1996. High resolution sequence stratigraphy of the Natih Formation (Cenomanian/Turonian) in northern Oman: distribution of source rocks and reservoir facies. GeoArabia, 1(1), 65-91.

van Helmond, N.A., Papadomanolaki, N.M., Plint, A.G., Gröcke, D.R., Pearce, M.A. and Eldrett, J.S., 2016. Equatorward phytoplankton migration during a cold spell within the Late Cretaceous super-greenhouse. Biogeosciences, 13(9), p.2859.

van Helmond, N.A., Sluijs, A., Reichart, G.J., Sinninghe Damsté, J.S., Slomp, C.P. and Brinkhuis, H., 2014. A perturbed hydrological cycle during Oceanic Anoxic Event 2. Geology, 42(2), 123-126.

van Ledden, M., Van Kesteren, W.G.M. and Winterwerp, J.C., 2004. A conceptual framework for the erosion behaviour of sand-mud mixtures. Cont. Shelf. Res., 24(1), 1-11.

Voigt, S., Gale, A.S. and Flögel, S., 2004. Midlatitude shelf seas in the Cenomani-anTuronian greenhouse world: Temperature evolution and North Atlantic circulation. Paleoceanog., 19(4).

Vorlicek, T.P., Kahn, M.D., Kasuza, Y. and Helz, G.R., 2004. Capture of molybdenum in pyrite-forming sediments: role of ligand-induced reduction by polysulfides. Geochim. Cosmochim. Acta 68, 547-556.

Wagner, T., Hofmann, P. and Flgel, S., 2013. Marine black shale deposition and Hadley Cell dynamics: A conceptual framework for the Cretaceous Atlantic Ocean. Marine and Petroleum Geology, 43, 222-238. Waite, L.E., Scott, R.W. and Kerans,

C., 2007. Middle Albian age of the regional dense marker bed of the Edwards Group, Pawnee Field, south-central Texas. Trans. Gulf Coast Assoc. Geol. Soc., 57, 759-774.

Waitt, R.B. and Dzurisin, D., 1980. Proximal air-fall deposits from the May 18 eruption-stratigraphy and field sedimentology. US Geological Survey Professional Paper 19811982, Report 1250, 1982, 601-616.

Watson, A.J., 1997. Volcanic iron, CO2, ocean productivity and climate. Nature, 385(6617), 587.

Webster, R. E., 1980, Structural analysis of Devils River Upliftsouthern Val Verde Basin, southwest Texas: AAPG Bull., 64, 10, 221-241.

Weissert, H. and Lini, A., 1991. Ice age interludes during the time of Cretaceous greenhouse climate. Controversies in Modern Geology. Academic Press, Lon., 173, 191.

Weissert, H., 2000. Deciphering methane's fingerprint. Nature, 406(6794), 356-357.

Wells, M.L. and Hoisch, T.D., 2008. The role of mantle delamination in widespread Late Cretaceous extension and magmatism in the Cordilleran orogen, western United States. Geol. Soc. Am. Bull., 120(5-6), 515-530.

Wendler, J.E., Wendler, I., Vogt, C., Kuss, J., 2016. Link between cyclic eustatic sea-level change and continental weathering: Evidence for aquifer-eustasy in the Cretaceous. Palaeogeography, Palaeoclimatology, Palaeoecology, 441, 430-437.

Westphal, H., Hilgen, F. and Munnecke, A., 2010. An assessment of the suitability of individual rhythmic carbonate successions for astrochronological application. Earth-Sci. Rev. 99, 19-30.

Whalin, L., Kim, E.H. and Mason, R., 2007. Factors influencing the oxidation, reduction, methylation and demethylation of mercury species in coastal waters. Mar. Chem., 107(3), 278-294.

White, R. and McKenzie, D., 1989. Magmatism at rift zones: the generation of volcanic continental margins and flood basalts. J. Geophys. Res.: Solid Earth, 94(B6), 7685-7729.

Whitfield, M., 2002. Interactions between phytoplankton and trace metals in the ocean. Adv. Mar. Biol. 41, 3-120.

Wigley, T.M. and Raper, S.C.B., 1987. Thermal expansion of sea water associated with global warming. Nature, 330(6144), 127-131.

Wignall, P., 2005. The link between large igneous province eruptions and mass extinctions. Elements, 1(5), 293-297.

Wignall, P.B., 2001. Large igneous provinces and mass extinctions. Earth Sci. Rev., 53(1), 1-33.

Wilbert, W.P., 1966. Stratigraphy of the Georgetown Formation, Bell, Williamson and Travis counties, Texas. GCAGS 11, 15-24.

Wilson, P.A. and Norris, R.D., 2001. Warm tropical ocean surface and global anoxia during the mid-Cretaceous period. Nature, 412(6845), 425.

Wilson, P.A., Norris, R.D. and Cooper, M.J., 2002. Testing the Cretaceous greenhouse hypothesis using glassy foraminiferal calcite from the core of the Turonian tropics on Demerara Rise. Geology, 30(7), 607-610.

Winker, C.D., and R.T. Buffler, 1988. Paleogeographic evolution of early deep-water Gulf of Mexico and margins, Jurassic to Middle Cretaceous (Comanchaean). AAPG Bull., 72, 318-346.

Winter, J.A., 1961. Stratigraphy of the lower Cretaceous (subsurface) of South Texas. Trans. GCAGS. 11, 15-24

Witt, M.L.I., Mather, T.A., Pyle, D.M., Aiuppa, A., Bagnato, E. and Tsanev, V.I., 2008. Mercury and halogen emissions from Masaya and Telica volcanoes, Nicaragua. J. Geophys. Res.: Solid Earth, 113(B6).

Young, H.P. and Lee, C.T., 2009. Fluid-metasomatized mantle beneath the Ouachita belt of southern Laurentia: Fate of lithospheric mantle in a continental orogenic belt. Lithosphere, 1(6).

Young, K., 1977. Guidebook to the geology of Travis County. University of Texas at Austin: The Student Geol. Soc., 171.

Young, K., 1986. Cretaceous, marine inundations of the San Marcos platform, Texas. Cretac. Res., 7(2), 117-140.

Zheng, X.Y., Jenkyns, H.C., Gale, A.S., Ward, D.J. and Henderson, G.M., 2013. Changing ocean circulation and hydrothermal inputs during Ocean Anoxic Event 2 (Cenomanian-Turonian): evidence from Nd-isotopes in the European shelf sea. Earth Planet. Sci. Lett., 375, 338-348.

Zheng, X.Y., Jenkyns, H.C., Gale, A.S., Ward, D.J. and Henderson, G.M., 2016. A climatic control on reorganization of ocean circulation during the mid-Cenomanian event and Cenomanian-Turonian oceanic anoxic event (OAE 2): Nd isotope evidence. Geology, 44(2), 151-154.

Zheng, Y., Anderson, R.F., van Geen, A. and Fleisheir, M.Q., 2002a. Preservation of non-lithogenic particulate uranium in marine sediments. Geochim. Cosmochim. Acta 66, 3085-3092.

Zheng, Y., Anderson, R.F., van Geen, A. and Fleisheir, M.Q., 2002b. Remobilization of authigenic uranium in marine sediments by bioturbation. Geochim. Cosmochim. Acta 66, 1759-1772.

Zumberge, J.E., 1984. Source rocks of the La Luna Formation (Upper Cretaceous) in the Middle Magdalena Valley, Colombia.

8 Appendix

Appendix A: Supplementary Figures and Material for Chapters 3 and 5

Diagenesis

Based on the thin section petrography of this study, diagenetic constituents are generally minor in the Lower and Upper Eagle Ford and moderate in the Buda Formation, they consist of a calcite cement, authigenic kaolinite, pyrite, and bitumen. Calcite is the most common cement, mainly filling intraskeletal pores and foraminifer chambers (Figure 8.1AB). Authigenic kaolinite is present in small amounts and also fills foraminifer chambers in some samples (Figure 8.2B; Kaol). Authigenic pyrite fills intraskeletal pores, displaces the matrix, and is associated with organic matter (Figure 8.1AB, 8.2B). Bitumen is found to partially fill some skeletal grains and can be seen as a dark-brown stain within chambers previously filled with kaolinite (Figure 8.1B, 8.3B). Localized, rhombic dolomite crystals replace the matrix in several of the Buda Limestone samples (Figure 8.4AB). Some samples show sharp contacts between dolomite-rich and dolomite-poor beds (Figure 8.4A) while others exhibit a gradational contact between the dolomite-rich and dolomite-poor beds (Figure 8.5A). Many thin section samples contain dolomite grains that exhibit a pinkish hue. However, identification is possible due to the rhombic nature of the crystals which is characteristic of authigenic dolomite (Figure 8.5B). In addition to cementation, the results of this study suggest that both compaction and pressure dissolution also occurred and resulted in a number of samples exhibiting microstylolites, which are defined by the concentration of mostly organic matter and pyrite (Figure 8.6AB). Many exhibit dogtooth structures that are over two millimeters in width (Figure 8.6A). Fractures are also abundant in the Buda Limestone. Some of these fractures are calcite-filled while others are very fine, open hairline fractures. Early stage fractures appear to be mostly cemented and vertical (Figure 8.7AB). Late-stage hairline

microfractures are observed in various orientations (Figure 8.7AB).

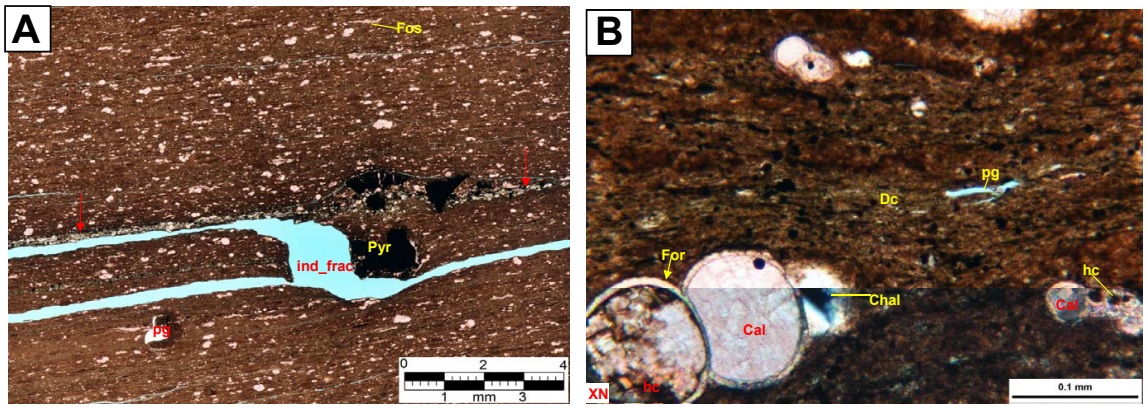

Figure 8.1: Argillaceous foraminiferal wackestone from the Upper Eagle Ford. Several fossil fragments, including planktonic foraminifers (For) and undifferentiated fossil fragments (Fos), show similar alignment to parallel, mostly pyritized, silty laminae (possibly volcanic ash layers; red arrows). Foraminifers are cemented by calcite (Cal), kaolinite, and pyrite and/or hydrocarbons (dead oil; hc); note large pyritized phosphatic grains in Photo A (Pyr). Photo B shows an area of the sample taken in plain polarized light (upper; PPL) and cross polarized light (lower; XL). Cross polarization shows chalcedony (Chal) and hydrocarbons (hc) in a few of the foraminifer chambers. Mixtures of detrital clay (Dc) and micrite (some being possibly peloidal in origin) dominate the matrix. A few dolomite rhombs and pyrite framboids are observed displacing the matrix. Rare pores are evident and are due to the dissolution of a few siliceous-rich, discontinuous laminae. Note sample damage: (ind_frac) and plucked grains (pg).

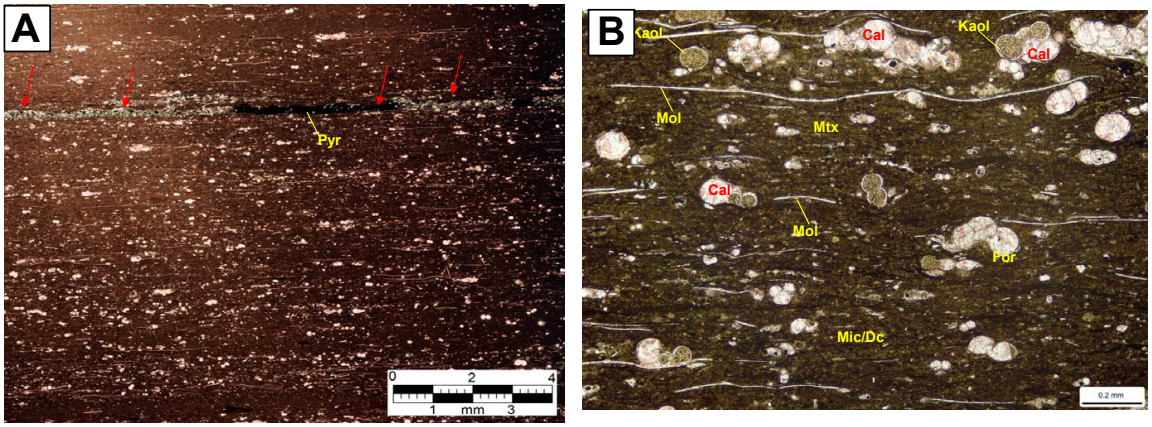

Figure 8.2: Argillaceous foraminiferal wackestone from the Upper Eagle Ford. This sample exhibits faint lamination defined by changes inallochem concentrations and the alignment of several elongated mollusk fragments (Mol). One continuous feldsparrich silt layer (red arrows) contains replacement cements that include pyrite (Pyr) and kaolinite. Besides elongated mollusk fragments, other skeletal grains include planktonic foraminifers (For) and spherical, undifferentiated skeletal grains, possibly calcispheres; note the abundance of calcite cement replacement within the fossil debris (Cal). Other authigenic minerals include kaolinite (filling foraminifer chambers; Kaol), pyrite (Pyr), and matrix-displacing dolomite and chert. This sample contains roughly equal amounts of micrite and detrital clay as the matrix (Mic/Dc). Under the petrographic microscope, these two matrix components are indistinguishable, appearing well mixed without obvious zonation. No open pores are visible.

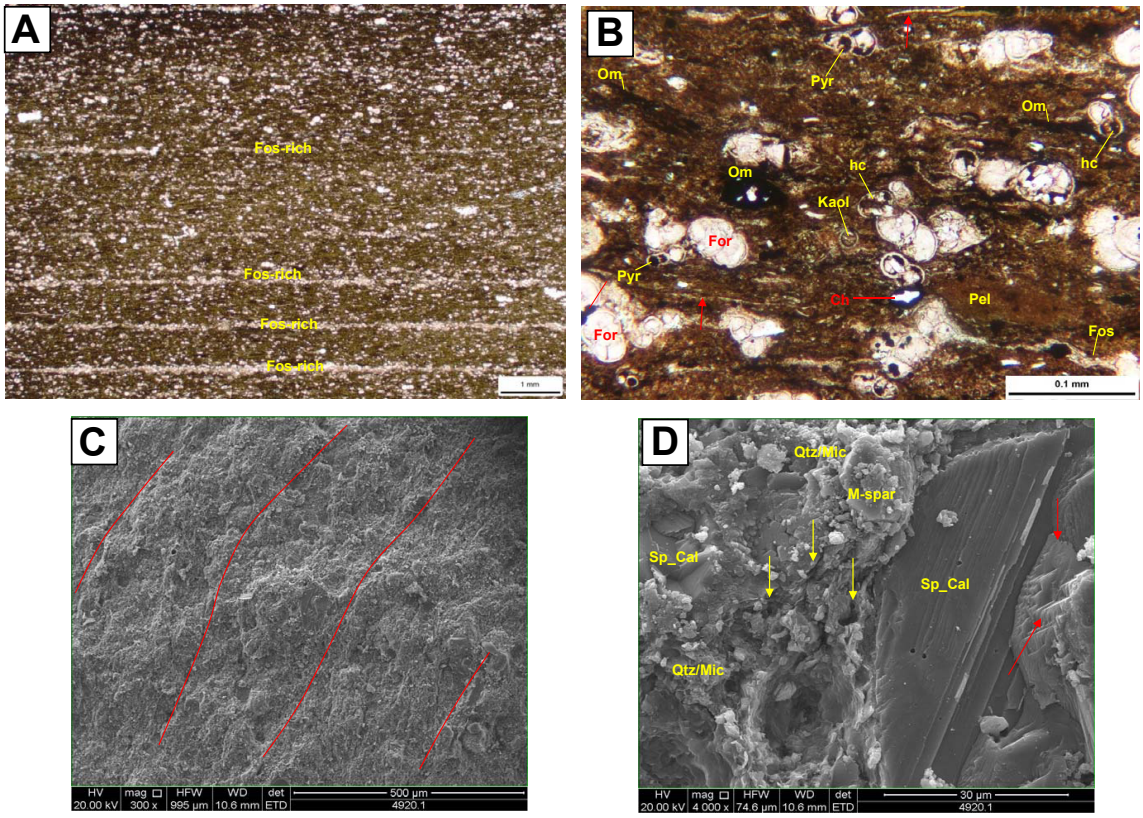

Figure 8.3: Laminated argillaceous foraminiferal wackestone from the Lower Eagle Ford. This sample is an organic-rich, argillaceous wackestone with a laminated fabric that resulted from alternating foram-rich laminae (Fos-rich) and foram-poor beds (Photo A). This sample contains the highest percentage of kerogen (9.9%) in the dataset. Organic material is dispersed throughout the matrix as wispy, discontinuous, organic-rich stringers (Om) that appear to thicken near allochem, outer skeletal borders. The most abundant allochems are planktonic foraminifers (For), characterized by thin, calcitic, tests with chambers cemented by calcite (Cal), kaolinite (Kaol), and pyrite (Pyr); note a chambers are stained dark brown due to hydrocarbons (hc). Mollusk fragments and unidentified skeletal grains are similarly aligned probably due to compaction (red arrows). Micritic peloids (Pel) are randomly dispersed and are lenticular due to compaction. Pyrite framboids and dolomite rhombs are dispersed throughout the matrix. Photo C is an SEM overview photo indicating a faintly laminated texture (Photo C; red lines) comprised of an abundant amount of matrix material. Higher magnification imagery in Photo D reveals a micritic matrix intermixed with a common amount of silt and clay-sized quartz (Qtz/Mic). Microspar (M-spar) and sparry calcite (Sp_Cal) are likely grain-replacing and are not part of the matrix. Thinly foliated, calcareous sheets (red arrows) surrounding sparry calcite-filled, spherical grains indicate the presence of planktonic foraminifers. Kerogen for this sample measures 9.9%. Micropores (yellow arrows) appear more abundant and faintly aligned with skeletal debris. Most are less than 10 microns in diameter.

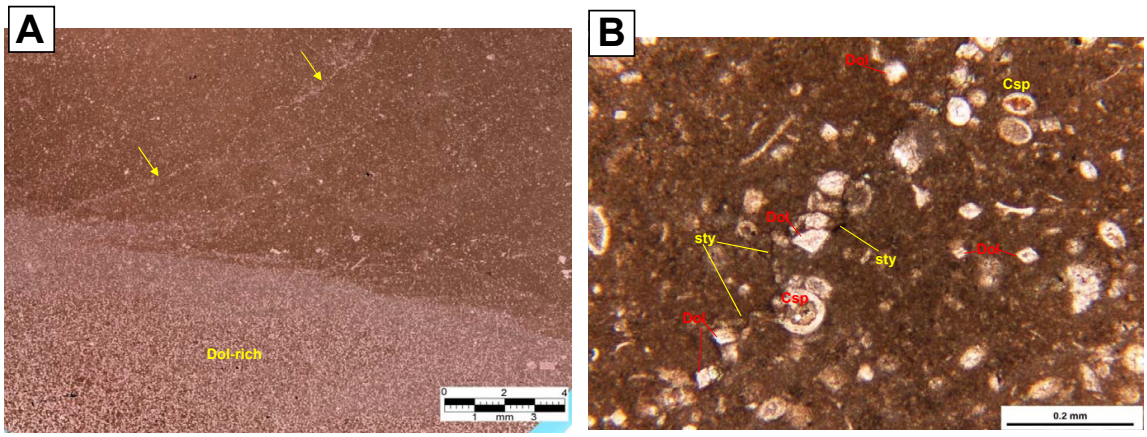

Figure 8.4: Calcispheral wackestone from the Buda Formation. This calcispheral dolomitic wackestone exhibits a sharp contact between a slightly dolomitic wackestone (upper portion in Photo A) and a pervasively replaced, dolomitic wackestone (lower portion of Photo A; Dol-rich). A later stage of diagenesis produced abundant amounts of finely crystalline, subhedral to euhedral floating dolomite rhombs (Dol) that is replacing both matrix and grains. Concentrated dolomite rhombs surround some microstylolites that appear to radiate from contact (yellow arrows). Photo B illustrates a higher magnification of such microstylolites (sty) and surrounding dolomite rhombs (Dol). Predominant grains are calcispheres (Csp) and lesser amounts of mollusk and unidentified skeletal grains. Calcite cement has replaced most grains and fills a few, open, discontinuous fractures (not pictured). Visible pores are only identified within one microfracture that occurs within the dolomitic-rich portion.

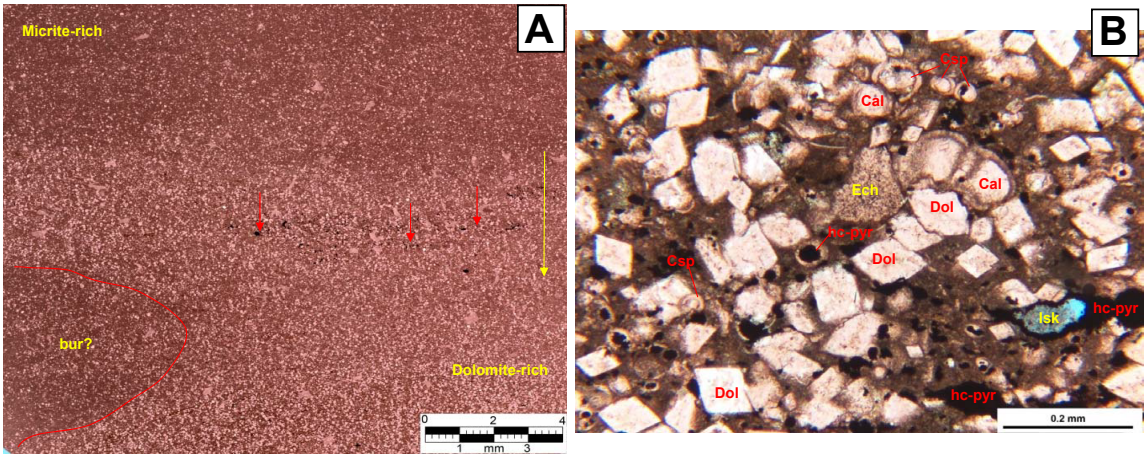

Figure 8.5: Calcispheral wackestone from the Buda Formation. This limestone exhibits a gradational increase of matrixreplacing dolomitic rhombs (yellow arrow in Photo A). Possible burrows occur within the dolomite-rich portion of the sample. Calcispheres (Csp) and unidentified skeletal grains show calcite cementation especially within their internal chambers (Cal). A few echinoderms (Ech) and foraminifers are also noted. Micrite matrix is abundant in over half of the sample in areas where dolomite replacement is less common. A later stage of diagenesis produced abundant amounts of medium crystalline, euhedral dolomite rhombs (Dol). Pyritized organic matter appears enclosed within several skeletal grains and is also present throughout the matrix (hcpyr). Heavier accumulations of these concretions occur in dolomite-rich sections of the sample. Trace intraskeletal pores (Isk) are noted.

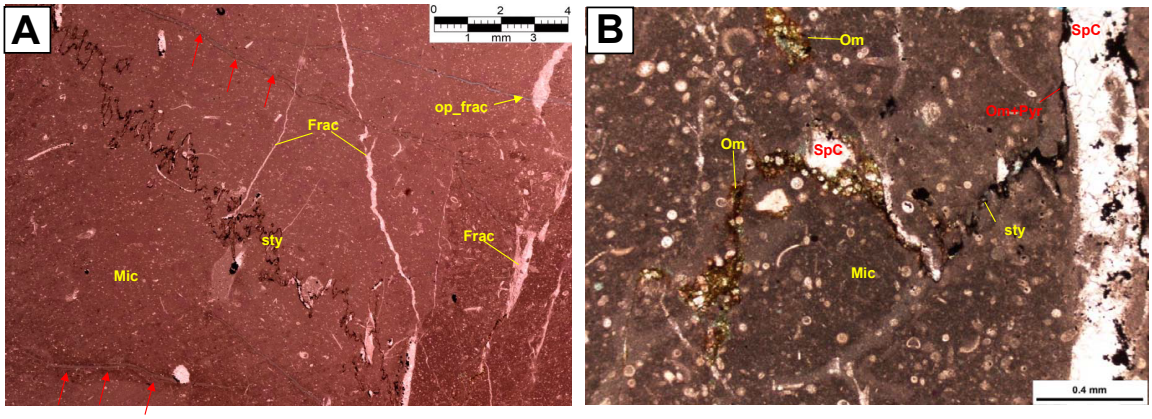

Figure 8.6: Skeletal packstone-wackestone from the Buda Formatio. Fractures of varying thicknesses, orientations, and lengths characterize this skeletal wackestone. Several open fractures (op_frac) are subparallel to organic-rich seams and stylolites (note the dogtooth structure indicating severe compaction; sty). The residual hydrocarbon composition varies and is most concentrated in the large stylolite (Om). Pyritization of the organic material tends to occur near cemented fractured areas (Om+Pyr) and within several allochem chambers. Calcite-cemented fractures (Frac) tend to crosscut open fractures, stylolites, and organic seams. Some cemented fractures show open, intercrystal porosity due to the continuation of newer, open fractures (op_frac). Sparry calcite is noted within cemented fractures (SpC) and is also the dominant mineral within recrystallized, undifferentiated allochems. Micrite matrix is abundant (Mic) The only visible pores are found within fractures.

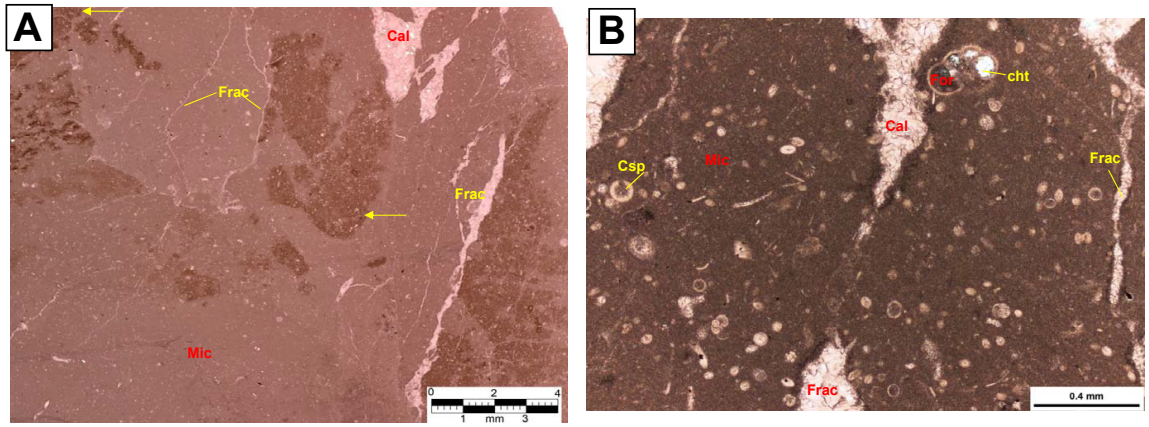

Figure 8.7: Calcispheral wackestone from the Buda Formation. This calcispheral wackestone's distinctive features are the multiple fractures (Frac). Some fracture sets cross others at oblique angles. Most fractures are filled with sparry and/or microsparry calcite (Cal). The splotchy appearance seen in Photo A is due to organic matter dispersed within the matrix (yellow arrows). Spherical calcispheres (Csp) are abundant, with minor to trace amounts of planktonic foraminifers (For) and mollusk fragments. Some of the foraminifer chambers are filled with micrite, whereas others are cemented with calcite or rarely, dolomite. Foraminiferal chambers are occasionally filled with authigenic quartz (chert; cht). Micrite matrix (Mic) is abundant. Macropores are absent. Only a few areas of micropores exist within the micritic matrix.

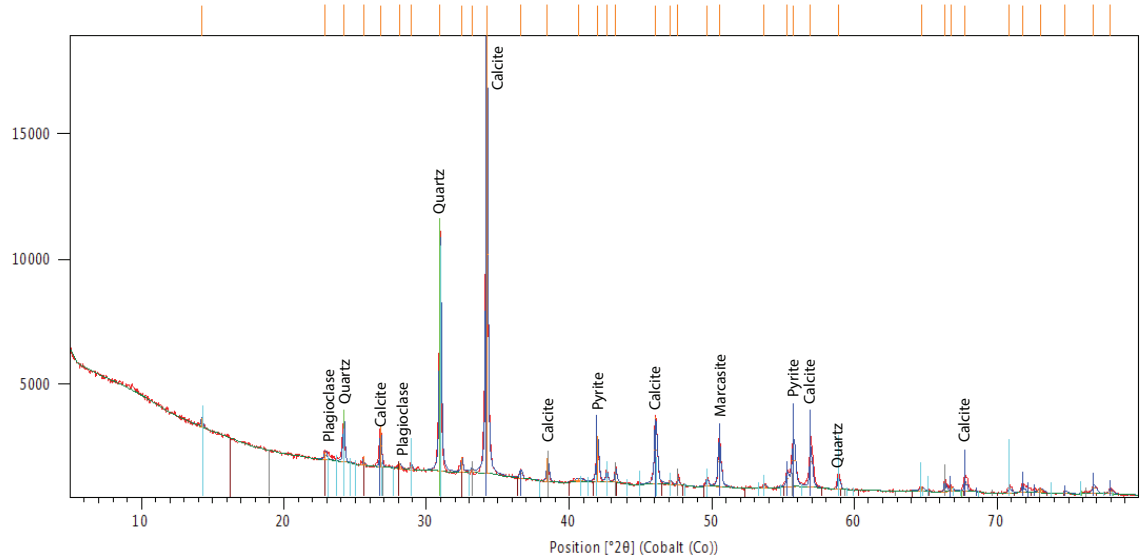

Figure 8.8: Bulk mineralogy XRD pattern from 1515.25 m in the Chittim-2H core showing typical patterns for large concentrations of calcite and quartz as well as smaller concentrations of pyrite and plagioclase.

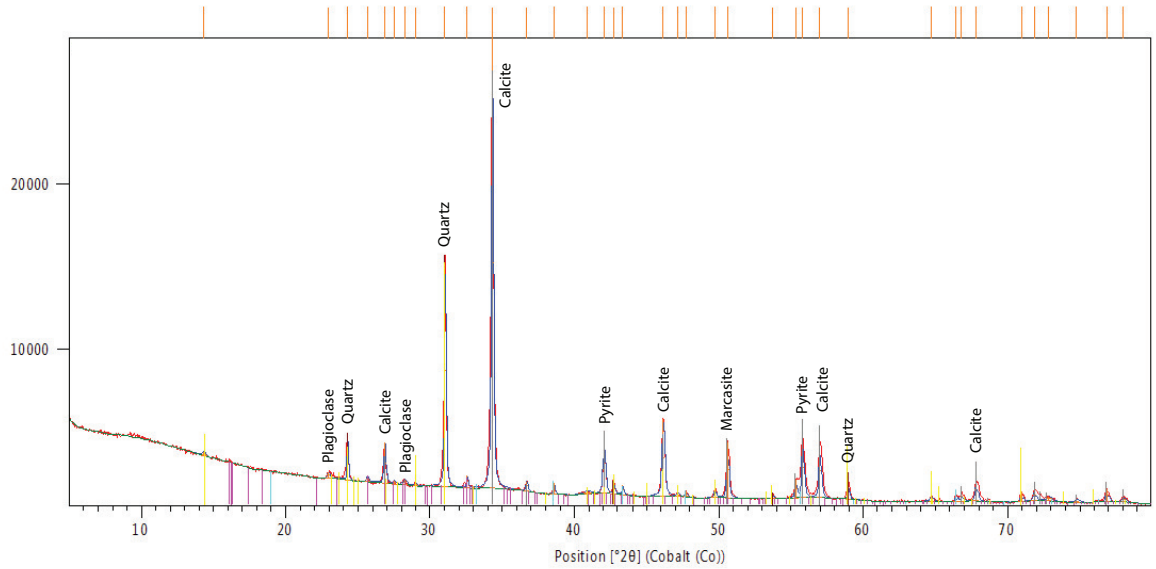

Figure 8.9: Bulk mineralogy XRD pattern from 145.90 m in the Innes-1 core showing typical patterns for large concentrations of calcite and quartz as well as smaller concentrations of pyrite, plagioclase and marcasite.

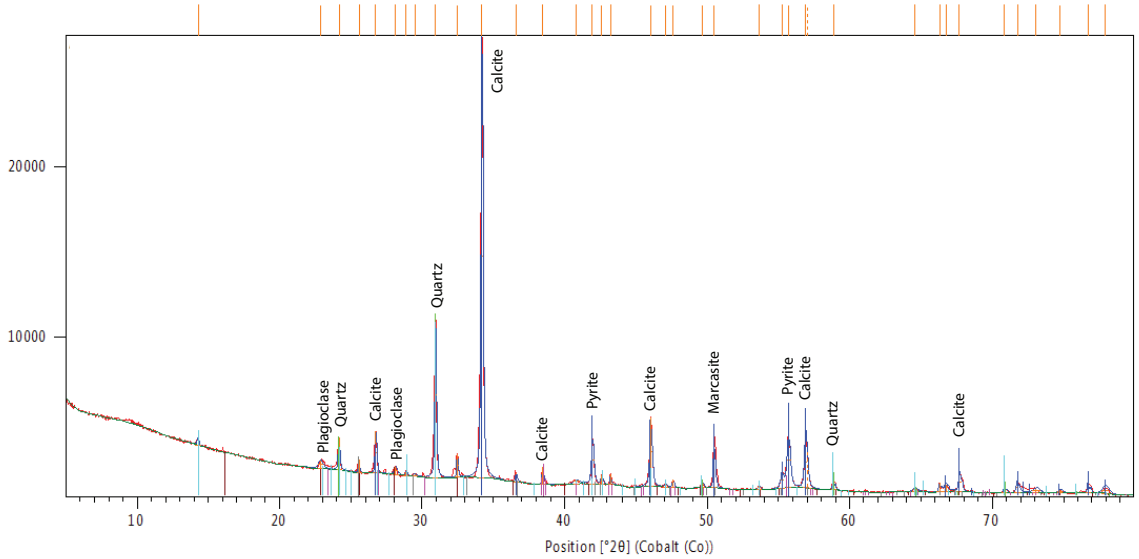

Figure 8.10: Bulk mineralogy XRD pattern from 72.37 m in the Iona-1 core showing typical patterns for large concentrations of calcite and quartz as well as smaller concentrations of pyrite, plagioclase and marcasite.

Appendix B: Supplementary Figures and Material for Chapter 4

Total Organic Carbon and Mercury

As the use of Hg to detect ancient major volcanic events is a relatively new technique the processes that effect the sequestration and concentration of Hg in sedimentary rocks are yet to be fully constrained. Therefore, its important to investigate potential mechanisms that may significantly effect Hg/TOC results in varying sedimentary records such as the thermogenic release of Hg. The Innes, Iona and Site 1258 cores exhibit a strong positive correlation between TOC and Hg (Figure 4.3). However, Chittim-2H displays a dramatic, exponential like increase in mercury at $\sim$7 wt%TOC. Chittim-2H is significantly more thermally mature than the other Western Interior Seaway cores (pers. comm. Lavern Stasiuk) with an average Tmax 30℃ higher than Innes-1 (see Figure 8.8) and a core from a very similar basinal position to Chittim-2H displays vitrinite reflectance data up to 1.0 R_o, which is 0.4 R_o higher than Innes-1 at similar stratigraphic levels (pers. comm. Lavern Stasiuk). The effects of increasing organic-matter maturity on Hg distributions is poorly understood and further work needs to be undertaken to understand how thermal maturity and subsequent thermogenic gaseous release may impact mercury distributions in these sediments. However, the volatility of mercury and its potential for thermogenic release during the magmatic intrusion of organic-rich shales, such as in the Karoo Basin (McElwain et al., 2005; Svensen et al., 2007) has been speculated as a source for significant flux of Hg to the atmosphere (Sanei et al., 2012; Percival et al., 2015). Though it would be expected that the maturation of an organic rich shale would result in the thermogenic release and migration of volatile mercury, counterintuitively it may actually act as a source and result in the concentration of mercury in the Chittim-2H core resulting in the significantly higher concentrations of Hg in this core in comparison to Innes-1 and Iona-1.

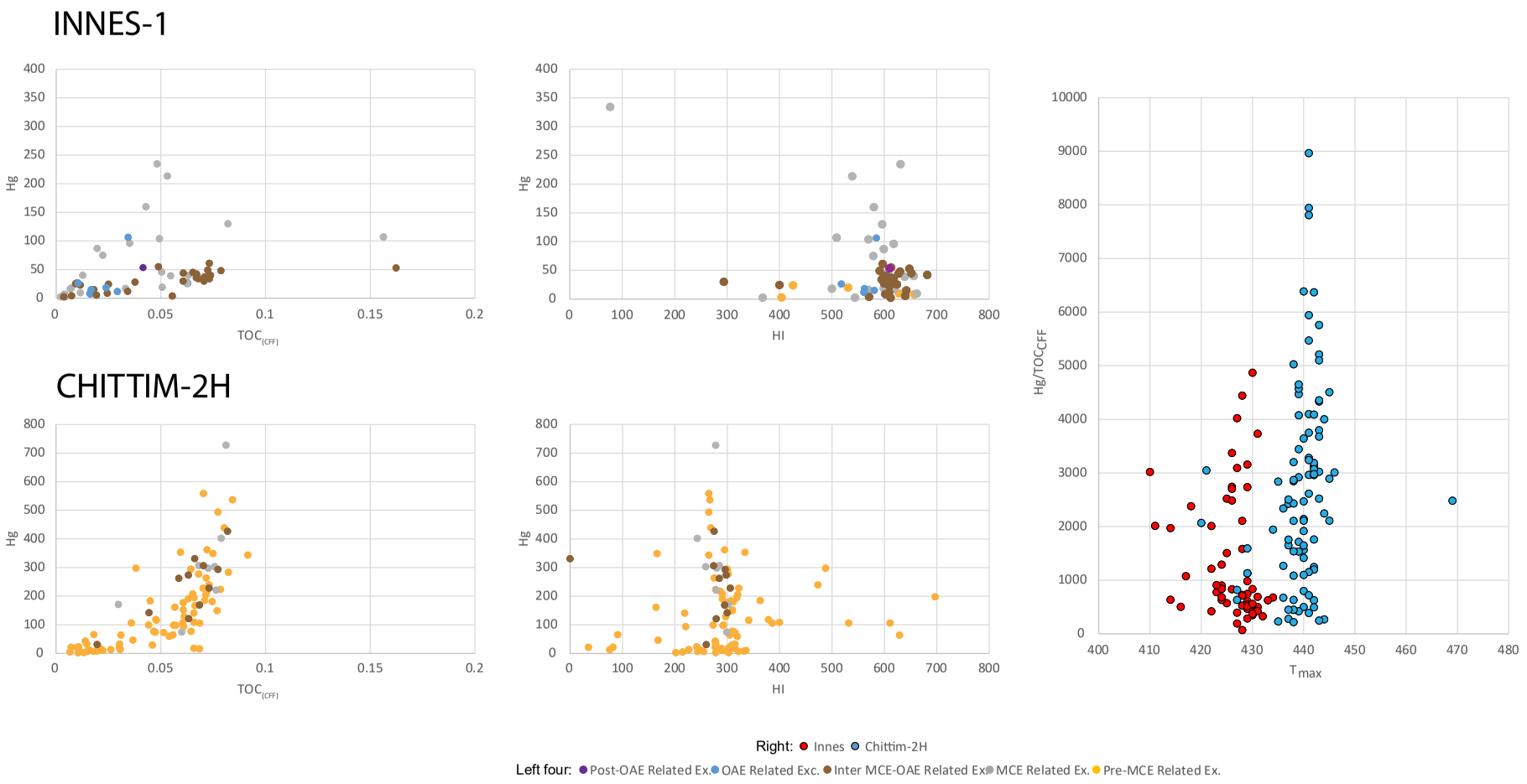

Figure 8.11: Crossplots between Hg and TOC_{CFF} (Carbonate-Free Fraction), Hi and T_{max} from the Innes-1 and Chittim-2H cores. The carbonate-free fraction is calculated by dividing TOC (wt%)by 100 minus the mineral carbonate (wt%)

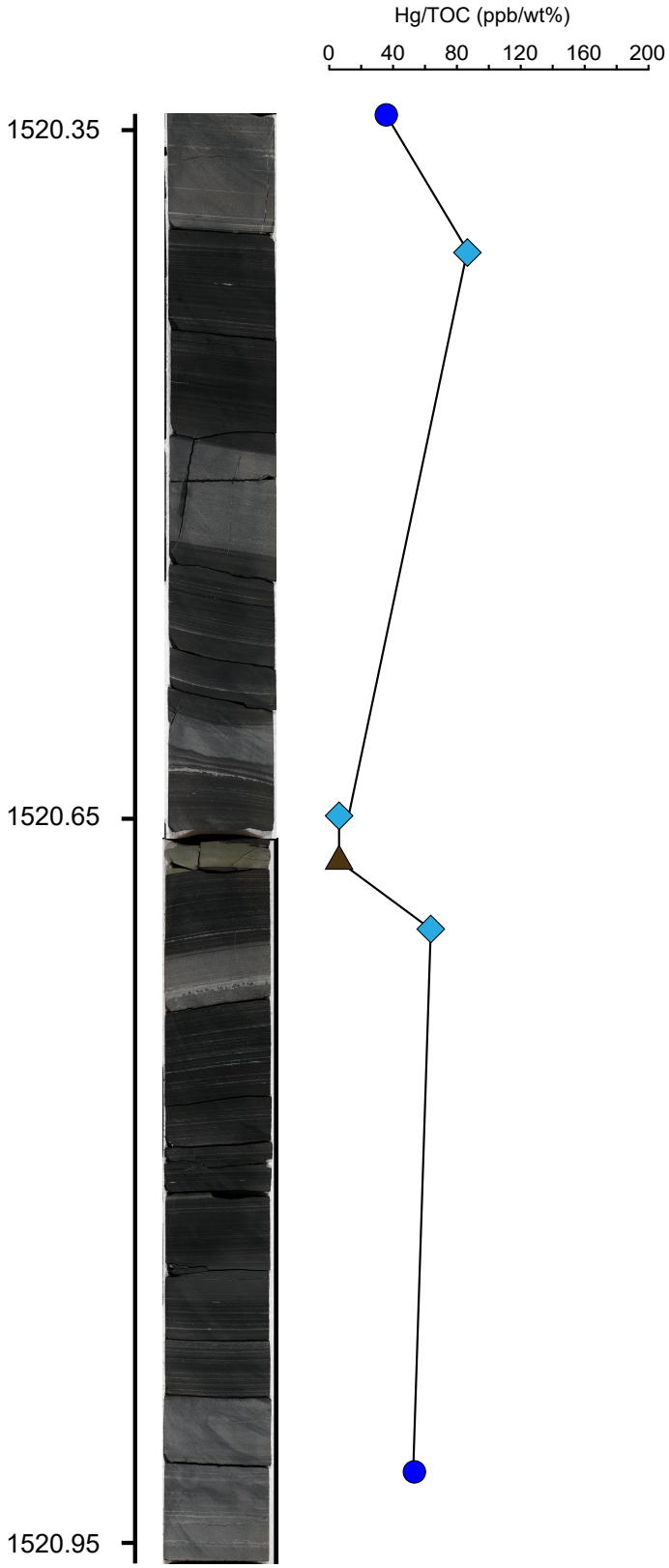

Figure 8.12: Sedimentary Hg values from the stratigraphical intervals directly pre- and succeeding a pronounced bentonite in the Chittim-2H sedimentary record.

Appendix C: Supplementary Figures and Material for Chapter 5

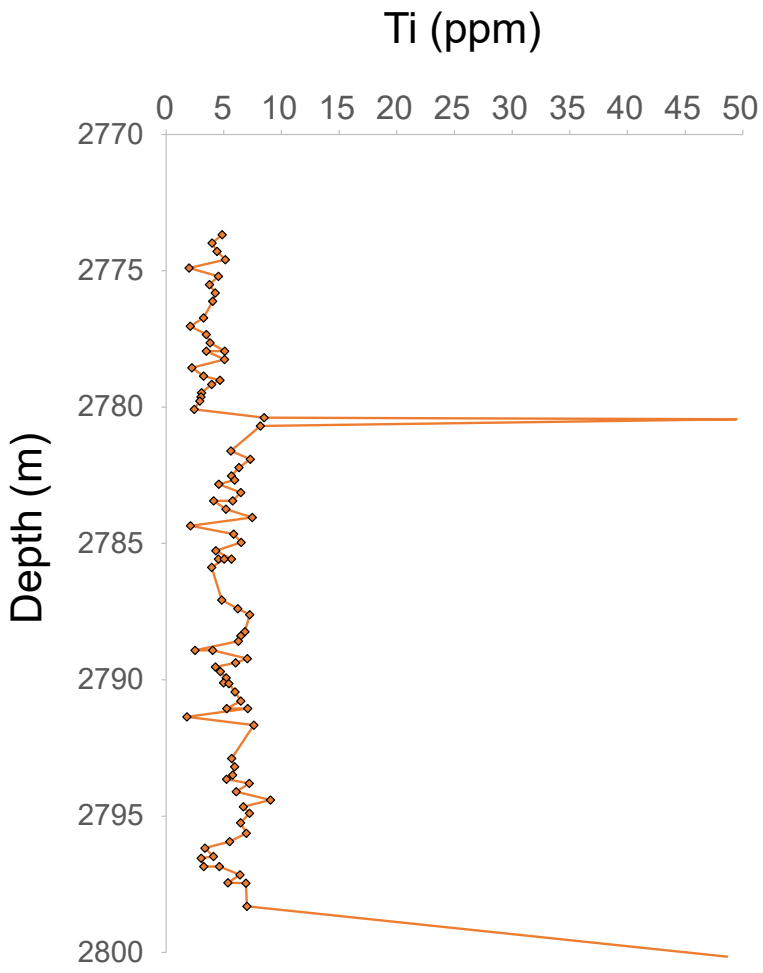

Figure 8.13: Ti (ppm) concentrations from the C4H core between 2800-2770 m.

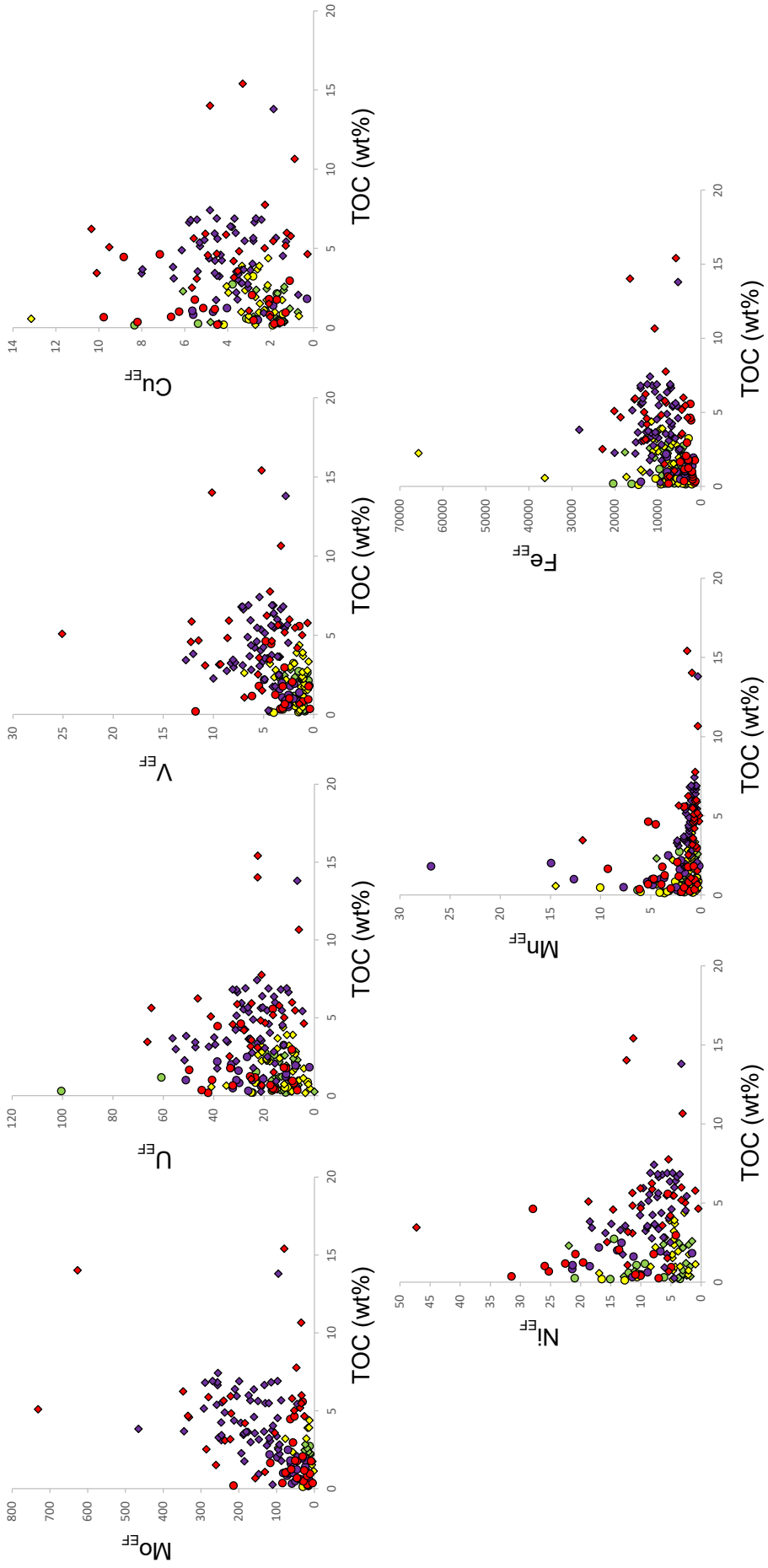

Figure 8.14:Total Organic Carbon (TOC) versus trace element enrichment factors (Mo_{EF}, V_{EF}, U_{EF}, Ni_{EF}, Cu_{EF}, Mn_{EF} and Fe_{EF}) from the Innes-1 core. TOC vs. trace element enrichment factor cross-plots show higher trace-element concentrations with higher TOC values. Cores are divided into depositional units: A is represented by red symbols, B is represented by purple symbols, C is represented by yellow symbols and D is represented by green symbols. Circles denote limestones, diamonds denote marlstones and triangles denote bentonites in all three cores. The XRF and TOC measurements compared in this diagram all correspond in sample depth or the Coulomat/Rock-Eval sample depth is within 1 cm vertical depth, upwards or downwards, of the XRF measurement taken on the slabbed archive core.

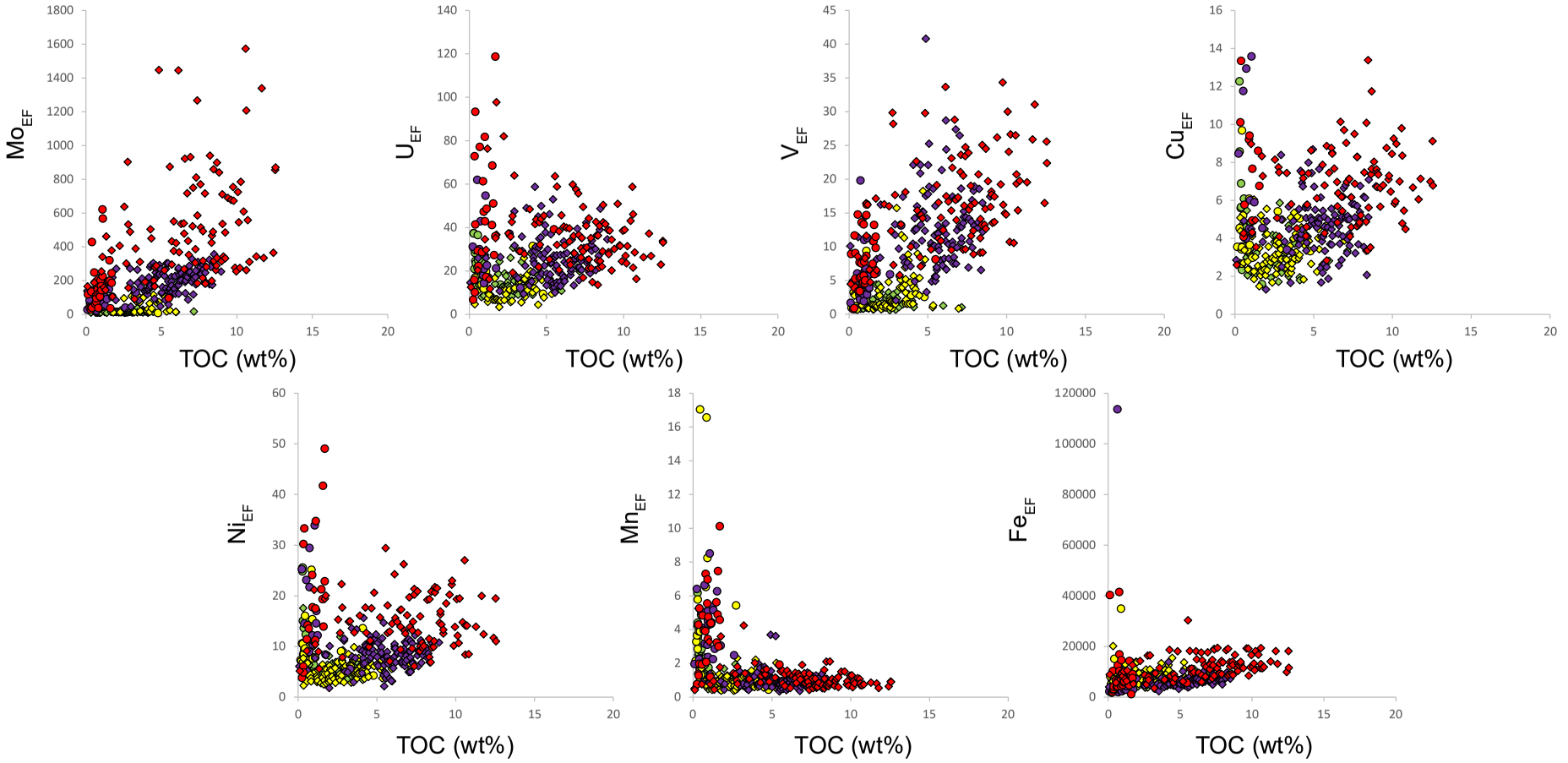

Figure 8.15: Total Organic Carbon (TOC) versus trace element enrichment factors (Mo_{EF}, V_{EF}, U_{EF}, Ni_{EF}, Cu_{EF}, Mn_{EF} and Fe_{EF}) from the Iona-1 core. TOC vs. trace element enrichment factor cross-plots show higher trace-element concentrations with higher TOC values. Cores are divided into depositional units: A is represented by red symbols, B is represented by purple symbols, C is represented by yellow symbols and D is represented by green symbols. Circles denote limestones, diamonds denote marlstones and triangles denote bentonites in all three cores. The XRF and TOC measurements compared in this diagram all correspond in sample depth or the Coulomat/Rock-Eval sample depth is within 1 cm vertical depth, upwards or downwards, of the XRF measurement taken on the slabbed archive core.

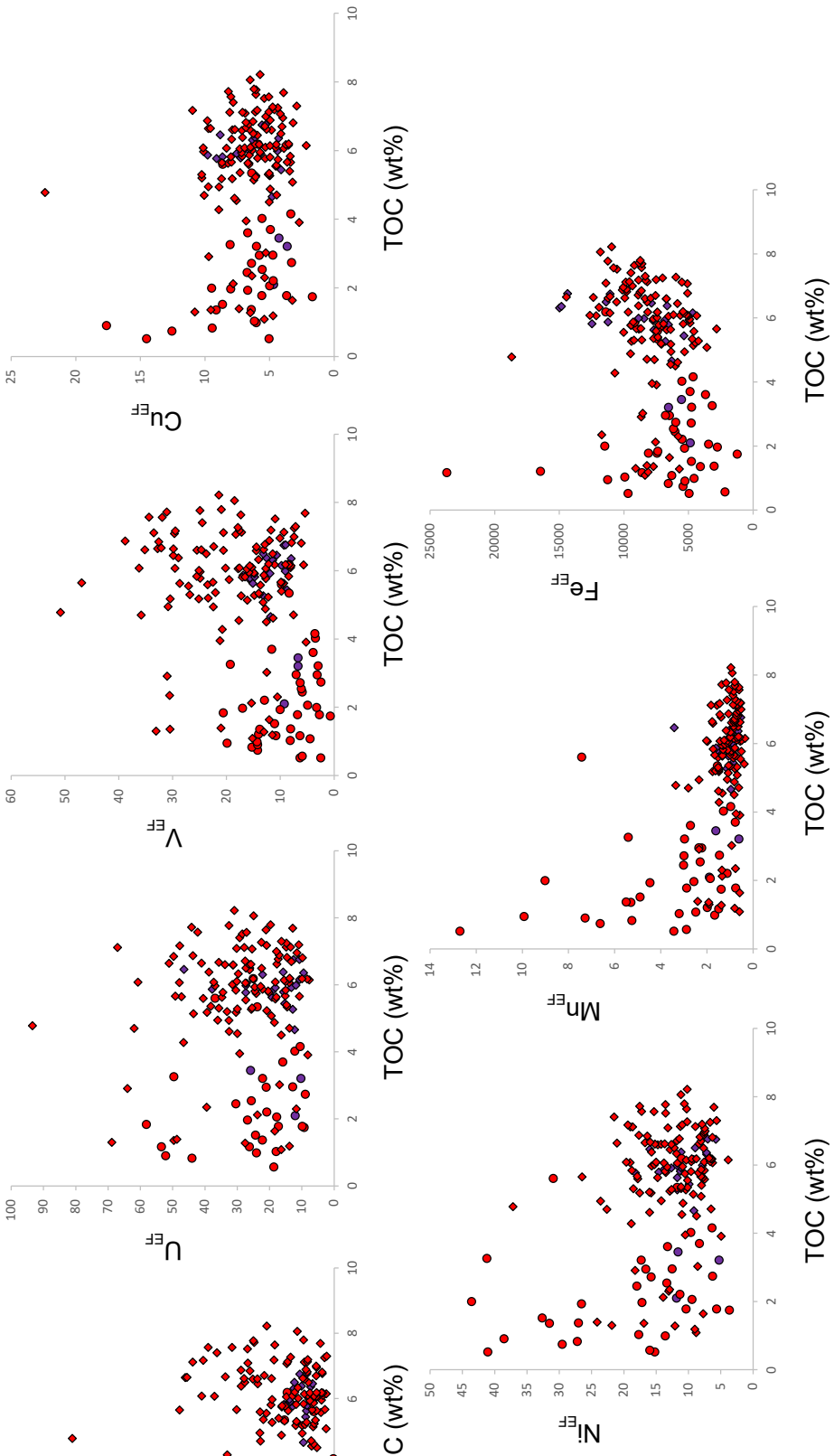

Figure 8.16: Total Organic Carbon (TOC) versus trace element enrichment factors (Mo_{EF}, V_{EF}, U_{EF}, Ni_{EF}, Cu_{EF}, Mn_{EF} and Fe_{EF}) from the Chittim-2H. TOC vs. trace element enrichment factor cross-plots show higher trace-element concentrations with higher TOC values. Cores are divided into depositional units: A is represented by red symbols, B is represented by purple symbols, C is represented by yellow symbols and D is represented by green symbols. Circles denote limestones, diamonds denote marlstones and triangles denote bentonites in all three cores. The XRF and TOC measurements compared in this diagram all correspond in sample depth or the Coulomat/Rock-Eval sample depth is within 1 cm vertical depth, upwards or downwards, of the XRF measurement taken on the slabbed archive core.

Appendix E: Data